Parametric Amplification, Shockwave Formation and Quasiparticle Generation in Superconducting Metamaterials

by
Searbhán Gearóid Ó Peatáin

This dissertation is submitted for the degree of
Doctor of Philosophy in Physics
from

Department of Physics, Lancaster University,
Lancaster, UK
and
Quantum Technologies Department,
National Physical Laboratory, Teddington, UK

March 2025

Declaration

I declare that that all research presented in this thesis is, to the best of my knowledge, my own original work. No material in this thesis has been submitted, either in whole or in part, for a degree at this, or any other university. This thesis has an approximate length of 73,000 words, including appendices and footnotes but excluding the bibliography, and therefore does not exceed the maximum permitted length of 80,000 words.

Searbhán Gearóid Ó Peatáin
March 2025

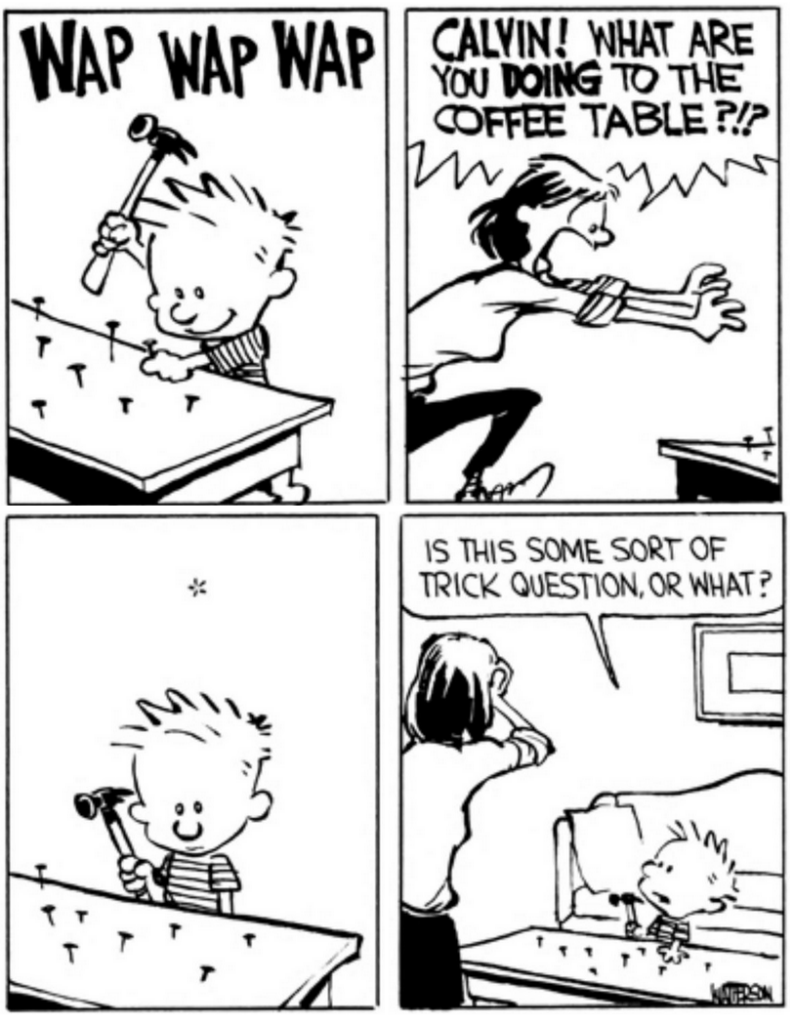
WAP WAP WAP
CALVIN! WHAT ARE YOU DOING TO THE COFFEE TABLE?!?
IS THIS SOME SORT OF TRICK QUESTION, OR WHAT?

Acknowledgements

To undertake doctoral studies I think you must be driven by a great passion, to make yourself write a thesis would then be a crime of passion. After a great many months full of long days, late nights and no weekends I am finally handing in my own thesis. It is a piece of work that I am proud of and can say that I have given my full effort to completing. However, it is impossible that I would have succeeded in this without the help and care of family and friends, for whom I am incredibly fortunate to have in my life.

The first and foremost thanks must go to my parents, Chris and Colette, without whom I would not have been born. On top of this, they are responsible for ingraining in me a strong work ethic as I watched them study and work full time jobs as a child, and inspiring me to follow my own dreams. My little brother, Conáran, must be thanked for reminding me of interests outside of my studies. My sister, Ethlinn, must be thanked especially for giving me a home away from home whenever I needed one, she is also responsible for pushing me to start my academic journey through internships. This proved key, as without meeting Dr Sergey Kafanov I do not believe that I would have gone on to do graduate studies in physics. Sergey deserves massive thanks, a genuine inspiration to me, a great teacher and a source of sage advice (that I generally do not follow until it is already too late). In the same vein, I must give great thanks to Prof Yuri Pashkin, whose endless patience and incredibly broad and deep knowledge have taught me so much not only about physics but about how to face life. I could not have been luckier in getting such a fantastic supervisor.

As my NPL supervisor, Dr Jonathan Williams has also acted as an excellent teacher, a fantastic resource for superconductor circuit design and impressive insights that have the ability to simplify some apparently complex problems. During my studies I was fortunate to lean on the experience and knowledge of my predecessor, Dr Tom Dixon, who taught me most of what I know about simulating superconducting circuits. His (and Prof Phil Meeson's) input to the simulation works carried out in the early part of my studies proved to be foundational to the direction of my research. I have also been aided in my research by the acts of generous collaborators that have shared experimental devices with us, for which we must thank Dr Zorin, Dr Kissling, and Dr Dolata of PTB, Dr Rodoniov of Moscow Bauman State Technical University, and Dr Chen Chiidong of Academica Sinica, Taiwan.

Excellent friends are hard to come by, but during my studies I have met many that have driven my passion for my work and expanded my curiosity. Special thanks must go to George Ridgard for saving me a bus fare most days, which we instead spent on morning coffees, and to Saba Khan who made weekends in the lab bearable with frequent tea breaks.

Publications

The following publications were produced during theoretical research on the devices discussed in this thesis. The materials of both publications are covered in a portion of Chapter 3.

SG Ó Peatáin, T Dixon, PJ Meeson, JM Williams, S Kafanov, and YuA Pashkin, "Simulating the effects of fabrication tolerance on the performance of Josephson travelling wave parametric amplifiers", *Superconductor Science and Technology*, vol. 36, no. 4, p. 045017, Feb. 08, 2023. DOI: 10.1088/1361-6668/acba4e

SG Ó Peatáin, T Dixon, PJ Meeson, JM Williams, S Kafanov, and YuA Pashkin, "Modelling Losses in Superconducting Travelling Wave Parametric Amplifiers", *Proceedings of the 29th International Conference on Low Temperature Physics (LT29)*, Aug. 1 2022. DOI:10.7566/JPSCP.38.011188

Parametric Amplification, Shockwave Formation and Quasiparticle Generation in Superconducting Metamaterials

Searbhán Gearóid Ó Peatáin, MPhys (Hons)

Department of Physics, Lancaster University,

Lancaster, UK

and

Quantum Technologies Department, National Physical Laboratory,

Teddington, UK

A thesis submitted for the degree of *Doctor of Philosophy in Physics*, August 2024.

Abstract

Superconducting parametric amplifiers are an already widespread technology, but as the requirements of measurement become more and more stringent in new experiments an evolution of the technology is required. This thesis covers the theory, characterisation and design of superconducting travelling wave parametric amplifiers (TWPAs). The basic theory for this type of device is not new, as amplification in travelling wave structures can be achieved simply by embedding a non-linear reactance into a transmission line. For our purposes, we achieve this by utilising either the Josephson inductance of an rf-SQUID or the kinetic inductance of thin superconducting films.

This thesis covers in detail the theory of operation of these devices to achieve three wave mixing amplification at the quantum limit. We begin by discussing the basic theory of lumped element transmission lines and the nonlinearities of the superconducting elements. Simulation techniques are then introduced, validated and applied to the study of these devices and the detrimental effects of impedance mismatches, fabrication tolerances, parasitic reactances and losses on the TWPA performance. Two realised TWPA devices based on the nonlinearity of the rf-SQUID are investigated using transmission measurements, with the results compared to theory to improve our understanding. The effects and origins of losses in the devices are investigated thoroughly as this has been identified as key to the understanding and improvement of future devices.

We finish this thesis with a set of proposals for TWPA devices that should overcome the problems discovered in previous proposals and realised devices that are discussed in this thesis. The results of this thesis should allow for the final steps towards achieving three wave mixing in a Josephson travelling wave parametric amplifier to be taken, with key considerations in terms of fabrication and design of a new generation of devices discussed throughout.

Table of contents

List of figures

Link to ToC

List of tables

Link to ToC

Chapter 1

Introduction

Science is not driven by big ideas but instead incremental advances. In fact, often times big ideas get bogged down in unexplored and under-considered details for decades, just as the drive for nuclear fusion reactors and more recently quantum computers have done. In this sense, the saying that 'The devil is in the details.' is the perfect description of research into the topics on the frontiers of science. Surely this phrase should be printed on the walls of each laboratory with as great an emphasis as fire exits and magnetic field zones. At the very least, it exemplifies the work and challenges presented in this thesis, where details have been shown to hide not one, but many devils.

Hard fought improvements in measurement sensitivity have always driven advances in fundamental science and wider technologies. The last two decades are no exception, marked by incredible strides and breakthroughs in basic science such as the detection of gravitational waves at LIGO [1], and the measurement of entangled states in quantum bits [2]. There are many recent experiments that have required unparalleled sensitivity, impossible until recently, for the measurement and read-out of a single (or a few) photons. These experiments have relied heavily upon superconducting circuits in which losses and noise can be minimized while signals can be detected and amplified more efficiently than any comparable technology [3, 4].

While much of the last century was dominated by the use of semiconductor readout technologies there has been a relatively recent transition to superconducting circuits for low temperature experiments. The reason for this is twofold; improved fabrication technologies and techniques led to decreased losses and higher reproducibility in superconducting circuits, and the generation of entangled states in superconducting circuits allows for ultra-sensitive metrology [5–7]. The proliferation and rapid advancement of superconducting circuits has, to a large extent, been driven by its most famous application, the development of superconducting quantum computers. Since superconducting circuits for the generation of a quantum entangled state was first proposed [8] and demonstrated in 1999 [9] the technology has improved dramatically with recent demonstrations coming closer to quantum supremacy in useful tasks. Quantum advantage, i.e. the use of a quantum computer to solve problems faster than classical computers has been a fast approaching reality for a while now and been a significant driver in the research of superconducting circuits [10, 11].

Link to ToC

Further advancements in quantum computation will require measurement of very weak microwave signals in C-K_u bands, which just so happens to be a trait common to several of the most cutting-edge research areas. For instance, astronomical research, photonics research and the search for axionic dark matter each employ wide-band searches using superconducting microwave resonators to detect very weak or single photon events [12–14]. These measurements then require milli-Kelvin amplification above the noise floor of the system over a wide bandwidth which has been difficult to achieve with existing resonator based superconducting devices [4, 15].

A neat solution to this problem arose many years ago with the proposal to form a nonlinear superconducting transmission line from Josephson elements [16]. This device could theoretically achieve quantum-limited noise amplification of a weak microwave signal over an octave bandwidth [17, 18]. While such a device could not be demonstrated for a long time, the work on the redefinition of the voltage standard using long arrays of Josephson elements improved the fabrication techniques of such devices and interest soon arose in the topic again [19, 20]. Previously, such Josephson travelling wave parametric amplifiers (JTWPA's) and similar devices that utilize a kinetic inductance nonlinearity (KITWPA's) have been demonstrated to operate near the quantum limit for added noise in the four-wave mixing (4WM) regime [21], although the desired three-wave mixing (3WM) regime has not yet seen comparable success [22]. This thesis discusses the design, simulation and characterization of such 3WM TWPA's and the future work required to achieve the desired device.

While quantum computing and dark matter detection have been the driving force behind the development of these devices, the applications extend far beyond these fields. The work in this thesis should not only be of help to researchers that follow in these same investigations but also to those that wish to apply themselves to other developing fields. For instance, this work is inextricably linked to microwave quantum optics, computational metamaterials and radio-frequency engineering for the production of bespoke experimental environments. As such, many the techniques and mathematics presented from this point on can be thought of as a guide to the general practice of superconducting circuit design. What is not covered directly in the text should be found within the extensive bibliography that covers the history and applications of superconducting devices.

1.1 Literature Review

Superconductivity

First demonstrated by Kammerlingh Onnes in 1911, superconductivity is characterized by the absence of electrical resistance and the expulsion of magnetic field from a metal as it enters a superconducting state below a transition temperature, T_c [23, 24]. Although the study of superconductivity involved many of the brightest minds of the twentieth century, it was difficult for theorists to build a model that could properly describe the phenomenon. The first significant progress was made by H. & F. London in 1935 with a set of phenomenological equations in which the expulsion of magnetic flux was described by the formation of screening current at the surface of the superconductor [25]. Magnetic flux was then shown to penetrate a distance λ_L, the London penetration depth, beneath the surface of the bulk superconductor in which the strength of the field would reduce exponentially.

A set of rapid advances in the theory followed the publication of another paper by F. London in 1948 in which it was proposed that superconductivity is due to the formation of a condensate in which electrons of the Fermi sea enter a quantum mechanical ground state with zero total spin and momentum [26]. Shortly following this, in 1950, Ginzburg and Landau published a phenomenological model of superconductivity that went on to become fundamentally important to the future advances in the field [27–29]. Built upon Landau's work on the second order phase transitions, the model presupposed that the superconducting state is described by a 'pseudo-wavefunction' which introduced a temperature dependent characteristic length scale over which the wavefunction could vary without an increase in free energy, $\xi(T)$. It can be shown that in the low temperature limit this coherence length approaches the 1953 coherence length, ξ_0, for the superconducting state derived by Pippard as a non-local extension to the London equations [30].

Despite the advances in phenomenological theories a microscopic model that could explain how superconductivity arose in metals eluded researchers until the publication of the Bardeen-Cooper-Schrieffer (BCS) theory in 1957 [31, 32]. The key to this model came from Cooper's 1956 work showing that electrons in a region around the Fermi surface in a crystal lattice of an arbitrary metal will experience a small attractive force with each other [33]. This force, mediated by an electron-phonon interaction with the crystal lattice, leads to bound states in which the electrons with equal and opposite spin and momentum form pairs, dubbed 'Cooper pairs'. With a total spin of zero, these Cooper pairs have bosonic properties that allow them to condense into a quantum mechanical ground state. Therefore, superconductivity is an example of a macroscopic quantum system in which the number of charge carriers, N, and their shared superconducting phase, φ, are conjugated variables. As such there is some uncertainty in their measurement, $\Delta N \Delta\varphi \geq \hbar/2$, although due to the macroscopic nature of the system, N is of the order $\sim 10^{22}$, both variables can be known with small uncertainties [34].

Link to ToC

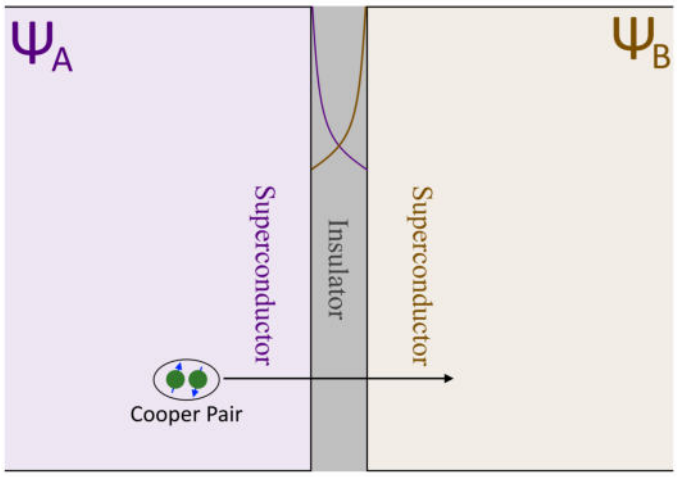

Fig. 1.1 Diagram of a superconductor-insulator-superconductor (SIS) junction in which the wave functions of the superconducting electrodes extend into the dielectric region. If the wave functions overlap, as is shown here, it allows for Cooper pairs formed of electrons with opposite spin and momentum to tunnel through the barrier.

The Josephson Effect

Following on from the work of Giaver [35, 36] and Nichols, Shapiro and Smith [37] on the tunneling of quasi-particles between superconducting electrodes through a dielectric barrier, Josephson predicted that the dissipationless tunneling of Cooper pairs would occur as the dielectric barrier became thin enough, ~10 Å [38].

Published in his seminal paper on the topic, Josephson described, to an initially sceptical reception, that the extension of the superconducting wave functions of the electrodes into the insulating region should lead to their overlap and the formation of a unified quantum state, as shown in Figure 1.1. As such, this state of weak superconductivity should allow for the flow of charge without a voltage drop, up until a certain critical tunneling current, I_c, is reached, after which the junction becomes dissipative. Josephson was able to reduce the complex equations for the tunneling current, I_J, to a simple product of this critical current and the sine of the difference in the superconducting phases of the two electrodes, $\varphi_B - \varphi_A$:

$$I = I_c \sin\left(\varphi_B - \varphi_A\right) . \tag{1.1}$$

The demonstration of this effect at Bell Labs by P.W. Anderson and J.M. Rowell [39] quelled any doubts over the theory's validity and led to an explosion of interest in the following decades on the theory and applications of such a device as well as the 1973 Nobel prize for B. D. Josephson [3, 40]. It was in this same paper that Anderson noted the similarity of the tunnel junction responses to direct (dc) and oscillating (ac) current excitations to the behaviour of a pendulum, which was developed further in the following years [41]. More importantly, a semi-classical electrical model for the junction was developed in the Resistively-Capacitively-Shunted-Junction (RCSJ) model [42–44]. This model can reproduce the dc and rf responses of a tunnel junction while being much easier to compute than alternative tunneling models.

One of the earliest applications of superconducting circuits was in metrology, particularly in magnetometry. It was shown early in the history of superconducting research that a current in a loop of superconducting wire will continue to circulate for at least 10^5 years

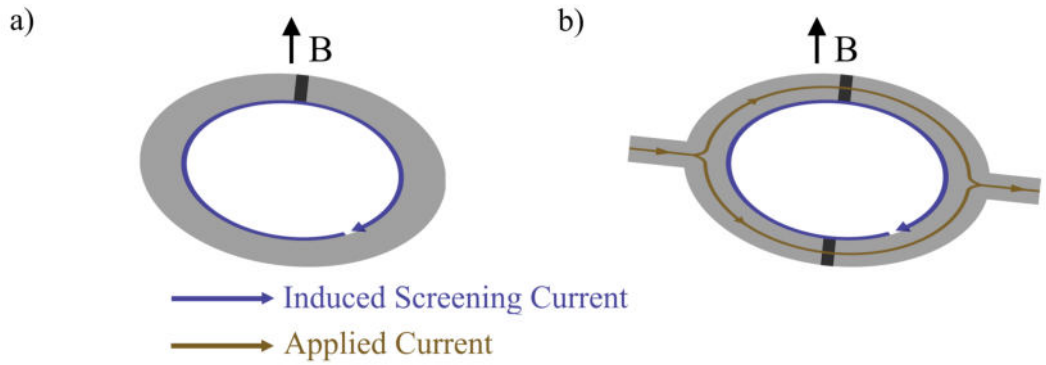

Fig. 1.2 a) An rf-SQUID and b) a dc-SQUID where a superconducting loop is intersected with one or two Josephson junctions, the flux through the loop alters the phase gradient across the junction and so the dc and rf response of it.

[34]. It was also shown that magnetic flux may only penetrate through the superconducting loop in steps of the magnetic flux quantum, $\Phi_0 = h/e$, where h is the Planck constant and e is the charge of an electron, as the superconducting phase around the loop must remain continuous [45]. As such, a superconducting loop segmented by one or two Josephson junctions can be used as an extremely sensitive measurement device of magnetic fields [46]. The phase gradient across the junction, due to the screening current induced by the flux penetrating the loop (shown by the blue arrow of Figure 1.2), can then be probed by the dc or rf response. This allows magnetic field measurements with sufficient sensitivity ($\sim 10^{-19}$ Wb) to image the firing of neurons in the human brain [47].

The one and two junction loop structures, shown in Figure 1.2, are called rf- and dc-SQUID's (Superconducting QUantum Interference Devices), respectively, and are still widely used for magnetometry, although their present applications extend far beyond this. The 1970's and 1980's saw widespread interest in the development of superconducting digital logic, in which SQUID's may be excited close to their critical current to generate pulses used for computation in the circuit. At one point, IBM intended to build a mainframe superconducting digital computer for which they developed a superconducting circuit simulation program [48]. Although this was not initially made available to the public, several research groups followed suit to develop and release their own simulators [49, 50]. These circuit simulation programs altered the already existing SPICE system (Simulation Program for Integrated Circuit Engineering), developed by the semiconductor industry, to allow for the addition of Josephson elements into the circuit alongside classical electrical components. The RCSJ model of the Josephson junction is used in a time evolution simulation in which Kirchoff loop laws are formulated in terms of superconducting phase at each time step and then solved using the Newton-Raphson method [51, 52].

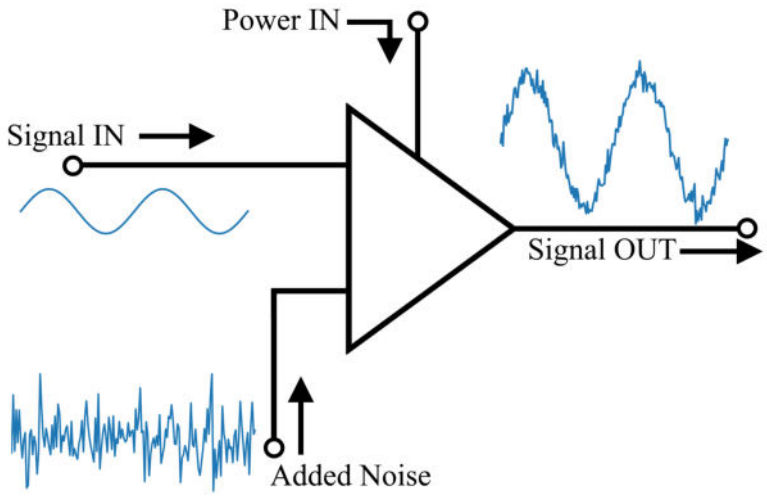

Fig. 1.3 Diagram of an example amplification process in which a weak signal is amplified, although the output signal has some added noise due to the amplification process or the effect of vacuum fluctuations [53].

Amplification in Electronic Circuits

In the early twentieth century, as radar, communication technologies and fundamental research sought to use ever weaker signals and so became increasingly sensitive to noise, attention turned to the study of amplification processes themselves. Around this same time, Johnson & Nyquist related the white noise present in electrical conductors to its temperature by the thermal agitation of the charge carriers [54, 55]. This phenomenon is used to characterize the noise added to a signal in the process of measuring or amplifying it, as shown in Figure 1.3, by a noise equivalent temperature. An ideal amplification process would have large gain and a noise temperature of 0 K, although this is not possible. Instead a system with a cascade of high gain amplifiers with low noise temperatures is used. For such a cascade the total system noise temperature, T_{sys}, can be defined as the available noise power that would be added to a signal on the measurement line. Friis showed that this would be dominated by the noise temperature of the first amplification stage, T_1, assuming that the gain of the signal on each stage, G_n is much greater than unity [56].

$$T_{sys} = T_1 + \frac{T_2}{G_1} + \frac{T_3}{G_1 G_2} + \ldots + \frac{T_n}{G_1 G_2 G_3 \ldots G_n} \tag{1.2}$$

Over the last century, the most effective method to maximize amplification while minimizing added noise, or equivalently to improve signal-to-noise ratio (SNR), has changed several times. While vacuum tube amplifiers dominated the early part of the century, they were replaced in the 1950's and 60's with semiconductor devices, namely MOSFETs, GaAs-FETs and then High Electron Mobility Transistor (HEMT) amplifiers [57]. HEMT amplifiers especially were impressive devices, remaining popular today with noise temperatures as low as 1.5 K having been demonstrated [58].

In the early 1980's Caves sought to examine the quantum limits on a linear amplification process of which a parametric amplifier well below its saturation point is a good example [53]. In a parametric amplification process, a weak signal field is amplified via the interaction with a stronger pump field via the modulation of a nonlinear reactance by that pump. Unless there are some dissipative elements in such a circuit there was thought to be no

added noise to the signal. However, it was shown that the minimum possible added noise would correspond to a half-photon of the input vacuum field at the generated idler frequency, in the microwave regime determined by $\hbar\omega/2k_B$ or $\sim 0.12\,\mathrm{K}$ for an idler at 5 GHz. The number of added noise photons for a cryogenic HEMT amplifier chain is typically an order of magnitude higher. For example, over a period 1/B, where B is the bandwidth of a measurement resonator, the number of photons incident at an amplifier after measuring a superconducting qubit is kept purposely small, $\mathrm{n} \leq 10$. In this measurement a cryogenic HEMT amplifier chain may add $\mathrm{n_{HEMT}} \geq 20$ photons, although a chain incorporating a parametric amplifier at the first stage may decrease this to $\mathrm{n_{PA}} = 1 - 4$, drastically improving SNR of the measurement [4].

Studies on parametric effects have been ongoing since the works of Faraday on water ripples in 1831 [59] and Melde in 1859 [60] before being formalized by Rayleigh [61–63]. However, parametric amplification has been widely used throughout human history for instance on children's play swings in which the child may periodically modulate their gravitational potential to increase the amplitude of the swinging (see Section 1.2.1).

This transfer of energy between two waves, which is valid to the photon level, will operate in certain wave mixing regimes in order to conserve energy. For example, a nonlinear reactance that has a quadratic dependence on the wave amplitude will lead to three wave mixing (3WM), in which a photon of the strong pump wave is converted into a photon of the weak signal and a generated idler photon at frequencies ω_p, ω_s and ω_i, respectively:

$$\hbar\omega_p = \hbar\omega_s + \hbar\omega_i \ . \tag{1.3}$$

A cubic dependence will lead to four-wave mixing (4WM) in which two pump photons are required instead of one and the energy relation, becomes:

$$2\hbar\omega_p = \hbar\omega_s + \hbar\omega_i \ . \tag{1.4}$$

The theory of parametric gain, while contributed to by many scientists over several decades was codified in the modern way mostly by van der Ziel, Manley and Rowe [17, 64, 65] in the 1950's. The introduction of parametric amplifiers into radio frequency electronics came in several phases beginning with the development of nonlinear inductance up-converters used for telecommunications in 1916 [66], and continuing with nonlinear capacitance devices after the demonstration of such an effect in varactor diodes in Bell Labs in 1958 [67, 68]. However, each time interest grew in parametric amplifier devices the developments in competing technologies provided better characteristics in terms of gain, bandwidth, and noise temperature. While parametric amplifiers were already well known to be capable of quantum-limited noise performance, difficulties with dissipation and noise in the nonlinear reactances available at the time severely limited their applications [57]. One final promising avenue discussed in the 1960's was the use of superconducting circuits in parametric amplifier devices to overcome these problems.

Link to ToC

Superconducting Parametric Amplifiers

The nonlinear kinetic inductance of a thin superconducting film first arose from Ginzburg and Landau's work in 1950 [27] although received some important further development by Parmenter in 1961 [69] which led to the first experimental observation of the effect by Gittleman *et al.* in 1963 [70]. It was Clorfeine that first proposed to use this effect to construct a parametric amplifier that would not be limited by dissipation as in the classical examples [71]. Using the odd functioned nonlinear inductance to form a resonant cavity, 4WM parametric amplification can be achieved where the quality factor of the resonator determines the coupling of the wave to the nonlinearity, and by extension the amplification.

It was demonstrated that despite concerns about carrier recombination time in superconductors [72], this nonlinear inductance was suitable for parametric devices up to the mm-wave regime [73, 74]. However, shortly after Clorfeine's studies, Zimmer attempted to reproduce the results using a tin film and came to the conclusion that the strong nonlinear effects previously seen were most likely due to the formation of small Josephson junctions on the film due to oxide impurities [75]. This device was the first demonstration of a Josephson parametric amplifier (JPA), although it provided very little gain due to poor coupling between the wave and the nonlinear resonator. This study showed that parametric amplification in Josephson junctions was feasible, and more desirable than that achievable in thin films due to the stronger nonlinearity.

Following this demonstration, several other groups demonstrated Josephson parametric amplifier devices throughout the 1970's while the theory of operation was developed concurrently. The 4WM and 3WM regimes (also termed doubly-degenerate and singly-degenerate in some publications) of amplification were achieved in these structures and were shown to achieve gains as high as 23 dB [76] and 16 dB [77], respectively. While some interesting designs were demonstrated at this time, including some ultra-low power devices in which the plasma frequency of a SQUID acted as the pump in an amplification process [78], the noise temperatures of these early devices remained well above 20 K, far from their theoretical limit despite operating temperatures at or below 4.2 K. This was most likely due to fabrication defects and parasitic sources of loss in the device, which limited their applications in comparison with the low noise and wide bandwidth of the HEMT amplifiers of the time [79].

This remained the case until the 1980's when Yurke *et al.* demonstrated quantum noise limited amplification and squeezed state generation in JPA's. Squeezed state generation uses phase-sensitive amplification to amplify the in-phase noise and de-amplify the out-of-phase noise to a level below the vacuum level, which proves very useful for sensitive measurements [80, 81]. This work was reproduced by Castellanos-Beltran *et al.* in 2007 [82, 83], following this the advances in fabrication technologies led to a revival of interest in the field. JPA's then became the standard technology for the most sensitive experiments. However, the limitations inherent to JPA's such as a gain-bandwidth trade-off, in which the narrowest bandwidth leads to the highest gain and vice versa, and a dynamic range limited by the Josephson energy, prevented widespread adoption.

Superconducting Travelling Wave Parametric Amplifiers

Perhaps, the move from a resonant to a travelling wave structure to improve bandwidth will not be much of a surprise to those familiar with the similar transition of microwave engineers in the design of wide-band antennas [84]. A Josephson travelling wave parametric amplifier (JTWPA) removes the resonant structure and embeds many Josephson junctions in a transmission line structure which both widens the bandwidth and improves the dynamic range of the amplifier many times over. These devices are good examples of metamaterials which can be defined as a periodic structure in which propagating waves behave in a desired fashion not readily achieved in natural systems [85]. Although the term itself is rather new, coming about in the last few decades, by the given definition the study has existed since at least 1898 with the work of J. C. Bose on microwave propagation through twisted structures [86]. The theoretical description of the wave propagation in periodic structures was then built up in the following century with the work of Bloch [87], Brillouin [88], and Veselago [89], amoung others.

The first travelling wave parametric amplifiers (TWPA's) appeared in the mid-twentieth century with the demonstration of such a device using varactor diodes in 1960 [90]. Just prior to this in 1958 the development of travelling wave MASERS (Microwave Amplification by Stimulated Emission of Radiation) began at Bell Labs and led to a demonstration of the device in 1966 by NASA with microwave amplification of $> 60\,\mathrm{dB}$ and a record low noise temperature of 16 K. This low noise temperature proved vital for the detection of very weak (-169 dB) signals from the Mariner IV space probe on the surface of Mars in 1965 [91].

The theoretical work on the travelling wave parametric amplification process was developed by Tien 1958 [92], deGrasse 1959 [93] and Cullen 1958/60 [94, 95]. It was later shown by Landauer in a series of papers in 1964 [96, 97] that the wave mixing in such a nonlinear transmission line would lead to the formation of shockwaves (i.e. harmonic generation of the pump wave) which would severely hamper amplification. However, this did not dissuade many and the development of TWPA's continued mostly unhindered, motivated by the low noise figures already demonstrated.

Crucial to the development of these devices is the development of fabrication technologies such that the dimensions of the Josephson elements can be made small compared to the wavelengths under study. The chain of Josephson junctions must appear as a distributed/continuous transmission line in order for waves to propagate (see Section 1.2.2). The first step towards a JTWPA was therefore arguably taken by Parrish & Chiao in 1975 in which a $\lambda/4$ lumped element transmission line resonator formed of an array of 80 Josephson junctions was implemented as a distributed resonator for a JPA [18]. Following this Sweeney *et al.* proposed a JTWPA formed of around 1000 junctions in 1985 [16], which was followed in 1996 by an experimental demonstration by Yurke *et al.* of a similar reflectometric device [98].

Despite this initial interest, the topic did not gather serious attention until the 2010's, most likely due to the fabrication difficulty of such a device limiting access. When the topic did reappear inspiration was taken from the fields of nonlinear optics [99] and microwave

Link to ToC

metamaterials [85] to improve the amplification of the devices by engineering the dispersion of the transmission structures. This idea of dispersion engineering essentially means preventing the generation of pump harmonics in the medium and the subsequent formation of shockwaves as described by Landauer. In fact, the first patent for a recognizable parametric amplifier by Peterson in 1932 noticed the benefit of preventing harmonic generation in the amplifier and added a tuned resonator to the previous designs to prevent this [100].

The first example in this vein follows Clorfeine's original intention and made use of the nonlinear kinetic inductance of a superconducting transmission line (KITWPA) with periodic impedance loadings added to provide wide-band gain in the 4WM regime [101]. A JTWPA demonstration swiftly followed in 2015, also in the 4WM regime, using a Josephson junction embedded transmission line with coupled $\lambda/4$ resonators to engineer the dispersion [102]. While no group has demonstrated quantum limited performance in these devices as of yet, several groups have come close in JTWPA's based on Josephson junctions [21], SNAILS (Superconducting Non-linear Asymmetric Inductive eLements) [103] and in KITWPA's with a Niobium-Titanium Nitride buried micro-stripline line device [104].

An alternative route in superconducting TWPA development that grew out of this progress had the intention to operate in the 3WM regime, which, amoung other things, would allow for simpler separation of pump, signal and idler waves on the output. For KITWPA devices this can be achieved by the addition of a dc bias in the transmission line which alters the wave mixing relations in the desired way as described by Erickson & Pappas [105] and demonstrated by Vissers *et al.* [106]. Zorin proposed two potential 3WM JTWPA schemes in 2016 [107] and 2019 [108] using rf-SQUID and dc-SQUID transmission lines, respectively. In these devices, a flux (or dc) bias is used to move the stationary position of the nonlinearity away from the unbiased, cubic, 4WM nonlinearity and into the quadratic, 3WM regime. The rf-SQUID scheme proved to be the more popular of the two designs due to simpler fabrication, however further analysis by Dixon *et al.* showed that the shockwaves predicted by Landauer are indeed formed and severely hamper amplification in these devices [109]. Further theoretical work has demonstrated that dispersion engineering similar to that used in the previous 4WM devices would lead to the expected high gain operation of the device [110], however despite these advances experimental demonstrations have not yet been made.

This thesis discusses the theoretical work on the design and analysis of these 3WM TWPA's alongside the experimental characterisation of the first generation JTWPA devices as described by Zorin in 2016 [107]. All work presented in this thesis has been completed by the author alone, including the experimental characterisations, microscopy, simulation and theoretical development, portions of which are yet to be published.

1.2 Prerequisite Understanding

1.2.1 Parametric Amplification

Parametric amplification is a fundamental effect in which two oscillating fields, in the presence of some nonlinearity, couple and transfer energy between them. While parametric amplification is most well-known in electrical circuits and optics, where it has been used for well over a century, the effect has been used by humans for time immemorial. A popular example of this is the children's play swing where in order to swing higher the child knows well to change their centre of gravity by moving their legs out and in (or equivalently by standing and squatting on the seat of the swing) with legs brought in when the swing is highest and brought out when it is lowest.

The first known practical application of this effect is the seven hundred-year-old custom of swinging of an incense burner called the 'O Botafumeiro' for certain ceremonies in the Santiago de Compostela Cathedral, Galicia, Spain [111].

The pendular motion of the burner, hung from the church rafters, is amplified by the modulation of its $\sim 20\,\mathrm{m}$ long rope twice each oscillation by a group of monks in a process described in Figure 1.4. This modulation, shortening the rope at the censer's lowest point and lengthening it at its highest, effectively adds energy into the censer's gravitational potential which is then, of course, transferred to its kinetic energy leading to top speeds of $\sim 60\,\mathrm{kmph}$ after as little as seventeen cycles.

Key to the amplification of the censer motion is that the modulation must be performed twice for every oscillation cycle of the burner. This condition may be elucidated by an analogy with an equivalent electrical scheme where gravitational potential goes to electrical potential, V, and kinetic energy goes to current, I. In the example scheme of Figure 1.5 two resonant circuits are formed by inductances, L_p and L_s, resistances, R_p and R_s, and nonlinear capacitance, $C(V)$.

When the resonant circuit is excited by a pair of oscillating voltages, a strong pump ($V_p = |V_p| \sin \omega_p t$) and a weak signal ($V_s = |V_s| \sin \omega_s t$), the two fields will interact via the nonlinear capacitance. The current-voltage characteristic of this nonlinear element can be approximated as:

$$I = C_0 \left(1 + \chi^{(2)}(V^2) + \chi^{(3)}(V^3) + \ldots\right) \frac{dV}{dt} \tag{1.5}$$

where C_0 is the linear magnitude of the capacitance and $\chi^{(2,3)}$ are the second and third order nonlinearities, which describe how the capacitance depends on the square and cube of the voltage across it. The two excitations can only interact in this way on the condition that they both fulfil the resonant condition of the circuit. In distributed systems the lowest order of this corresponds to the fundamental and second harmonic frequencies of the circuit. Although, for lumped element devices, as shown in Figure 1.5, a second tuned circuit is required to simultaneously couple the pump and signal tones to the nonlinearity. A signal

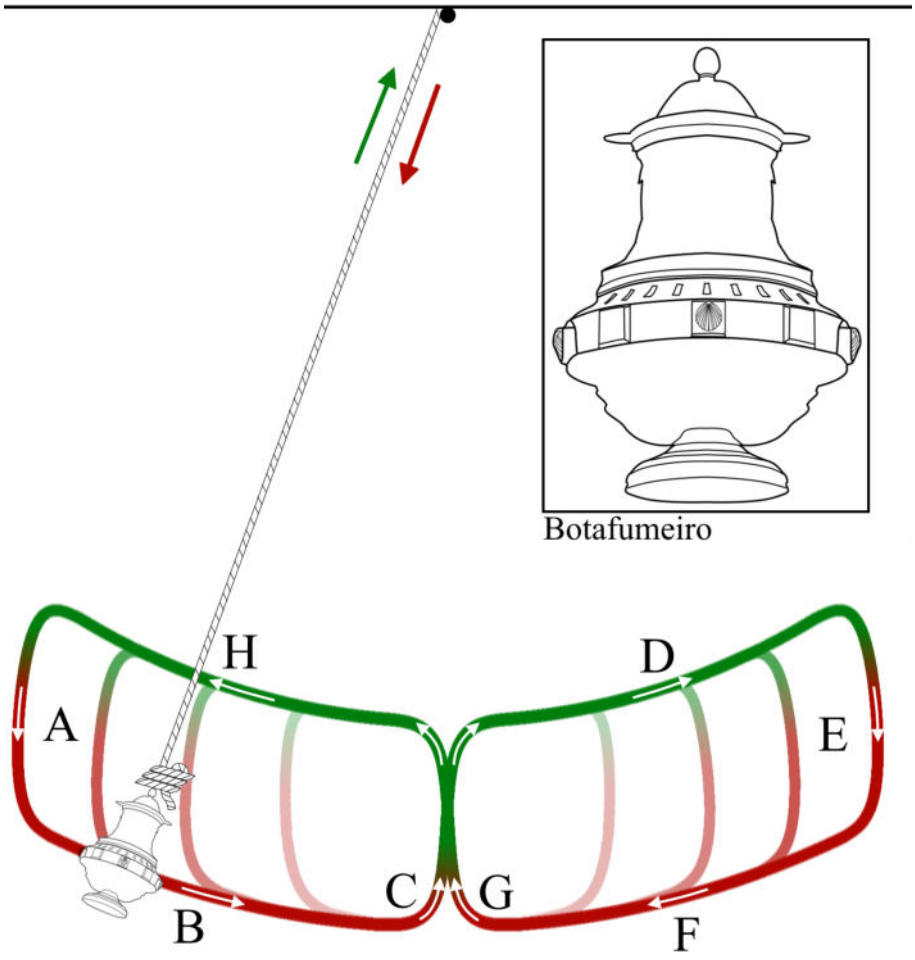

Fig. 1.4 Diagram of the 'O Botafumeiro' censer that is set into pendular motion where its amplitude is increased each cycle (faded to solid colour) by the modulation of the rope length. The modulation is repeated twice for every oscillation of the burner in a cycle from A-H where the red indicates longer rope and green indicates shorter rope. The censer is lowered at point A, completes half of its arc through B, is raised at C, completes the other half of its arc through D, is lowered at E and repeats this process through to H.

voltage de-tuned far from resonance may still interact with the pump, although with a very short interaction time and so amplification will be negligibly small. A signal only slightly de-tuned from resonance and well within the circuit's bandwidth will see some gain, although in order to conserve energy an idler tone will be created, the frequency of which will depend on the wave mixing regime as shown in Equations 1.3 and 1.4. To achieve a high gain in this case, a third circuit must be coupled to the nonlinear capacitance to act as a resonant circuit for the idler, at the difference frequency between the pump and signal.

A quadratic dependence in the nonlinearity leads to 3WM and a cubic dependence leads to 4WM and so on for higher orders. The reason for this becomes clear if the sum of the voltage excitations used in the resonant circuit of Figure 1.5 are raised to the second or third power. In the case of a quadratic nonlinearity, the pump with voltage $|V_p|e^{-i\omega_p t}$, and signal with voltage $|V_s|e^{-i\omega_s t}$, mix to produce their second harmonics, and two generated

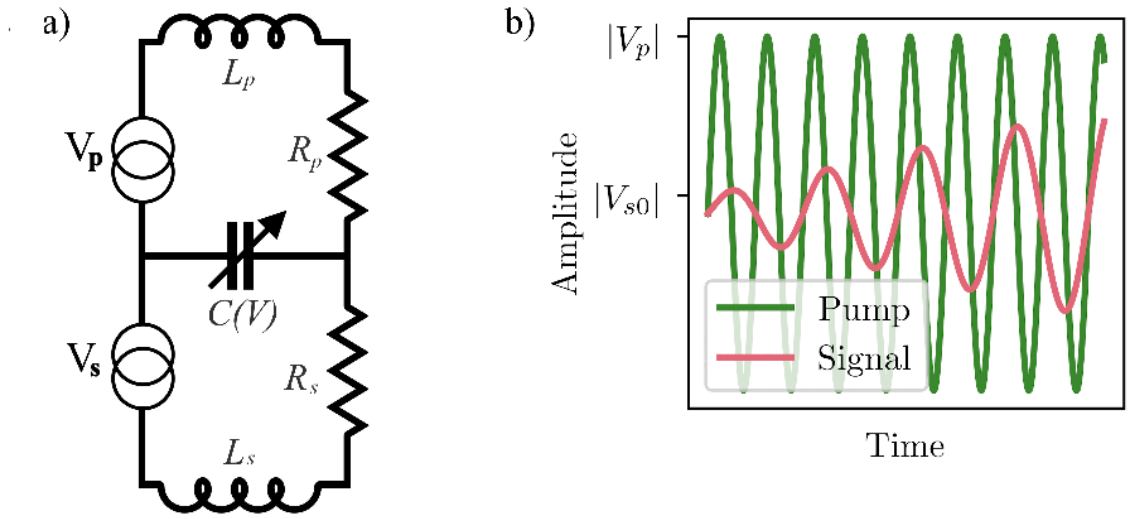

Fig. 1.5 a) A nonlinear resonant circuit with inductance $L_{s,p}$, resistance $R_{s,p}$, and nonlinear capacitance C, excited by oscillating pump voltage V_p and weak signal voltage V_s which mix due to the nonlinearity and b) the amplitudes of the pump and signal voltages through time where the signal voltage increases due to parametric amplification driven by the strong pump wave.

idlers with frequencies equal to the sum and difference of the pump and signal frequencies.

$$\begin{aligned}\left(|V_p|e^{-i\omega_p t}+|V_s|e^{-i\omega_p t}\right)^2 \quad \Rightarrow \quad & |V_p|^2 e^{-2i\omega_p t}+|V_s|^2 e^{-2i\omega_s t} \\ & +|V_p||V_s|e^{-i(\omega_p-\omega_s)t} \\ & +|V_p||V_s|e^{-i(\omega_p+\omega_s)t}\end{aligned} \tag{1.6}$$

Rectification terms are not shown here, although it is perhaps already clear that the energy and frequency conditions of the 3WM regime are a straightforward consequence of the wave mixing effect arising from a quadratic nonlinearity. The same holds true for 4WM from a cubic nonlinearity, in which third harmonics and further mixing products are generated, and extends in the same way to higher orders.

This resonant condition is equivalent to the phase-matching condition of travelling wave parametric amplifiers in which the phase velocities of the mixing waves must be related linearly in order to produce an ideal amplification process. Rewriting Equations 1.3 and 1.4 with this added condition we arrive at:

$$k_p\omega_p = k_s\omega_s + k_i\omega_i \tag{1.7}$$

for 3WM, and:

$$2k_p\omega_p = k_s\omega_s + k_i\omega_i \tag{1.8}$$

for 4WM where $k_{p,s,i}$ and $\omega_{p,s,i}$ are the wavevectors and frequencies of the fundamental mixing processes, respectively.

Link to ToC

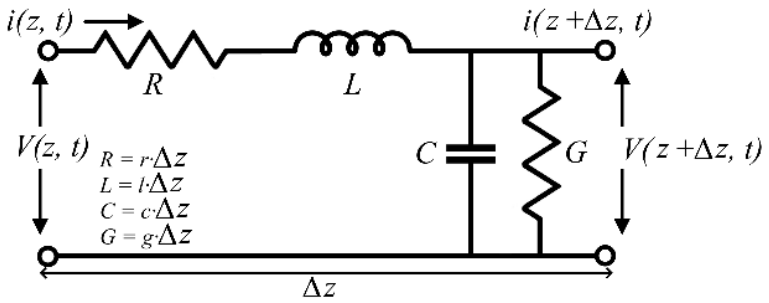

Fig. 1.6 Diagram of an electrical model of the transmission line where the wave propagation characteristics of the medium are set by the distributed inductance, l, capacitance, c, resistance, r and conductance, g per unit length of the transmission line. The equivalent lumped element values for a given length, Δz, are then $L = l \cdot \Delta z$, $R = r \cdot \Delta z$, $C = s \cdot \Delta z$ and $G = g \cdot \Delta z$.

1.2.2 Transmission Line Models

Transmission lines are quasi-one dimensional structures that confine electromagnetic waves into a geometry around a central line. Waves are allowed to propagate in the travelling electric (TE), travelling magnetic (TM) or, most importantly, the travelling electro-magnetic (TEM) modes depending on the geometry of the line and the frequency of the wave.

The characteristics of a continuous transmission line structure can be determined from its distributed inductance, l, resistance, r, capacitance, c, and conductance, g, per unit length, as shown in Figure 1.6. Solving the Kirchoff laws for an infinitesimal segment of the transmission line then leads to a set of partial differential equations of the form:

$$\frac{\partial V(z,t)}{\partial z} = -rI(z,t) - l\frac{\partial I(z,t)}{\partial t} \ , \tag{1.9}$$

$$\frac{\partial I(z,t)}{\partial z} = -gV(z,t) - c\frac{\partial V(z,t)}{\partial t} \ . \tag{1.10}$$

These are commonly referred to as the Telegrapher's Equations. Solving in the frequency domain, and assuming the current and voltage are sinusoidal in time with forms:

$$I(z,t) = I_0 \exp\left(i\omega t\right) \ , \tag{1.11}$$

$$V(z,t) = V_0 \exp\left(i\omega t\right) \ , \tag{1.12}$$

we can simplify these to a set of ordinary differential equations in space:

$$\frac{dV(z)}{dz} = -\left(r + i\omega l\right) I(z) \ , \tag{1.13}$$

$$\frac{dI(z)}{dz} = -\left(g + i\omega c\right) V(z) \ . \tag{1.14}$$

These equations may be combined to form a set of two wave equations that describe the distributions of current and voltage on the transmission lines:

$$\frac{d^2V(z)}{dz} + \gamma^2 V(z) = 0 \ , \tag{1.15}$$

$$\frac{d^2I(z)}{dz} + \gamma^2 I(z) = 0 \ . \tag{1.16}$$

Here γ is the propagation constant of the line which is a sum of the attenuation, α, and phase shift, β, per unit length: $\gamma = \alpha + i\beta$. As a function of the distributed elements, the propagation constant can be written as:

$$\gamma = \sqrt{(r + i\omega l)\,(g + i\omega c)} \ . \tag{1.17}$$

This wave equation may be solved using Ansatzs of the form:

$$A(z,t) = |A| e^{i(\gamma z - \omega t)} \tag{1.18}$$

where a wave of amplitude, $|A|$, propagates in the line and evolves in time and space based on its frequency and the characteristics of the transmission line, respectively.

These equations are sufficient to describe the propagation of waves on basically all transmission lines in the continuous limit, including the interference of forward and backward travelling waves. Such an effect would be caused by improper termination of the transmission line by an impedance not equal to the line's characteristic wave impedance. This characteristic impedance may be defined as a function of the distributed circuit parameters as:

$$Z = \sqrt{\frac{r + i\omega l}{g + i\omega c}} \ . \tag{1.19}$$

The distributed capacitance and inductance can be recovered from the measured values of wavenumber ($k = i\gamma$), and impedance by finding the phase velocity (or wave propagation speed on the line) via the relations:

$$v_{ph} = \frac{\omega}{k} \ , \tag{1.20}$$

$$c = \frac{1}{Z\nu_{ph}} \ , \tag{1.21}$$

$$l = \frac{Z}{\nu_{ph}} \ . \tag{1.22}$$

These equations are applicable for analysis of 0 Hz (direct current) up to any frequency of wave in the transmission lines, including the characteristics of the different modes of propagation (i.e. TE, TM and TEM).

Link to ToC

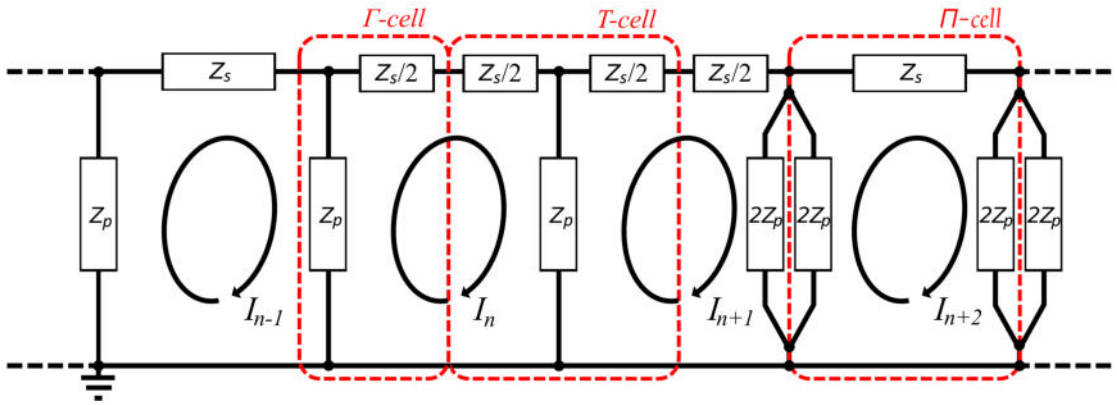

Fig. 1.7 An infinite chain of series impedances Z_s and parallel impedances Z_p to ground, that acts as a transmission line supporting quasi-TEM modes. It can be examined by segmenting the chain into a line of Γ-, T-, or Π-cells as shown in the red-dashed boxes.

Lumped Element Model

Continuous transmission lines can be converted into equivalent lumped element structures, which give equivalent transmission properties at low frequencies. At higher frequencies the characteristics diverge as the lumped element structure is no longer small compared to the wavelength [84, 112]. Segmenting the transmission line into lengths the distributed inductance and capacitance can be used to find equivalent series, Z_s, and parallel, Z_p discrete impedances for a lumped element impedance chain. Figure 1.7 shows the different ways to segment such a chain into cascaded Γ-, T-, and Π-cells respectively. The chosen unit cell should be symmetric (e.g. Π- and T-cells) for the results to be accurate, as S21 and impedance parameters of asymmetric unit cells (e.g. Γ-cells) diverge at higher frequencies, although the effect is small for very long chains [113].

Characteristic Impedance

The following analysis is correct only for infinite chains, although very long and properly terminated chains are described to a very good approximation. We use the Π-cell representation here, but the process is the same for whichever cell type is chosen. An infinite chain of Π-cells forms a transmission line of characteristic impedance Z_{TL}, if another identical Π-cell of impedance Z_π is placed on the end of the chain the impedance of the Π-cell can be found to be:

$$\mathrm{Z}_\pi^{-1} = \left[\left(\frac{2\mathrm{Z_{TL}Z_p}}{\mathrm{Z_{TL}} + 2\mathrm{Z_p}}\right) + \mathrm{Z_s}\right]^{-1} + [2\mathrm{Z_p}]^{-1} \ , \tag{1.23}$$

where Z_s and Z_p are the impedances of the series and return branches of the Π-cell respectively. With the condition that the newly added Π-cell is identical to the previous, and so load each other equally, i.e. $Z_\pi = Z_{TL}$ and some trivial manipulations, this equation

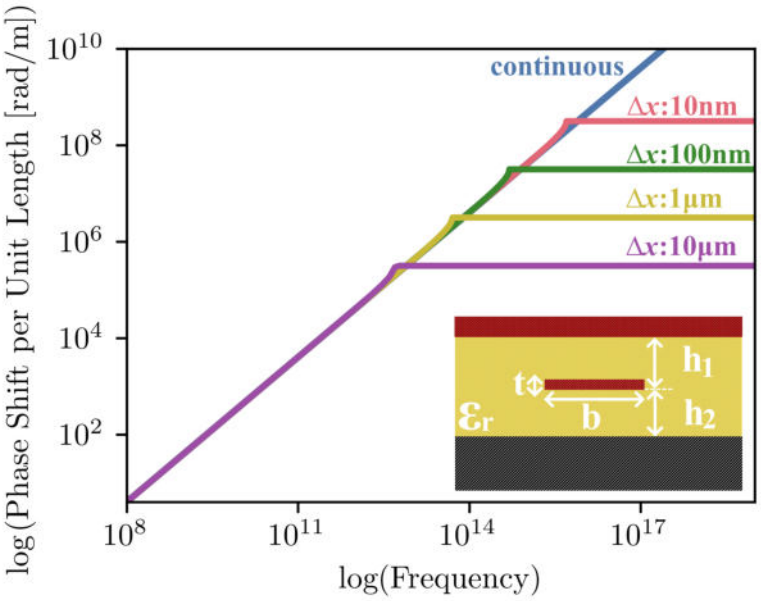

Fig. 1.8 Plot of the chromatic dispersions of continuous buried micro-stripline structure with dimensions: $b = 250\,nm$, $t = 20\,nm$, $h_1 = 50\,nm$, $h_2 = 250\,nm$, $\epsilon_r = 3.6$. Lumped element models with cell sizes equivalent to: $10\,\mu m$, $1\,\mu m$, $100\,nm$, and $10\,nm$ lengths of the continuous line which have nonlinear dispersion, unlike the continuous line, and increasing cut-off frequencies at which these unit cells act as $\lambda/2$ resonators.

can be reduced to:

$$Z_\pi = \sqrt{\frac{Z_s Z_p}{1 + Z_s/4Z_p}} \ . \tag{1.24}$$

In the case where the series arm is purely inductive and the return arm purely capacitive the low frequency limit $f \ll 1/\sqrt{L_s C_p}$ of this equation is simply $Z = \sqrt{L_s/C_p}$.

Wave Dispersion

All transmission lines will have some chromatic dispersion in which waves of different frequencies will propagate at different phase velocities. In the buried micro-stipline structure shown in the inset of Figure 1.8, this dispersion, due to fringing of the electric field, is very weak. The dispersion of a lumped element transmission line can be found by formulating the Kirchoff current law in the n^{th} and $(n+1)^{th}$ loops of the chain, as shown in black arrows in Figure 1.7. The current in the n^{th} loop, I_n, can then be shown to be:

$$\left[Z_p + Z_s + \frac{2Z_p Z_\pi}{2Z_p + Z_\pi}\right] I_n = Z_p I_{n-1} \ . \tag{1.25}$$

The transfer function, $\mathscr{T}$, which describes the transfer of the currents from the n^{th} to the $(n+1)^{th}$ cells can be described by taking the ratio of the currents in the two loops.

$$\mathscr{T} = \frac{\mathrm{I_n}}{\mathrm{I_{n-1}}} \equiv \frac{\mathrm{Z_p}}{\mathrm{Z_p} + \mathrm{Z_s} + \frac{2\mathrm{Z_p}\mathrm{Z}_\pi}{2\mathrm{Z_p}+\mathrm{Z}_\pi}} \tag{1.26}$$

The transfer function can then be related to the propagation constant through the relation:

$$\cosh\gamma = \frac{1}{2}\left(\mathscr{T} + \mathscr{T}^{-1}\right) \ . \tag{1.27}$$

We can rewrite this relation as a complex sum of the phase shift per cell, β and the attenuation per cell, α, or by the series and parallel impedance by:

$$\cosh\gamma = \cosh\left(\alpha + i\beta\right) \ , \tag{1.28}$$

$$= \cosh\alpha\cos\beta + i\sinh\alpha\sin\beta \ , \tag{1.29}$$

$$= 1 + \frac{Z_s}{2Z_p} \ . \tag{1.30}$$

When working in the passband of a lossless line, i.e. $\alpha = 0\,, \beta \neq 0$, we can directly relate the phase shift per cell to the wavevector:

$$k = \arccos\left(1 + \frac{Z_s}{2Z_p}\right) \ . \tag{1.31}$$

Important to note is that the lumped element transmission line has cut-off frequencies above which waves cannot propagate in the structure. As shown in Figure 1.8, lumped element transmission lines with unit cells equivalent to some length of the continuous structure have nonlinear dispersion relations due to the cell essentially acting as a $\lambda/2$ resonator at the cut-off frequency, f_c. Dispersion in the lumped element models are only approximately linear and comparable to the continuous case at low frequencies, $f \ll f_c$. A rule of thumb often used in microwave engineering is that the phase shift per unit cell be less than $\pi/5$ and the geometric size of the component be less than $\lambda/10$ of the highest frequency of interest for the structure to appear continuous [84, 114].

The Transfer Matrix Method

An alternative way to find the propagation characteristics of such a two-port structure is to use the transfer matrix method [115]. This is done by solving for the currents and voltages in two adjacent cells using four unknowns termed A, B, C and D:

$$\begin{bmatrix} V_i \\ I_i \end{bmatrix} = \begin{bmatrix} A_i & B_i \\ C_i & D_i \end{bmatrix} \cdot \begin{bmatrix} V_{i+1} \\ I_{i+1} \end{bmatrix} \ . \tag{1.32}$$

	Π-cell	T-cell
A	$1+\frac{Z_s}{2Z_p}$	$1+\frac{Z_s}{2Z_p}$
B	Z_s	$Z_s+\frac{Z_s^2}{4Z_p}$
C	$\frac{1}{Z_p}+\frac{Z_s}{4Z_p^2}$	$\frac{1}{Z_p}$
D	$1+\frac{Z_s}{2Z_p}$	$1+\frac{Z_s}{2Z_p}$

Table 1.1 Conversions of the series, Z_s, and parallel, Z_p, impedances of a lumped element transmission line into the ABCD transfer matrix coefficients for the chain.

A chain of such two port structures can then be described by a transfer matrix which is equal to the product of the constituent matrices:

$$\mathbf{T_{chain}} = \prod_i^n \mathbf{T_i} = \prod_i^n \begin{bmatrix} A_i & B_i \\ C_i & D_i \end{bmatrix} . \tag{1.33}$$

The series and parallel impedances, as previously described, can then be converted into the transfer matrix coefficients using the formulas of Table 1.1. This transfer matrix can then be used to find the coefficients of the scattering matrix, which is most often used for analysis of experimental results. This can be achieved using the conversions of Table 1.2.

Then from this scattering matrix the phase shift per cell, or the dispersion of the transmission line, can be found with the formula:

$$k = \arctan\left(\frac{\mathrm{Im(S21)}}{\mathrm{Re(S21)}}\right)/N , \tag{1.34}$$

where N is the number of cells in the transmission line.

S-Parameter	ABCD Conversion
S11	$\frac{A+B/Z_0-CZ_0-D}{A+B/Z_0+CZ_0+D}$
S12	$\frac{2\,(AD-BC)}{A+B/Z_0+CZ_0+D}$
S21	$\frac{2}{A+B/Z_0+CZ_0+D}$
S22	$\frac{-A+B/Z_0-CZ_0+D}{A+B/Z_0+CZ_0+D}$

Table 1.2 Table of the conversions from ABCD parameters into S-parameters where Z_0 is the system impedance, usually $50\,\Omega$.

Link to ToC

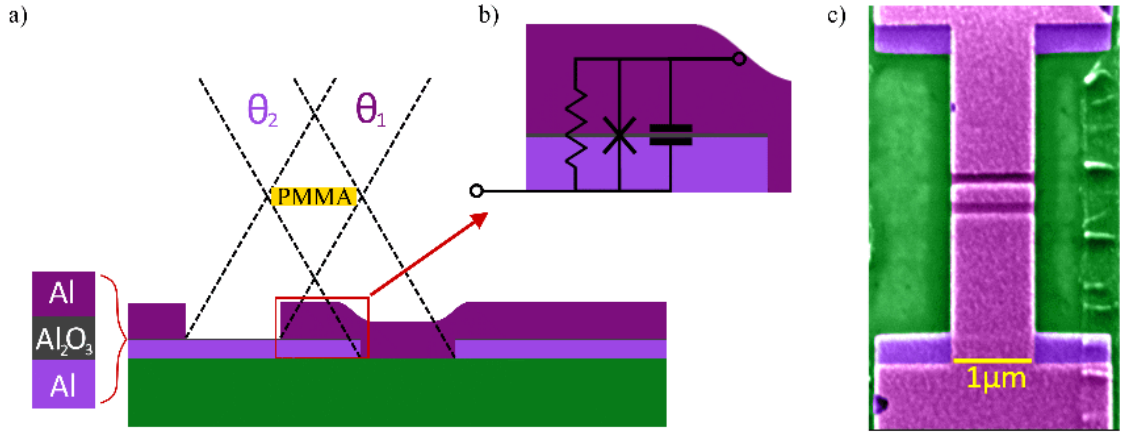

Fig. 1.9 Physical diagram of an overlap tunnel junction formed by the Dolan bridge technique where a bridge in the PMMA resist layers cast a shadow on the substrate [116]. Two aluminum films deposited at different angles to the substrate then form a confined overlap region, which allows Cooper pairs to tunnel through the thin oxide layer formed on the first layer. b) The confined tunnel junction region can be modeled by an equivalent resistively and capacitively shunted superconducting junction (RCSJ model) as shown overlaid on the tunneling barrier. c) A false colour SEM image of an aluminium tunnel junction formed by this shadow evaporation technique in a device shared with us by the Rodionov group of BMSTU.

1.2.3 Josephson Junctions

Josephson junctions, also referred to as superconducting weak links, can be formed in a variety of ways so long as two bulk superconducting regions are connected through a region that restricts the flow of charge. This can be achieved in several ways, for example, using a constriction in which the width of the superconducting 'nano-bridge' is smaller than the coherence length of the superconducting state, or junctions formed of normal metal barriers sandwiched by two superconductors. However, by far the most common kind is the SIS type junction in which two superconducting electrodes are separated by a thin insulating layer. In the example of Figure 1.9, the two electrodes are superconducting aluminium deposited at different angles such that they overlap in a confined area, while the insulating layer is formed by allowing the first aluminium layer to oxidize. Common to all of these technologies is that they can be modelled by an equivalent circuit with a dissipative, capacitive and superconducting current branches called the RCSJ model, (shown in Figure 1.9b) [3, 40].

Tunneling Current

In the weakly superconducting region Cooper pairs tunnel between the bulk states creating a non-zero flow of charge without any voltage drop. The first Josephson equation relates the tunneling current, I_J to the sine of the superconducting phase difference across the junction, $\varphi = \varphi_B - \varphi_A$:

$$I_J = I_c \sin\varphi \ , \tag{1.35}$$

Link to ToC

where I_c is the critical current of the junction above which a voltage drop occurs. This relation is also referred to as the current-phase-relation (CPR) of the junction and which has periodic behaviour in terms of the single flux quantum: $\Phi_0 = {}^{h}/_{e}$.

The second Josephson equation relates the voltage drop across a junction in the dissipative state, V_J with the rate of change of the superconducting phase difference across the junction:

$$V_J = -\frac{\Phi_0}{2\pi}\frac{d\varphi}{dt} \ , \tag{1.36}$$

where the superconducting phase difference across the junction has been expressed in terms of flux via the relation:

$$\varphi \equiv 2\pi\Phi/\Phi_0 \ . \tag{1.37}$$

The first and second Josephson equations can be combined to find the reactance of the Josephson element in the small current approximation, where:

$$V_J = \frac{\Phi_0}{2\pi I_c \cos\varphi}\frac{dI_J}{dt} \ , \tag{1.38}$$

is the oscillating voltage across the junction rewritten in terms of the tunneling current. This matches the form of the current-voltage relation for a classical inductance, where the derived 'Josephson inductance' then takes the form:

$$L_J = \frac{\Phi_0}{2\pi I_c}\frac{1}{\cos\varphi} \ . \tag{1.39}$$

Resistively and Capacitively Shunted Junction Model

The full current relation that takes into account the supercurrent, dissipative and capacitive branches as shown in Figure 1.9b) can be written as:

$$I_J = \frac{\Phi_0}{2\pi R_J}\frac{d\varphi}{dt} + C_J\frac{\Phi_0}{2\pi}\frac{d^2\varphi}{dt^2} + I_c\sin\varphi \ . \tag{1.40}$$

where R_J and C_J are the resistance and capacitance of the junction and voltage across the junction has been replaced by the superconducting phase gradient by Equation 1.36. This relation can be used to accurately model the dc and rf response of most tunnel junctions, as well as other formations such as constrictions and nanobridges where junction capacitance goes to zero.

The Josephson tunnel junction is an active element that converts applied dc to rf by the self-oscillations induced in the junction. The rf tone, called the junction plasma frequency, is a function of the voltage across it and can be written as:

$$\omega_p = \frac{1}{\sqrt{L_J C_J}} \ . \tag{1.41}$$

Link to ToC

1.2.4 Kinetic Inductance

Kinetic inductance is an effect that arises from the movement of charge carriers due to an applied electric field. It can in essence be described from the Drude model of conductivity [117–119] which describes the conductivity of a metal, σ, by the number of electrons in unit cross section, n, their mass, m_e, charge, q_e, and the scattering time of electrons in the crystal, τ_e:

$$\sigma = \frac{nq_e^2}{m_e\left(i\omega + \tau_e^{-1}\right)} \ . \tag{1.42}$$

The real part of this conductivity is the dc conductivity while the imaginary part is related to the energy stored in the kinetic motion of the electron. In normal metals $\tau \sim 10^{-14}s$ and so the real part dominates until the millimeter wave regime where $\omega \sim \tau^{-1}$. Although a superconductor in which $\tau \to \infty$ has a significant imaginary component for microwave frequencies.

Superconductivity is, of course, governed by different set of physical laws that conduction in normal metals, however Ohm's law can still be applied when the mean free path of the charge carriers is short compared to the penetration depth of EM fields [118, 119]. The Mattis-Bardeen theory of superconductivity allows us to write the complex conductivity of a superconductor as a sum of a real and imaginary part [120].

$$\sigma_n = \sigma_1 + i\sigma_2 \tag{1.43}$$

The components of the conductivity are then shown to be:

$$\begin{aligned}\frac{\sigma_1}{\sigma_n} &= \frac{2}{\hbar\omega}\int_{\Delta}^{\infty}\frac{\left(f(E)-f(E+\hbar\omega)\right)\left(E^2+\Delta^2+\hbar\omega E\right)}{\sqrt{E^2-\Delta^2}\sqrt{(E+\hbar\omega)^2-\Delta^2}}dE \\ &\quad + \frac{2}{\hbar\omega}\int_{\Delta-\hbar\omega}^{-\Delta}\frac{\left(1-2f(E+\hbar\omega)\right)\left(E^2+\Delta^2+\hbar\omega E\right)}{\sqrt{E^2-\Delta^2}\sqrt{(E+\hbar\omega)^2-\Delta^2}}dE \ ,\end{aligned} \tag{1.44}$$

and

$$\frac{\sigma_2}{\sigma_n} = \frac{2}{\hbar\omega}\int_{max(\Delta-\hbar\omega,-\Delta)}^{\Delta}\frac{\left(1-2f(E+\hbar\omega)\right)\left(E^2+\Delta^2+\hbar\omega E\right)}{\sqrt{E^2-\Delta^2}\sqrt{(E+\hbar\omega)^2-\Delta^2}}dE \ . \tag{1.45}$$

where Δ is the superconducting energy gap, E is the energy of the charge carrier, ω is the angular frequency of the applied excitation, and $f(E)$ is the Fermi-Dirac distribution of electrons:

$$f(E) = \left(e^{E/k_BT}+1\right)^{-1} \ . \tag{1.46}$$

The electrons in a superconductor can be described as a two-fluid system, similar to He-II, where the ratio of normal electrons to electrons in Cooper pairs approaches zero exponentially with temperature below T_c. Therefore, at low temperature ($T \ll T_c$) and low

frequency ($\hbar\omega \ll \Delta_0$ where Δ_0 is the superconducting energy gap at $T = 0$) the number of quasi-particles in the superconductors goes to zero. The real part of conductivity, σ_1 becomes negligibly small while the imaginary part, σ_2 approaches $\pi\Delta_0/\hbar\omega$.

The surface impedance of a thin film in the low-temperature limit and where the film thickness, t, is much less than the London penetration depth, $\lambda_L \ll t$, can be written as the quotient of the normal state resistivity, ρ_n, and the thickness.

$$\begin{aligned} Z &= \frac{1}{i\sigma_2 t} \\ &= -i\omega \underbrace{\frac{\hbar\rho_n}{\pi\Delta_0 t}}_{L_{k_\square}(0)} \end{aligned} \tag{1.47}$$

This appears as a reactance of equivalent form to an inductance, dubbed the kinetic inductance of the film $L_{k_\square}$.

The superconducting state is weakened by current flowing in the film due to a loss of time inversion symmetry [69, 121]. The change in the superconducting energy gap due to a flowing current has been widely studied and approximately takes the form:

$$\frac{\Delta(I)}{\Delta_0} \approx 1 - \left(\frac{I}{I_*}\right)^2 \ , \tag{1.48}$$

where,

$$I_* = \left[\frac{4\pi\Delta^3 N_0 V t}{\hbar\rho_n}\right]^{1/2} \ . \tag{1.49}$$

Here V is the volume of the trace and N_0 is the spin density of states per unit volume and unit energy. Then the kinetic inductance for non-zero current can be found via the relation $L_k(I)/L_k(0) \equiv \Delta_0/\Delta(I)$ leaving a simple and widely valid approximation for the nonlinear kinetic inductance:

$$L_k(I) = \frac{\hbar\rho_n}{\pi\Delta t}\left[1 + \frac{I^2}{I_*^2}\right] \ . \tag{1.50}$$

Key here is that the kinetic inductance of a film is directly proportional to the normal state resistivity just before the transition to a superconducting state. It is essential to maximize this term as, unlike a Josephson inductance, the application of a bias current will only increase the total kinetic inductance fractionally.

Link to ToC

1.3 Thesis Overview

Chapter 2 introduces the theory of operation of three wave mixing in rf-SQUID based transmission lines as well as the limits placed on the operation based on the physical structures. The simulation methods developed in this thesis for the study of travelling wave parametric amplifiers are also described. Both commercial lumped element simulation program (WRspice) and a set of coupled differential equations solved numerically in Python are tested and compared. By thoroughly investigating the validity of these simulation methods we remove any lingering doubts about the results obtained from simulations in later chapters.

Chapter 3 covers some theoretical studies performed using these simulation methods. The work in this chapter covers some important topics in the design of these lumped element TWPA devices, including the effects of flux bias, impedance mismatches and reflected waves, parasitic reactances and losses due to capacitive structures. Some of the content presented in this chapter, including some significant work on the effects of unavoidable fabrication defects and tolerances on device performance, have been published in [122, 123].

Chapter 4 describes the work done on the characterisation and modelling of a JTWPA device shared with us by the Rodionov group of Bauman Moscow State University. The experimental results are compared to simulations, the differences then allow us to comment on the shortcomings of the design of the device. These include gradiometric effects in which the rf-SQUID geometric inductance appeared to have a spatially dependent value, and losses that would make any possible amplification in such a device void.

Chapter 5 covers another JTWPA device shared with us by the Zorin group of PTB, which uses a more advanced fabrication technology based on the niobium tri-layer Josephson junction process. A key focus in this chapter was the effects and origin of the significant losses observed in the experimental results. Experiments were performed and compared to theory and simulations to draw conclusions on the viability of a device fabricated with this technology. This chapter has proven key in understanding the difficulties faced by multiple groups in producing a 3WM JTWPA device.

Chapter 6 presents two proposals that seek to overcome all of the problems so far discussed. Both a KITWPA and an rf-SQUID based JTWPA device are proposed, each of which includes some form of dispersion engineering to minimise pump harmonic generation and maximise signal gain. The theory and methods of device design are covered with particular attention paid to finding the optimal fabrication process and circuit design. We have high confidence that these proposals will function as desired when fabricated, due to the care and effort that has been put into the understanding and simulation of these devices.

Chapter 7 concludes on the work presented in this thesis and looks forward to future work and potential applications of these devices.

Link to ToC

Chapter 2

Simulation Methods

2.1 Introduction

Analog circuit design in both classical and quantum electronics is an arduous and repetitive task for which the process has remained relatively unchanged over the last fifty years. A circuit design is first made by the designer's intuition followed by a series of simulations of that circuit in a SPICE based program or electric field simulator. This iterative process is key to the production of a working device as it leads to consideration of the parasitic and dissipative effects that are often neglected in initial proposals.

This chapter discusses the methods of simulating and analysing superconducting TWPA behaviour using both a SPICE based circuit simulation program called WRspice which contains Josephson junction models. Another simulation option is the more bespoke coupled mode equation simulation derived from the works of Manley and Rowe [17], Tien [92], Yaakobi [124] and others.

These, or similar, tools have been used by several groups over the last ten years to understand and inform the design of superconducting parametric amplifiers. While this chapter should give the reader a good understanding of the process of derivation, interpretation and analysis of these simulations, further information can be found in articles by Eom [101], Yaakobi [124], Zorin [107] and Dixon [109]. Parts of this chapter have also been published in [122] and [123].

We begin this chapter by describing how current may flow through an rf-SQUID based transmission line, as well as the important wave propagation characteristics (impedance and dispersion) of such a structure. From this we can formulate a wave equation in terms of magnetic flux for the effective medium (or metamaterial) and in the case of parametric wave mixing we can derive a set of coupled mode equations to describe how these waves interact. Finally, we look at the use of the WRspice superconducting circuit simulator for design and analysis of these same devices, comparing and contrasting the two simulation techniques. We primarily study Zorin's proposed 23 Ω JTWPA device [107] in this chapter, building upon the theoretical works of Dixon [109, 125].

Link to ToC

2.2 Characteristics of a Josephson Transmission Line

The following section discusses specifically a transmission line structure formed of rf-SQUID's, although the process is generic and can be applied to any micro- or nano-structured superconducting transmission line. We begin by drawing an equivalent circuit for a unit cell of the transmission line described by Zorin [107] that can be analysed using the methods of Section 1.2.2. For this purpose the RCSJ model of the Josephson junction, described in Section 1.2.3, is essential.

2.2.1 Circuit Model

While the frequency range dubbed rf or 'radio frequency' has expanded greatly since the name was first chosen, the rf-SQUID is named as such as it will only show a response to an oscillating current. It consists of a geometric loop inductance in parallel with a Josephson junction, a direct current will therefore flow without impedance so long as the film is superconducting. However, as already described in Section 1.2.3 ,the impedance of a Josephson junction is of the same form as an inductance. Therefore, an oscillating current will be impeded by the change in total inductance of the loop as the phase gradient across the junction changes.

Actual rf-SQUIDs are only coupled inductively, whereas the structures discussed here have a galvanic connection to the measurement ports (although for convenience we shall continue to refer to them as rf-SQUIDs or rf-SQUID based structures). As such, we should investigate the effect of a static bias current (or equivalently a static magnetic field) on our loop structure. Assuming there is initially no phase difference between the superconducting electrodes of the junction, the flow of direct current through the geometric inductance produces a flux which then threads the loop, creating a phase gradient and causing a supercurrent to flow across the junction. This induced current screens this magnetic field, flowing on the inside of the loop (shown as the blue arrow in Figure 2.1) and allowing flux to penetrate the loop only in quantised steps equal to $\Phi_0 = {}^{h}/_{e}$. This is equivalent to the relation described for an rf-SQUID by Silver and Zimmerman [126]:

$$I_{appl.} = I_{dc} + I_c \sin\left(2\pi \frac{\Phi_{dc}}{\Phi_0}\right) , \tag{2.1}$$

where I_{dc} is the current flowing through the geometric inductance and the last term is the induced screening current.

An additional oscillating current applied to the rf-SQUID will split into both arms proportional to the impedance, then Equation 2.1 will take the form:

$$I_{appl.}(\varphi) = I_L + I_c \sin\left(2\pi \frac{\Phi_{dc} + \Phi}{\Phi_0}\right) - I_c \sin\left(2\pi \frac{\Phi_{dc}}{\Phi_0}\right) \tag{2.2}$$

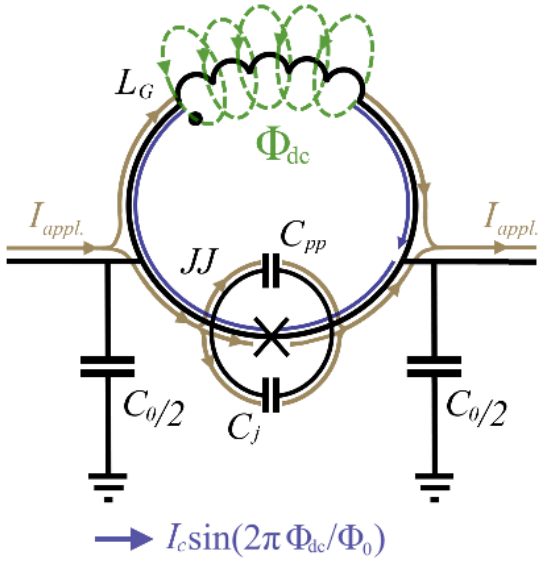

Fig. 2.1 An rf-SQUID like structure is shown in which a loop consisting of both inductive and capacitive elements is sandwiched by capacitances to ground, C_0 to allow for propagation of electromagnetic radiation. The arrowed lines in the figure show how an applied current (beige) induces a screening current (blue) due to the flux that threads the loop as a consequence of current flowing through the geometric inductance, L_G. The Josephson junction element opposite this then has its reactive response determined by the magnitude of the screening current, while the junction structure's capacitance, C_j and any other added capacitance, C_{pp} may alter the rf response of the device.

where, we have assumed that the self-induced magnetic field of the oscillating current is small and the dc effects are subtracted to leave only the current phase relation for an oscillating tone. We can then rewrite the current through the geometric inductance in terms of the flux penetrating the loop by: $I_L = \Phi/L_G$. In order to write the supercurrent branch similarly we must take a Taylor expansion of the sinusoidal terms:

$$I_J = \frac{I_c \varphi}{\beta_L} + \varphi \tilde{\chi}^{(1)} + \varphi^2 \tilde{\chi}^{(2)} + \varphi^3 \tilde{\chi}^{(3)} + \varphi^4 \tilde{\chi}^{(4)} + \mathscr{O}(\varphi^5 \tilde{\chi}^{(5)}) \tag{2.3}$$

where, we have replaced flux with superconducting phase by Equation 1.36 for convenience and β_L is the hysteresis parameter:

$$\beta_L = 2\pi L_G I_c / \Phi_0 \ . \tag{2.4}$$

The $\tilde{\chi}^{(n)}$ terms are the prefactors of the Taylor expansion ($\tilde{\chi}^{(1)} = I_c \cos\varphi_{dc}$, $\tilde{\chi}^{(2)} = -1/2 I_c \sin\varphi_{dc}$, etc.) with each being considered the strength of the respective nonlinearity. The nonlinear terms, which depend on the second, third, fourth, etc., power of the superconducting phase determine the wave mixing regimes as described previously, (see Section 1.2.1). The higher order nonlinearities are very weak by comparison with the quadratic and cubic and so can often be considered negligible.

A flux bias can then be chosen in such a way that a purely quadratic or purely cubic nonlinearity is achieved in the device, as the odd and even nonlinearities have out-of-phase dependences on flux. Shown in Figure 2.2 is the induced flux (Φ_{dc}) for an externally applied flux (Φ_e) and the strength of the second and third order nonlinearities that arise in the condition that the loop structure has hysteretic ($\beta_L > 1$) or non-hysteretic ($\beta_L \leq 1$) behaviour in flux.

In order for optimal operation of these devices as amplifiers we would wish to maximize the quadratic and minimize the cubic nonlinearity so as to achieve pure 3WM. As can be

Link to ToC

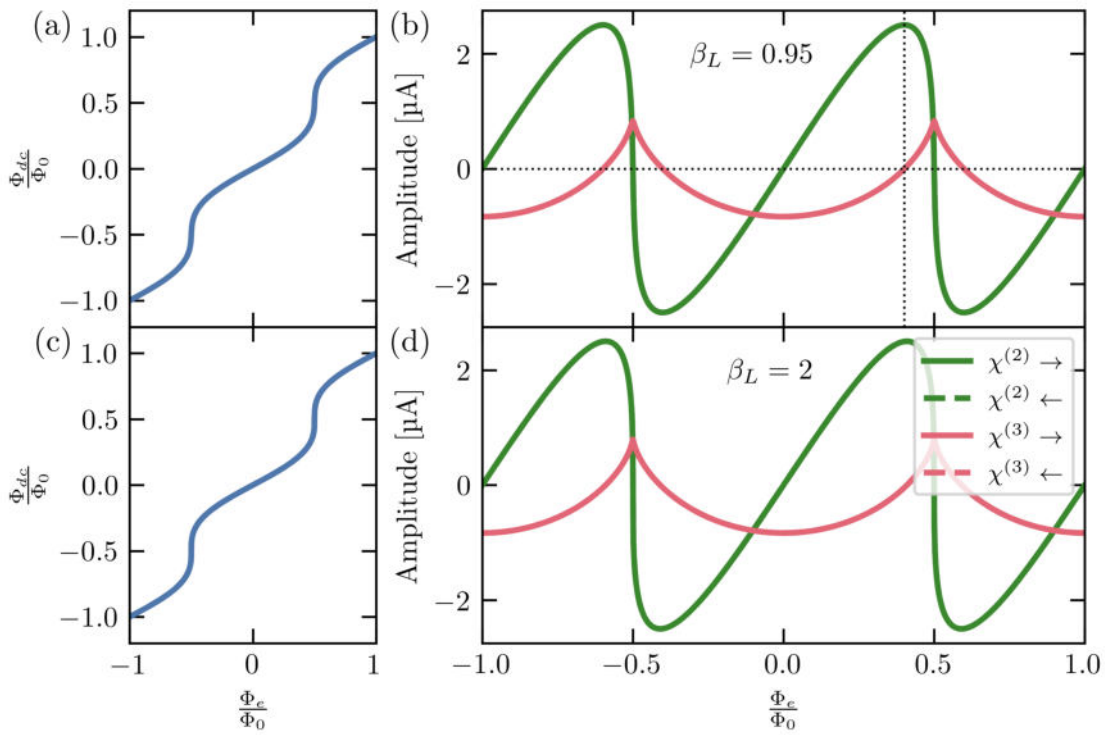

Fig. 2.2 a) Translation of the externally applied flux (Φ_e) to the induced flux (Φ_{dc}) through the geometric rf-SQUID loop as described by Silver and Zimmerman [126] for a hysteresis factor, $\beta_L = 0.95$ and b) the $\chi^{(2)}$ and $\chi^{(3)}$ nonlinearity strengths against applied flux for the same parameters. While c) and d) show the similar cases for a hysteresis factor $\beta_L = 2$ which leads to different behaviour for increasing applied flux (solid lines) than for decreasing applied flux (dashed lines).

seen in Figure 2.2 a hysteresis parameter less than one will allow for this rather simply with the dotted lines showing such a bias condition. However, for $\beta_L = 2$ the region of interest is in a portion of the plot which is multivalued with the strength of the nonlinearity depending on the direction of approach to it.

To finish our discussion on the current through these rf-SQUID based structures, we must include the other current branches of the Josephson junction as per the RCSJ model, although we will continue to neglect the current through the return capacitances C_0 for now. We then arrive at an altered form of Equation 2.2 in which the current through the capacitive and resistive branches of the junction are defined by the flux penetrating the loop (parallel plate capacitance and junction capacitance have been combined into a single C_j for brevity).

$$I_J = \left[\frac{I_c}{\beta_L} + \tilde{\chi}^{(1)}\right]\varphi + \varphi^2\tilde{\chi}^{(2)} + \varphi^3\tilde{\chi}^{(3)} + \frac{1}{R}\frac{d\Phi}{dt} + C_j\frac{d^2\Phi}{dt^2} \tag{2.5}$$

2.2.2 Impedance and Dispersion

Shown in Figure 2.3 is an example circuit model of the rf-SQUID based transmission line that we study. Following the example of Section 1.2.2 we can determine the wave

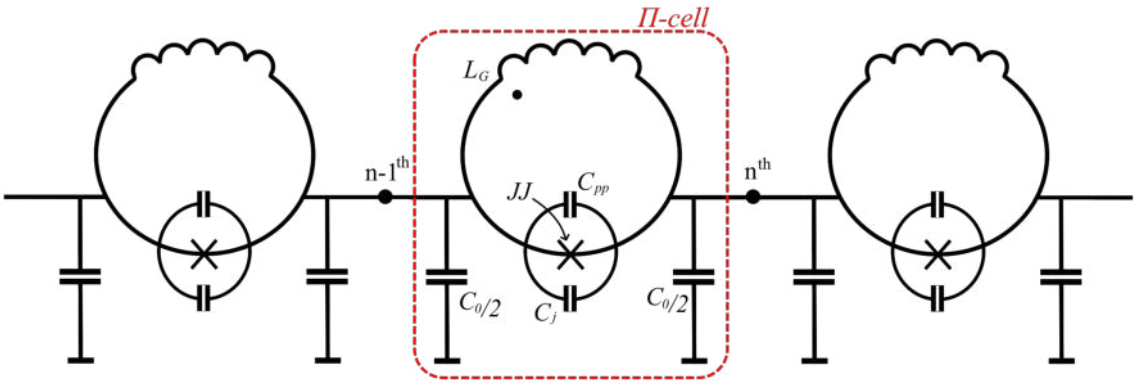

Fig. 2.3 A transmission line structure formed of a chain of the rf-SQUID based cells described previously, in which the mainly inductive elements of the loop structure (geometric inductance, L_G and nonlinear inductance of the Josephson junction, L_J) are sandwiched by return capacitances to a ground plane, C_0 in order to allow for quasi-travelling-electromagnetic (quasi-TEM) wave propagation that can be tuned to match the $50\,\Omega$ measurement environment. The additional capacitive elements of the loop structure (junction capacitance, C_j and any additional parallel plate capacitance, C_{pp}) are normally unavoidable and alter the transmission properties of the device if not controlled carefully.

propagation characteristics of the device rather simply. We prefer to not split the rf-SQUID loop into different cells so we will analyse the structure using the Π-cell model.

Characteristic Impedance

The presence of a Josephson junction shunting the series arm inductance complicates the analysis a little due to its nonlinear Josephson inductance and the associated junction capacitance. Disregarding, for the time being, any losses in the circuit and setting, from Figure 2.1, the return branch impedance as,

$$Z_p = \frac{1}{i\omega C_0}\,, \tag{2.6}$$

and the series branch,

$$Z_s = \left[\frac{1}{i\omega L_T(\varphi)} + i\omega C_j\right]^{-1}, \tag{2.7}$$

where,

$$L_T(\varphi) = \frac{L_G L_J(\varphi)}{L_G + L_J(\varphi)}\,. \tag{2.8}$$

we can come to a final relation for the impedance of an rf-SQUID based transmission line which is a function of both frequency and superconducting phase gradient across the

Parameter Set:	I_c [µA]	L_G [pH]	C_j [fF]	C_0 [fF]
	5	57	60	100

Table 2.1 The parameters of the transmission line unit cells used through the following chapters where critical current, I_c geometric inductance, L_G junction capacitance, C_j and return capacitance C_0 are the same as those suggested in [107].

Josephson junction, φ:

$$\mathrm{Z}_\pi(\omega,\varphi) = \sqrt{\frac{\mathrm{L_T}(\varphi)}{\mathrm{C_0}\,(1-\omega^2/\omega_\mathrm{c}(\varphi)^2)}}\,, \tag{2.9}$$

where, the cut-off frequency for the metamaterial, ω_c, is:

$$\omega_c(\varphi) = \frac{2}{\sqrt{L_T(\varphi)\cdot(C_0+4C_j)}}\,. \tag{2.10}$$

While it was already known from Section 1.2.2 that perfect matching to a 50 Ω environment is impossible over a very wide bandwidth, as is apparent in Figure 2.4 for the parameter set of Table 2.1, we now also see the effect of the flux bias on impedance. This dependence on flux bias (or dc bias) can be a practical way to characterise the nonlinear

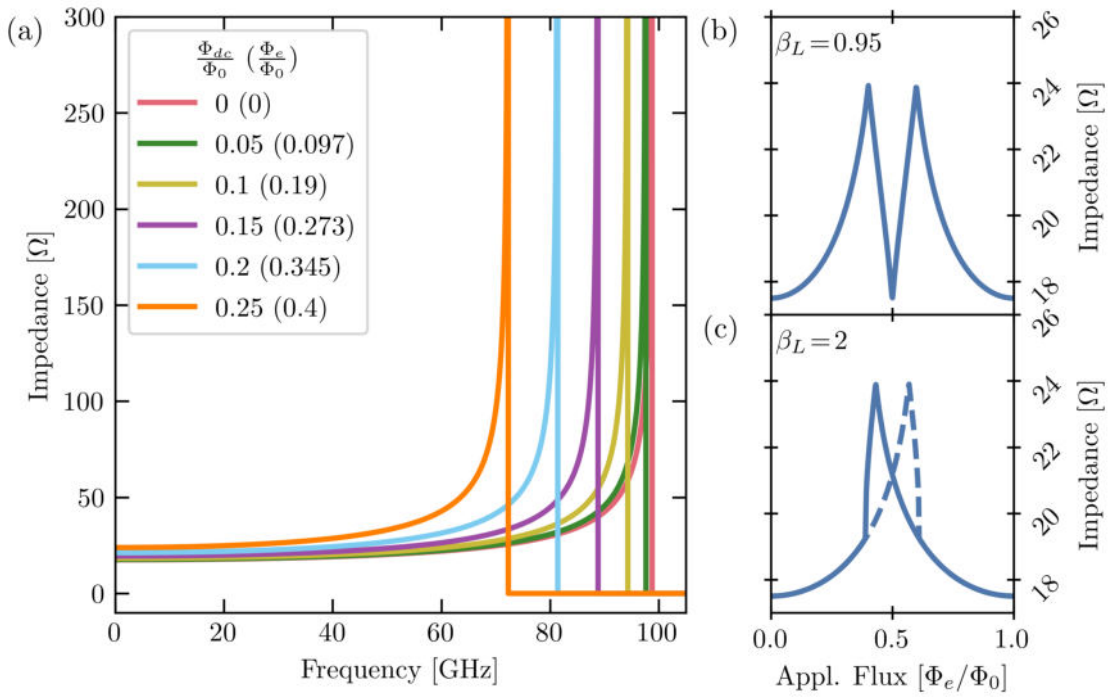

Fig. 2.4 a) The impedance of an rf-SQUID based transmission line versus the frequency of the wave travelling through it for a selection of induced flux biases in the loops with the applied flux shown in brackets. b) and c) The impedance of the same transmission line for a 5 GHz tone against the externally applied flux for the hysteresis parameters $\beta_L = 0.95$ and $\beta_L = 2$, respectively.

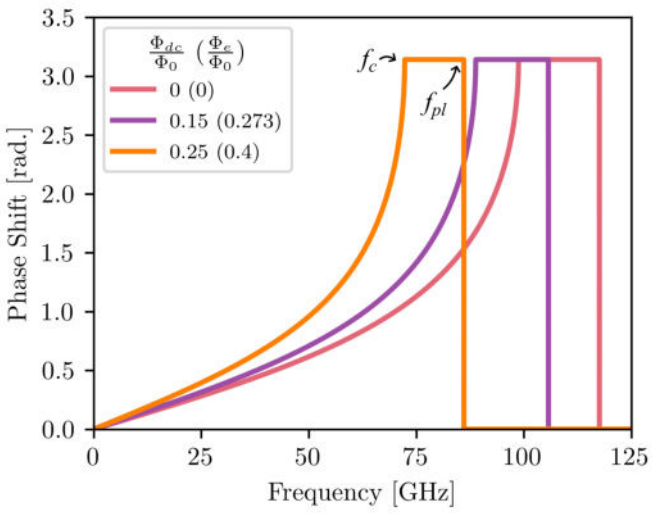

Fig. 2.5 Plot of the dispersion relation for non-hysteretic rf-SQUID based transmission line ($\beta_L = 0.95$) where the effect of flux biasing shows a clear effect. The orange curve, corresponding to maximised $\chi^{(2)}$ nonlinearity has the lowest cut-off and plasma frequency response due to the higher effective inductance of the loop structure at that bias point.

inductance of a device under test. Shown in Figure 2.4 (b) a wave of 5 GHz encounters significantly different impedances over a flux period ($\sim 6\,\Omega$) while a similar hysteresis parameter set leads to an asymmetric shape in (c). The peak impedance at the 3WM regime ($\Phi_{dc}/\Phi_0 = 1/4$) and the minimum impedance at the 4WM regime ($\Phi_{dc}/\Phi_0 = 0$) also makes for a simple method of correctly biasing such a device.

Wave Dispersion

Substituting the relations for Z_s and Z_p that we have determined for the structure into Eq. 1.31 and using the small angle approximation we come to:

$$\beta = 1 + \frac{\omega C_0 L_T(\varphi)\,/C_j}{2\omega L_T(\varphi) - 2/\omega C_j}\ , \tag{2.11}$$

or, approximately:

$$\beta = \frac{\omega}{\omega_c}\frac{1}{\sqrt{1-\omega^2/\omega_{pl}^2}} \tag{2.12}$$

assuming $\omega \ll \omega_{pl}$, where $\omega_{pl} = 1/\sqrt{LC_j}$ and $\omega_c = 1/\sqrt{LC_0}$. These are defined as the rf-SQUID plasma frequency and transmission line cut-off frequency at the 3WM bias point where L is the unbiased inductance of the rf-SQUID, as per Zorin [107]. As is clear this dispersion relation is both a function of frequency and dc bias (or flux bias), similar to the transmission line impedance. This is shown in Figure 2.5 for the parameter set of Table 2.1 where the nonlinearity is tuned from a 3WM to 4WM bias point. The key result is that there exists always in these devices chromatic dispersion, which has been shown to adversely affect parametric amplification in Section 1.2.1.

Link to ToC

2.2.3 Wave Equation

To derive a wave equation for the structure described, we follow a process similar to the formulation of telegrapher's equations in a classical transmission line. We consider the Kirchoff current law at the n^{th} node of the array shown in Figure 2.3. At this node there is current entering the node from the $(\mathrm{n}-1)^{\mathrm{th}}$ SQUID and leaving to the return line through the capacitance C_0 or continuing on to the n^{th} SQUID.

$$I_{n-1} = I_n + I_{Cn} \tag{2.13}$$

As shown previously the current through the series branch of the transmission line can be described by the magnetic flux penetrating the loop of the rf-SQUID. This flux can be written in terms of the voltage drop across the SQUID as:

$$-\frac{d\Phi_n}{dt} = V_{n+1} - V_n \ . \tag{2.14}$$

Normally, to formulate the Kirchoff laws for superconducting circuits the concept of voltage drop is replaced instead by nodal fluxes. This unifies the methods for describing current flow through reactive and resistive elements in the circuit. The concept of nodal fluxes, where the voltage at a node, V_n, is equal to the rate of change of flux at that node, can be expressed mathematically as:

$$V_n = \frac{d\tilde{\Phi}_n}{dt} \ , \tag{2.15}$$

which allows us to rewrite Equation 2.14 as:

$$\Phi_n = \tilde{\Phi}_n - \tilde{\Phi}_{n+1} \ . \tag{2.16}$$

Using Equation 2.5 and re-writing Equation 2.13 in terms of nodal fluxes we arrive at:

$$\begin{aligned}
&-\left[\frac{1}{L_G} + \tilde{\chi}^{(1)}\left(\frac{2\pi}{\Phi_0}\right) + C_j\frac{d^2}{dt^2} + \frac{1}{R_j}\frac{d}{dt}\right]\left(\tilde{\Phi}_{n-1} - \tilde{\Phi}_n\right) \\
&+ \tilde{\chi}^{(2)}\left(\frac{2\pi}{\Phi_0}\right)^2\left(\tilde{\Phi}_{n-1} - \tilde{\Phi}_n\right)^2 + \tilde{\chi}^{(3)}\left(\frac{2\pi}{\Phi_0}\right)^3\left(\tilde{\Phi}_{n-1} - \tilde{\Phi}_n\right)^3 \\
&= \\
&C_0\frac{d^2\tilde{\Phi}_n}{dt^2} - \left[\frac{1}{L_G} + \tilde{\chi}^{(1)}\left(\frac{2\pi}{\Phi_0}\right) + C_j\frac{d^2}{dt^2} + \frac{1}{R_j}\frac{d}{dt}\right]\left(\tilde{\Phi}_n - \tilde{\Phi}_{n+1}\right) \\
&+ \tilde{\chi}^{(2)}\left(\frac{2\pi}{\Phi_0}\right)^2\left(\tilde{\Phi}_n - \tilde{\Phi}_{n+1}\right)^2 + \tilde{\chi}^{(3)}\left(\frac{2\pi}{\Phi_0}\right)^3\left(\tilde{\Phi}_n - \tilde{\Phi}_{n+1}\right)^3
\end{aligned} \tag{2.17}$$

The linear parts of the geometric and Josephson inductances can be combined at this point as the total linear inductance, L.

$$\frac{1}{L} = \frac{1}{L_G} + \tilde{\chi}^{(1)}\left(\frac{2\pi}{\Phi_0}\right) \tag{2.18}$$

If similar terms are grouped and the continuum approximation is made, where the difference in flux between nodes is made a continuous function of space and time, $\Phi(z,t)$, as detailed in Appendix B, we can arrive at a wave equation for the Josephson transmission line.

$$\begin{aligned} &-\frac{\Phi_0}{2\pi}\left[\frac{1}{L} + C_j\frac{\partial^2}{\partial t^2} + R_j\frac{\partial}{\partial t}\right]\frac{\partial^2\tilde{\varphi}}{\partial x^2} + 2\tilde{\chi}^{(2)}\frac{\partial}{\partial x}\left(\frac{\partial\tilde{\varphi}}{\partial x}\right)^2 + 3\tilde{\chi}^{(3)}\frac{\partial}{\partial x}\left(\frac{\partial\tilde{\varphi}}{\partial x}\right)^3 \\ &+ \frac{\Phi_0 C_0}{2\pi}\frac{\partial^2\tilde{\varphi}}{\partial t^2} = 0 \end{aligned} \tag{2.19}$$

Then for the time being, disregarding dissipation, R_J, making some substitutions, and redefining the nonlinearities $\chi^{(2,3)} = 2\pi\tilde{\chi}^{(2,3)}L/\Phi_0$, we arrive at the following equation:

$$-\frac{\partial^2\tilde{\varphi}}{\partial x^2} + \frac{1}{\omega_J^2}\frac{\partial^4\tilde{\varphi}}{\partial x^2\partial t^2} + 2\chi^{(2)}\frac{\partial}{\partial x}\left(\frac{\partial\tilde{\varphi}}{\partial x}\right)^2 + 3\chi^{(3)}\frac{\partial}{\partial x}\left(\frac{\partial\tilde{\varphi}}{\partial x}\right)^3 + \frac{1}{\omega_c^2}\frac{\partial^2\tilde{\varphi}}{\partial t^2} = 0\ . \tag{2.20}$$

This wave equation can then be reduced to a simpler form using the dispersion relation for a transmission line absent of nonlinearities, Equation 2.11, and the slow wave approximation:

$$d^2A/dx^2 \ll kdA/dx \ll k^2A\ . \tag{2.21}$$

The resulting wave equation has only derivatives in space:

$$\left[ik\frac{dA}{dx}e^{i(kx-\omega t)} + \text{c.c.}\right] = \chi^{(2)}\frac{\partial}{\partial x}\left(\frac{\partial\varphi}{\partial x}\right)^2 + \chi^{(3)}\frac{\partial}{\partial x}\left(\frac{\partial\varphi}{\partial x}\right)^3\ . \tag{2.22}$$

The full derivation of the above equation is available in Appendix B.

2.3 Coupled Mode Equation Simulations

Waves propagating through this structure interact with each other via the modulation of the nonlinear Josephson inductance which, at the desired 3WM bias point, will have a quadratic dependence on the phase gradient across the junction. Of course, this phase gradient has itself a relation to the total current through the junction by Equation 1.35. To describe how the amplitudes of the travelling waves may change over the length of

the structure we form a set of coupled ordinary differential equations (CME's) from the reduced wave Equation 2.22.

We begin by considering the fewest travelling waves for which parametric amplification is viable by conservation laws from Equation 1.7, a pump, a weak signal and a generated idler wave at the difference frequency. The form of this excitation in flux takes the form:

$$\varphi = \begin{cases} 1/2\left(A_p e^{i(\omega_p t - k_p x)} + A_p^* e^{-i(\omega_p t - k_p x)}\right) , \\ 1/2\left(A_s e^{i(\omega_s t - k_s x)} + A_s^* e^{-i(\omega_s t - k_s x)}\right) , \\ 1/2\left(A_i e^{i(\omega_i t - k_i x)} + A_i^* e^{-i(\omega_i t - k_i x)}\right) , \end{cases} \tag{2.23}$$

where the transform of pump and signal current to unitless amplitude takes the form:

$$I_n = \frac{\beta_n A_n \Phi_0}{\pi L_G} , \tag{2.24}$$

where, β_n is the phase shift per cell for the considered wave, I_n is its current amplitude, and A_n is the unitless amplitude of the wave.

To form coupled mode equations from this 'wave packet' as we will call it, is fairly simple. Substituting φ into the reduced wave equation leads to us taking its derivative:

$$\begin{aligned} \frac{\partial \varphi}{\partial z} =& 1/2\Big\{ ik_p A_p e^{i(k_p x - \omega_p t)} - ik_p A_p^* e^{-i(k_p x - \omega_p t)} && (2.25)\\ &+ ik_s A_s e^{i(k_s x - \omega_s t)} - ik_s A_s^* e^{-i(k_s x - \omega_s t)} && (2.26)\\ &+ ik_i A_i e^{i(k_i x - \omega_i t)} - ik_i A_i^* e^{-i(+k_i x - \omega_i t)}\Big\} && (2.27) \end{aligned}$$

where, we have again used the slow-wave approximation, Equation 2.21, to neglect the derivatives. Considering here only the quadratic nonlinearity (although the cubic 4WM nonlinearity follows the same process), we take this to the second power to find:

$$\begin{aligned} \left(\frac{\partial \varphi}{\partial x}\right)^2 =& 1/4\,\{ - \overbrace{2k_s k_i A_s A_i e^{i(k_p x - \omega_p t)}}^{P} + \overbrace{2k_p k_i A_p A_i^* e^{i(k_s x - \omega_s t)}}^{S} \\ &+ \overbrace{2k_p k_s A_p A_s^* e^{i(k_i x - \omega_i t)}}^{I} - \overbrace{2k_p k_s A_p A_s e^{i(\kappa_\sigma x - \Omega_\sigma t)}}^{\sigma} \\ &- \overbrace{k_p^2 A_p^2 e^{i(\kappa_{2p} x - \Omega_{2p} t)}}^{2P} - \overbrace{k_s^2 A_s^2 e^{i(k_{2S} x - \omega_{2S} t}}^{2S} - \overbrace{k_i^2 A_i^2 e^{i(k_{2i} x - \omega_{2i} t)}}^{2I} \\ &- \overbrace{2k_p k_i A_p A_i e^{i(\kappa_{P+I} x - \Omega_{P+I} t)}}^{P+I} + \overbrace{2k_s k_i A_s A_i^* e^{i(\kappa_{S-I} x - \Omega_{S-I} t)}}^{S-I} \\ &+ \mathbf{c.c.} + \mathbf{OR}\} \ . \end{aligned} \tag{2.28}$$

where the labels refer to the mixing product (i.e. pump P, signal S, idler I, sum-frequency-generation σ etc.) and **OR** refers to rectification in a process inverse to second harmonic generation. The sums of wavevectors or frequencies have been written as $\kappa_{a+b} = k_a + k_b$ or $\Omega_{a+b} = \omega_a + \omega_b$ for brevity.

To then find the coupled mode equations for each propagating wave, we separate these mixing products into sets with product frequency equal to the frequency of the propagating wave that we consider for that equation. For example, the pump wave CME will take the form:

$$\frac{dA_p}{dx} = \overbrace{-\frac{\chi^{(2)}}{2} e^{i(\kappa_3 x - \Omega_3 t)} \left[k_s k_\delta A_s A_\delta\right]}^{3WM} + \frac{\chi^{(3)}}{8} \Bigg[\overbrace{6ik_p A_p \left(k_s^2 A_s A_s^* + k_\Delta^2 A_\Delta A_\Delta^*\right)}^{XPM} \\ \underbrace{+3ik_p^3 A_p^2 A_p^*}_{SPM} \underbrace{+ik_\Delta k_s \left(k_\Delta + k_s - k_p\right) A_p^* A_\Delta A_s e^{i(\kappa_4 x - \Omega_4 t)}}_{4WM} \Bigg] \ , \tag{2.29}$$

where κ_3 refers to the phase mismatch between the pump, signal and idler waves in the 3WM regime, $(k_p - k_s - k_\delta)$, κ_4 is the equivalent for the 4WM regime $(2k_p - k_s - k_\Delta)$ and a similar replacement is made for frequencies Ω_3, Ω_4 and to avoid confusion the 3WM idler is denoted by δ while the 4WM idler is denoted by Δ. The SPM and XPM labels in the 4WM terms refer to self- and cross-phase modulation terms.

The signal and idler CME's can then be formulated in the same way.

$$\frac{dA_s}{dx} = \frac{\chi^{(2)}}{2} e^{i(\kappa_3 x - \Omega_3 t)} \left[k_p k_\delta A_p A_\delta^*\right] + \frac{3\chi^{(3)}}{8} \Big[2ik_p^2 k_s A_p A_p^* A_s + 2ik_\Delta^2 k_s A_\Delta A_\Delta^* A_s \\ + ik_s^3 A_s^2 A_s^* + k_\Delta k_p^2 A_\Delta^* A_p^2 e^{i(\kappa_4 x - \Omega_4 t)}\Big] \ , \tag{2.30}$$

$$\frac{dA_\delta}{dx} = \frac{\chi^{(2)}}{2} e^{i(\kappa_3 x - \Omega_3 t)} \left[k_p k_s A_p A_s^*\right] \ , \tag{2.31}$$

$$\frac{dA_\Delta}{dx} = \frac{3\chi^{(3)}}{8} \Big[2ik_p^2 k_\Delta A_p A_p^* A_\Delta + 2ik_s^2 k_\Delta A_s A_s^* A_\Delta + ik_\Delta^3 A_\Delta^2 A_\Delta^* \\ + ik_s k_p^2 A_s^* A_p^2 e^{i(\kappa_4 x - \Omega_4 t)}\Big] \ . \tag{2.32}$$

The change in a waves amplitude is therefore equal to the product of the waves that mix to form it at that point in the metamaterial.

Assuming no pump depletion and a small phase mismatch, these relations for the basic mixing processes can be rewritten in a simpler fashion from which an analytical expression of the gain can be found. Usually, this solution introduces too many approximations to be useful to us with our focus on simulation, however it can be found in [107], [127] Appendix D.

2.3.1 Generic CME Composition

Where these simple relations fail, however, is that in reality many more mixing products than just the idler are generated as shown in Figure 2.6, leeching power from the intended

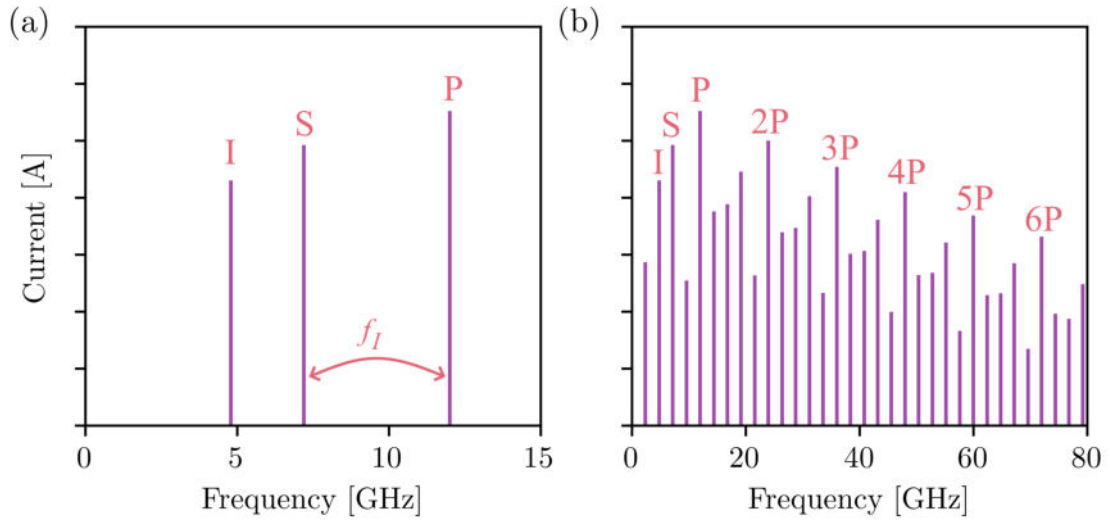

Fig. 2.6 Tones considered in the parametric amplification process in a) the simplest case of three wave mixing where a pump frequency (P) and a signal frequency (S) and the generated difference frequency idler tone (I) are the only mixing products and b) the more complex case of multi-wave mixing that is more likely to occur where power is drawn away from the three wave mixing amplification process into higher order processes, expecially that of pump harmonic generation (2P - 6P).

amplification process of the signal. The cascading effect of parasitic wave mixing is apparent if we consider that each of the waves that encounters a discrete nonlinearity will mix with all other waves propagating through the nonlinearity and itself. This produces an ever expanding wave packet diminishing the amplification of the signal wave, this topic has been discussed at length by Dixon *et al* [109].

To more properly predict the performance of a given travelling wave parametric amplifier design, we must formulate coupled mode equations for arbitrary nonlinearity and include all wave mixing products within the passband of the device. This leads us to a series of coupled mode equations of the form:

$$\begin{aligned}
\frac{dA_f}{dx} =& \frac{\chi^{(2)}}{4} e^{-ik_f x} \left[2 \sum_{n,m}^{N} k_n k_m A_n A_m e^{i(k_n - k_m)x} \Big|_{\substack{\omega_n, \omega_m < \omega_c \\ \omega_n - \omega_m = \omega_f}} \right. \\
& \left. -2 \sum_{n,m}^{N} k_n k_m A_n A_m e^{i(k_n + k_m)x} \Big|_{\substack{\omega_n, \omega_m < \omega_c \\ \omega_n + \omega_m = \omega_f}} \right] \\
& + \frac{\chi^{(3)}}{8} e^{-ik_f x} \left[3k_f^3 |A_f|^2 A_f + 6 \sum_{j}^{N} k_f k_j^2 |A_j|^2 A_f \right. \\
& + 3 \sum_{n,m,j}^{N} k_j k_k k_m A_j A_k A_m e^{i(k_j + k_k + k_m)x} \Big|_{\substack{\omega_p l, \omega_k, \omega_m < \omega_c \\ \omega_p l + \omega_k + \omega_m = \omega_f}} \\
& - 3 \sum_{n,m,j}^{N} k_j k_k k_m A_j A_k A_m e^{i(k_j + k_k - k_m)x} \Big|_{\substack{\omega_p l, \omega_k, \omega_m < \omega_c \\ \omega_p l + \omega_k - \omega_m = \omega_f}} \\
& \left. + 3 \sum_{n,m,j}^{N} k_j k_k k_m A_j A_k A_m e^{i(k_j - k_k - k_m)x} \Big|_{\substack{\omega_p l, \omega_k, \omega_m < \omega_c \\ \omega_p l - \omega_k - \omega_m = \omega_f}} \right]
\end{aligned} \tag{2.33}$$

Link to ToC

When attempting to simulate these devices it is perhaps simplest to find all possible mixing products in a frequency range first and from this formulate the specific CME's. For an arbitrarily deep complexity both 3WM and 4WM will produce all possible tones, as they are all linear combinations of the pump and signal frequency. Therefore a useful measure of the complexity of a CME simulation is the depth to which these combinations are calculated, e.g. for a depth of N all tones up to $Nf_p \pm Nf_s$ should be considered.

Shown in Figure 2.7 is the effect of increasing the highest order of pump or signal tone mixing, N, on the 'amplitude profile' of the wave as it travels through the rf-SQUID array. Decreasing from exponential gain in the case of simple 3WM as described earlier to a much more complex case in which higher harmonics and reflections from impedance mismatches begin to play very significant roles in the wave mixing process, diminishing the amplification. In order to capture dynamic changes in the amplification process a time domain simulation technique, such as WRspice, is required. As can be seen, increasing complexity of CME simulations leads to ever improving agreement with WRspice simulation results for the same structure which speaks to its validity for application to this device.

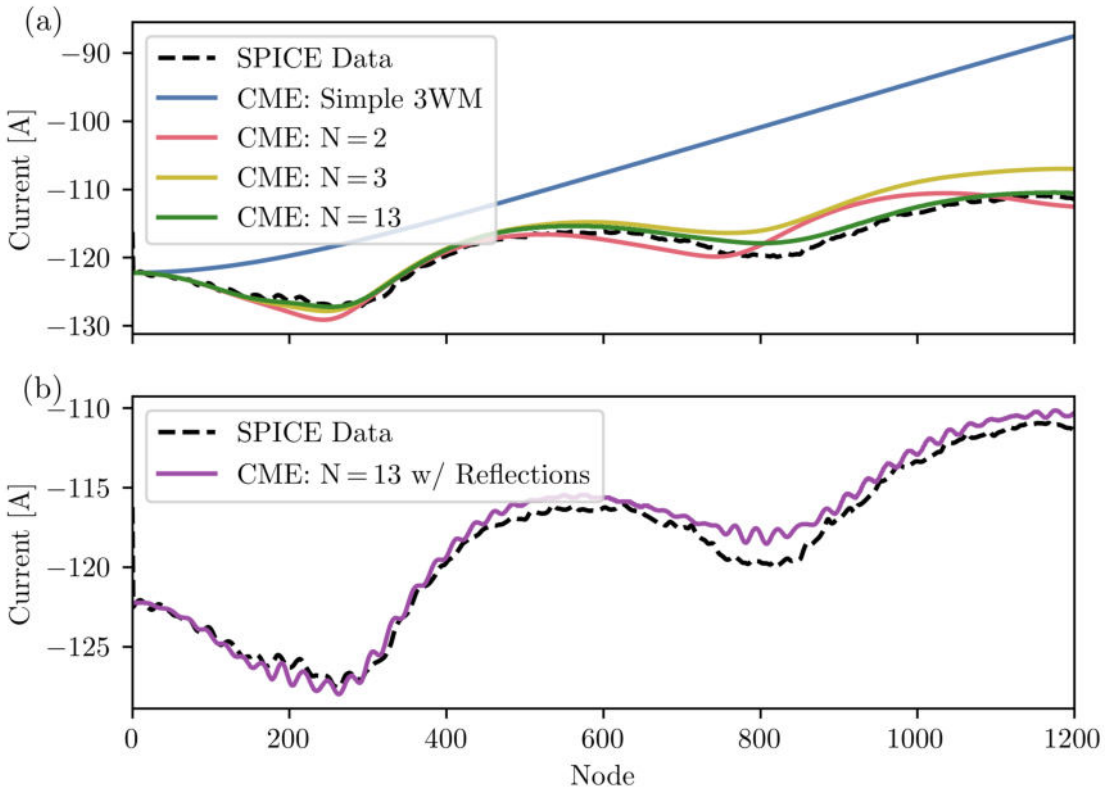

Fig. 2.7 a) As the complexity of the coupled mode equation simulations increases, by including contributions of wave mixing products up to the N^{th} harmonic of the pump and signal tones, better agreement is seen with the output of equivalent circuits taken from the WRspice circuit simulator. b) Shown is the effect of including reflections in the coupled mode equation simulations at N = 13 by including the complex conjugate of each term in the coupled mode equations leading to yet better agreement with the time domain circuit simulation results.

Link to ToC

2.4

Superconducting SPICE Circuit Simulations

SPICE (Simulation Program for Integrated Circuit Engineering) is a widespread lumped element circuit simulation platform, first developed in the computer science labs of UC Berkely, in 1972 [128]. While initially developed to make use of newly available computing power to aid in IC design, it became the standard way to test all circuits pre-fabrication. As IBM endeavoured to build a Josephson based computing system in the 1980s, attention turned to creating a robust circuit simulator for superconducting devices. SPICE was modified to include Josephson junction models in several iterations made by different groups and companies, including JSPICE [50], Hyspice [49, 129], and WRspice [51] which is used to great extent in this thesis to model superconducting parametric amplifiers and metamaterials.

Common to all SPICE-based programs is the process of solving for the voltage at the nodes between components of the circuit using a combination of Kirchoff's laws and constitutive equations. To make these systems of equations computationally simple, they must be organised into matrices using Modified Nodal Analysis to arrive at an equation such as:

$$[\mathbf{Y}] \cdot [\mathbf{V}] = [\mathbf{I}], \tag{2.34}$$

where $\mathbf{Y}$ is an NxM matrix containing the information on the small-signal admittances between nodes and the positions and polarities of voltage sources, $\mathbf{V}$ are the unknown node voltages and currents through voltage sources and $\mathbf{I}$ is a column matrix of the excitation currents and voltages of sources.

These matrices are by nature sparse, in that most elements are zero as it is rare to have any individual node in a circuit connected to more than three or four other nodes. In order to solve for matrix $\mathbf{V}$, matrix decomposition techniques are applied, usually LU (Lower-Upper) decomposition, and in particular for WRspice a sparse matrix solver algorithm is used to greatly speed up computation time [130].

A Josephson junction represented by the RCSJ model represents a problem for this type of program in that superconducting phase must replace voltage in the Kirchoff loop laws. Although aside from this the process of solving a circuit containing a Josephson junction is essentially the same as solving that with other nonlinear elements such as transistors, for which the program was built.

The supercurrent branch in a Josephson element, being a nonlinear function of phase, must be linearized for processing in SPICE programs. This is achieved using the Newton-Raphson method which states that the zero-point of the tangent to a curve, $f(x)$, at a point, x_0, will be closer to the zero-point of the function than the original point:

$$x_{n+1} = x_n + \frac{f(x_n)}{f'(x_n)} \ . \tag{2.35}$$

Link to ToC

Here f is a single valued function of x. The process of finding the tangent and the zero-point to the nonlinear function is repeated until the zero-points of the tangents converge around the function zero-point. In this way a solution for the phase gradient across a junction can be found from the information on the excitation currents through it.

The linearisation process involves replacing nonlinear components in the circuit matrix with a linear admittance, g, and a current source, I, in which the higher order nonlinear terms are 'hidden'.

The process of this solution for voltage nodes can be stepped through time using trapezoidal numerical integration techniques where the solutions at the previous timestep are used as the initial estimation for the following. WRspice completes this process with a variable time step to decrease computation time without sacrificing accuracy, although as the circuits increase in size the computation time increases exponentially. With most simulations completed in this thesis taking ~ 15 minutes, it becomes difficult to complete on a large scale without dedicated hardware.

2.4.1 DC Josephson Effect

To demonstrate WRspice's suitability to the tasks of this thesis we begin with a simulation of the most recognisable characteristic of Josephson junction circuits, the current-voltage relation. We complete a series of time domain simulations on the current biased junctions described in Table 2.2. The models used in these simulations are the built-in RCSJ model in mode `rtype = 1`, which considers the quasi-particle branch across the junction in calculations.

The junction parameters are chosen for the first two examples such that the first junction is non-hysteretic, the second hysteretic and the third is hysteretic with the parameters of an experimental Niobium-Aluminium Oxide-Niobium junction fabricated in KIT [131]. The hysteresis of a junction is determined by the parameter β_C, which can be written as:

$$\beta_C = \frac{2\pi I_c R_N^2 C_j}{\Phi_0} \ , \tag{2.36}$$

where I_c is critical current, R_N is the normal state resistance of the junction and C_j is the junction capacitance.

The simulation data for these junctions can be seen in Figure 2.8, where each data point required a 20 ns transient evolution simulation in which bias current is ramped to its final value after which a time average of the voltage across the junction is taken. A comparison of simulation results for the third junction can be made to experimental results

I_c [µA]	C_j [fF]	R_N [Ω]	β_c
5	0.6	23.87	0.01
5	500	23.87	4.33
1200	1000	1.4	7.15

Table 2.2 Junction parameters for dc Josephson effect WRspice simulations. First junction is non-hysteretic, second hysteretic, and third matches parameters extracted for a junction in [131].

Link to ToC

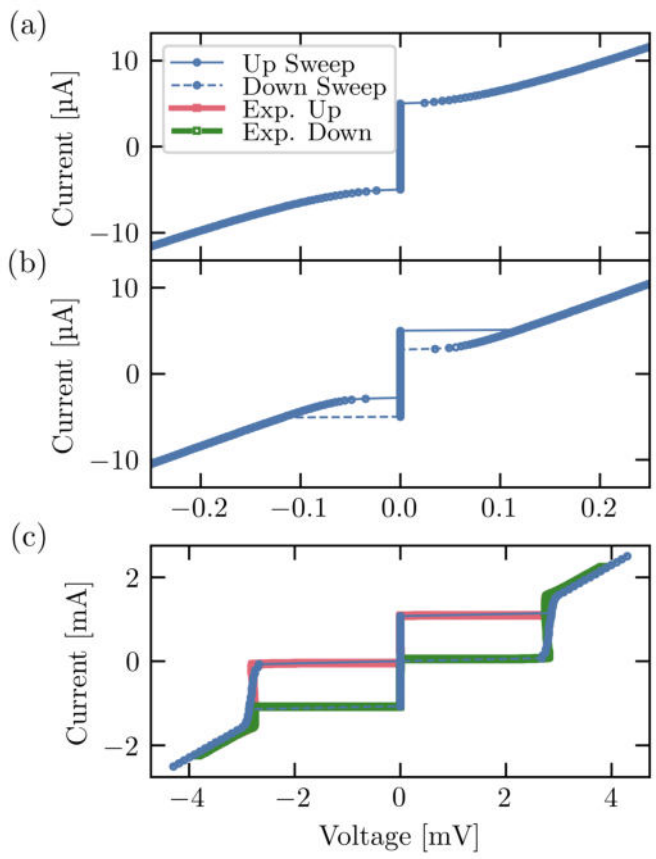

Fig. 2.8 Current-voltage characteristics of three example junctions with parameters given in Table 2.2. Each data point is an average of the voltage across the junction in a transient evolution simulation completed in WRspice. a) Non-hysteretic behaviour is seen as the junction is fully shunted by a resistor, while in b) significant hysteresis is seen as the capacitance of the junction increases with the solid line indicating up sweep of the bias current and the dashed indicating down sweep of bias current. c) Shows the simulation results in blue for the extracted junction parameters and experimental results (extracted from [131] using DataThief) in red. The negative differential resistance apparent in experimental results is suggested to be a thermal effect which is difficult to reproduce in WRspice, showing its limitations.

from which these parameters were extracted in [131]. This experimental data is shown in red of 2.8 c) and has been extracted from the figures of [131] using DataThief.

It is in this comparison that the major shortcoming of WRspice becomes apparent. The negative gradient evident in the experimental data as the junction enters into its normal state was thought to be a thermal effect in which the junction resistance changed as it was heated by the current through it. As WRspice is not a multi-physics simulator it becomes rather difficult to model the effects of such temperature dependent parameters, however, methods to do so do exist [51]. Such work has been completed for nano-wires and constrictions in the past [51, 132], although outside of specific circumstances this could be considered the reasonable limit of WRspice applications in circuit analysis, after which more complex multi-physics simulators like COMSOL may be more appropriate.

The quasi-particle model used in this set of simulations (`rtype = 1`) is comparatively computationally intense and does not scale well to the large arrays of junctions that we intend to investigate. As such, now that we have demonstrated the viability of this simulation platform, we make the reasonable assumption that we do not drive the junctions above the critical current and so disregard the quasi-particle branch (`rtype = 0`) from this point forward.

2.4.2 Josephson Transmission Line

We now extend our WRspice simulations to the rf-SQUID based transmission lines shown in Figure 2.3. The code for a 'single cell' transmission line structure is demonstrated in the appropriate format below and can be extended to a maximum length of ∼1200 cells. An empty voltage source (`Vcur`) placed between each cell of the array allows for the recording of current in time at these points. These circuits are then simulated and a 10 ns window at the end of the simulation (when transients from ramping currents have damped sufficiently) with a 1 ps step are selected for analysis. A Fast Fourier Transform (FFT) in the time domain is then performed to produce frequency-current amplitude spectra at the meeting points of each cell in the array. The sampling rate of 1 ps corresponds to a Nyquist frequency of 500 GHz which is the maximum resolvable frequency in this simulation. The frequency resolution of the FFT is then double the ratio of the Nyquist frequency to the number of samples in the window (∼10,000), giving a resolution of 100 MHz for these simulations which aligns with the centres of FFT spectrum peaks for all waves of interest.

These simulations, including the necessary data read/write operations and analysis, take a total of around 15 - 20 minutes, many times longer than the previously discussed CME simulations (max. ∼1 minute). Although this increased compute difficulty leads to the consideration of many transient effects that may occur in these devices including dynamic impedance mismatches, reflections from discrete nonlinearities and the behaviour at higher frequencies where the continuum approximation is no longer valid. Such effects are difficult to reproduce in CME simulations making time evolution simulations key to properly predicting device behaviour.

```
1  *** JTWPA 1 Cell Array
2  *** Junction model
3  .model jj0 jj(rtype=0, icrit=5uA)
4  *** Input current soruce
5  Ip 0 1 sin(0 2.4uA 10GHz 9ns 0 0)
6  *Empty Voltage Source as Ammeter
7  Vcur0 1 2 ac 0
8
9  *** termination resistor
10 Rfront 2 0 23.8747Ohm
11
12 *** SQUID embedded, flux biased
13 *** transmission line
14 Vcur1 2 3 ac 0
15 *Flux Biasing
16 Idc1 0 1252 pwl(0ns 0uA 5ns 14.068uA)
17 Lflux1 1252 0 57.0pH
18 K1 Lg1 Lflux1 1
19 *rfSQUID
20 Cg1 3 0 50fF
21 Lg1 3 4 57pH
22 B1 3 4 2502 jj0
23 Cgg1 4 0 50fF
24
25 *** termination resistor
26 Rend 2402 0 23.8747Ohm
27
28 *** Define measurement time
29 *** & use initial cond. (uic)
30 .tran 1p 25n 0n uic
31 .control
32 set steptype = hitusertp
33 set noaskquit
34 run
35 quit
36 .endc
```

Link to ToC

We begin with the 23 Ω impedance transmission line, flux biased into the 3WM regime and excited by a single 1.2 µA amplitude, 10 GHz frequency input wave. Due to the previously described wave mixing effects in the presence of the Josephson nonlinear inductance, harmonics of this input wave are formed.

Shown in Figure 2.9 is the input and output FFT's from this simulation while the heatmap shows the evolution of the input wave amplitude and the amplitude of the harmonics. As can be seen harmonics up to the 5^{th} are generated, although they have some pattern in the spatial amplitude which is related to the phase mismatch between the input wave and the given harmonic. This means that while a high up-conversion efficiency is possible in Josephson transmission lines reaching 100 % up-conversion efficiency

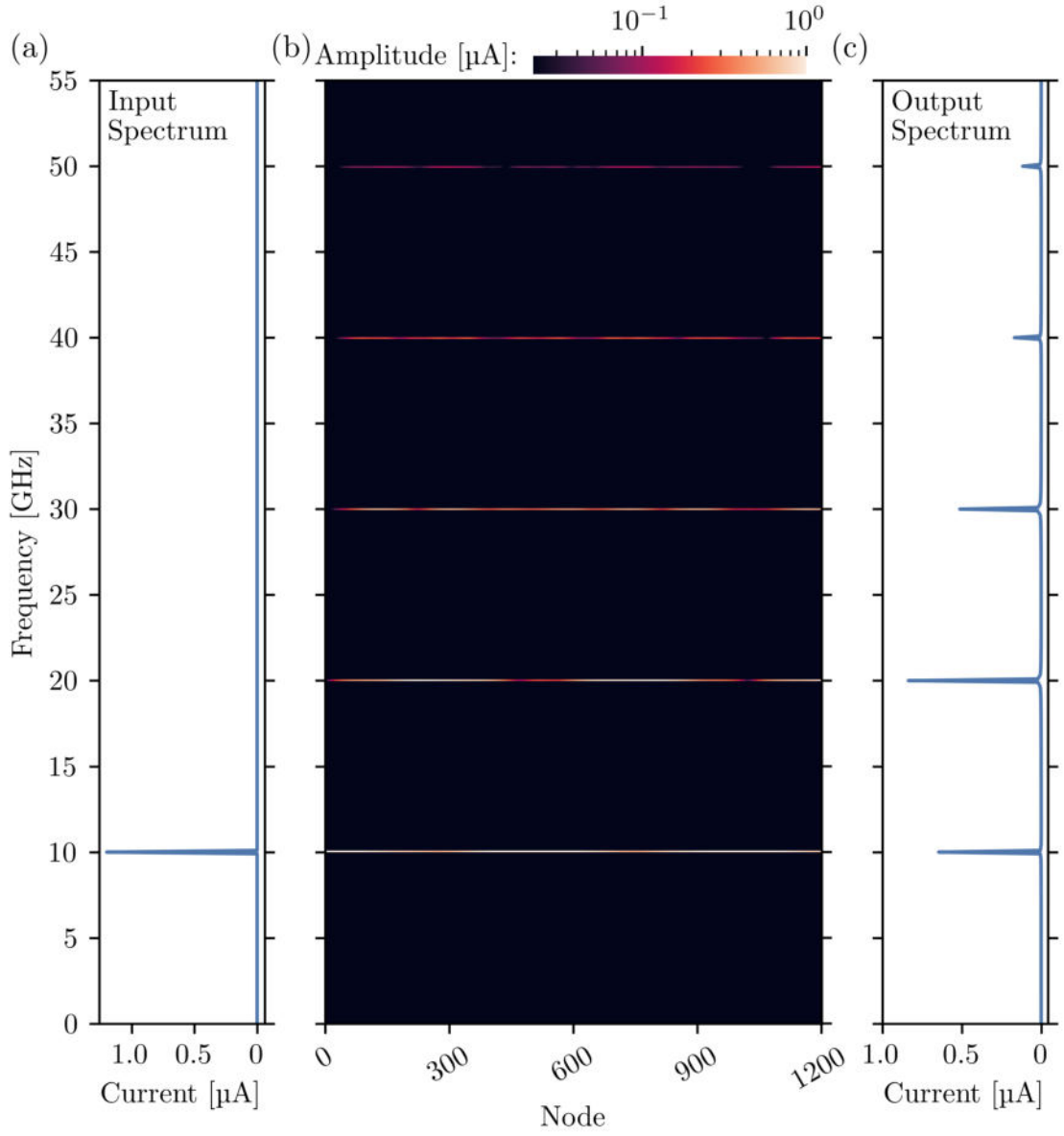

Fig. 2.9 FFT's of the time domain data at the input of the flux biased rf-SQUID transmission line in a) and its output node in c) with b) being a heatmap showing how the amplitudes of the harmonics generated in 3WM process from the 1.2 µA, 10 GHz input wave evolve in space.

Link to ToC

would be difficult without some resonant condition due to the chromatic dispersion in the transmission line.

The same transmission line biased into the 4WM regime now has an impedance of 17.5 Ω as the Josephson inductance and geometric inductance of the loop are of a similar size. This means that alongside the weaker 4WM non-linearity the input wave splits between the arms of the loop proportionally to these inductances making the up-conversion process considerably less efficient. As such the input wave has had its amplitude increased to 4 µA in order to make the odd harmonic generation effect more apparent in the simulation results of Figure 2.10.

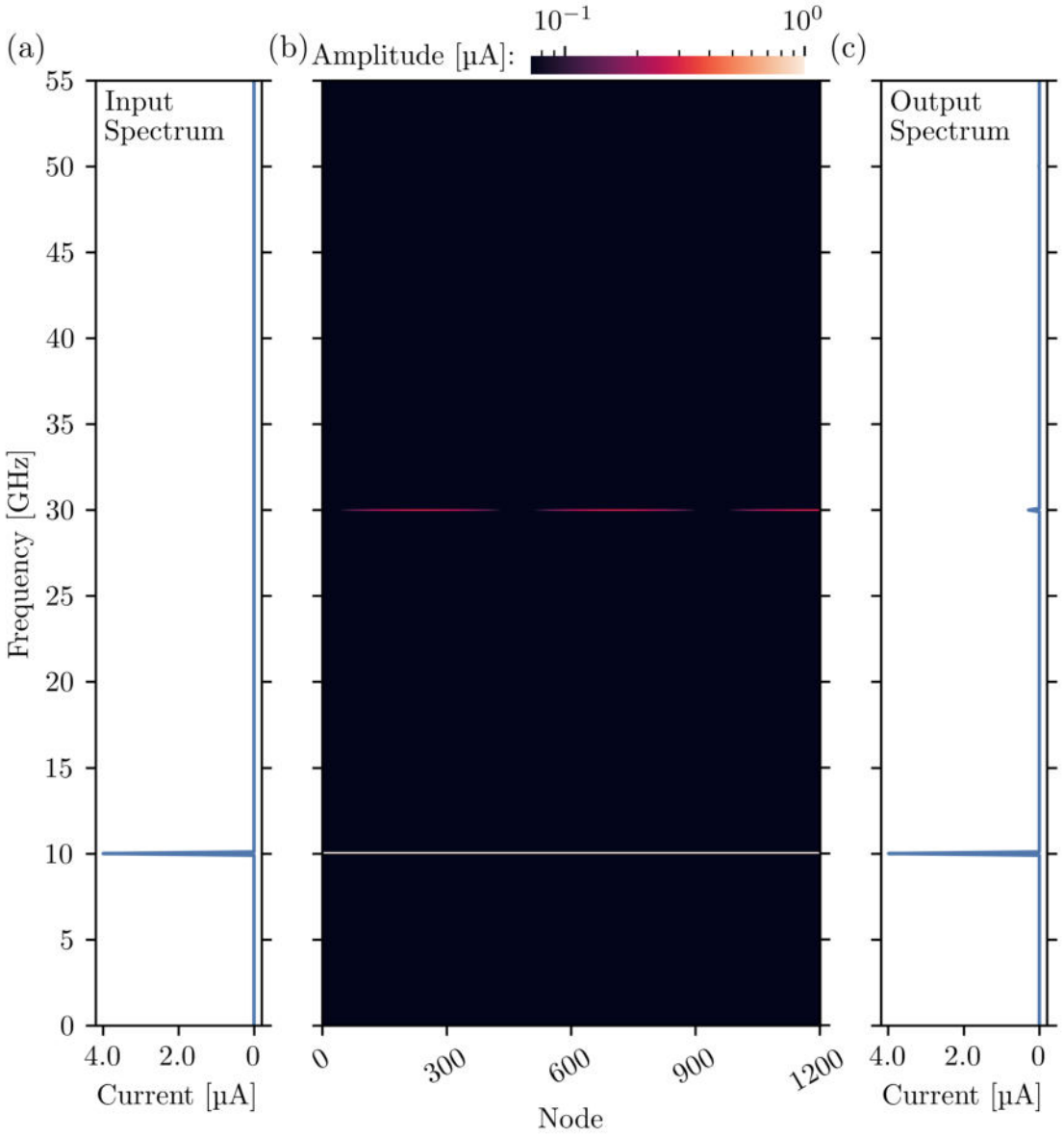

Fig. 2.10 FFT's of the time domain data at the input of the unbiased rf-SQUID transmission line in a) and its output node in c) with b) being a heatmap showing how the amplitudes of the harmonics generated in a 4WM process from an increased 4 µA, 10 GHz input wave evolve in space.

Link to ToC

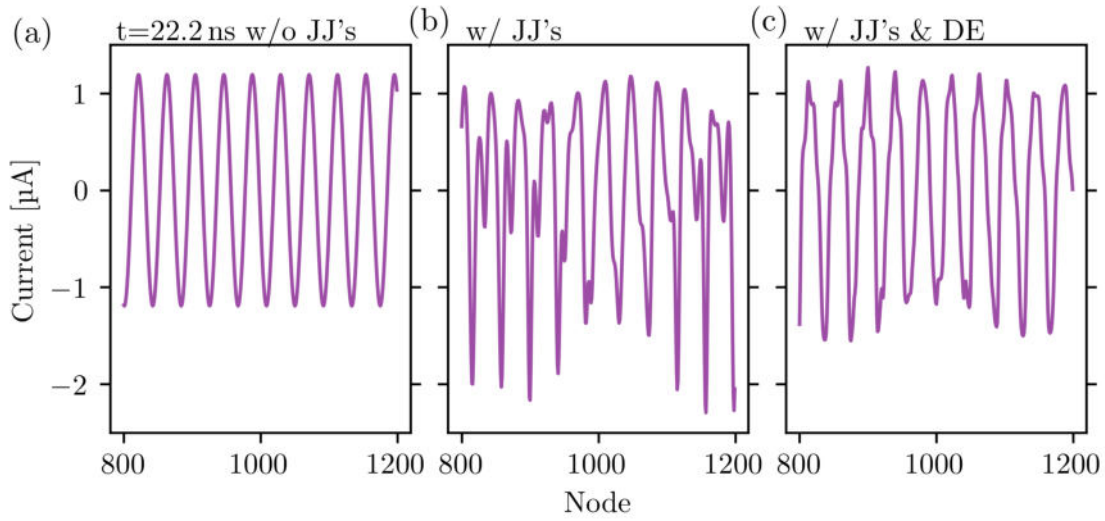

Fig. 2.11 a) Wave form in space for a 10 GHz, 1.2 μA input tone measured between the 800^{th} to the 1200^{th} cell of the linear array (without the Josephson junctions included) b) A similar waveform from an array that includes Josephson junctions and is biased into the 3WM regime, therefore generating harmonics of the input wave and leading to shockwave formations as described by Landauer, while c) shows a similar array with modulated return line capacitances as a form of dispersion engineering to minimize such effects.

The harmonic generation present in both wave mixing regimes will lead to the formation of the shockwaves in the array as predicted by Landauer [96]. They will not, however, fully form as the chromatic dispersion of the line prevents this. Shown in Figure 2.11 is a comparison between a linear transmission line (i.e. no Josephson junctions or wave mixing present), the 3WM rf-SQUID based transmission line and a similar transmission in which the phase mismatch between the input wave and its harmonics is purposefully made greater via 'dispersion engineering'. The distortion of the waveform seen in (b) in which current spikes $>$ 2μA are formed by interference of the input wave with its generated harmonics. This effect may of course be detrimental to performance should the spikes exceed or approach the critical current of the junctions. The sinusoidal modulation of the return capacitance along the length of the array in (c) has made it such that the 2^{nd} and higher order harmonics are prevented from forming in the array due to significant phase mismatch. This dispersion engineering greatly helps to retain the proper waveform shape and can also be applied to improve small signal amplification as will be discussed later in this thesis.

Finally, we investigate the envelope of instantaneous phase gradients on each junction in the array to see if a large input wave would alter the phase bias position significantly enough to impact the strength of the wave mixing regime. Shown in Figure 2.12 we see an envelope which is not negligible compared to the ideal phase bias position for 3WM of $\pi/2$. However, given our previous and coming comparisons with 3WM CME simulation this does not greatly affect the wave mixing regime, in principle agreeing with the conclusion of [133].

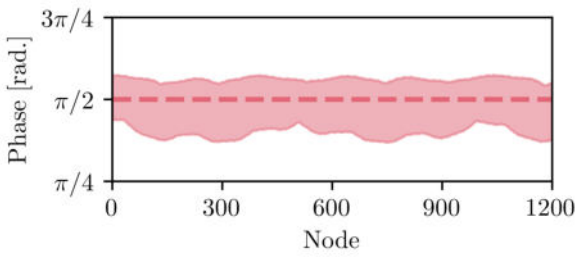

Fig. 2.12 Envelope showing the recorded phase gradients for each junction in the array over the 10 ns measurement window, where the ideal phase position for 3WM is shown as a dotted line.

2.5 Comparison of Simulation Methods

Just as you do not use a hammer to tighten a screw, you must know when best to use each of these simulation tools as well. While the coupled mode equation approach has been shown to be quite powerful it is also clear that it will consider in its calculations only as much as you are willing to code. Whereas, a lumped element simulator such as WRspice will simulate the circuit that it is given, providing detailed results on the internal dynamics of the circuit as a result. However, this is only as good as your circuit design, understanding of the program and the computing power available to you. With this in mind we look now at a more detailed comparison of the CME results to those taken from WRspice in order to understand where best these tools can be applied. For this comparison we have set the input amplitudes and frequencies as constant ($I_p = 1.2\,\mu\text{A}$, $I_s = 5\,\text{nA}$, $f_p = 12\,\text{GHz}$, $f_s = 7.2\,\text{GHz}$) and changed the flux biasing condition from the purely 4WM regime to the purely 3WM regime.

We begin by comparing the already discussed rf-SQUID based transmission line of length 1200 cells simulated in WRspice and CME's in the purely 4WM regime ($\varphi_{dc} = 0$) and in the purely 3WM regime ($\varphi_{dc} = \pi/2$). For this we must consider the effective pump amplitude which comes as a result of waves splitting at the arms of the rf-SQUID loop and leads to the use of the pump wave amplitude as a fitting parameter in the CME simulations. As a rough guide for the effective pump would be the product of the applied pump with 'participation ratio' P_R, the ratio of the Josephson to the total inductance.

$$P_R = \frac{L_J}{L_G + L_J} \tag{2.37}$$

While this works well, an analytical solution may show that a nonlinear relation exists for this fitting due to the self-induced screening current of a pump wave, along similar lines to Equation 2.1.

The comparison of the CME to WRspice results in the purely 3WM or 4WM regimes can be found in Figure 2.13 where the CME results are the solid line superimposed on the lighter coloured WRspice results. Very good agreement is seen in the shapes of the 'amplitude profiles' which indicates that the CME simulations take into account all of the major wave mixing effects in these two regimes and any higher order effects not considered may only be a small correction. It is worth noting that the presence of a ripple in the

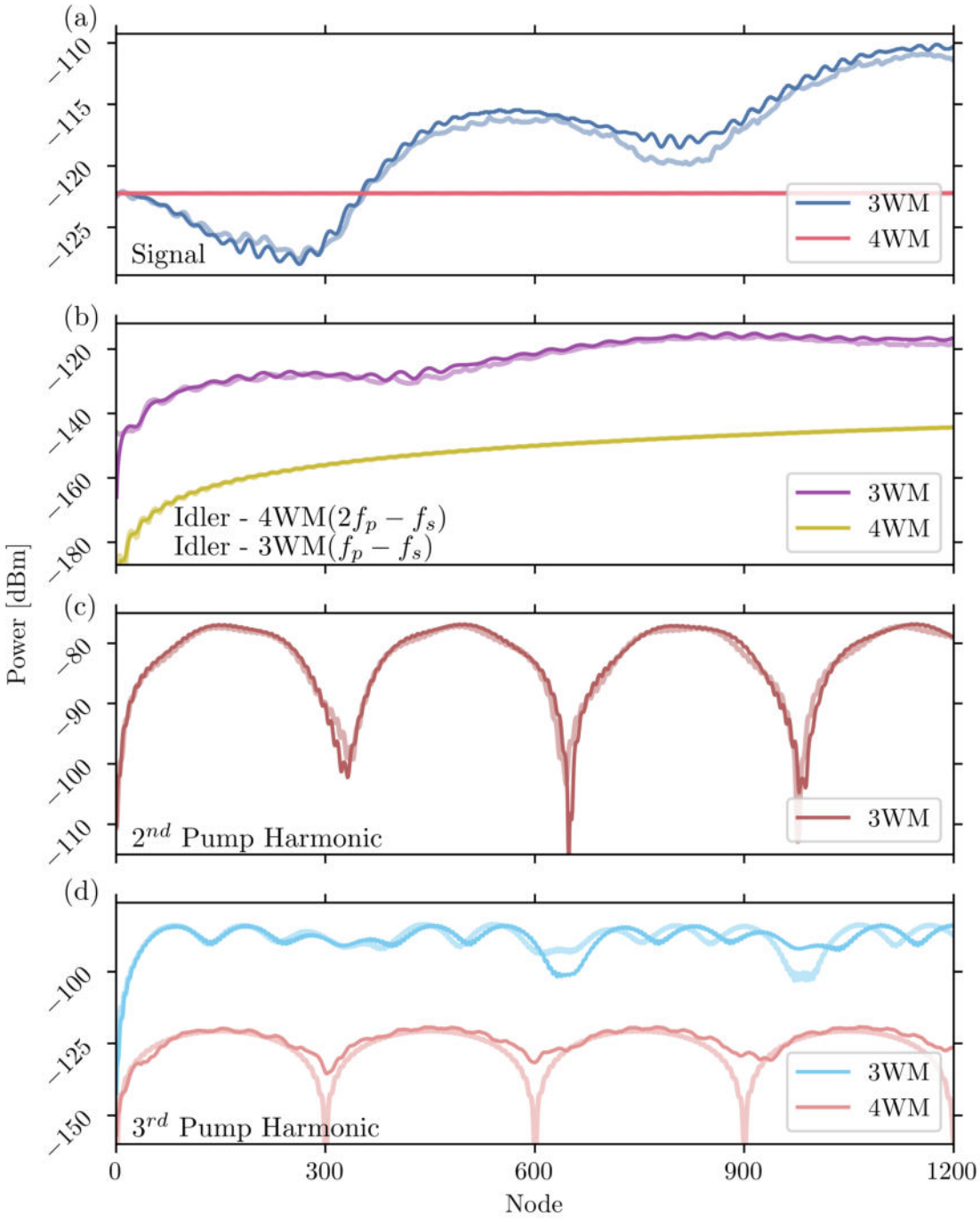

Fig. 2.13 Figure showing the agreement of CME simulation outputs for the signal and other wavemixing products in solid lines overlaid upon their WRspice couterparts in translucent. a) The signal amplification in the array is much more signifcant in the 3WM regime, nevertheless good agreement is seen between the CME results and WRspice output which is similar for the b) 3WM and 4WM idler tones c) the second harmonic generation (present only in 3WM). d) Third harmonic generation has some periodicity mismatch, perhaps showing that the derived phase relation does not match the actual circuit at frequencies closer to the cut-off frequency for the array.

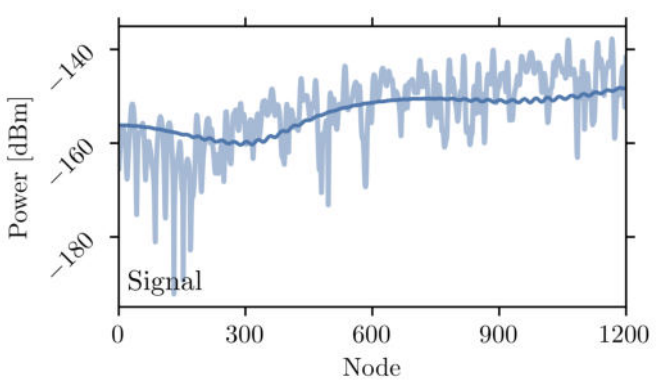

Fig. 2.14 A comparison of the CME (solid line) and WRspice (faded line) results for signal amplification in the JTWPA in the 3WM regime with an input signal power at -156 dBm. The effects of reflections in the WRspice simulations become much more apparent at these very low powers.

amplitudes of all tones indicates reflections are present for all frequencies in the device, most likely from the device ends as perfect termination is impossible.

In both these wave mixing regimes the coupled mode equation simulations are consistently more optimistic than the WRspice equivalents. The possible reasons are simply too numerous to list, although my expectation is that it would be due to a bad estimation of the wavevectors or the effective pump wave amplitude in the CME simulations.

This comparison can be extended to the case of an extremely low power input signal wave power to test if amplification may be improved by the relative strength of the pump wave. The result shown in Figure 2.14 for a signal input power of -156 dBm shows that the total gain does not significantly change which is due to the decreased rate of generation of an idler wave that depends on the signal power. In fact, we can say that, outside of the case of pump depletion, input signal power will have little effect on total gain in this circuit.

Now the situation of multiwave mixing is investigated, where both 3WM and 4WM process can take place, for example, at the bias condition $\varphi_{dc} = \pi/4$. The pump in this case can be used as a fitting parameter with the ratios of the Josephson inductance to the geometric inductance used as a guide for the 'participation ratio' of the pump wave in this mixing process. As can be seen in Figures 2.15 (a-e), very good agreement for the wave mixing process between the pump and signal waves can be achieved, as well as for the generated idler waves. However, the agreement of the CME simulation and WRspice is less optimal for the higher harmonic generation, where the shape is correct but the CME results predict significantly lower amplitudes. This, as well as the slight disagreement in shape of the third harmonic results between WRspice and the CME's, may indicate that the wave-vector calculation is incorrect for frequencies closer to the cut-off frequency of the array. This could be due to the fact that we approximate our wave-vector solution for an infinite array, whereas this 1200 cell long array must be terminated which has an unavoidable effect on the wave propagation characteristics. Possible also is that a pump wave self-induces some flux in the rf-SQUID via Equation 2.1 leading to some dynamical feedback effect that favours harmonic generation over other wave-mixing processes. Equally, some other dynamic effect that would be hard to capture with CME solutions could be at fault.

Link to ToC

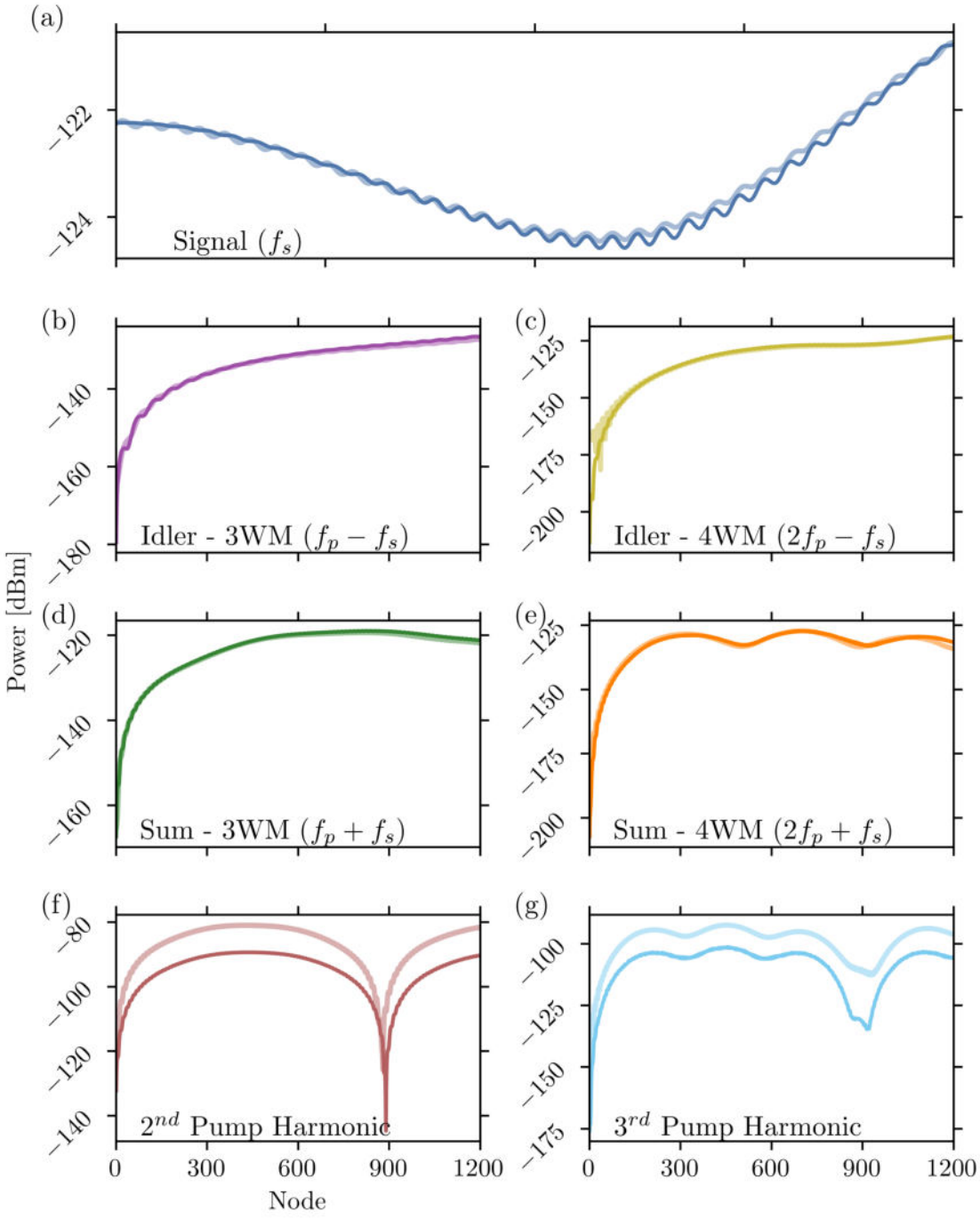

Fig. 2.15 Good agreement is seen for many of the lower power tones a) signal, b) 3WM idler, c) 4WM idler, d) 3WM sum-frequency generation and e) 4WM sum-frequency generation in this case with a phase bias of $\varphi_{dc} = \pi/4$. Although, the pump harmonic generation is significantly underestimated.

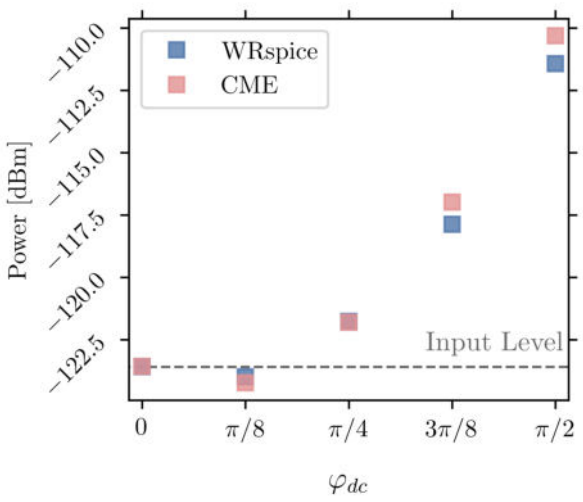

Fig. 2.16 A comparison of the final node signal gains calculated using the CME method (red) and WRspice method (blue) under different flux biases in a 1200 cell long array of the rf-SQUID transmission line already described. For the same input conditions the CME simulation results consistently produce a 'larger' wave-mixing effect which may show as a larger gain for phase biases $3\pi/8$ or $\pi/2$ or larger parametric attenuation in the case of phase bias of $\pi/8$.

Additional flux bias points have been considered to further compare the methods, with the final signal wave power at the 1200^{th} node shown in Figure 2.16. Clearly, the largest gain occurs at the optimal 3WM bias point ($\varphi_{dc} = \pi/2$) which is no surprise to us, however, this coincides with the largest disagreement between the CME results and WRspice results. In fact, the CME results consistently show a larger wave-mixing effect so that if amplification occurs ($\pi/4 \leq \varphi_{dc} \leq \pi/2$) then the CME result shows a larger gain, or if 'parametrically attenuated' ($\varphi_{dc} = \pi/8$) the CME results shows an even greater attenuation. The reason for this is, perhaps, rather simple in that the estimation of the Josephson nonlinearity is incorrect. For example, the 3WM bias point would correspond to an infinite Josephson inductance which is not correct. Both experimentally and in WRspice, an infinite inductance cannot exist, as such there will necessarily be some disagreement between these methods.

2.6 Conclusion

The primary goal of this chapter has been to introduce and develop the simulation techniques used throughout the rest of this thesis. This began with a derivation of the wave propagation characteristics of, and the nonlinearities that arise within, the rf-SQUID based transmission lines under study. By making a Taylor expansion of the current phase relation of the rf-SQUID we have shown how both three and four wave mixing (3WM, 4WM) come about in the device, as well as the benefits of pursuing the three wave mixing regime, specifically the approximately three times larger nonlinearity.

A numerical simulator of lumped element superconducting circuits called WRspice was then introduced. To test its capabilities the current-voltage relations of a series of Josephson junctions were simulated, including the reproduction of results from an experimental dataset of a 1.2 mA critical current, heavily hysteretic niobium tri-layer junction. This simulation also shows the limitation of WRspice in that thermal effects are not easily reproduced,

although as the JTWPA devices are intended for use at milli-kelvin temperatures this does not hinder us.

We then move on to simulations of the JTWPA device proposed by Zorin which has a characteristic impedance of 23 Ω. This is simulated using either the WRspice tool already introduced or the more computationally efficient method of finding numerical solutions to a set of coupled mode equations (CMEs) that describe the transfer of power between waves propagating in the device. CME simulations and lumped-element WRspice simulations have been shown in this chapter to both give accurate representations of the wavemixing dynamics in metamaterials, with results agreeing within 2 dB of each other. However, these methods are best applied in different situations, for example when a good understanding of the prospective device is already developed, the CME simulations can be a quick and reliable way to predict the wavemixing characteristics. Although, to properly understand the dynamics of a device and make apparent effects that had not previously been considered in CME models, the transient evolution simulation of WRspice is key. We then analysed harmonic generation in simulations of the proposed device operating in the purely 3WM and purely 4WM regimes. The results show a much increased efficiency of harmonic generation in the 3WM regime with output third harmonic amplitude at 80% of the fundamental while it is only 7% in the 4WM regime. This is primarily driven by the much increased strength of nonlinearity in the 3WM regime, further motivating our pursuit of 3WM amplification in these devices.

Efficient harmonic generation as well as some other 'parasitic' wave-mixing effects are also one of the greatest hindrances to the proper operation of these devices as amplifiers, limiting the amplification to ~ 12 dB gain in the 3WM regime and only ~ 2 dB in the 4WM regime. This limited amplification has been shown to be the case even at very low input signals powers due to the decreased generation rate of the idler wave which is key to the amplification of the weak signal. We have also shown that the generation of harmonics produces current spikes - or shockwaves - which can exceed the applied wave amplitude by almost a factor of two. These shockwaves have been hypothesised to lead to dissipation and other undesirable effects that would further hamper amplification processes.

To recap, we have shown that our simulation methods can reliably model the wave mixing effects in the metamaterials under study and we have identified some key hindrances to their good operation as amplifiers, including harmonic generation and phase mismatch of the mixing waves. So far, I have compared two simulation methods directly and with limited comparison to experimental data, i.e. comparing apples with apples. However, experimental data to date has often been more like an orange, so few comparisons to simulation have been forthcoming in the published literature. In the next chapter I analyse and attempt to quantify the uncertainty on the simulation methods when considering fabricated devices so that direct experimental comparisons can be made.

Chapter 3

Simulations of a Josephson Travelling Wave Parametric Amplifier

3.1 Introduction

Simulations form the bedrock of this thesis and they have proven key for the understanding and improvement of travelling wave parametric amplifier devices. This chapter gives particular focus to a series of simulations run mainly in WRspice, performed partially on the MINERVA High Performance Cluster (HPC) at Cambridge University.

The previous chapters have shown that the original proposal by Zorin is unlikely to provide the 20 dB amplification desired. In fact, even a more reasonable 10 dB amplification has proven difficult to achieve in realised devices. This chapter more closely investigates Zorin's ~23 Ω impedance theoretical device proposal which should achieve 12 dB 3WM amplification. First, an investigation is performed to simulate the same datasets that may be collected experimentally, to allow for comparison between this theoretical device and any realised device. Following this, the parasitic effects such as losses or inter-SQUID magnetic coupling are investigated and then the effects of the unavoidable variation of circuit parameters from cell-to-cell are studied.

The input of Tom Dixon (NPL/RHUL) and Phil Meeson (RHUL) cannot be overstated in the development of these simulation techniques and for the help provided in interpreting the complex problems and dynamics of JTWPA devices. Portions of the data presented in this chapter have been published in [122] and [123]. The work presented here has contributed to the development of a set of trustworthy and reliable simulation methods that have improved the analysis of experimental results, and produced improved device designs that may deliver on the promise of broadband, quantum limited amplification.

Link to ToC

3.2 Wave Mixing Characteristics

For a detailed discussion on the dynamics of parametric amplification via wave mixing, see Chapter 2. However, it is worth restating at this point that the desired exponential gain along the length of this theoretical device is not achieved due to the generation of higher harmonics of the pump and signal and other 'parasitic' wave mixing effects.

To investigate this device in WRspice a transient evolution simulation is performed on the circuit shown in Figure 2.4, from which the current amplitude of the signal wave at each node of the artificial transmission line is extracted via a Fast Fourier Transform. The results of these simulations for this device are shown in Figure 3.1 for an applied signal wave at 7.2 GHz, 5 nA, an applied pump wave at 12 GHz, 1.2 µA and a generated 3WM idler at 4.8 GHz. Reflections due to imperfect impedance matching at the device ends add a ripple to the power profiles of the waves, which can affect the wave mixing if it is large enough [134].

The signal power profile is quite interesting as it is 'parametrically attenuated' at the start of the array as power is leeched from it to generate wave mixing products such as the idler wave. As the idler tone increases in power the signal starts to be amplified past its input power for a total gain of 12 dB at the device output. While this is not as high of a gain as desired, it would still be reasonable for a first stage amplifier in many applications. In fact, the signal power is still trending upward at the end of the device and further gain

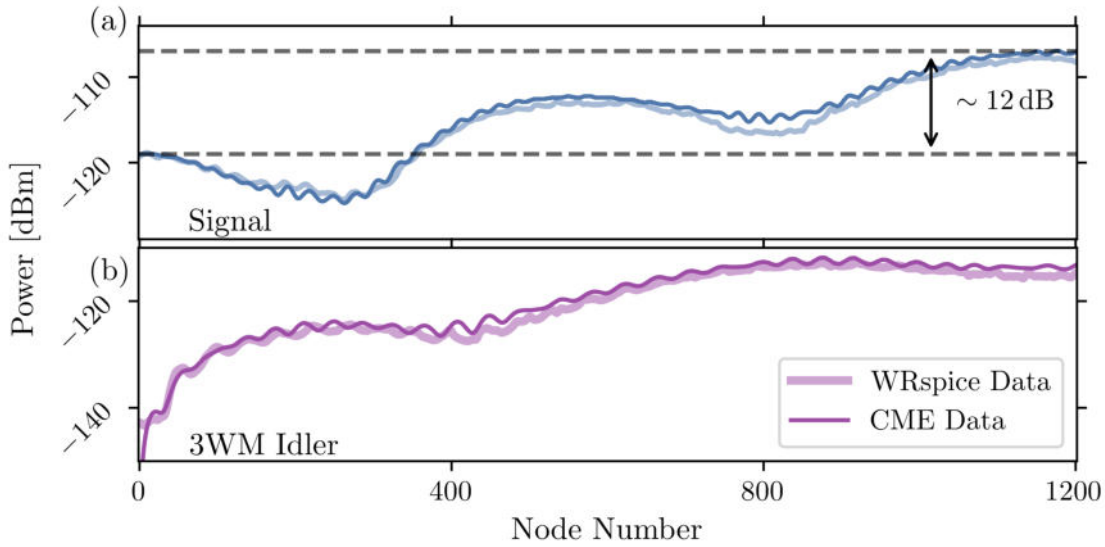

Fig. 3.1 Power of the signal (7.2 GHz) and the three-wave mixing idler (4.8 GHz) generated from a pump at 12 GHz with input power -75 dBm. along the length of the JTWPA of characteristic impedance 23 Ω. Simulation results from WRspice are shown as pale lines and CME resuts are shown as solid lines. The low amplification is due to generation of harmonics and other 'parasitic' wave mixing products while the ripple effect is due to the reflections from the device ends where impedance cannot be perfectly matched for all frequencies.

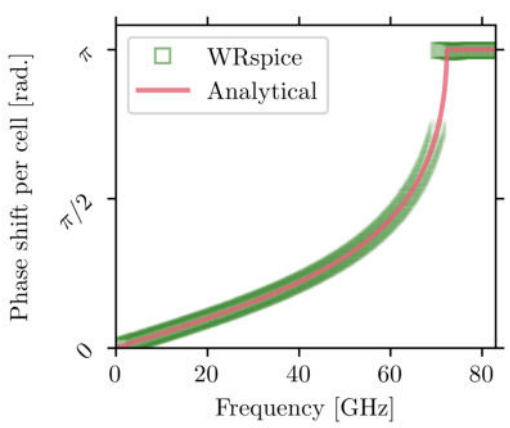

Fig. 3.2 The phase shift data calculated analytically for the JTWPA device (solid line) and the data collected from WRspice (squares). The phase shift per cell follows an approximately linear trend against frequency well below the artifical transmission line's cut-off frequency of ~ 72 GHz.

could be achieved if the amplifier length is extended, although this is not done here due to the constraints imposed by WRspice on circuit size.

The key to achieving a reasonable gain in this device despite the adverse effects of harmonic generation is the small phase mismatch between the pump at 12 GHz, and the sum of the signal and idler which are well below 10 GHz. The phase shift data can be found in WRspice by inputting a single probe frequency, performing an FFT on the time series data as normal, then performing a second FFT on the amplitude of the current for the probe signal at each node in the device. This produces a value for the phase shift of the probe signal through a single cell of the device, which can be compared to the expected value taken from Equation 2.11, as shown in Figure 3.2.

The relatively high cut-off frequency for this device in the 3WM regime of around 72 GHz allows for an almost linear relation between phase shift and frequency in the C- and X-bands that we are most interested in. While a lower cut-off frequency may prevent the generation of pump harmonics benefiting amplification, the diminished phase matching may prove to be a large detriment. As such (and a little counterintuitively), a higher cut-off frequency may be preferable to achieve the largest possible amplification without additional dispersion engineering.

3.2.1 Transmission and Gain vs Φ

In an experiment, one of the first pieces of data taken for a JTWPA device would be a transmission measurement on a vector network analyzer. Assuming transmission through the device occurs, an applied flux bias will modulate the S21 parameter in both magnitude and phase. This modulation will be a function of both the wave mixing effects and impedance mismatch between the device and the measurement environment. As discussed in the previous chapter, JTWPA's designed to operate in the 3WM regime are only impedance matched to the measurement environment at the optimal 3WM bias point. Therefore, we would expect the largest transmission at this point if only impedance mismatches are considered. On the other hand, wave mixing effects are also expected to be strongest at this bias point so parametric attenuation due to harmonic generation of the probe signal may lead to worse transmission at this point.

Link to ToC

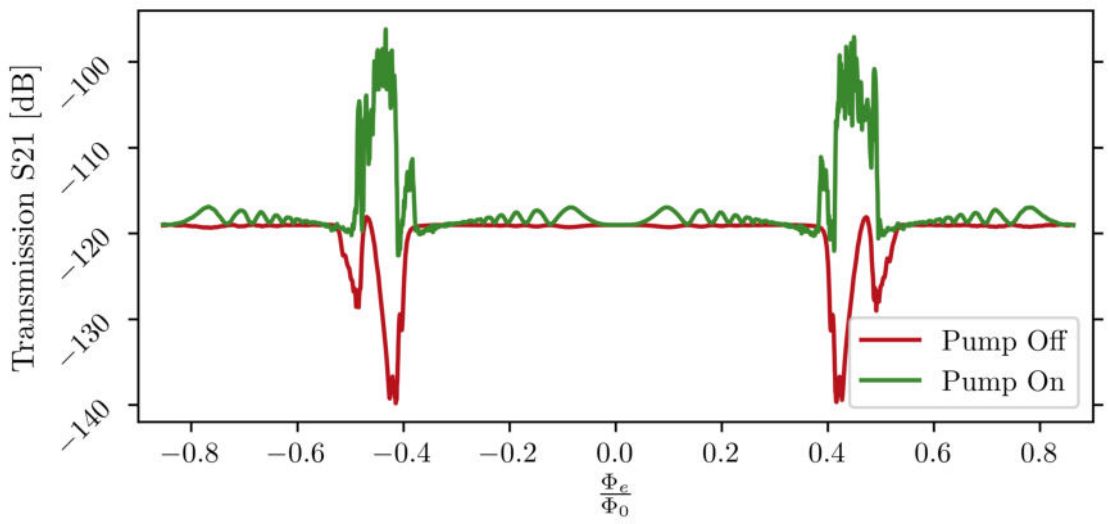

Fig. 3.3 The transmission of a signal wave through the JTWPA device with an applied pump (green) and without (red), simulated in WRspice. The large change of shape between the pump on and pump off case is a demonstration of the strong wave mixing effects that may take place in a device with low phase mismatch. The particular shape of the transmission will change depending on the power of the applied signal and pump.

In order to distinguish between these two opposing effects and determine the shape of the transmission curve for a probe signal across two flux periods we perform simulations in WRspice, extracting the signal output power in the cases of with and without an applied pump wave. The results of these simulations are shown in Figure 3.3 for an input wave of 7.2 GHz frequency.

There are two important things to note from these results. First, signal transmission with pump off is at a minimum near the optimal 3WM bias point, in part due to the strong wave mixing effects present in these devices. On the flip side transmission with pump on is at or near a maximum in this same region, ideal as the intention is to make an amplifier after all. The problem occurs if one uses a common method of characterising gain in these devices, by checking signal transmission with **Pump ON** versus **Pump OFF**, which is clearly not accurate in this case at certain bias points.

3.2.2 Wave Mixing Product Flux Dependence

Looking more at this situation in which both a signal and pump wave are injected into the device, the wave mixing products generated during the amplification process can be studied. Wave mixing products might be expected to change with applied flux bias as the output power of each tone should depend on the strengths of the wave mixing regime in which that tone is generated most efficiently. For instance, an idler tone at a frequency equal to the difference between the pump and signal frequencies will, of course, be generated to greater degree in the 3WM regime than in the 4WM regime. This is because the process to generate this 3WM idler in a 4WM process involves a larger number of intermediate mixing steps, making it less likely (efficient) in a similar logic to Feynman diagrams of particle physics.

Link to ToC

Plotted in Figure 3.4 are the powers of the tones of most interest, deemed to be the tones that appear to affect the amplification processes to the greatest degree, taken at the output of the device over two flux periods (except for the signal which is plotted over four). The solid lines show the case in which the device is terminated with a static 23 Ω impedance while the lighter lines show the case where the termination impedance is always matched to the characteristic impedance of the transmission line at that flux bias for a 5 GHz wave.

The first obvious detail is that many of the tones follow a similar trend in that they have maxima around the optimal 3WM bias point followed by a sharp minimum at the half flux bias quantum point. The greatest difference between the tones that are generally related to 3WM (b, d, f) and those that are generally related to 4WM (c, e, g) are that the latter have an absence of a sharp minium at the zero bias point which would be the purely 4WM regime. As we know that the quadratic (3WM) nonlinearity is considerably stronger than the cubic (4WM), it is straightforward to interpret these results as even second, or third order 3WM processes are more efficient than first order 4WM processes.

An interesting result in the study of these devices has come from Kern *et al.* where it was showed that impedance mismatches at the device terminals between the device and the measurement environment lead to a intermediate wave mixing state between resonant and travelling wave parametric amplification [134]. It was shown that this can lead to enhanced gain in TWPA devices, although at the cost of a significant ripple in the amplifier spectrum. While Kern considers a large impedance mismatch, it is also worth to investigate the effects on gain due to impedance modulation across a flux period, which is unavoidable in these devices. By comparing the light to the dark lines in the plots of Figure 3.4 it can be seen that affect on the power of the 3 and 4WM idler and sum tones is present, but the significant improvement in signal amplification is not. Most likely, a designer must intentionally produce a large impedance mismatch between the device and environment to achieve this enhancement, although the usefulness of it, given the added ripple in amplifier bandwidth, is questionable.

3.2.3 Harmonic Generation

Studying specifically harmonic generation now, we simulate the case where only a single wave is input into the device which allows us to investigate the dependence of harmonic generation on input wave power and flux bias. The power of the fundamental through to the fifth harmonic generated in the device were recorded at the device output in a WRspice transient simulation. The dependence on flux is considered first, using an input wave of frequency 3 GHz and an input current of 1.2 µA (or $\sim I_c/5$) as suggested in Zorin's proposal. The results of this simulation set are shown in Figure 3.5 The reason that the pump transmission has a shape different to the plot of Figure 3.3 is due to the larger input power used in this simulation which leads to depletion of the input wave due to parametric attenuation. This is an interesting effect seen in some experiments where the shape of the flux period loses important details as the input power is increased, as will be shown in later chapters.

Link to ToC

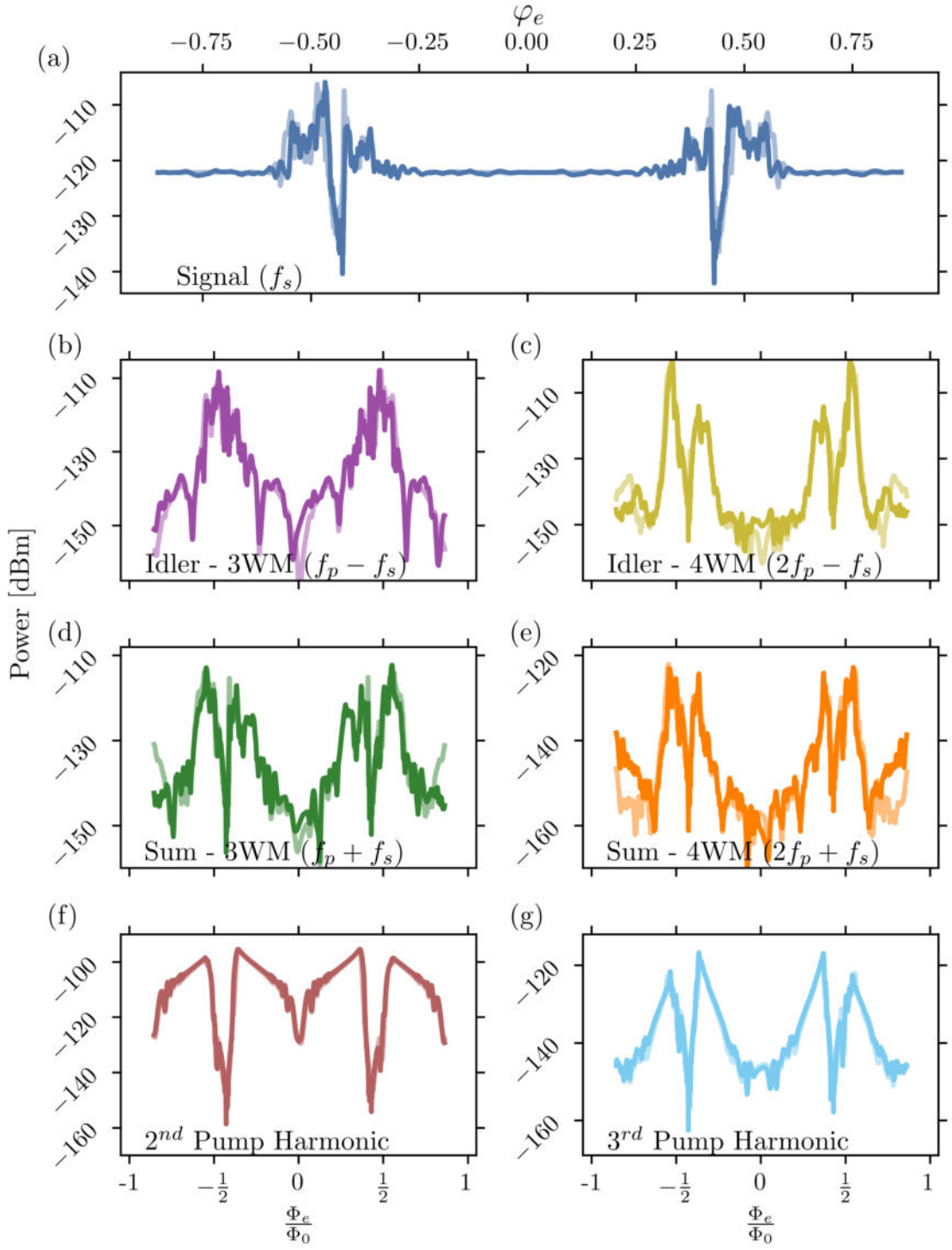

Fig. 3.4 Results of a WRspice transient simulation in which the applied flux is swept while the signal frequency, current and pump frequency, current are held constant at 7.2 GHz, 0.005 µA and 12 GHz, 1.2 µA, respectively. The power of the wave mixing tones are determined on the output of the JTWPA and are plotted across two flux periods for the signal (a), 3WM and 4WM idlers (b) and (c), 3WM and 4WM sum frequency generation (d) and (e), and the second and third harmonics of the pump wave in (f) and (g). The faded lines in each plot show the results of an impedance matched device at all flux biases, while solid lines are results from devices only matched at the impedance of optimal 3MW flux bias.

Link to ToC

The different shapes of the harmonic dependence on flux bias compared to the simulation presented in Figure 3.4 is due to the absence of the second input wave and a simpler mixing process. This should make it easier to compare the second and third harmonic power to the strength of the 3WM and 4WM nonlinearities, shown in Figure 3.5 (b) and (c), respectively. As before, both the second and third harmonics closely follow the trend of the 3WM nonlinearity strength, however, the third harmonic does not have as low of a minimum at the zero bias point due to the presence of 4WM effects.

We now look at the effect of input power on harmonic generation output power at a set of distinct flux points. The results of this are shown in Figure 3.6, where the flux points chosen correspond to optimal 4WM bias (a), optimal 3WM bias (d) and two intermediate states (b, c). First, we can say that the gradients of harmonic growth against input power change significantly with the wave mixing regime. At the zero bias, where there is no 3WM, only the third and fifth harmonics grow considerably, agreeing with the predictions of 4WM.

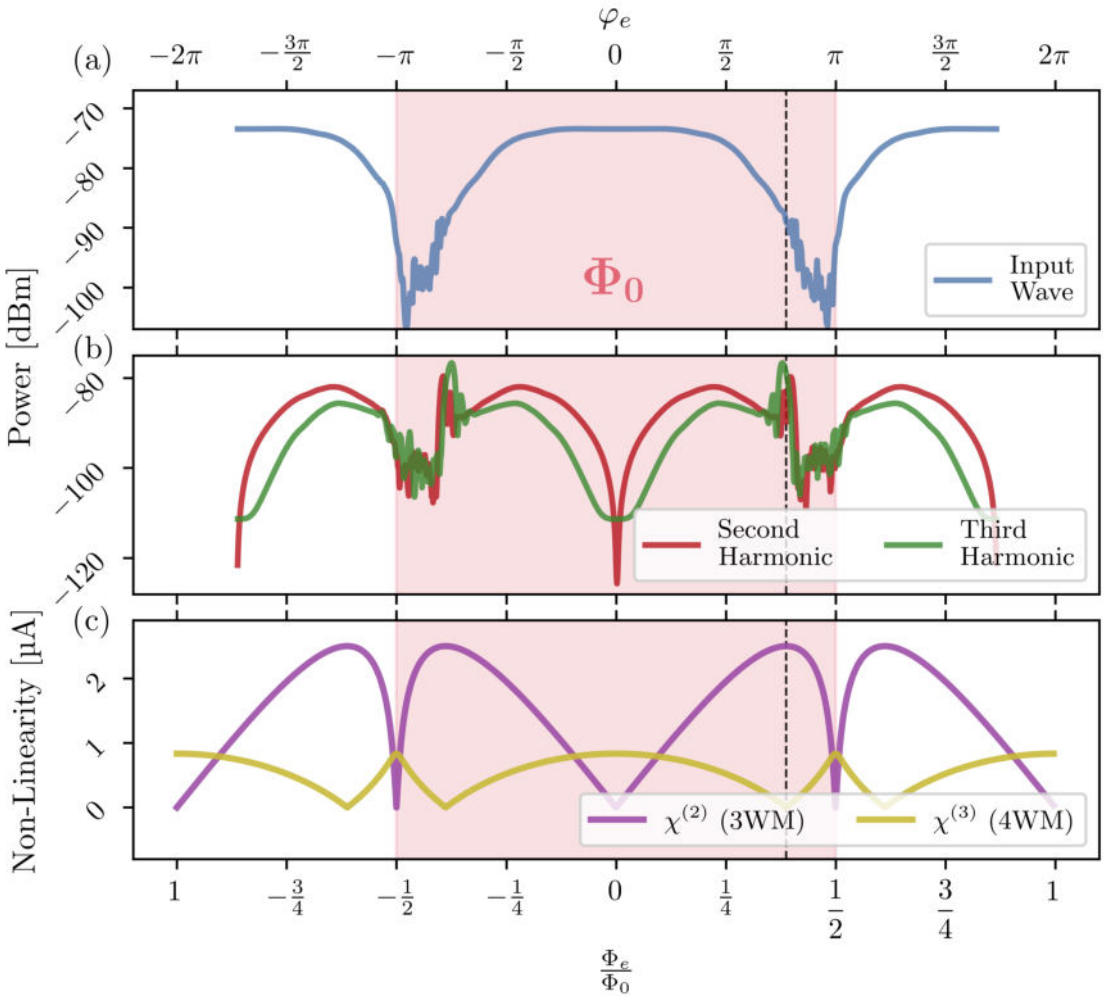

Fig. 3.5 WRspice simulation results in the case of a single input wave at 3 GHz, 1.2 µA where the flux is swept. The transmission of the input wave is shown in (a), while the behaviour of the generation of the second and third modes is shown in (b) which can be compared to the strengths of the 3WM and 4WM nonlinearities in (c). The dashed line in each plot corresponds to the calculated optimal 3WM bias position.

Link to ToC

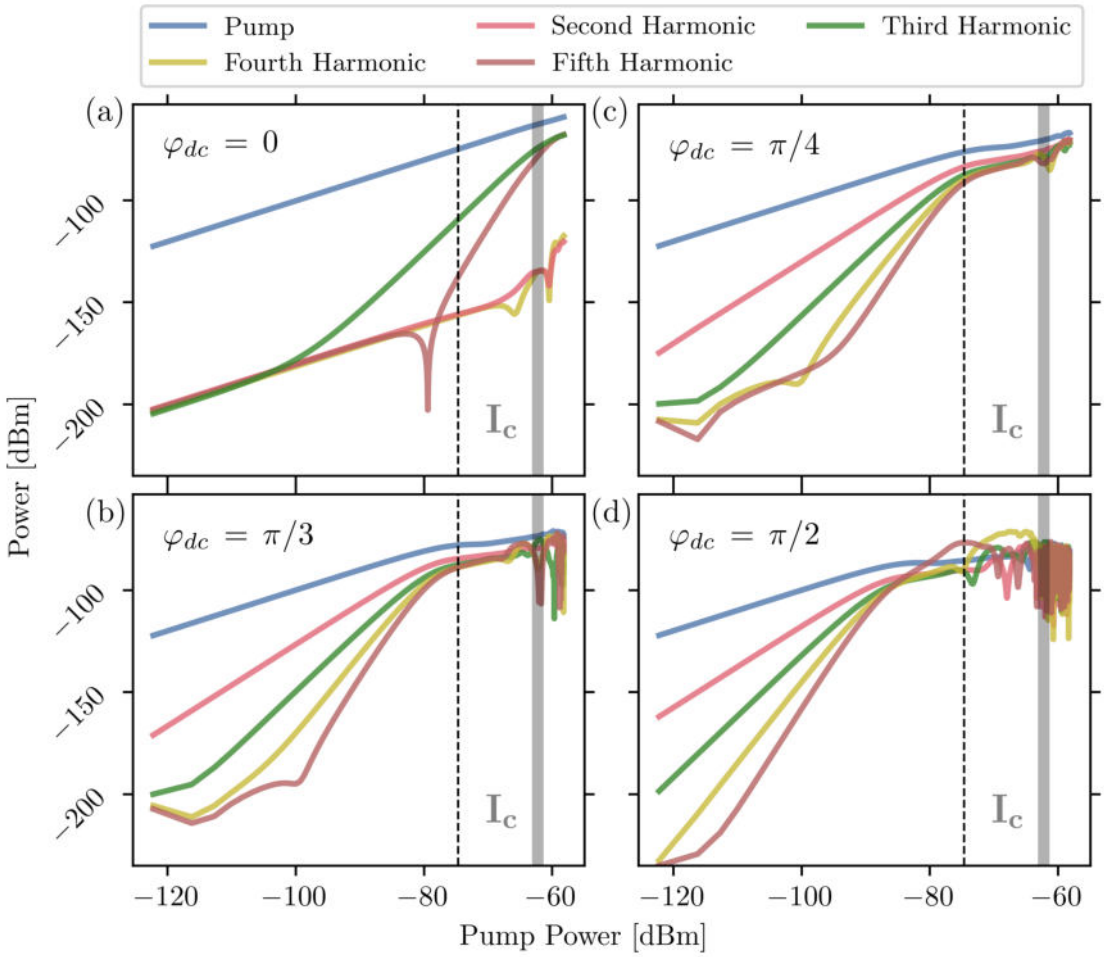

Fig. 3.6 Simualtions of the harmonic generation of a pump wave applied to the JTWPA at 3 GHz with a power that is swept from −120 dBm to −56 dBm. The gradients of the harmonic power grow with the harmonic number, with most finishing close to or at a higher power than the pump at pump powers > -80 dBm, indicating pump depletion occurring in the device. At pump currents above the critical current of the junctions, indicated by the grey vertical line, the output power remain level, although the trace becomes a lot denser. The dashed line in each plot corresponds to the input wave power used in the previous flux sweep simulations.

As the 3WM nonlinearity increases through the intermediate bias points up to the optimal 3WM bias point, we can see that all harmonics grow at a much faster rate and pump depletion occurs at lower input powers. This is not only a sign of a stronger nonlinearity but also may be used as an indicator of the wave mixing regime, where gradients of even number harmonics should be highest for low pump powers in the optimal 3WM regime.

There are several unexplained effects in this data, including the sharp dip in output power before a significant gradient increase for the fifth harmonic at $\varphi_{dc} = 0$ and a negative gradient at very low powers for the fourth and fifth harmonics in the intermediate bias points. At such low powers it is possible that these effects are artefacts of the simulation method. More important to our applications are the effects close to the critical current, where sharp dips are seen. I hypothesise that these dips are due to either the input power being on the order of the critical current and so the phase bias position ceases to be

Link to ToC

well-defined, or the pump becomes depleted and erratic behaviour ensues. If these dips can be seen in experimental data, it may enlighten us as to which hypothesis best fits this effect, they may also be of use as an indicator of the critical current value.

The depletion of the input wave at higher input powers is evidenced by a change in gradient of the fundamental tone power recorded at the output. The power at which this gradient change occurs seems to depend on the flux bias as this sets the strength of the wave mixing nonlinearity. In many publications on the theory of these devices, the small pump approximation is used, as well as the strong pump approximation. Simply stated, these approximations mean that the pump is simultaneously much smaller than the junction critical current and also large enough not to be depleted via wave mixing processes. Clearly, these approximations can be met simultaneously but only at powers 20 - 30 dB less than the power corresponding to the critical current, although most suggested operating parameters offer a value of only ~6 dB smaller. This is not an indictment of the validity of the suggested operating parameters, as experimental devices have been shown to work well in this range, but instead a comment on the validity of the approximations used to model the devices.

3.3 Parasitic Impedances in JTWPA Devices

Traditional circuit design, and the approach taken so far in this thesis, is only practical if parasitic impedances are either engineered to be negligibly small or included as additional components. A parasitic impedance refers to some non-ideality in a physical device, which is present in every microwave circuit as all lumped element components have some parasitic component. For example, a length of wire acting as an inductance also has a parasitic resistance due to surface losses and a parasitic capacitance between its ends and to ground. Another example would be that of sharp bends in microstriplines which have been modelled well for decades by the addition of a lumped capacitance in the equivalent circuit models.

Often these parasitic impedances are initially thought to be negligible, but can in fact be quite detrimental to the design. Including these effects requires a more involved simulation method, and much thought on what may couple to or otherwise effect the device. The difficulty of this task for lumped element modelling is perhaps best demonstrated by its absence in modern superconducting circuit literature, with most groups instead opting for a full wave EM field simulation in its stead. Nonetheless, it is a worthwhile task that can guide us on improved designs in a systematic way. In this section we simulate the effects of some likely parasitic impedances on JTWPA performance and comment on the importance of considering these.

3.3.1 Inter-SQUID Inductive Coupling

In these one dimensional Josephson transmission lines it should be possible for a parasitic inductance effect to exist due to the magnetic coupling of neighbouring geometric inductances. This type of coupling will affect the operation of the device in several ways, especially if neighbouring SQUID's have opposing orientations, as is shown in the micrograph of Figure 3.7 (a) with its equivalent circuit model shown in (b).

The screening of magnetic flux from the rf-SQUID cells must now be rewritten to included the extra inductive terms introduced by these couplings. Equation 2.1 should now take the form:

$$\Phi_e = \Phi_{dc} + \Phi_p + L_g I_c \sin\left(\varphi_{dc} + \varphi_p\right) + 2k\left[\Phi_{dc} + (1+\Delta)\Phi_p\right] \ , \tag{3.1}$$

where the Φ_e and Φ_{dc} terms are the external and threaded fluxes as described previously, while Φ_p is the flux due to the applied pump field and k is the coupling constant between neighbouring inductances.

The current induced in each cell by nearest neighbour inductive coupling would now be in opposition to the effects of the applied dc bias. This would essentially make the effective inductance per cell lower, and so the device would be less responsive to applied flux than expected. Additionally, the hysteresis parameter (β_L) would also be decreased leading to a weaker wave mixing nonlinearity as coupling increases.

The simulation results presented in Figure 3.7 (c), where the coupling constant between cells is varied from 0 to 0.3, match our prediction of decreased amplification as coupling increases. Clearly, at a coupling of 0.3, no amplification is seen, in fact a lower output power is seen as compared to the input. The reduced output power is most likely due to the impedance mismatch of the device to the termination impedances due to the low effective inductance per cell. The low amplification may be explained by the fact that the optimal 3WM bias point will have shifted significantly from its expected position. As well as this, the coupling ensures that a signal in one cell of the array screens the signal in neighbouring cells, directly acting in opposition to amplification.

We only consider nearest neighbour coupling as the coupling coefficient falls off with the cube of the distance between the loops. Using the approach of Lazarides *et al.* [135] we can estimate the coupling by:

$$k = \frac{\pi^2 \mu_0 \, r}{L_G} \left(\frac{r}{d}\right)^3 \tag{3.2}$$

where r is the approximate radius of the rf-SQUID loop and d is the separation of SQUID centres. Using approximate values for the device shown in Figure 3.7 (a) of 10.5 µm radius and 26 µm separation, we expect a coupling constant of ~ 0.15. Given the complex shape of the SQUID loop, this approximation may be some distance off and a full wave simulator like FastHenry or Inductex may produce a more trusted value for a designer.

With the simulation results of Figure 3.7 (c) in mind, this coupling may be very detrimental in a realised device. However, it may be also intentionally exploited in the

design of these devices. Many groups have avoided producing devices with a hysteresis parameter of unity ($\beta_L = 1$) even though this would be optimal for maximising 3WM and minimising 4WM effects. The reason is that some rf-SQUID's will unavoidably be hysteretic in a fabricated product due to variation of the circuit parameters. Engineering this negative coupling into the device may allow for the achievement of β_L much closer to unity by limiting the effect of variations in geometric inductance values. Larger geometric inductance values will couple better to neighbouring cells, leading to a lower effective inductance and vice versa. This would reduce the spread of inductance values and make the production of a hysteretic rf-SQUID element less likely for a given fabrication process.

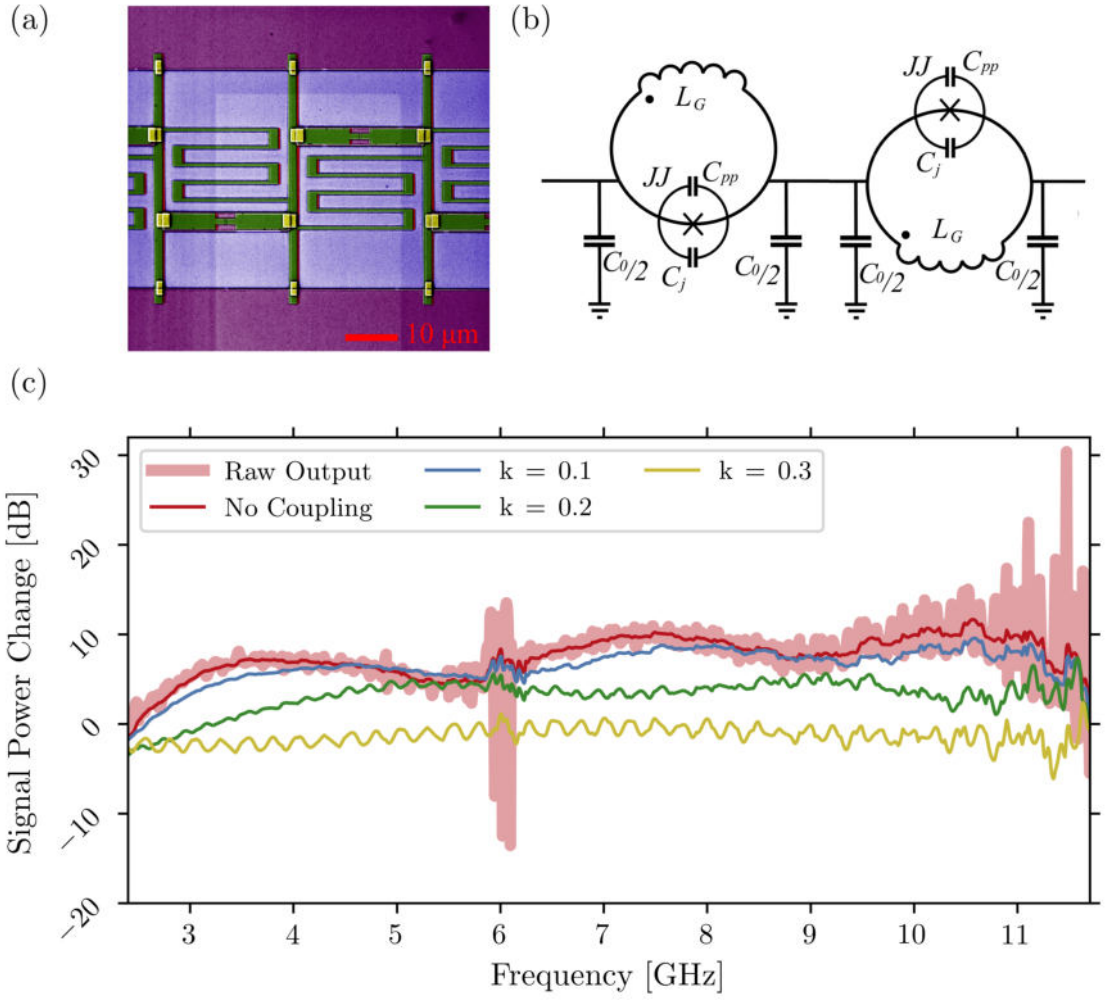

Fig. 3.7 (a) A false coloured SEM image of a JTWPA device which shows the opposite orientations of neighbouring rf-SQUID cells. (b) An equivalent circuit of this device that includes the opposite orientations of the SQUID loops and some mutual inductive coupling between nearest neighbours which is a negative coupling due to this orientation. (c) WRspice simulation results of such a circuit where the applied signal frequency is swept from 2.4 GHz to 11.7 GHz while its current is held constant at 0.05 µA and the pump frequency and current are held constant at 12 GHz and 1.2 µA, respectively. The negative mutual coupling between cells increases via the coupling constant k, where a value of $k \geq 0.3$ leads to a flat band without any amplification of the signal in the device as each cell acts in opposition to its neighbours.

Link to ToC

3.3.2 Dielectric Losses

Losses can occur from a few different mechanisms in these one-dimensional metamaterials, the most often considered are the dielectric losses, specifically those due to penetration of the electric field. The equivalent circuit for modelling these losses for a lumped element transmission line, where the electric fields are strongest at the capacitive elements, is shown in Figure 3.8 (c). The unit cell circuit includes shunt resistances across the capacitances to ground producing a frequency dependent loss per cell of the transmission line. Other loss mechanisms such as magnetic losses (confined mostly to the geometric inductance), and losses caused by quasi-particle tunneling across the Josephson element (as shown in Figure 3.8 (d)), may also be considered in a similar fashion. Although, we focus now only on dielectric losses as these are expected to dominate [136–138].

While this simulation can be completed straightforwardly in WRspice, a comparison to CME results requires an understanding of how losses alter wave propagation in the transmission line. The propagation factor for each wave in the device must now have a real part that describes attenuation due to losses, and an imaginary part which describes phase shift in the pass band. This is calculated in the same way as before for these devices:

$$\gamma = \alpha + i\beta = \left(1 + \frac{Z_1}{4Z_2}\right) , \tag{3.3}$$

where γ is the propagation constant, α the attenuation constant, β the phase shift. The impedance in the direction of propagation, Z_s, and to the return line, Z_p, as described in Chapter 2, need added loss terms. For dielectric losses this is achieved by shunting the capacitance to ground with a loss resistance, R_d. A suitable value for this resistance can then be calculated from:

$$\tan\delta = \frac{\epsilon''}{\epsilon'} = \frac{1}{\omega C_0 R_d} \tag{3.4}$$

where δ is the loss tangent of the dielectric used, ϵ' and ϵ'' are the real and imaginary parts of the dielectric constant, and C_0 is the capacitance to ground [139, 140].

This altered propagation constant then replaces the wave vector, k, in Equation 2.33. The results of this simulation performed for a series of dielectric loss resistances are shown in Figure 3.8 (a) and (b) for CME and WRspice, respectively.

For low enough shunting resistances, the device acts mostly as an attenuator, although evidence of wave mixing may still be seen in the modulation of signal power across the device length. So long as the pump power is much larger than the signal power, amplification will still occur, however, as the pump attenuates more by the end of the array this may no longer be the case. If this happens, as is the case for loss resistance less than 50 kΩ, pump depletion occurs and both the signal and pump are attenuated in similar ways. This implies that a lossy device may still provide amplification so long as the input pump is large enough or the device short enough.

The differences between the CME and WRspice results can be well explained by an additional impedance mismatch caused by the presence of the loss resistances which is not

considered in the CME simulations. This would cause a lower pump than expected in the device and so depletion occurs sooner.

Clearly, a lossy capacitance to ground due to a bad dielectric will be very damaging to the operation of this device as an amplifier, however, it is unlikely to be a big problem in reality. The complex part of the relative permittivity of SiO_2 as an example, is very small, so using Equation 3.4 we find $R_d > 3\,\mathrm{M\Omega}$.

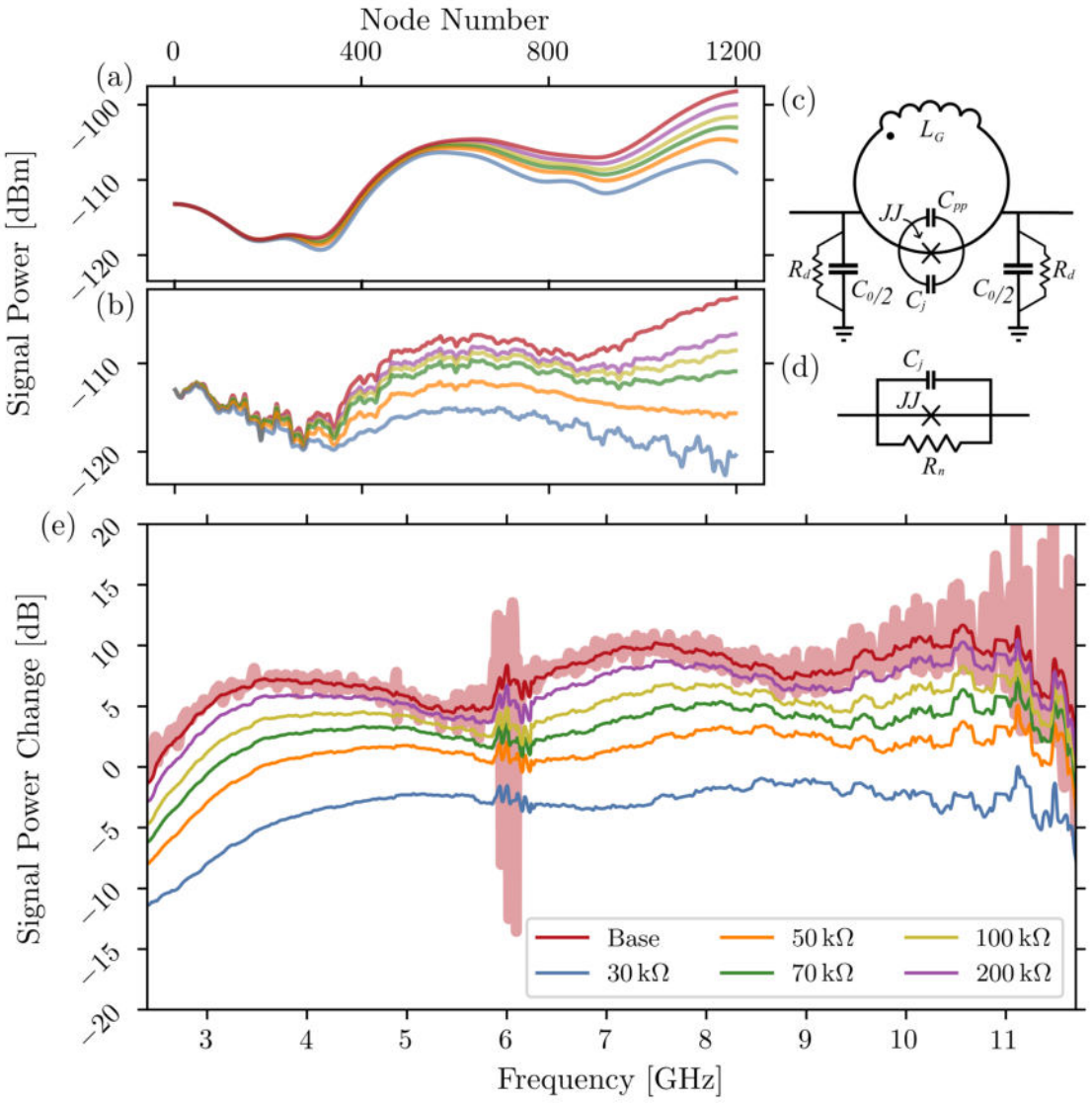

Fig. 3.8 (a) and (b) CME and WRspice simulation results showing the power of a signal at 7.2 GHz frequency and initial power of 10 nA, at each point in the 1200 cell long array as it mixes with a pump wave of frequency 12 GHz and initial current of 1.2 µA. Losses are simulated in the device by assuming some dielectric loss modelled by a shunt resistance across the capacitor to ground as shown in the circuit diagram of (c). Alternatively, losses could be modelled by a shunt resistance across the Josephson junction as shown in (d), while these circuits would have different effects in terms of the frequency response we can draw some conslusions about losses common to both in this simulation. The loss resistance (R_d) is decreased in value to investigate the effects on amplification in the array and across a frequency range of 2.4 GHz to 11.7 GHz, as shown in (e).

Link to ToC

3.4 Fabrication Tolerances

Aside from the unlikely event that Josepshon junction chips start growing on trees, these JTWPA devices will continue to be produced using advanced nanofabrication processes. The most common fabrication method for research groups is to use a series of electro-beam lithography steps interjected by metal evaporation steps to produce nano-/micrometer sized Josephson junctions and other circuit elements. While this method has been phenomenally successful for the last four decades and has produced massive advances in the fields of nanotechnology and quantum device research, it is not without fault. As opposed to the semiconductor fabrication industry, research nanofabrication has not had as large of an emphasis on yield and consistency, until recently. This does not matter if the goal is to produce a single device of individual elements, such as a single electron transistor, or a device that is mostly robust to defects and variations like resonant Josephson parametric amplifiers. However, in the scheme of an rf-SQUID based JTWPA thousands of individual circuit elements load each other to produce a transmission line with a desired nonlinearity and impedance.

It is straightforward to say that to produce a properly functioning device the variation and defects present in the array must be kept as close to zero as possible. Although, no measure of what is an acceptable tolerance was known which remained an important question as to the viability of these devices. We now investigate these questions and attempt to put bounds on the acceptable variation of circuits parameters in each unit cell that may still lead to acceptable amplifier performance.

The work presented in this section can be applied to similar schemes with the same method, and many of the conclusions can be applied directly to other more complex JTWPA devices, although only phenomenologically. These results have been published previously in [122]

3.4.1 Point Defects

We have analaysed in the course of these simulations many types of defects, for instance, shown in Figure 3.9 are the effects of a shorted capacitance to ground at different points along the array. This type of defect can be regarded easily as a large impedance mismatch from which all incident waves are reflected. Apart from the large ripple created by the interference of forward and backward travelling waves, there also seems to be some dependence of the signal power profile on the particular location of the defect. While for this two-port device this behaviour is inconsequential, for a TWPA operating in the reflectometric mode this could be a key detail in design. Of course, any type of defect of this kind would be very detrimental to the device performance and may be caused by any number of possible fabrication hiccups, which are left to the reader's imagination.

It should be mentioned that this type of rf-SQUID based JTWPA is quite robust against a particular kind of common defect. Should the Josephson junction not be formed

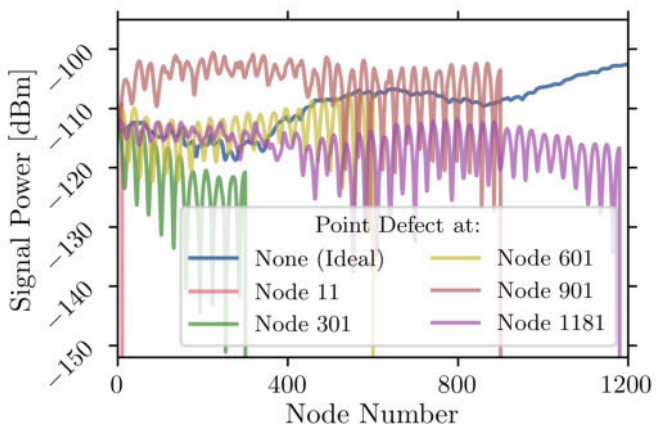

Fig. 3.9 WRspice simulations showing the effects of point defects in the form of shorted ground capacitances in the 1200 long JTWPA array. The power of a signal at 7.2 GHz at each point in the device is shown in blue for a pump wave of frequency 12 GHz and current 1.2 µA. A large impedance mismatch occurs at the defect site, fully relfecting the incident signal wave and producing a ripple with period of half the signal wavelength.

correctly such that there is no Josephson effect then the impedance of the unit cell shall not be greatly affected as an absent inductance behaves rather similarly to an infinite inductance. However, should the junction be shorted, as is another common defect, then the problem of a large impedance mismatch will occur.

3.4.2 One-Parameter Variation

The variation of circuit parameters in each cell of the artificial transmission line is an unavoidable reality. There is guaranteed to be some degree of variation in each of the circuit parameters. This begs the question, what is an acceptable level of variation in each parameter that can still lead to a functioning device? This is a question that cannot have a definitive answer as it depends on the particular device design and circuit characteristics. However, for the well studied circuit of Zorin's proposal we now try to put bounds on the acceptable parameter variation.

To do this, we use a stochastic simulation method, where a given circuit parameter is varied in each unit cell such that the histogram of the parameter values follows a Gaussian distribution. Results of this sort of method are shown in Figure 3.10 where the geometric inductance of each unit cell has been randomly varied around its design value with a standard distribution of 10%. Two simulations performed with the same standard deviation can lead to very different results, as shown by the roughly 5 dB difference between the yellow and pink curves of final signal gain. Although, there are also some similarities, for instance, the large ripple present in the signal power profile.

Unless the particular values of the circuit parameters are known accurately for every cell in a device, this type of result is not of much help to us. Instead, the simulation must be performed many times for a given standard deviation and an envelope of possible signal powers at each point in the array recorded.

This has been done for each of the circuit parameters in the device for standard deviations of 0 %, 1 %, 5 % and 10 %. The results of this are shown in Figure 3.11 for geometric inductance (a), capacitance to ground (b), Josephson junction critical current (c) and junction capacitance (d).

Link to ToC

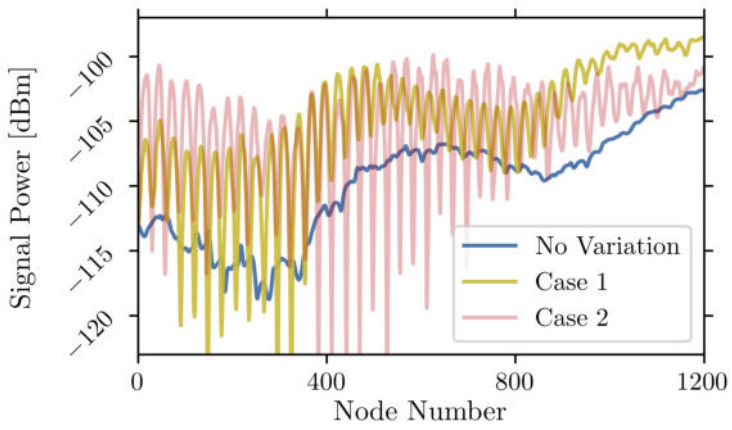

Fig. 3.10 WRspice simuation results from three JTWPA circuits, an ideal one with no variations (blue), while case 1 and case 2 in which the geometric inductance is randomly varied in each cell. Both of the two obey a Gaussian distribution with standard deviation of 10 % of its central value (L_G = 57 pH).

For geometric inductance, which has a large effect on both the characteristic impedance and on the wave mixing in the device, the envelope is the largest amoung all the circuit parameters. The envelope for capacitance to ground variation on the other hand, which only effects characteristic impedance, is only slightly smaller. Josephson junction critical current variation should significantly affect wave mixing in the device, although may not affect impedance greatly as the Josephson inductance is theoretically infinite at this bias point. It seems that impedance variations play a much larger role in affecting amplifier performance than variation of the wave mixing regime given the small size of this envelope in comparison to the previous two. Finally, junction capacitance plays a relatively small role in both the characteristic impedance of this device and theoretically no role in the wave mixing effects. As such, it has by far the smallest effect in its parameter variation, with even large variations causing little change on the signal power profile.

There appears to be a direct correlation between the impact of a parameter on the characteristic impedance of the device and the resulting width of the envelope for each standard deviation in these simulations. The bounds of the envelope of variation in a parameter are plotted against the standard deviation in that parameter in Figure 3.12.

Given the large ripple on the envelope bounds, it seems reasonable to claim that impedance mismatches are the cause of this uncertainty in signal power output. With this is mind, we might try to recreate this trend by propagating the uncertainties in each parameter through to the characteristic impedance of the transmission as calculated via Equation 2.9.

$$\sigma_Z^2 = \left(\frac{\partial Z_\Pi}{\partial L_G}\right)^2 \sigma_{L_G}^2 + \left(\frac{\partial Z_\Pi}{\partial C_0}\right)^2 \sigma_{C_0}^2 + \left(\frac{\partial Z_\Pi}{\partial I_c}\right)^2 \sigma_{I_c}^2 + \left(\frac{\partial Z_\Pi}{\partial C_j}\right)^2 \sigma_{C_j}^2 + \dots \tag{3.5}$$

Here, Z_Π is impedance of a Π-cell and, for convenience, we have redefined $\sigma(L_G) \cdot L_G$ as σ_{L_G} and equivalent for other parameters. This results in a value for the standard deviation of the characteristic impedance, σ_Z. From this we can define the reflection coefficient at the end of the array, Γ, which describes the portion of the wave amplitude that is reflected

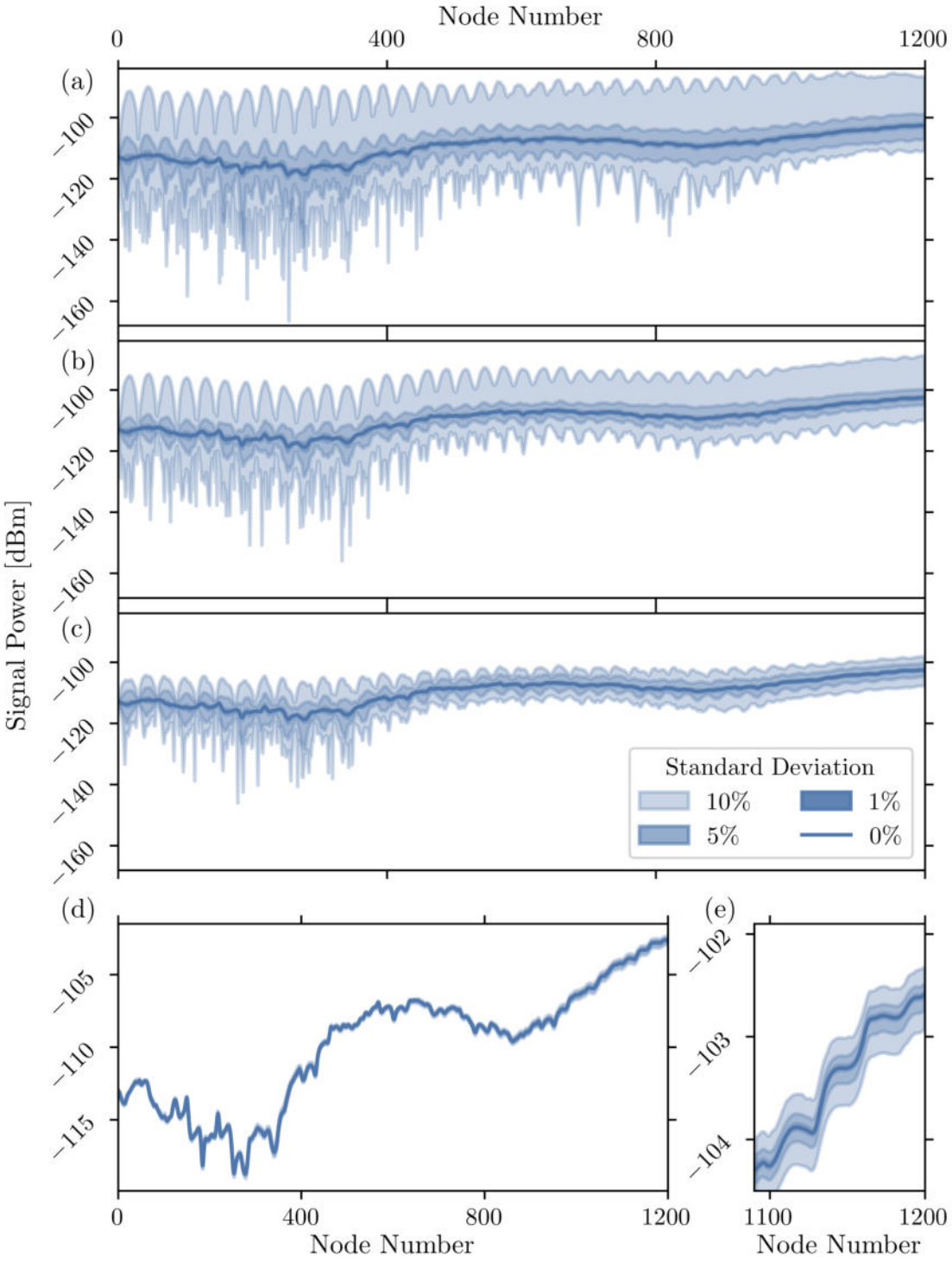

Fig. 3.11 WRspice simulation results in which the circuit parameters are varied from cell to cell with a Gaussian distribution and standard deviations of 0%, 1%, 5% and 10%. Simulations are run 100 times for each of the standard deviations and each of the circuit parameters, geometric inductance in (a), capacitance to ground in (b), critical current of the junction in (c) and junction capacitance in (d) and (e).

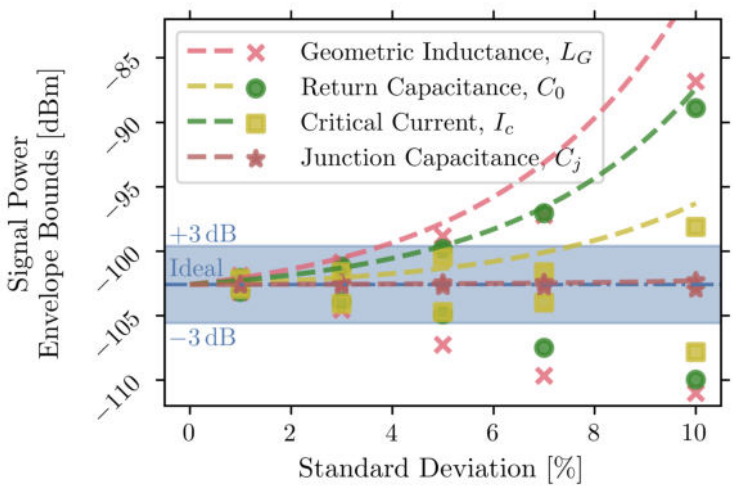

Fig. 3.12 Maxima and minima of the envelopes at the array end are extracted from the simulations of parameter variation and plotted as points against the standard deviation used in that simulation set. The approximations based on the VSWR are plotted as dashed lines. The ideal case of no parameter variation is shown in the dashed blue line, while a blue region around this shows the permittable region of gain variation for a useful device.

to travel backwards in the device and form a ripple, as:

$$\Gamma = \frac{Z_\Pi + \sigma_Z - Z_l}{Z_\Pi + \sigma_Z + Z_l} \ , \tag{3.6}$$

where Z_l is the termination resistance at the end of the array.

Often in microwave circuit design, engineers use this coefficient to define the voltage standing wave ratio within the device, which is the ratio of the voltage maximum to its minimum.

$$VSWR = \frac{1 + |\Gamma|}{1 - |\Gamma|} \ . \tag{3.7}$$

Suppose then, that the ripple seen in the power profiles on the signal in the device with cell-to-cell random variations is caused mostly by reflections of the amplified signal from the transmission line termination. This VSWR should then be related to the envelope width through some function of the final signal power of the ideal amplifier in which there are no variations. We have come upon a purely phenomenological formula, shown below, that produces an expected envelope width that is similar to the values achieved in simulation, although the derivation is not rigorous.

$$\log\left(1 + 100\frac{\sigma_X}{X}\right) = 10\log\left(P_{out}\right) + \left[10\log\left(P_{out}\right) \cdot 10\log\left(VSWR\right)\right] \ , \tag{3.8}$$

Here X represents the parameter being considered and P_{out} is the final signal power from an amplifier with no parameter variations (referred to as 'Ideal Case' in simulation results). There is high chance that a more rigorous approach will find a more suitable relation that will fit this data, but for the time being it escapes me. For any that seek to find such a relation, the need for taking the logarithm of the standard deviation in Equation 3.8 is perhaps due to the exponential component of the signal gain in the device.

Apparently, this method overestimates the effects of variation in both critical current and geometric inductance. Due to the nature of the equation that describes flux screening

Link to ToC

in this device (Equation 2.1), it is not reasonable to model the effects of parameter variations on this factor. In place of a taxing iterative method to calculate these effects, an approximation has been used where phase is equal to $\pi/2 - \pi/12$, approximately corresponding to the lower bound of the junction phase swing as shown in Figure 2.12. This allows for the effects of critical current variation to be calculated, but I believe that much better agreement with the simulation results can already be achieved if a suitable approximation for screening can be found.

3.4.3 Multi-Parameter Variation

Now that the effects of variations in each individual parameter are known, we look at the situation in which all circuit parameters are varied simultaneously, as this is what would be closest to reality. As such the standard deviations of each parameter are chosen to approximately reflect what might be achieved in a better or worse fabrication run.

The parameters chosen to reflect a bad case scenario are a standard deviation of 2 % in geometric inductance, 7 % in capacitance to ground, 5 % in critical current and 5 % in junction capacitance. Meanwhile, the parameters chosen to reflect the good fabrication case were 0.5 % in geometric inductance, 4 % in capacitance to ground, 2 % in critical current and 2 % in junction capacitance. Importantly, neither set of tolerances can be achieved without great effort on the part of fabricators and surpassing these tolerances would undoubtedly be a great achievement for the field of superconducting circuits.

The results of this are shown in Figure 3.13 (a) where the envelopes for the good case and bad case tolerance sets are plotted around the ideal signal power profile. It is quite clear that very unpredictable performance arises from the worse case of parameter tolerances. With an envelope width of around 30 dB producing an amplifier that may have either incredible or underwhelming amplification of the signal wave at 7.2 GHz, depending solely on luck. On the other hand, the good case of parameter tolerances produces a more reasonable envelope of width around ±2 dB. This falls within our defined acceptable range of ±3 dB as might be expected by the linear combination of the individual envelope widths.

As a large amplification is seen in the worse case parameter tolerances simulation set, the particular circuit that led to the upper bound of the envelope has been extracted and simulated over a frequency range to investigate whether this high amplification extends to the broadband as desired. As can be seen in Figure 3.13 (b), it does not. It seems likely that the large amplification at a signal frequency of 7.2 GHz and 7.6 GHz is instead due to a coincidental internal resonance formed with the JTWPA device. This can be considered a type of accidental dispersion engineering formed by the dynamic impedance mismatches occurring in the device as waves propagate through it, meaning this high amplification can probably not be considered reliable and certainly not wideband.

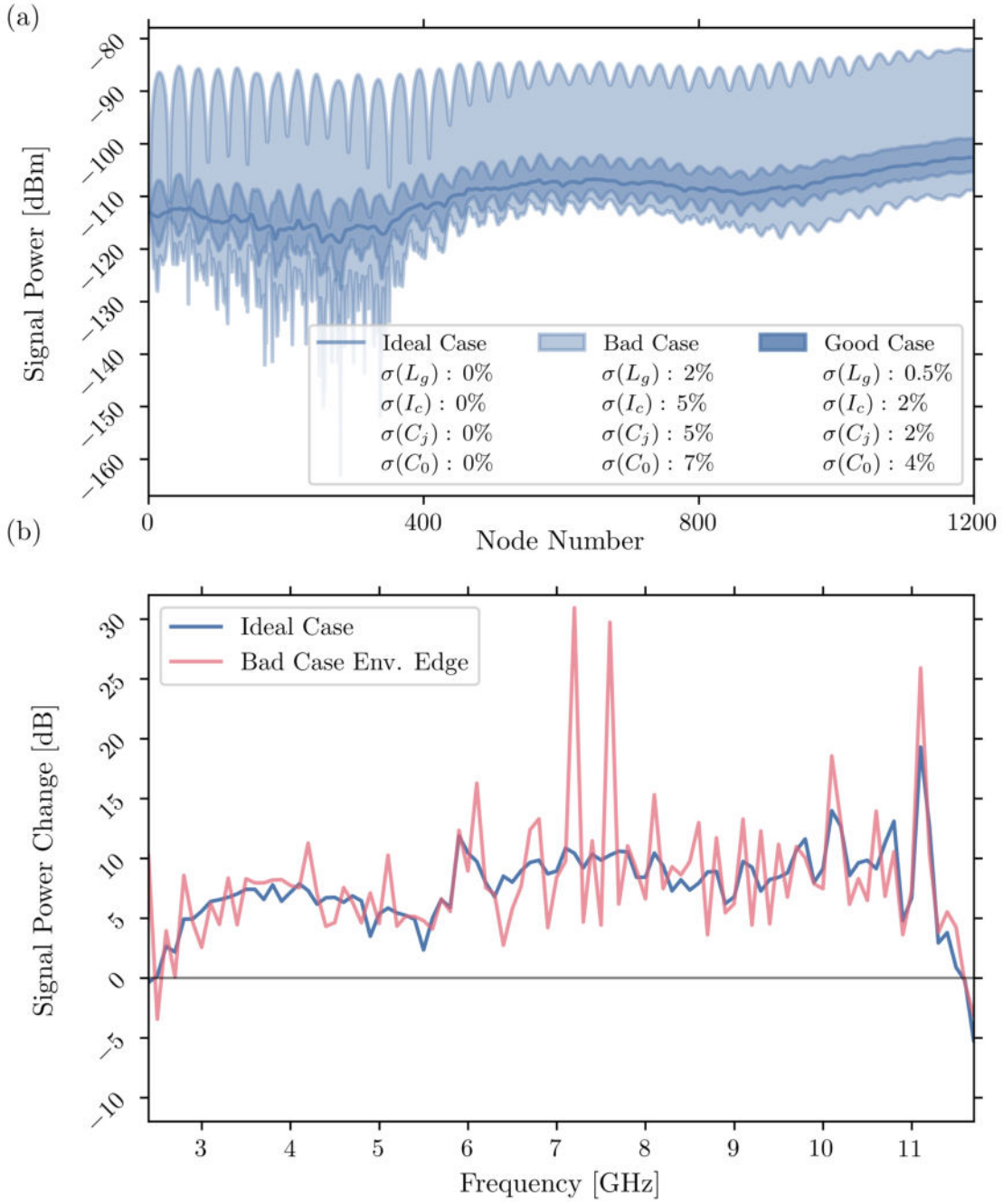

Fig. 3.13 WRspice simulation results where all circuit elements in each unit cell are subject to a Gaussian distribution with a greater or smaller standard deviation to mimic the behaviours one might see in devices fabricated using a better or worse process. (a) The envelopes of possible performance that one might expect for a device fabricated with the better or worse circuit parameter tolerances. (b) The amplification of a weak signal in the range $2.4 - 11.7\,\text{GHz}$ in the ideal case of no variation (blue) and an instance of a circuit with the worse case parameters that corresponds to the upper bound of the envelope plotted in (a).

3.5 Conclusion

Through the course of this chapter, based on Zorin's proposal [107], simulation tools have been developed for the study of Josephson travelling wave parametric amplifiers. These have then been used to investigate questions important to both the theoretical and experimental understanding of these devices. First, the transmission line theory has been investigated with the phase shift extracted and compared to the analytical model for this device. The numerical simulation results show strong agreement with analytical predictions both above and below the device cut-off frequency of 72 GHz. A good agreement has been found at all frequencies using the approximation of phase shift per cell presented earlier in this thesis, which can now be used with confidence in the analysis and design of TWPA devices.

Some common experimental methods have been analysed in simulation, investigating the transmission of waves and wave mixing effects with either a single or two input waves. For a single input wave, the transmission with varying flux in the device has been simulated to mimic an experiment that may be carried out using a vector network analyser. It has been found that due to the strong wave mixing effects in the device, the transmission is lowest near the optimal 3WM bias point, with a maximum difference in S21 magnitude of around 20 dB between the extremities. The behaviour of harmonic generation for a single input wave has also been used to investigate the effects of flux bias and input wave power. It has also been shown that at the optimal 3WM bias point, the input wave is depleted at the device output for input currents higher than -75 dBm, or about a tenth of the critical current of the Josephson junctions. This gives some basis to say that both the small pump approximation and the strong pump approximation used to model these devices may only be valid at input powers much smaller than are commonly used in experiments.

For simulations that use two input waves, a small signal wave and a strong pump wave, we have investigated a common method of characterising gain and locating the optimal 3WM bias points in these devices. It has been found that the method of comparing signal transmission with and without an applied pump wave is not an accurate determinant of gain in these devices. This is due to the strong parametric effects leading to attenuation of the signal wave when no pump is applied, due to harmonic generation. When a pump is then applied and the signal is amplified, a comparison of transmission would lead to a much higher apparent gain than the actual gain achieved, especially at the optimal 3WM flux bias. The method of locating the optimal 3WM bias position by its coincidence with the maximum of the second harmonic of an input wave is found to be accurate. In fact, all harmonics can be used to equal effect due to the strong 3WM nonlinearity with the difference in harmonic output power between 3WM and 4WM regimes being > 10 dB.

Certain questions that cannot be reasonably experimentally investigated have also been studied via these simulation methods. The effects of parasitic inductive coupling between neighbouring rf-SQUID's of opposite orientations has been found to nullify amplification for coupling coefficients, $\kappa \geq 0.3$. This apparent drawback has also been discussed as a

tool for the design of an optimised JTWPA with a hysteresis parameter close to unity. The intentional coupling of neighbouring inductances can be used to minimise parameter spread, lossening restrictions on acceptable hysteresis parameter values.

The possible effects of dielectric losses due to the strong electric fields at the lumped element capacitors have also been investigated. It is found that amplification may still take place despite attenuation so long as the pump amplitude is much greater than the signal. If this condition is not met then all propagating waves are attenuated. It was shown that for parasitic resistances across the lumped capacitors of $R \geqslant 50\,\mathrm{k}\Omega$ no amplification is seen but instead loss at all frequencies. Of particular interest is that the shape of the VNA trace may look identical for a lossy TWPA as it would for a loss-less TWPA, due to the similar wave mixing behaviours. In order for experimentalists to correctly identify amplification, a calibration line is needed to determine the signal power at the JTWPA input port. Fortunately, likely values of parasitic resistances in SiO_2 deilectric layers are estimated to be $\sim 3\,\mathrm{M}\Omega$, which is shown to have a very small impact on signal gain.

Finally, the effects of unavoidable parameter variations have been investigated via a stochastic simulation approach in which each circuit element in each cell of the JTWPA device was simulated with a Gaussian distribution and a series of standard deviations. This was done for each circuit element individually to quantify its affect on the whole, with standards deviations of 0%, 1%, 3%, 5%, 7% and 10%. We saw that the affect of variations in the geometric inductance and ground capacitance elements were severe on device performance leading to envelopes of possible amplification as wide as $\pm 15\,\mathrm{dB}$ which is a $> 100\%$ uncertainty in device gain. This study was the extended to investigating a set of reasonable fabrication tolerances that might be seen in realised devices. The results showed a large uncertainty in final gain values of $\pm 10\,\mathrm{dB}$ for even very tight tolerances of 0.5%, 2%, 2% and 4% in the geometric inductances, junction critical currents, junction capacitances and ground capacitances, respectively. Fortunately, this uncertainty was shown to be strongly frequency dependent, only severely impacting a limited set of signal frequencies across the device bandwidth. An alternative analytical method of estimating these effects has been proposed that may be applied to other circuit designs without the need for the computationally intense simulations that were performed here.

To recap, this chapter has shown that devices can realistically be produced in research facillities common in medium and large size institutions across Europe. Parasitic reactances have been shown to cause significant problems for devices if they have not been sufficiently reduced during design, while parasitic resistances due to dielectric losses have been shown to be most likely insignificant. The effects of parameter variation have been demonstrated to be quite obviously detrimental and dramatic in their affects on the uncertainty in gain that may be produced. However, with tight fabrication tolerances this uncertainty should be confined to a few frequency points across the device bandwidth. Fabrication defects that result in large impedance mismatches, like a shorted ground capacitance, have been demonstrated to lead to almost no transmission through the device. This means that while low yield of fabricated devices may prove to be a persistent issue in JTWPA development,the commonly considered parasitic reactances, dielectric losses and fabrication

tolerances are unlikely to prevent the realisation of a functional 3WM travelling wave parametric amplifier.

Chapter 4

Characterisation of an Aluminium based Josephson Travelling Wave Parametric Amplifier

4.1 Introduction

The experimental results presented in this chapter relate to a Josephson travelling wave parametric amplifier of the first generation. This generation of devices closely follow the proposed design of Zorin [107] in which a one-dimensional transmission line formed of rf-SQUID's provides a medium for travelling waves to interact and amplify/de-amplify each other. The designed circuit parameters are such to achieve a $50\,\Omega$ impedance, and no additional dispersion engineering or resonant structures are used to alter the wave propagation. The aim being that a long enough waveguide of this type should produce reasonable amplification of a weak signal, despite parasitic wave mixing effects. However, it will be shown in this chapter there are some complications that prevent this.

This device was shared with us by the Rodionov group of Bauman Moscow State Technical University as part of a collaboration with Lancaster University. The data for this device was collected in Lancaster University during a series of cooldowns between December 2021 and February 2022.

This chapter will cover the device design and predicted behaviour before discussing the experimental results taken for the JTWPA. We focus on the transmission properties of the device, investigating how they are affected by the power and frequency of applied waves and flux bias. The analysis of these results leads to the formation of a theoretical model based on known and estimated device parameters. This model is then shown to reproduce some key aspects of the experimental results in simulations performed in WRspice using both the transient and AC analysis techniques. The work presented in this chapter aids in

the understanding and design of future generations of JTWPA's to overcome the drawbacks of this first generation demonstrated hereafter.

4.2 Device Design

The device under test (DUT) is a chain of rf-SQUID's segmented by capacitances to ground, as described in Chapters 2 and 3. The micrograph of Figure 4.1 (a) shows the structure of the device fabricated in three layers. The first layer contains a ground plane and the bottom electrode of parallel-plate junction capacitors (shown in purple). The second layer contains aluminium Josephson junctions formed with a shadow evaporation technique,

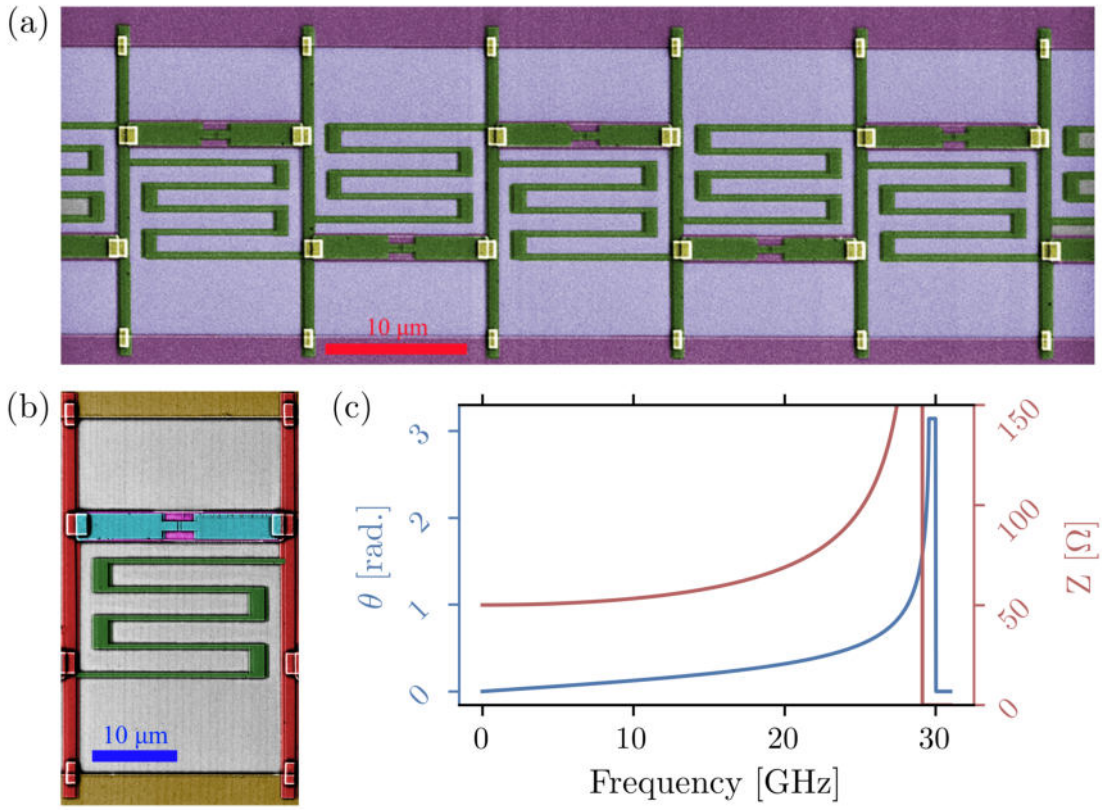

Fig. 4.1 a) A false colour SEM image of a portion of the JTWPA device experimented upon, in which a chain of rf-SQUID's is formed of patterned and overlapping superconducting films (green and purple) on silicon dioxide (magenta). The green (aluminium) film forms the Josepshson tunnel junctions, geometric inductance and capacitances to ground via a shadow evaporation technique while the purple film provides a ground plane and shunt capacitance beneath the Josephson tunnel junction structure. The yellow pads are used to ensure continuity in the aluminium film. (b) An individual unit cell of the JTWPA in which a Josephson junction (blue) is shunted by a large capacitance (formed by the pink and blue electrodes) and a geometric inductance (green) while capacitive pads (red) on each side of the cell shunt the cell to ground (yellow). (c) The impedance, Z, and dispersion, θ, of the structure, calculated using the device design parameters.

I_c [µA]	R_{RT} [Ω]	L_G [pH]	C_j [fF]	C_0 [fF]
2.2	120 - 130	132.6	212	53

Table 4.1 The parameter sets of the transmission line unit cells used through the following chapters where critical current, I_c, geometric inductance, L_G, junction capacitance, C_j, and ground capacitance, C_0, are the same as those suggested in [107].

as described in Chapter 1, geometric inductances and the top electrodes of capacitances to ground and junction capacitors (shown in green). The third auxiliary layer (shown in yellow) has small portions of aluminium to ensure continuity of the aluminium films.

The portions of these metallisations responsible for each of the lumped circuit elements that make up this metamaterial are highlighted in Figure 4.1 (b). We can reasonably assume that parasitic impedances of each circuit element is small, for example, the geometric inductance of the Josephson junction ~ 17.1 pH is negligible in comparison to its nonlinear inductance $\gtrsim$ 149.6 pH. The estimated parameters for each of these circuit elements are listed in Table 4.1, where critical current is estimated from test junctions of the same batch in which the room temperature normal state resistance, R_{RT}, has been measured. The values for geometric inductance, parallel plate junction capacitance and capacitance to ground have been estimated from formulae. Using Equation 1.24, the effective impedance of the medium is found to be approximately 50 Ω in the 3WM regime throughout the C- and X-frequency bands of most interest to us, as shown in Figure 4.1 (c).

The total length of the array is 2189 rf-SQUID cells and has an electrical length roughly equivalent to a 160 MHz wave, with the wavelength of a 5 GHz tone equivalent to roughly 32 cells. The long length of the device was intended to ensure a weak signal is provided sufficient amplification despite the potential of inefficient wave mixing due to the generation of higher harmonics. A rather low cut-off frequency of ~ 30 GHz helps to limit the generation of pump harmonics, although it also leads to a strong dependence of impedance and phase shift on frequency, as shown in Figure 4.1 (c).

4.3 Experimental Apparatus

The data presented in this chapter was collected in a BlueFors LD250 dilution refrigerator with a base temperature of ~ 8 mK on the mixing chamber (MXC) plate. Two rf input lines were organised for the pump and signal waves which were attenuated at each temperature stage to minimise thermal radiation that reaches the device, an additional 20 dB at room temperature is used for some measurements [141]. The pump and signal waves are combined onto a single input line at the MXC plate via a directional coupler[1] that has a − 20 dB coupling of the signal line onto the pump line. A dc bias can be added through the DUT

[1] Pasternack - PE2CP000-20

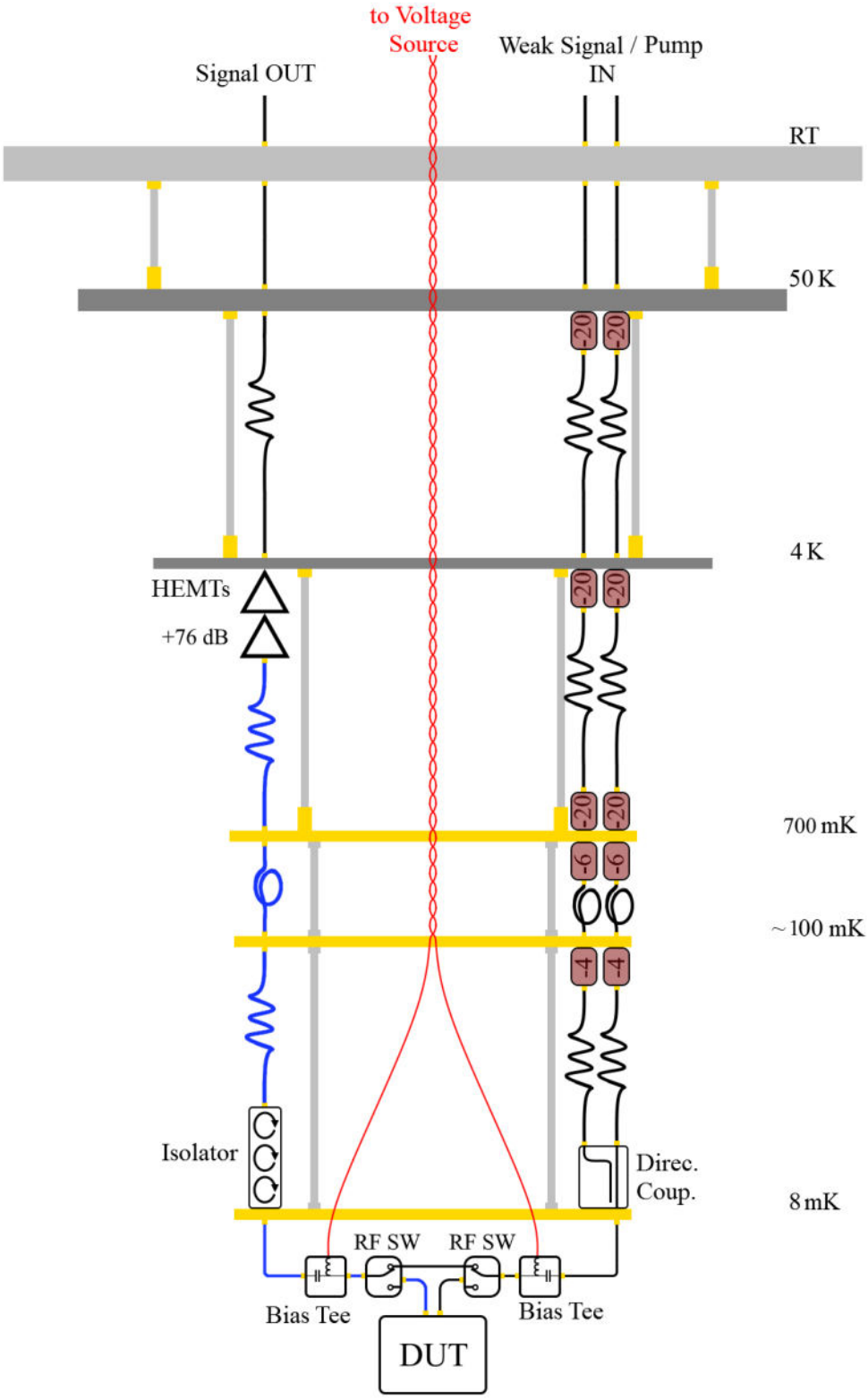

Fig. 4.2 Experimental set-up used for the characterisation of the JTWPA device with 70 dB attenuation on both input lines, with the signal line having a further decrease of 20 dB due to the directional coupler. A direct current can be applied to the device via a pair of bias tees while mechanical coaxial switches (RF SW) allow for the callibration of the system to a through line. HEMT amplifiers on the output line provide ~ 80 dB signal gain at a noise temperature ~4.5 K while the DUT is protected from any reflected waves in the output line via a triple junction isolator on the MXC plate. The rf lines coloured blue are superconducting coaxial SMA cables, otherwise steel coaxial cable is used between temperature stages and copper coaxial cable is used on the MXC.

Link to ToC

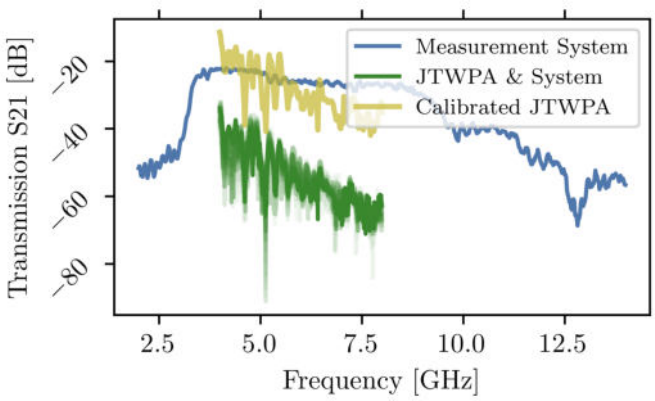

Fig. 4.3 Transmission (S21) trace of the measurement system (blue line) compared to transmission through the DUT at various flux biases (faded green lines) and the difference between the two traces (yellow line). The negative gradient in the green and yellow traces imply some losses in the transmission line.

using a pair of bias tees[2], after which a pair of 2-way latching rf relays [3] allows for the characterisation of a calibration line.

On the single rf output line, superconducting coaxial cables are used up to the 4 K plate to minimise losses before the HEMT amplifiers[4]. An isolation of 60 dB between the HEMT amplifier and the DUT is achieved using a triple junction isolator[5] to eliminate noise signals coming from the HEMT amplifiers to the DUT.

Transmission data is collected primarily on an Agilent E5071C vector network analyzer and an Agilent N9030A signal analyser, Agilent E8275D and Anritsu MG3692B microwave sources were used to provide input tones, and a dc bias was supplied by a Keithley 33521B. Each of these instruments is connected to a clean laboratory ground which was organised to minimise the system noise temperature [142].

The S21 data presented in Figure 4.3 was taken from a cooldown immediately preceding that of all the following data in this chapter, although the same attenuation and microwave devices were used. The large drop in transmission of the DUT compared to the through line implies some significant impedance mismatch between the device and the 50 Ω measurement system, while the gradient of the transmission signifies some losses in the device.

4.4 Measurement Results

The intended application of most superconducting travelling wave parametric amplifiers is as a two-port device on the output line of a cryostat. As such, we focus here on transmission measurements, although the process presented below can equally be applied to alternative schemes that use reflectometric measurements.

Application of a flux bias, achieved via a direct current in the device, leads to the variation of the Josephson inductance in each unit cell and hence the characteristic impedance and wave mixing regime of the device. Data is first presented that confirms modulation of Josephson inductance, via the change in the S21 parameter of the device

[2]Marki Microwave - BT0018
[3]Radiall - R570432000
[4]Low Noise Factory - LNF-LNC1_12A s/n 764B & LNF-LNC1_12A s/n 761B
[5]Low Noise Factory - LNF-ISISISC4_12A

Link to ToC

against dc bias. Afterwards, the presence of wave mixing is confirmed by analysing harmonic generation of a single input wave in the device.

The three wave mixing regime is further investigated by measurement of the 3WM idler and signal tone on a signal analyser against applied flux, as well as the amplification / de-amplification of the signal tone across a frequency range. The phase shift data for a signal undergoing parametric wave mixing is then analyzed, with a comparison made to the assumed optimal 3WM bias point.

Portions of the data presented here are taken from a preliminary dataset for this device. As the device was damaged by an electrical fault in the laboratory not all of the data could be retaken with a more thorough methodology. As such, some aspects of particular measurement details are missing. Notes have been added to the text where the precise operating conditions are unknown, although these details are not key to the understanding of this data.

4.4.1 Flux Modulation

The dependence of transmission on bias voltage, as shown in Figure 4.4, was obtained as a time trace on a VNA for a probe frequency of 8 GHz. The VNA sweep time was set to half the length of a triangular voltage waveform which provided the up-sweep of dc bias. The transmission through the device is periodic in the flux bias, where a single period should follow the relation:

$$\Delta V_{app} = \frac{\Phi_0 R}{L_G} \, . \tag{4.1}$$

This relates the change in applied voltage over a period to the magnetic flux quantum via the circuit parameters L_G and R which correspond to the geometric inductance of the unit cell and the total resistance of the dc bias lines, respectively.

The periodicity may be expected to follow a trend similar to that of Figure 2.4 (b) where the transmission is maximal at the 3WM bias point as the impedance is matched to the system. However, this is clearly not what is seen above with the shape of the period

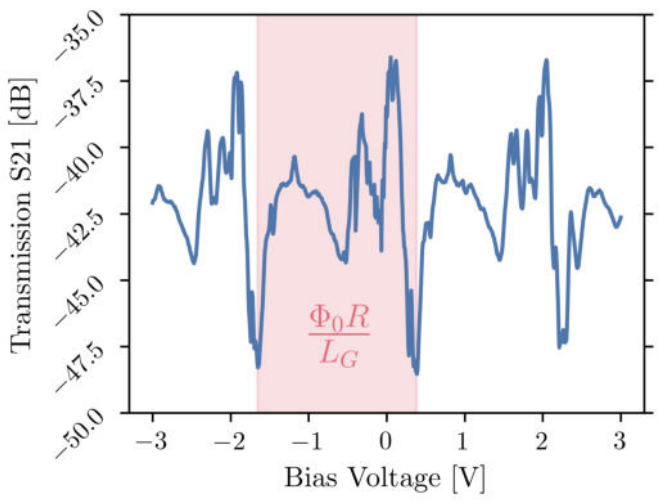

Fig. 4.4 Bias dependence of S21 captured on a VNA with a signal frequency of 8 GHz while a triangular voltage wave form is applied synchronously. A periodic behaviour is apparent, with a single period (highlighted in red) being equivalent to a change in the flux bias position of one flux quantum, Φ_0. The assymetric shape of the period makes the true zero flux position difficult to know at this point.

in S21 being somewhat difficult to interpret. There are multiple possible explanations for this which are tested later in this chapter. The strange shape may be largely due to wave mixing effects where the transmission is altered by power 'leaking' from the signal tone into its harmonics. Alternatively, the geometric inductance of the rf-SQUID's in the array may be slightly different from each other, either randomly or in some gradiometric distribution. This would cause an offset in the flux periods which may produce the complex shape seen here for the entire array.

4.4.2 Harmonic Generation

Generation of harmonics of an input wave to the JTWPA is a useful measure of the wave mixing effects occurring in the device, as has been discussed in Chapter 3. By inputting a pump wave into the JTWPA its peak and the peaks of the generated harmonics can be measured so long as they lie within the measurement range of our system. To do this, a signal analyzer is used to measure the spectrum around each of the tones of interest, the areas of the peaks are then extracted.

The peak area of the pump at 4.5 GHz and its second harmonic at 9 GHz are plotted in Figure 4.5 (a). The pump power plotted corresponds to the power output of the E8257D signal generator minus the total attenuation of the input line.

Interestingly, there are two distinct gradients present in this plot which is not expected, although the general trend of the second harmonic increasing at a faster rate than the fundamental is as predicted. Furthermore, the plateauing of pump peak area at higher

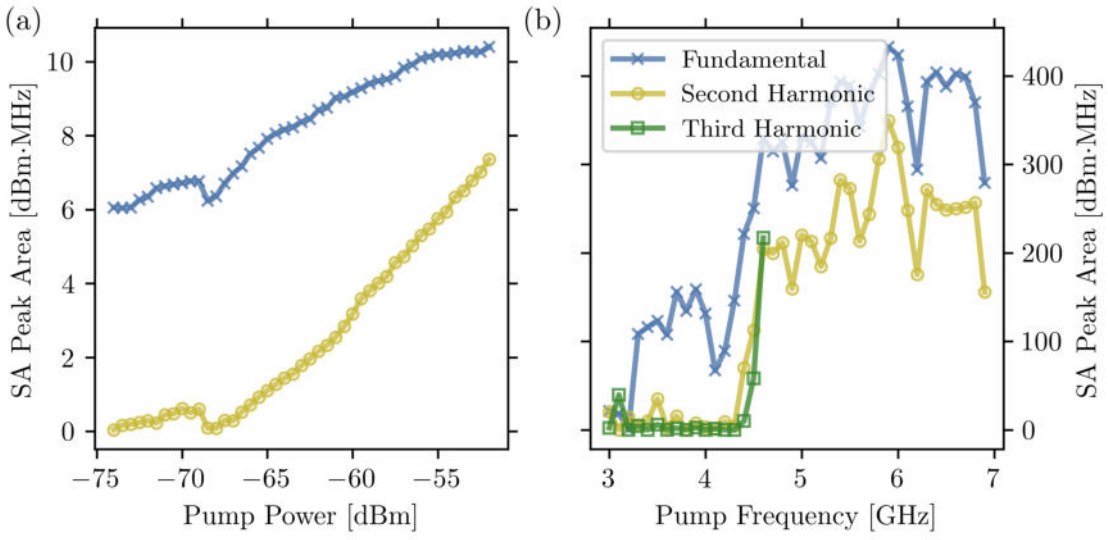

Fig. 4.5 (a) Generation of pump harmonics of an applied pump wave, held static at 4.5 GHz while pump power is swept in (a), where the second harmonic has been tracked, and (b) where pump frequency is swept and third harmonic has been tracked additionally. Both show some correlation between the area of the pump wave peak captured on a signal analyzer and its harmonics, although a distinct gradient change in both plots implies some optimal operating conditions for maximal wave mixing in terms of both power and frequency.

Link to ToC

powers follows a similar effect as in the simulated data of Chapter 3 which may indicate pump depletion via harmonic generation.

The dip followed by an increased gradient increase in the generation of the second harmonic may imply a 'turn-on' power after which wave mixing becomes more efficient. The dip resembles similar features seen in the simulation data for pump powers near the critical current, which for this device would be $\sim -67\,\mathrm{dBm}$. Given this alignment we might expect that applied power $\simeq$ delivered power, although the delivered pump power on chip was expected to be 20 - 30 dB lower than this given the data of Figure 4.3. Of course, this dip may be caused by other effects and its positioning merely be a coincidence, however, if it is a direct effect of $I_p = I_c$ this can be used to measured the critical current of an array of rf-SQUID's. To my knowledge this is not a measurement that is possible with any other technique.

The frequency of the pump tone can then be swept with the results of this shown in Figure 4.5 (b). Interestingly, at pump frequencies below $\sim 4\,\mathrm{GHz}$ the harmonic generation is suppressed. The pump and second harmonic should remain within our measurement band at these frequencies, so the most reasonable explanation is that there is some perturbation in the dispersion relation of the device below this frequency. This would diminish the phase matching of the pump with its harmonics, and by extension the efficiency of their generation. We can expect mixing of the pump and second harmonic to remain the dominant mechanism for third harmonic generation, as described in the previous chapter. Hence, we can determine that the perturbation in the phase relation for this device occurs between 6 and 9 GHz, based on the behaviour of the peak areas.

4.4.3 Idler Generation and Signal Amplification

To further investigate three wave mixing, a common method is to track the 3WM idler against flux bias, the peak in this relation is often considered to be the optimal 3WM bias point. While this is not quite true for reasons that will be discussed later in this chapter, it is useful for now to confirm the variation of the powers of 3WM tones against the applied flux bias. This is achieved by inputting a 12 GHz pump tone and a 6.02 GHz signal tone, which gives rise to an idler tone at 5.98 GHz via 3WM. This is clearly seen in the plots of Figure 4.6 (a) where the idler tone power is altered by the voltage bias position, although the signal tone power is perturbed very little in comparison.

The comparison of the variation in signal and idler amplitudes against flux bias is plotted in Figure 4.6 (b) where the peak areas have been extracted and plotted. It should be noted that the idler is not at its minimum at zero bias meaning 3WM is non-zero, most likely due to trapped flux in the device as it was cooled to base temperature. The coloured bands on the right side of the plot correspond to the biases used in the traces of Figure 4.6 (a), where red is an idler minimum, green is an intermediate state and purple is an idler maximum. Interestingly, the signal plateaus at a higher power after the idler maximum implying higher transmission. This may imply a larger amplification in an intermediate wave mixing regime where phase mismatch is corrected somewhat by the cross- and self-phase modulation effects in 4WM, but 3WM remains dominant regime.

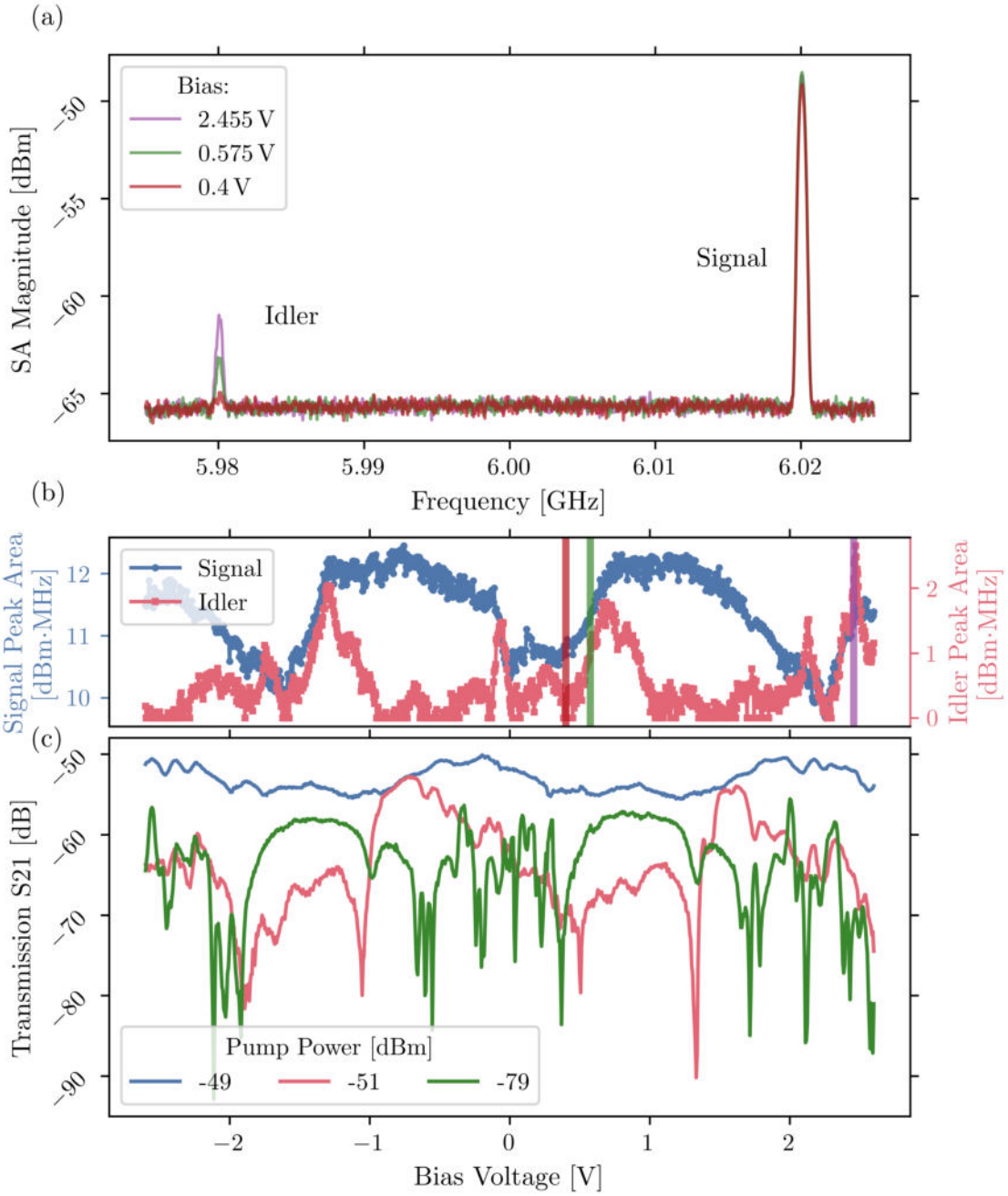

Fig. 4.6 (a) Three VNA traces taken at different dc biases with a signal input at 6.02 GHz, a pump at 12 GHz and an idler tone generated at 5.98 GHz. The impact of dc bias on the idler peak height, and by association 3WM efficiency, is clear. (b) The peak area of the signal and idler are extracted from the signal analyzer traces and plotted across a flux period, with the red, green and purple bands corresponding to the traces at these flux biases shown in (a). (c) The change in amplitude of a signal tone at 6.5 GHz is shown for a selection of pump powers. Increasing S21 of the signal at higher pump powers indicates amplification, although the abrupt change in the shape of the flux period at pump powers above −50 dBm may indicate departure from the small pump approximation.

Link to ToC

However, it may also be an effect of change of characteristic impedance in these regions. In reality, it is most likely a combination of the two of these effects, although the power change of the signal is too small to actually determine between the two in this case.

This difficulty in determining the cause of the change in signal amplitude is exemplified by Figure 4.6 (c) where the S21 of a signal at 6.5 GHz is plotted against applied voltage. The very small signal has a modulation in flux of similar order to the case without an applied pump in Figure 4.4. If we take it that there is essentially no gain at the 4WM bias points as the 4WM idler would be badly positioned for phase matching, then we would also have to conclude that there is little to no gain at the 3WM bias points either. At least, no amplification distinguishable above the effects of characteristic impedance changes.

There are two more noteworthy aspects of this plot, one is that the periodic shape at lower pump powers is quite hard to understand which will be resolved later in this chapter. The other interesting aspect is that the complex period shape quickly becomes lost as power pump is increased above the -52 dBm threshold. This may be a sign that the applied pump is much too large, far from the small pump approximation, so the effect of flux bias position is blurred by the large modulation of the bias by the pump. This is supported by evidence of erratic behaviour at high pump powers reported in other literature for similar devices [125].

4.4.4 Wideband Response

The transmission line structure of this JTWPA device should allow for wave mixing across a wide frequency band. The S21 data over a frequency range 4.3 - 6.8 GHz, with a static pump frequency and power[6], is shown in Figure 4.7 (a). The dc bias was swept to investigate the change in transmission due to wave mixing of the signal and pump, with some clear effects taking place. Given the magnitude of change in S21 these changes are as likely to be due to the modulation of the characteristic impedance and electrical length of the device as due to wave mixing.

In order to investigate the possibility of gain across the frequency band, the same measurement is run both with the pump on and the pump off and the difference plotted in Figure 4.7 (b). The effect of flux bias in this case is vastly more clear, although there does not appear to be any significant change in the transmission between the 3WM idler minimum and its maximum at bias points 0.4 V (red) and 2.455 V (purple), respectively. In fact, the most clear effects of the bias are at the 2.125 V (yellow) and 0.05 V (blue) points where the behaviour of no transmission change (yellow) indicates no significant wave mixing and a behaviour that resembles a ripple indicating impedance mismatches (blue).

Perhaps, the most interesting aspect of these plots is the behaviour at some sort of resonance around 6.5 GHz which changes shape with applied flux. This means the resonator is formed within the JTWPA structure itself but the length scale does not match any design parameters. Half of a wavelength of 6.5 GHz corresponds to approximately 12 unit cells of the transmission line, but no significant change on this length scale could be seen

[6]The pump frequency was found to be either 12 or 18 GHz via an experimental comparison.

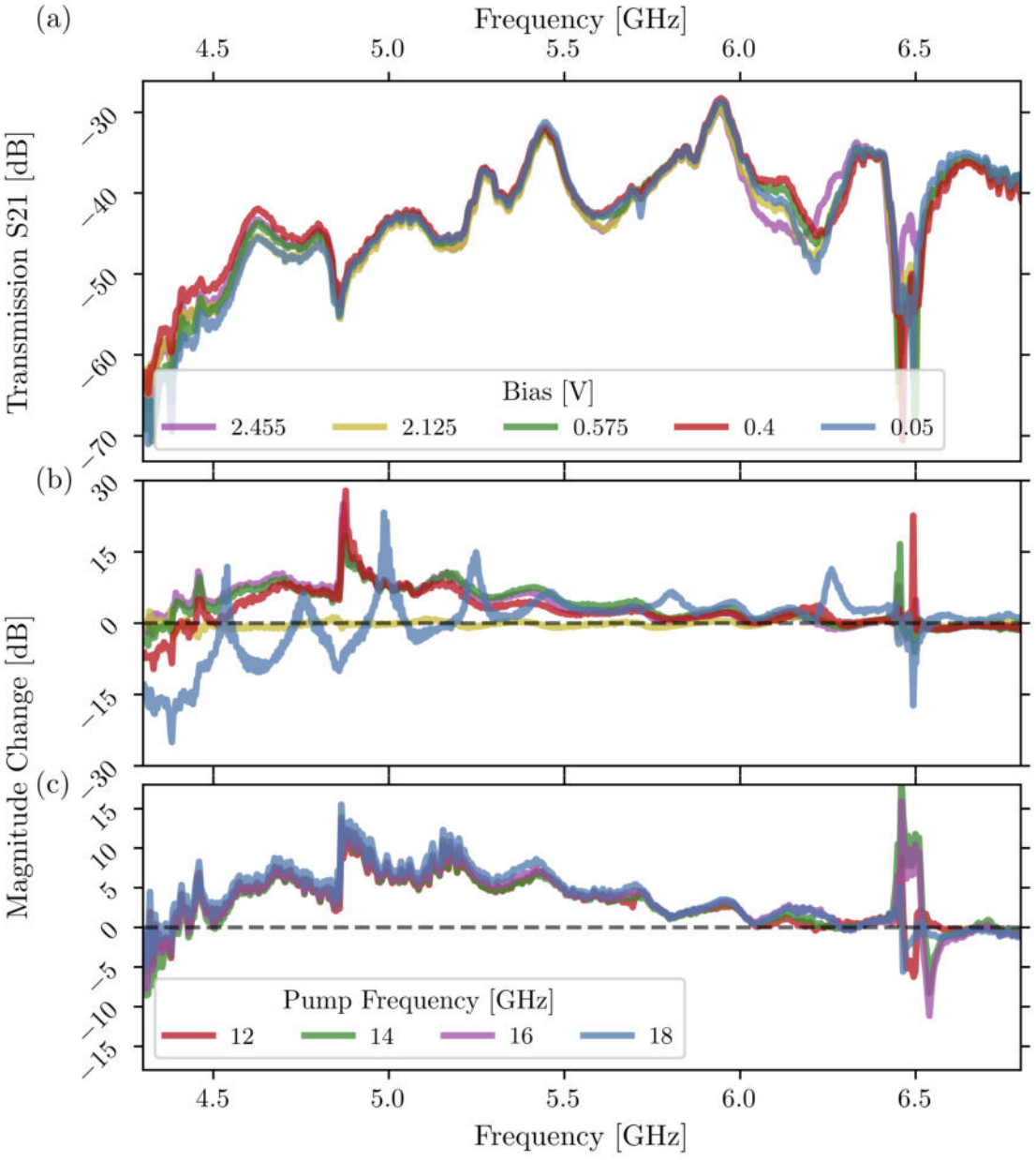

Fig. 4.7 VNA traces of a signal tone swept over a frequency range of 4.3 GHz - 6.8 GHz with an applied pump wave and dc bias that should allow for parametric amplification. (a) Altering the flux bias changes the transmission spectrum evidently, although with a transmission of approximately −45 dB relative changes due to the flux bias are small. To more clearly show the effects of transmission change with applied flux, the difference between transmission with pump on compared to pump off is plotted in (b). (c) With flux bias held constant and pump frequency instead swept, relative changes in the transmission of the signal are less pronounced across the signal range, although the effects of pump frequency change are more pronounced near an apparent resonance around 6.5 GHz.

Link to ToC

on SEM images of the device. The effect may be due to the Gaussian variation of circuit parameters detailed in Chapter 3 which lead to a similar effect in simulations.

This behaviour shows an even stronger response to the effects of pump frequency where the flux bias is held steady[7] in Figure 4.7 (c). This may imply some sort of accidental resonant phase matching is occurring within the device where some defects have formed a weakly coupled resonant structure around 6.5 GHz. Amplification for signals around this frequency would then be altered due to a perturbation in the dispersion relation of the device, either improving or diminishing phase matching between the mixing waves. While a number of effects external to the JTWPA structure may explain this behaviour, this hypothesis is supported by the harmonic generation data that showed very poor up-conversion at pump frequencies below 4 GHz.

4.4.5 Phase Shift

While the S21 magnitude has been shown to be rather difficult to interpret, the S21 phase shift data is now shown to be comparatively straight forward. As the electrical length of the JTWPA device will be related to the Josephson inductance per cell and by extension the flux bias, the phase shift per cell will also be modulated by applied voltage. The total phase shift recorded by a VNA includes the effects of all microwave components and lines in the measurement system, although only the JTWPA should be affected by the dc bias. Shown in Figure 4.8 is the phase shift data recorded for a signal at 5.5 GHz extracted from the same dataset as Figure 4.7 (a). The red, green and purple bands mark the 3WM idler minimum, intermediate state and maximum bias points as before, while the blue line shows the expected phase shift per cell for this device as per Equation 1.31. A flux offset of $-0.7\,\Phi_0$ was found to be present, otherwise the experimental data agrees quite well with the analytical predictions based only on the designed parameters of the device.

Although the phase shift per cell cannot be compared directly to expected values due to the lack of a calibration line for this measurement, the behaviour is very similar to what is expected. The apparent upwards trend that is present in the data may be explained by

[7] The flux bias point was found to be 0.85 V via an experimental comparison.

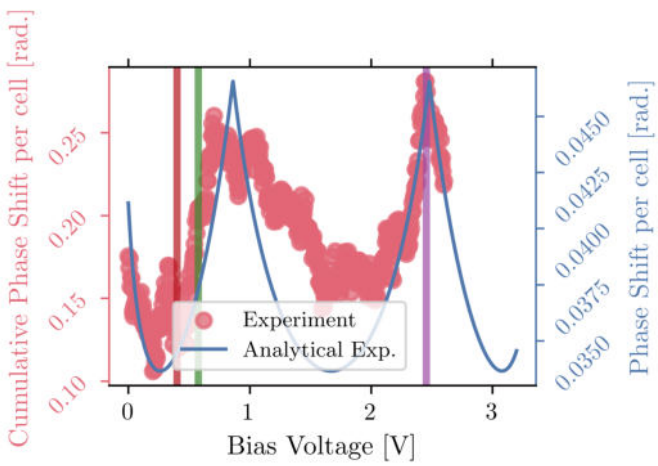

Fig. 4.8 Phase shift of a signal wave at 5.5 GHz extracted from the VNA data recorded for the sweep of signal frequency versus flux with pump on. The maxima in phase shift are located at the optimal 3WM bias points where the electrical length is longest, which coincide well with the location of the idler maximum (purple band). The red band corresponds to the optimal 4WM bias point, while the green band is an intermediate point between the two wave mixing regimes.

Link to ToC

an additional reactance in the unit cell that has an almost linear relation with the phase bias across the junction. While any number of parasitic effects may cause this I would propose to first try to limit the additional tunnel junction structures formed during shadow evaporation on all of the other circuit elements in these device. This can be achieved by switching to niobium tri-layer technologies or a two layer aluminium process with an intermediate argon milling step.

This method of analysing phase shift seems to be a useful and dependable method for determining the optimal 3WM bias position, given that locating the idler maxima may not always be perfectly accurate as will be discussed later in this chapter.

4.4.6 Discussion

In these results we have seen clear evidence of the modulation of the Josephson inductance by the application of a dc bias, as well as three wave mixing. However, it has proved difficult to distinguish the effects of wave mixing (or parametric amplification) from the effects of impedance mismatches in the transmission data of the device.

Of course, if the parametric amplification was as large as intended then this complication would be much easier to overcome. Theoretically, the change in S21 due to wave mixing should be much larger than that due to impedance mismatches. This does not appear to be the case in this device, likely due to a large phase mismatch between the 3WM tones.

The greatest difficulty in measuring this device was determining the optimal 3WM bias position, made more difficult by the large flux offset of $-0.7\,\Phi_0$. This flux offset is likely an average of the individual flux trapped in each rf-SQUID along the device. The flux offset may be prevented to some degree by better magnetic shielding to prevent flux trapping during cooling. However, it is not clear if the complex S21 data shown in Figure 4.4 will be greatly improved by this. It is not currently clear whether this transmission data complexity is due to a gradiometric distribution of circuit parameters, flux trapping or some other effect.

While these questions can be explored further in this chapter it has fortunately been found that measurement of the phase shift through the device can be a reliable indicator of the optimal 3WM bias position. We have also found tentative evidence that a dip in the relation of applied pump power to second harmonic output power may be an indicator of Josephson junction critical currents in the device. While no broad band amplification of the signal was seen (although some narrow band gain around 6.5 GHz may have been present), the method of determining the optimal bias position is a fruitful result in and of itself.

4.5 Performance Analysis

To better understand the behaviour of this device, the simulation methods discussed in Chapter 3 are now used to reproduce some of the key experimental results. With the goal of discerning the effects of impedance mismatch from wave mixing more clearly in the experimental results, we first investigate the expected amplification of a signal wave in this device. Following this, the transmission characteristics of the device can be simulated with any wave mixing effects removed. This result shines light on the detrimental aspects of the JTWPA design and experimental setup that have so far been neglected. By investigating the transmission of a signal wave over a flux period, both considering and neglecting wave mixing effects, we can begin to make conclusions about the device and the viability of similar designs.

4.5.1 Simulation of Idealised Circuit

This device was designed primarily with the goals of achieving a 50 Ω impedance at the 3WM bias point and minimising harmonic generation of the pump by decreasing the cut-off frequency. We comment now on the resulting amplification that might theoretically result from such a device, without considering any further mitigating conditions, i.e., there are no losses, no impedance mismatches, etc.

Running a transient simulation in WRspice and injecting a weak signal of 20 nA current at 7.2 GHz frequency, alongside a strong pump wave of 0.4 µA current at 12 GHz frequency with a bias current set at 5.89 µA, we witness a 3WM idler tone formed in the device. The power of the signal and idler are plotted in Figure 4.9, where the WRspice is in the faded lines up to node 1200 (the maximum length of a WRspice simulation), while solid lines show CME results extended up to the actual device length of 2189 nodes. Before commenting on the other aspects, the close agreement between the WRspice and CME results gives confidence to their accuracy for this device.

As is clear the amplification is very small, less than 1 dB, while the signal and idler powers are periodic in position along the length of the device [8]. Importantly, the period for the signal and idler are equal so this is not an effect of impedance mismatches or reflected waves but instead a finger print of the phase mismatch between the pump, signal and idler waves. The signal has a wavelength in this device of ~ 22 nodes, the idler ~ 32 nodes and the pump ~ 12 nodes, while this period appears to be ~ 400 nodes. This corresponds to double of the inverse of the phase mismatch between the mixing waves, or $2/\kappa_3 \sim 5 \times 10^{-3} \Rightarrow 400$ nodes. To maximise amplification in a device the phase mismatch should be low enough that the periodicity in amplification is more than twice as long as the device.

[8] This simulation was repeated for a signal power an order of magnitude lower and the behaviour was the same.

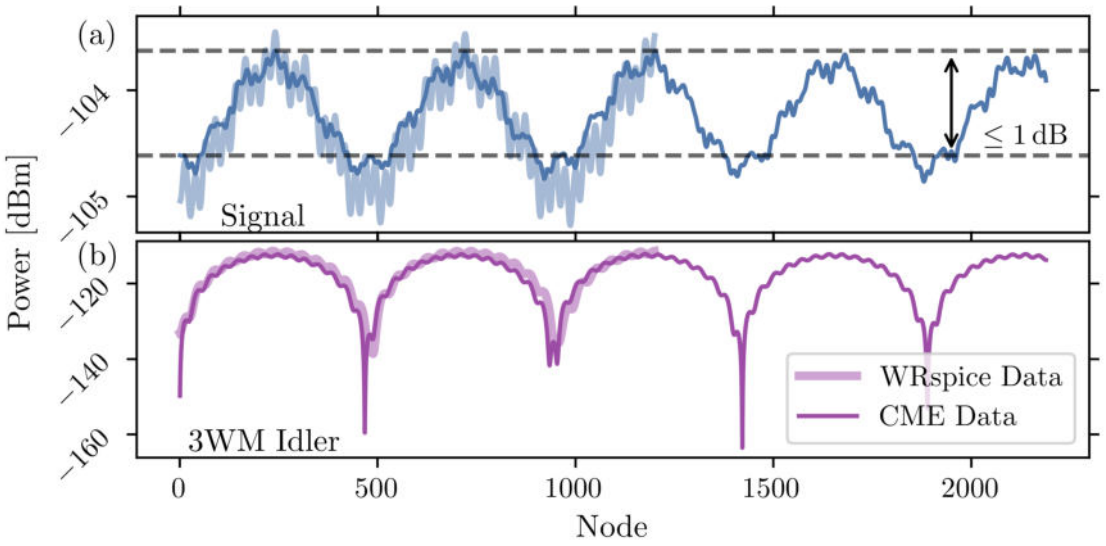

Fig. 4.9 Simulation results for the model of the measured device. (a) WRspice simulation (light blue) and CME simulation (solid blue) of the model of the JTWPA device which shows several periods of amplification/de-amplification of the signal wave across the length of the device due to a large phase mismatch between the signal, pump and the idler (shown in (b)).

These amplification periods are also a reason that the aforementioned method of using the maximum idler power to identify the optimal 3WM bias point is not recommended. Should the end of the array not coincide with the maximum in idler power then a small alteration of the bias away from the optimal 3WM point may lead to a lower maximum of the idler overall but a larger value on the output.

4.5.2 Device Model

The model of JTWPA device analysed in Chapters 2 and 3 has mostly focussed on the simpler picture of the device. While impedance mismatches to the measurement circuitry and losses within the device have been analysed for the theoretical device in the previous chapter, we now pursue a more thorough model that accurately represents these factors. We have investigated this using the AC analysis simulation technique in WRspice for a linearised version of the JTWPA circuit.

Shown in Figure 4.10 (a) is a drawing of the transmission line structure of the JTWPA under study, where lengths of rf-SQUID chains are linked at their ends by curved co-planar waveguides to form a meander structure. This combination of transmission lines, for which a micrograph of the point where the rf-SQUID chain meets the co-planar waveguide is shown in Figure 4.10 (b), is a consequence of the fabrication method used. The difficulty of producing rf-SQUID's reliably on curved structures using double angle evaporation is not small and so the rf-SQUID chain portions are restricted to the horizontal lengths of the meander. While only three lengths of 221 rf-SQUID's are drawn, the actual device has nine of these lengths for a total of 2189 rf-SQUID cells.

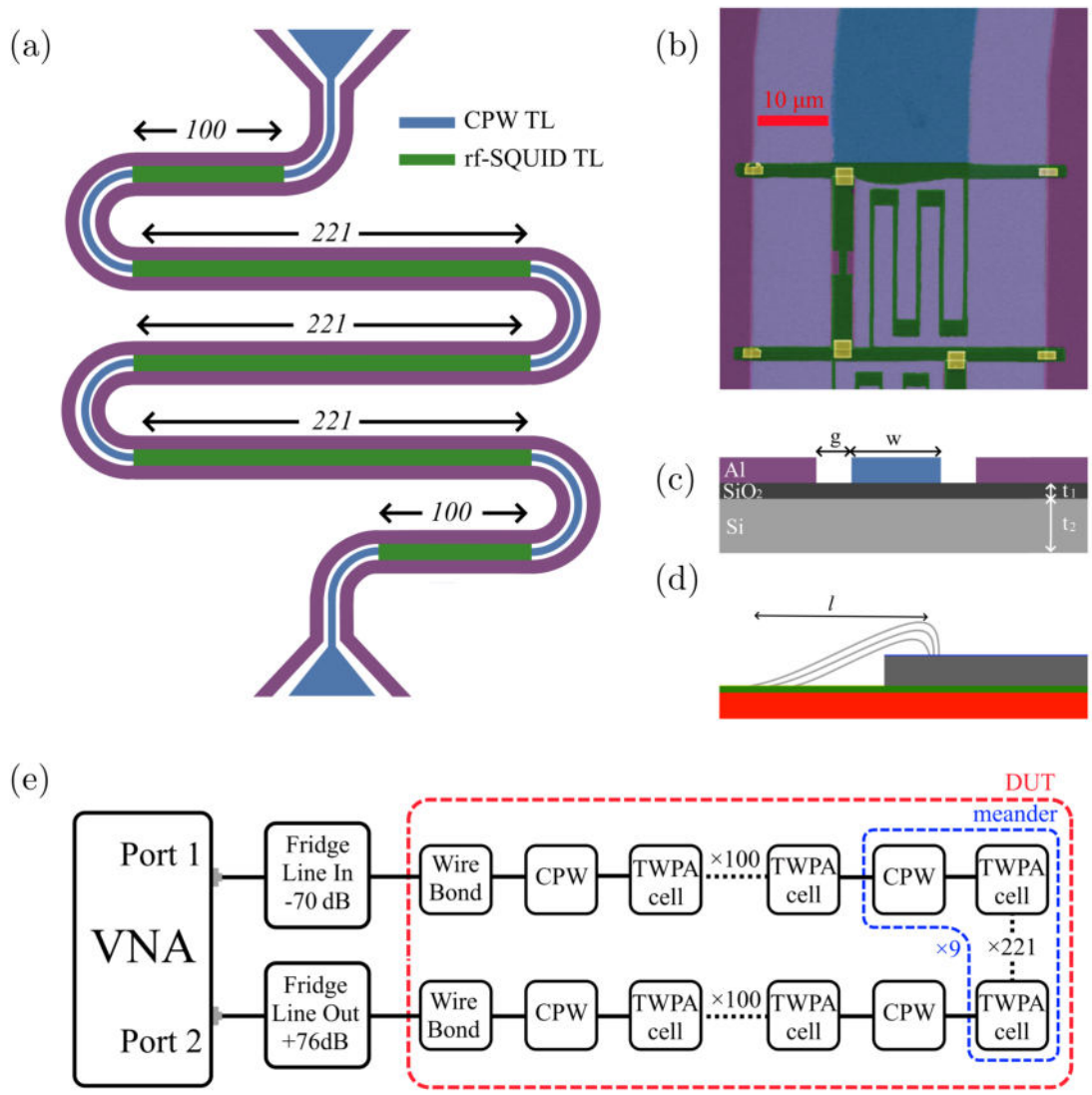

Fig. 4.10 (a) Representative diagram of the JTWPA device under study where lengths of rf-SQUID's (green) are segmented by lengths of coplanar waveguide (blue) to form a meander structure of the device. In reality, the DUT has nine lengths of 221 rf-SQUID's, as opposed to the three shown, for a total of 2189 rf-SQUID cells. (b) False colour SEM image showing the point at which the rf-SQUID lumped element transmission line meets the coplanar waveguide portion of the meander. (c) Diagram showing the stack-up of the device under study which consists of a high-resistivity silicon substrate with a 300 nm layer of SiO_2 on top, followed by patterned layers of superconducting thin films to form the rf-SQUID's and coplanar waveguides. (d) Diagram of the wirebond structures connecting the JTWPA device to test PCB and the measurement system, these bonds will cause some impedance mismatch dependent on their length and quantity. (e) A block diagram of the measurement system including a model of the JTWPA which can be analysed or simulated to understand the transmission through the device better.

Impedance Mismatch

A stack-up of the CPW structure is shown in Figure 4.10 (c), showing that the aluminium layers that form the trace and the ground plane are separated by a distance $g = 12\,\mu m$. The trace width ($w = 20\,\mu m$) has been set so that on a high resistivity silicon wafer, topped with a 300 nm layer of SiO_2, an impedance of $56\,\Omega$ is achieved. The electrical length of each CPW length is approximately 140 GHz, well outside of the measurement range.

The effects of these small impedance mismatches at the points where the rf-SQUID's meet the CPW's are shown in Line B of Figure 4.11. Line A is the transmission of just the JTWPA structure without these additions, and it is clear that these impedance mismatches are the cause of a significant dip in transmission at 6.75 GHz and 7.7 GHz. This aligns with the region of poor phase matching observed in the experimental results relating to harmonic generation and wide band response. This may imply that the device design has accidentally caused the formation of a type of dispersion engineering through the placement of the CPW segments, which could be quite a powerful design tool if it can be harnessed.

To connect the JTWPA device to the measurement circuitry, Al-Si wire bonds are used from the chip to the circuit board, as drawn in Figure 4.10 (d). We can calculate the approximate inductance of a single wire bond, where we assume wire length is equal to the horizontal length, via the equation:

$$\mathscr{L} = 2l\left[\ln\left(\frac{l}{r}\left(1+\sqrt{1+\left(\frac{r}{l}\right)^2}\right)\right) - \sqrt{1+\left(\frac{r}{l}\right)^2} + \frac{\mu_0\mu_r}{4} + \frac{r}{l}\right] . \tag{4.2}$$

The resultant inductance is given in nano-Henries, μ_0 and μ_r are the vacuum and relative permeabilities, l is wire length (~8 mm) and r is wire radius (~25 µm). An inductance of 10.3 nH for a single wire is reduced to a total inductance of ~2.5 nH as four bond wires are used in total [143].

It should be noted that the impedance mismatch at the wire bonds, although not shown here in isolation, causes a large ripple in the device with period equal to ~ 110 MHz. This ripple, which matches the electrical length of the device, is commonly seen in experimental devices and limits the bandwidth of the amplifier. Perhaps an improved packaging method for these devices could limit this and improve device performance.

Losses and Attenuation

As wave mixing is relatively weak in this device, it is expected that parametric attenuation does not play a large role in the total observed attenuation for the experimental data of Figure 4.11. Parametric attenuation would be inversely proportional to frequency as phase mismatch is smaller at lower frequencies, which would display an opposite trend to the observed data.

The attenuation observed in this device must be mostly due to losses occurring within the JTWPA. This attenuation was found to have a value of ~ 4.9 dB/GHz through a least squares fitting algorithm. The apparent behaviour of this transmission spectrum resembles that for a co-planar waveguide, in which dielectric losses accurately describe the behaviour.

Link to ToC

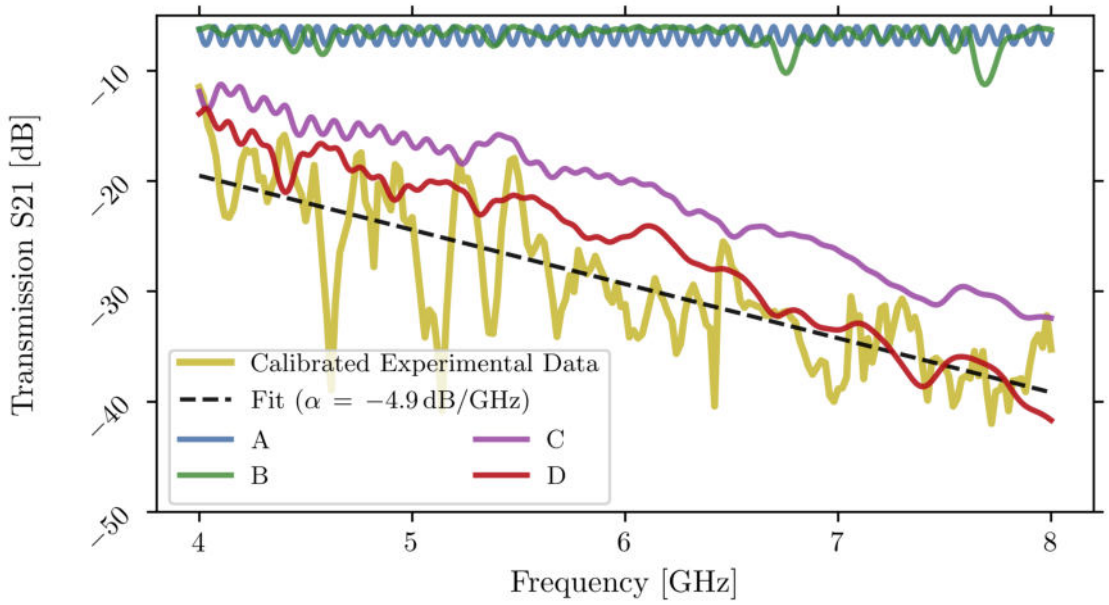

Fig. 4.11 Plots of the simulated measurement system model and the actual experimental data normalised to the system through line (yellow). Improved agreement between the simulated simple JTWPA structure (A) and experimental data is achieved by considering the effects of impedance mismatches at coplanar waveguide segments (B), wire bond impedance mismatches and subgap junction resistance of 160 Ω (C), and cell-to-cell paramerter variation (D). The particular extent of what is considered in each simulation (A-D) is summarised in Table 4.2.

Label	CPW	Wire Bonds	Junction Resistance	Cell-to-Cell Variation
A	×	×	×	×
B	✓	×	×	×
C	✓	✓	✓	×
D	✓	✓	✓	✓

Table 4.2 Summary of the make-up of the simulations presented in Figure 4.11 where the simulations increase in complexity from A to D by considering the effects of impedance mismatches at the wire bonds and coplanar waveguide segments of the JTWPA device. Subgap junction resistance is also considered as well as random cell-to-cell variation of the circuit parameters in the lumped element transmission line lenghts.

The loss tangent of the dielectric, δ, can be related to the attenuation coefficient, α, via

$$\alpha\ [\mathrm{dB/GHz}] = 8.686\,\frac{\omega C Z_0}{2}\tan(\delta)\ , \tag{4.3}$$

where the attenuation (in deciBel per gigahertz) is a function of the angular frequency, ω, capacitance per unit length, C, characteristic impedance of the CPW, Z_0, and the loss tangent of the substrate [115].

Some have used this model to describe the behaviour seen in TWPA devices, although I would argue that this not accurate for a lumped element transmission line where the fields do not penetrate the substrate in the same way as in a continuous structure [137, 138]. In the case of the JTWPA, the electric field is confined to the region of the lumped element capacitors, which should confine dielectric losses to occurring mostly in these small areas. For an attenuation commonly observed in TWPA devices in the range of 1 - 5 dB/GHz, a loss resistance of $< 5\,\mathrm{k}\Omega$ shunting the ground capacitance would be required. This is not likely for a number of reasons, first being that the dielectrics grown in nanofabs are generally of much higher quality that this. Furthermore, it has been demonstrated in Chapter 3 that such a loss would result in no amplification in even a relatively good amplifier (although apparent gain may still be present). Finally, the behaviour in frequency would not match what is observed. We would expect losses to follow the trend of the ratio of the loss resistance to the reactance of the capacitor: $R/\omega C$, inversely proportional to frequency and again, opposite to the observed trend.

I hypothesize that the observed attenuation has three components, two of which are small in this device (dielectric losses and parametric attenuation) and a larger contribution due to the subgap resistance of the Josephson junctions used. The losses then would be expected to follow the ratio of the reactance of the inductance to the junction resistance: $\omega L/R$, directly proportional to frequency. This nicely explains the transmission spectrum observed, and in the case of this device, a shunt resistance of approximately $160\,\Omega$ accounts for the attenuation as is shown in Line C of Figure 4.11. This matches closely the expected quasi-particle tunneling resistance of the junction at low temperatures, which should have increased from the room temperature measurement by ~36% [144].

Cell-to-Cell Random Variations

The effects on amplification of random variations of the circuit parameters in each cell of the transmission line were shown in Chapter 3. We now investigate whether these variations might explain the choppiness of the collected transmission data. For a standard deviation of 10 % in each parameter in each cell the result of line D is achieved. This appears to agree slightly better with the experimental results, but is still some distance off. It is possible that the variation present in the circuit parameters of the device is even larger than simulated, although it is equally possible that this choppiness is due to other effects related to the through line used for calibration.

At this point we have reproduced, to a reasonable degree, the experimental data of the transmission spectrum for this device using a rather fast and reliable simulation technique in WRspice. There is some remaining disagreement in terms of offset of the simulation versus experimental data which can be explained quite easily by an impedance mismatch caused by a deviation from the design values of the geometric inductance, smaller capacitance to ground or both. This could very well be caused by the parasitic coupling of neighbouring geometric inductances, which was calculated in Chapter 3 to possibly be as high as 15% for this design. Instead of chasing such minor details, it is now more useful to investigate the effects of flux biasing and wave mixing on the transmission through this device.

Link to ToC

4.5.3 Simulated Effects of Flux Bias

We have purposely neglected the effects of wave mixing so far as they complicate the understanding of the device in simulation. Fortunately, we can build and simulate circuit models that separate the nonlinear from the linear effects and so resolve the processes from each other. We do this using two different simulation techniques, both in WRspice, to first analyse the effects of impedance mismatches/losses and wave mixing in isolation before investigating the effects of all at once.

Impedance Mismatch

To isolate the effects of impedance mismatches and losses in the device, a linearised circuit model is created where the rf-SQUID is replaced with an equivalent inductance for a given flux bias. This model can be simulated in AC analysis of WRspice in the same way as was done in the previous section. This allows for data on transmission across two flux periods to be collected quicker compared to the transient analysis of WRspice.

The results of this simulation are shown in Figure 4.12 (a) where the transmission S21 is shown in decibel over two flux periods. Interestingly, this is essentially the inverse of the expected shape, as where one would expect to see maximum transmission at the optimal 3WM bias points we instead see a minimum. While perplexing at first the reason becomes clear when you consider the losses branch in the circuit. At the 3WM bias point, the SQUID equivalent inductance is largest and so the losses through the subgap resistance are also at a maximum[9]. This effect can obviously be minimised in a device where the impedance of the subgap resistance is much larger than the impedance of the SQUID equivalent inductance at all frequencies of interest: $R_{sg} \gg \omega L_{SQUID}$.

Wave Mixing

The effects of wave mixing on transmission can be analysed in isolation using a transient simulation in WRspice, in which losses are omitted and the JTWPA array is terminated with an impedance matched to the characteristic impedance at the operating flux bias. The results of this are shown in Figure 4.12 (b) where we again see a minimum in transmission at the optimal 3WM bias point. As has been discussed in the previous chapter this is due to parametric attenuation having the largest effect when wave mixing is maximised, i.e. in 3WM regime.

As the wave mixing effects are rather weak in this device, the parametric attenuation is not as large as for the theoretical device of the previous chapter. Still, despite the weaker effects, an apparent gain of $\sim 14\,\mathrm{dB}$ is achieved if the transmission of the signal with Pump ON versus Pump OFF is compared, importantly the true 'gain' is $\sim -2\mathrm{dB}$.

[9]This may also explain the difficulty in demonstrating 3WM in a SNAIL based JTWPA despite the successes seen in the 4WM regime.

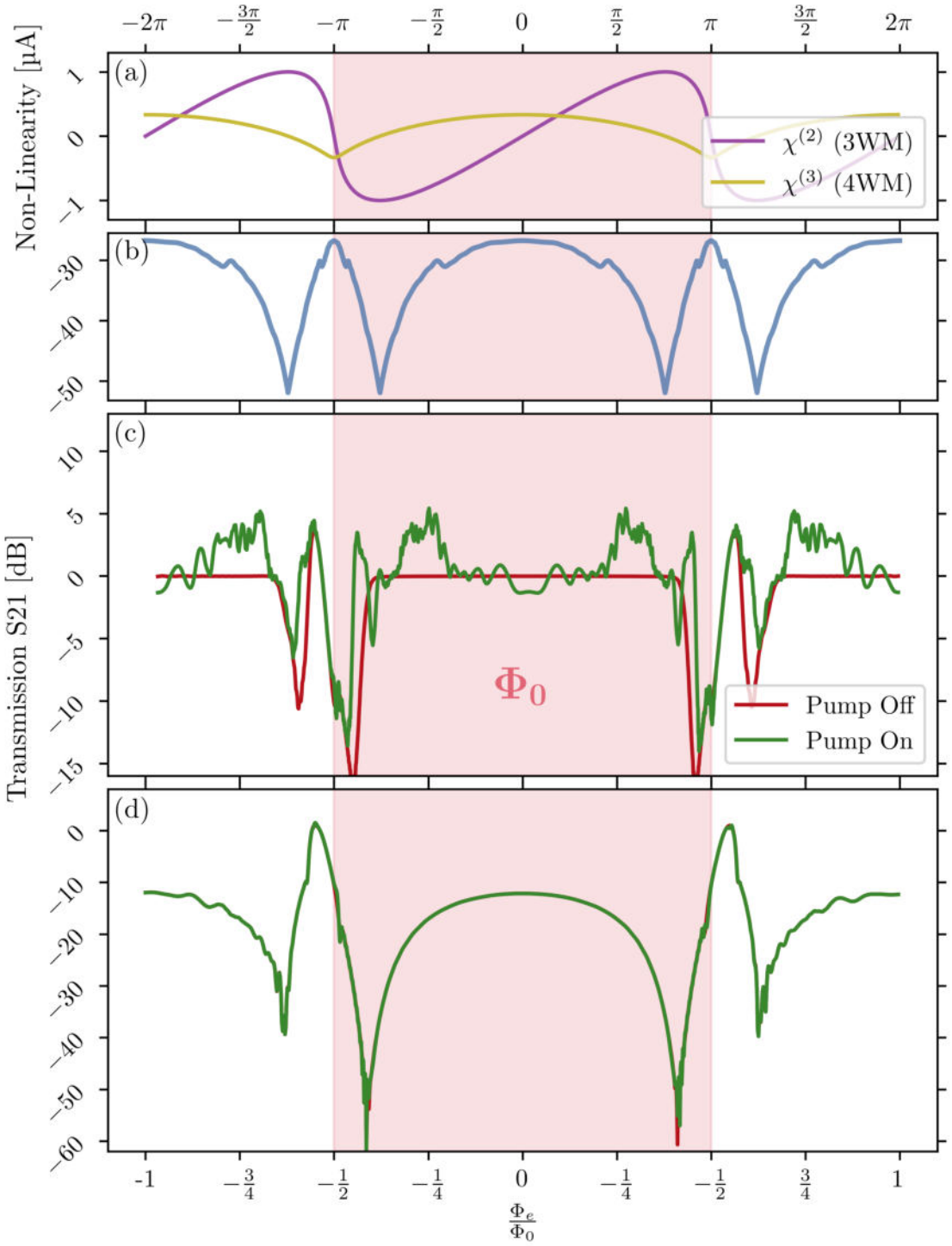

Fig. 4.12 Simulation results for the model of the measured device. (a) Strength of the 3WM and 4WM nonlinearities in this device over two flux periods. (b) Transmission versus flux for a signal frequency of 7.2 GHz in a lumped element transmission line absent of any nonlinearity such that any change in transmission is solely due to change in total inductance per cell of the device. (c) Transmission versus flux simulation takes into account only the wave mixing effects on transmission at most biases. However, the > 0 dB transmission at the $\varphi_e = \pi$ bias points are due to standing waves in the device caused by the poor impedance matching to the negative Josephson inductance at these points. (d) Transmission versus flux simulation that includes the effects of impedance mismatches, losses and wave mixing. As is evident, it is essentially the sum of the previous plots although the effects of impedance modulation and losses appear to drown out the effects of wave mixing in this device.

Link to ToC

Combined Effects of Impedance Mismatches, Wave Mixing and Losses

Shown in Figure 4.12 (d) is the combined effects of the impedance mismatches, losses and wave mixing on the transmission through the device, analysed using a transient simulation in WRspice. We see now that the effect of a pump on the transmission is negligible meaning there is no amplification in the device. We can also say that the shape of the transmission curve as a function of flux is similar to the experimental data of Figure 4.4. This indicates again that the model built in this analysis is a good match for the actual device.

Key to this agreement is the inclusion of losses via the subgap resistance in the simulations. Without this the shape of the transmission against flux curve is less rounded and has a sharper decline at the 3WM bias points. While the contribution of the parametric attenuation ($\sim -15\,\mathrm{dB}$) should be zero when a pump wave is applied, the attenuation due to losses remains. Given that this is on the level of $-20\,\mathrm{dB}$, without first tackling this problem by improving junction quality an amplifier would have to produce 40 dB of signal amplification to have 20 dB of output gain. The task of building such amplifiers is already difficult enough without this complication.

The maximum in transmission at $\varphi_{dc} = \pi$ is due to an interesting and often neglected effect. The Josephson inductance at this point is simultaneously at a minimum and is negative, putting the total inductance of the rf-SQUID at a maximum of 682 pH. The characteristic impedance is therefore badly matched to the measurement circuitry, and by extension any simulation that uses the absolute value of the Josephson inductance. This effect may make this type of rf-SQUID chain, often only thought of for applications in 3WM, as a useful scheme for 4WM as well.

4.5.4 Gradiometric Effects

Gradiometric effects may come about in these devices in a number of ways, the most obvious being the effects of a slowly varying resist thickness that forms the mask for the layers of aluminium to be deposited. This effect can then be regarded horizontally (parallel to the rf-SQUID lengths), vertically (perpendicular to rf-SQUID lengths), or both.

These effects have been simulated in WRspice with the results for the perpendicular gradiometric simulation shown in Figure 4.13 (a). The geometric inductance in every set of 200 rf-SQUID's was increased by 6% from 15% below to 15% above the design value. As the WRspice simulation is limited to 1200 rf-SQUID's this makes for a total of 6 rows similar to the 11-rowed meander of the measured device. Only the geometric inductance is varied for simplicity as the intention is to show the effects of overlapping flux periods, in reality critical current would also follow the same gradiometric trend.

As can be seen the maximum that was a sharp peak in the previous simulations has split into a set of 6 peaks, marked with stars. This makes clear the slight offset of the maximum due to the smaller or larger flux periods for each row. We can see that this result now better agrees with the experimental data due to this peak splitting. In fact, if we follow this logic we can say that the measured device has three distinct geometric inductances in different regions as its maximum splits into at least three peaks.

It should be noted that horizontal gradiometric variation (parallel to the axis of the SQUID chain) does not lead to this same effect as the geometric inductance does not have six discrete values but instead a gradient of values along each row. The peak for this type of variation, as shown in Figure 4.13 (b), does not split in such a way, although further features do appear. The case of perpendicular variation seems to match the observed effects in the experimental results a little better, but both types of variation are likely to be present to some degree.

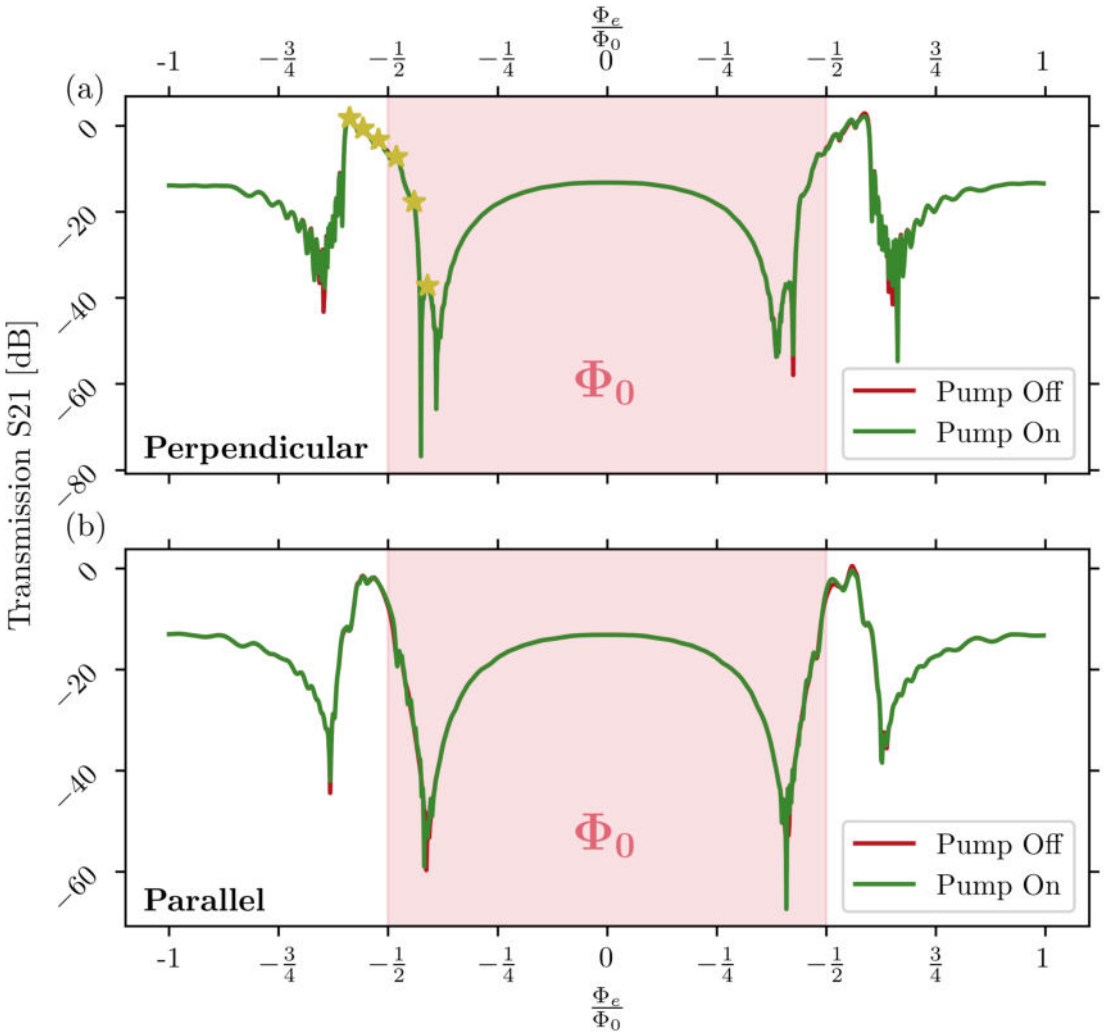

Fig. 4.13 Simulation results for the model of the measured device. Transmission versus flux for a signal frequency of 7.2 GHz in a lumped element transmission line where the geometric inductance per cell has been linearly changed from −15 % to +15 % of the design value, perpendicularly (a) or in parallel (b) to the axis of the rf-SQUID portions of the transmission line meander. The difference between Pump On and Pump off is almost imperceptible due to the large losses in this device.

Link to ToC

4.6 Conclusion

This chapter has presented experimental data for a first generation Josephson travelling wave parametric amplifier device. The device was designed to have a characteristic impedance of 50 Ω to match the measurement environment, with a hysteresis parameter, β_L of 0.89 to ensure that no rf-SQUID in the device would be hysteretic. The aluminium based Josephson junctions used had a critical current, I_c of 2.2 µA corresponding to an on-chip power of approximately −66 dBm. A series of simulations built on a comprehensive model of the measured device have accurately reproduced key results of the device characteristics, including its transmission spectrum and response to an applied flux.

Transmission through the device shows a significant attenuation of probe signals of about -4.9 dB/GHz. The most likely cause for this loss was determined to be a shunt resistance across the Josephson junction with a value 160 Ω, which matches closely the expected quasi-particle tunneling resistance for these aluminium tunnel junctions. The appearance of these losses implies a higher than expected quasi-particle population in the device, the root cause of which is not fully explored in this chapter. This effect may explain the difficulty faced by groups in achieving 3WM in SNAIL based transmission lines despite previous successes with 4MW, as at the 3WM bias point losses in this branch will be at a maximum. Modulation of S21 parameter was achieved by flux bias with periodicity evident in both magnitude and phase of the received signal. A single flux period corresponded to a bias voltage change of 2.04 V, asymmetry seen in the period of the S21 magnitude makes this straight forward to identify. This asymmetry of S21 period was explored in simulation with the most likely cause being a gradiometric change of the geometric inductances in the transmission line circuit. The S21 phase shift data proved to be simpler to match to an analytical model, that was then useful in determining the optimal 3WM bias voltage of 2.455 V with a flux offset of approximately $0.7\,\Phi_0$. This value matches well with the alternate method of identifying the optimal 3WM bias point by finding the bias at which the 3WM idler has a maximum in amplitude. The same bias point in S21 magnitude shows a minimum instead of the maximum that would be expected from perfect impedance matching. This is due to the increased effect of the junction resistance on transmission at this bias where the junction inductance is approximately infinite.

The required three wave mixing processes for weak signal amplification were confirmed to occur in the device by the analysis of a generated 3WM idler tone and its response to flux bias. Apparent gain of the signal tone of ~ 10 dB was also observed in VNA traces comparing transmission with pump off and on in the device at some flux biases. However, this change in signal transmission was determined to be most likely due to the modulation of impedance and losses in the circuit and not any significant amplification. A transient analysis in WRspice on an idealised model of the device showed that, without any other mitigating circumstances, the amplification of a signal was limited to less than 1 dB due to the large phase mismatch between the pump, signal and idler waves.

The close agreement between simulations of the device model developed in this chapter and the experimental results allows us to verify the application of the WRspice and CME simulation tools developed in this thesis for applications to as-of-yet unrealised devices. Furthermore, the details extracted from the experimental results using these tools have allowed us to determine a preferred method for locating the optimal 3WM bias point, associating losses in the device to a subgap resistance and explained the absence of the expected amplification by the presence of a large phase mismatch between the mixing waves. This allows us to design better devices in the future with a higher cut-off frequency to minimise phase mismatch, and a larger quasi-particle tunneling resistance.

Link to ToC

Chapter 5

Characterisation of a Niobium based Josephson Travelling Wave Parametric Amplifier

5.1 Introduction

The device presented in this chapter is another first generation JTWPA, although it has some key differences from the previous design that make the results presented here particularly interesting. The characterisation of this device follows much the same approach as that of the previous, with particular attention paid to the generation of harmonics and losses in the device. This device has been shared with us by collaborators from Physikalisch-Technische Bundesanstalt (PTB), Ralf Dolata, Christoph Kißling and Alexander Zorin, as part of the Joint Research Project 17FUN10 ParaWave of the EMPIR Programme. The fabrication of the device was carried out in PTB using the wafer-scale niobium tri-layer process developed there, while experiments were carried out in Lancaster between December 2022 and April 2023.

Initial tests on this device sought amplification, as was the intention of the project. However, it became apparent from our own measurements and simulations, as well as the work of others, that these first generation devices were not optimised to produce significant gain. Further work was carried out to characterise the dynamics of the superconducting circuit with the goal of extracting circuit parameters. To this end, the response of the device to input wave power and applied dc bias via transmission and harmonic generation measurements was recorded, the data was analysed and compared to expected results from theory and simulation. Key differences are addressed and discussed, with particular attention paid to the apparent losses in these JTWPA devices and the relation to both parametric attenuation and quasiparticle generation.

Link to ToC

This work improves the understanding of these devices, providing key details for the further development of the artificial transmission lines for applications as amplifiers and in basic science. This work also informs the design choices made for TWPA proposals presented later in this thesis, aiding not only dispersion engineering choices but also in suggesting fabrication processes.

5.2 Device Design

There are a few key differences between the design of this device and the previous device, the first and most apparent being the number of rf-SQUID's between neighbouring ground capacitances. This changes from one in the previous design to six here, which is quite a clever alteration that overcomes a fundamental constraint of the rf-SQUID based transmission line. As we wish to keep the hysteresis parameter, β_L, below 1 it becomes a set variable and the critical current is now indirectly proportional to the geometric inductance of the SQUID. Therefore, using a larger critical current due to fabrication constraints or a desire to improve dynamic range, limits the maximum geometric inductance and therefore increases the cut-off frequency of the transmission line.

As has been discussed earlier in this thesis, a higher cut-off frequency may actually be beneficial to some amplifiers, although it is certainly a design constraint that can be a hindrance. By using several series rf-SQUID's per cell, the hysteresis parameter can be kept near unity and the total geometric inductance can be increased thereby decreasing the cut-off frequency while maintaining 50 Ω impedance. A major downside of this approach is that the physical size of a given cell increases. This means that even though the physical length of the device is similar to the device in the Chapter 4, its electrical length is much shorter. The transmission line circuit parameters used for this device are summarized in Table 5.1 while the physical structure takes the form of a meander as shown in Figure 5.1 (a). The green lengths along the horizontal represent rf-SQUID chains for which a micrograph of the physical device is provided in Figure 5.1 (b) and its equivalent circuit diagram in (c).

Another important change is that the niobium tri-layer process developed in PTB for wafer scale production of superconducting circuits has been used to produce this device.

Transmission Line Parameters							
L_G [pH]	L_6 [pH]	C_G [fF]	Z_π [Ω]	f_c [GHz]	$\#_{arm}$	$\#_{cell}$	$\#_{SQUID}$
27	170	68	50	47	17	272	1632

Table 5.1 The design parameters of the transmission line including geometric inductance per rf-SQUID, L_G, inductance per cell, L_6, return capacitance per cell, C_G, as well as the expected impedance for 3WM operation, and the cut-off frequency of the transmission line. The number of lengths of rf-SQUID chain are also given, alongside total number of transmissision line cells and total number of rf-SQUID's.

Link to ToC

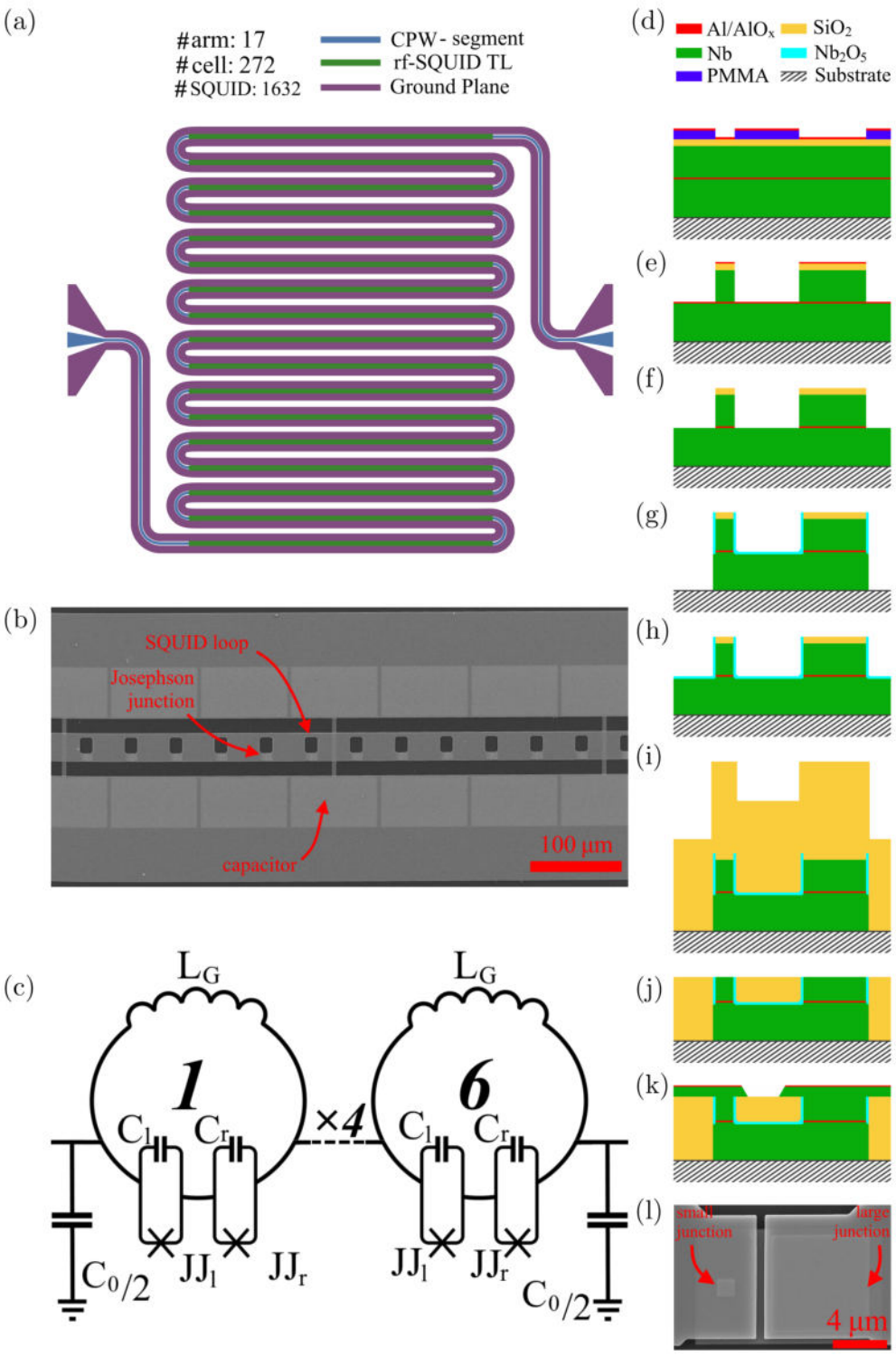

Fig. 5.1 (a) Diagram of the meander structure of the JTWPA device where horizontal rf-SQUID chains (green) are interspliced with lengths of continuous transmission line (blue), both of which are capacitively coupled to the ground plane (purple) to produce a lumped element co-planar transmission line. (b) Micrograph of the JTWPA structure where sets of 6 rf-SQUID's are separated by capacitances to ground. (c) Equivalent circuit diagram of a single unit cell of the rf-SQUID based transmission line, where two junctions are present per SQUID. (d-k) Diagram of the fabrication process of the Josephson junction based superconducting ciruits (description in text) as developed by PTB [145]. (l) Micrograph of the Josephson junction elements in each rf-SQUID where both a small junction and a large junction (which is normally ignored in analysis) are shown.

Link to ToC

This process offers a remarkable improvement in consistency and predictability compared to the lift-off processes commonly used for the aluminium tunnel junction devices in research laboratories. The fabrication process for this device is shown in the diagram of Figure 5.1 (d-k), as reported in [146] and adapted from the description given in [145]. First a niobium - aluminium (Al_2O_3) - niobium - silicon dioxide sandwich is deposited on a substrate, after which a lift-off process is used to deposit a patterned aluminium film for use as an etch mask (d). A fluorine based etch then removes the SiO_2 and niobium down to the aluminium layers (e), an argon ion etch is then used to remove the remaining exposed aluminium (f). The metal is then anodized (g) growing a layer of oxides on the niobium (supposedly Nb_2O_5) which protects the junction from aging and has been said to decrease sub-gap leakage currents i.e. produces higher quality junctions. A thick SiO_2 layer is grown by PECVD (i) which is then removed by chemical mechanical polishing (CMP) to expose the tops of the niobium electrodes (j). After an argon clean more niobium is deposited which can then be patterned and etched leaving the desired tunnel junction structure (k). Importantly, this process produces two junctions in series on the lower electrode as is shown schematically in (k) and in an SEM image of the actual device in (l). Given that the small junction area is $\sim 1.5625\,\mu m^2$ while the large junction area is $\sim 49\,\mu m^2$ this design choice, made simply to avoid more complex fabrication, was thought to be unlikely to effect device performance as the nonlinearity of the large junction is quite weak. It will be shown later in this chapter why we believe the presence of this junction can significantly hamper the performance of this device.

Only a critical current value was provided for the smaller junction, although a value of junction capacitance is estimated from the information given in [145] ($C_j = 60\,fF/\mu m^2$) and normal state resistance estimated from the Ambegaokar-Baratoff formula given below [147].

$$I_c = \frac{\pi}{2e}\frac{\Delta(T)}{R_n}\tanh\left(\frac{\Delta(T)}{2k_BT_c}\right) \tag{5.1}$$

Here I_c is the junction critical current, R_n is the normal state tunneling resistance, T_c is the superconducting transition temperature and T is the operating temperature. Using a transition temperature found from experiment to be approximately 8.6 K, the normal state quasiparticle tunneling resistance is found and the important parameters for both junctions are summarised in Table 5.2.

It should be noted from Equation 5.1 that the critical current depends on the superconducting energy gap of the terminal superconductors, which itself depends on

Junction Parameters					
Small			Large		
I_c [µA]	R_N [Ω]	C_j [fF]	I_c [µA]	R_N [Ω]	C_j [fF]
10	170	93.75	314	5	2940

Table 5.2 Expected parameters of the Josephson junction elements present in each rf-SQUID element of the transmission line. Each parameter is estimated from the designed junction size and provided critical current estimation for the smaller junction.

Link to ToC

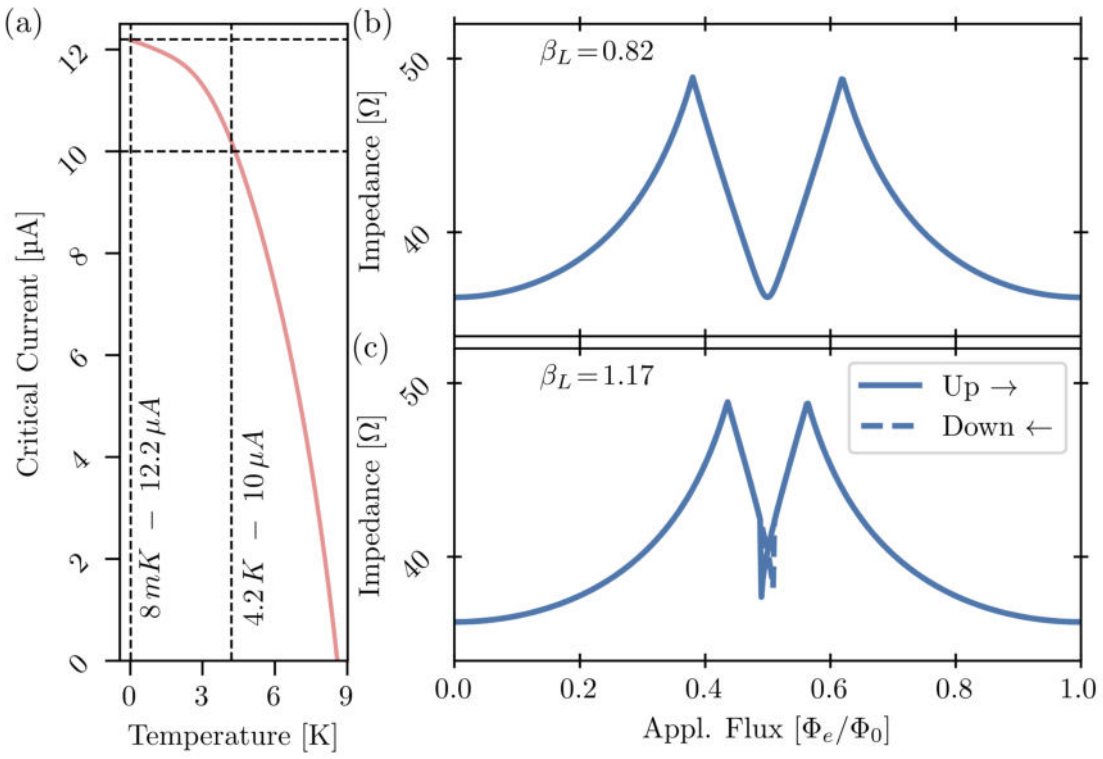

Fig. 5.2 (a) Plot of the expected critical current value using the expected value of 10 µA for the smaller junction at liquid helium temperatures, and the measured value of transition temperature. (b) The impedance versus applied flux relation for the designed device when operated at 4.3 K and (c) at 8 mK.

the measurement temperature as described by the equation:

$$\frac{\Delta(T)}{\Delta_0} = \tanh\left(1.74\sqrt{1-\left(\frac{T}{T_c}\right)}\right). \tag{5.2}$$

Δ_0 being the superconducting energy gap at zero temperature [148]. This relation between critical current and temperature is plotted for this niobium junction in Figure 5.2 (a). The expected critical current at 4.2 K that produces a hysteresis parameter of $\beta_L = 0.82$ is extrapolated to 8 mK to find a critical current >14 µA and $\beta_L = 1.17$. As a result, the rf-SQUIDs of the transmission line will be hysteretic when operated at the base temperature of a dilution refrigerator. The expected impedance relationships for the transmission line are then shown in Figure 5.2 (b) and (c) for the 4.2 K and 8 mK temperatures, respectively. Although there is hysteresis at the lower temperatures, we expect it to be small and perhaps not very noticeable for these estimated parameters. Should the hysteresis be considerably larger than expected, it will be clear by the behaviour of the local minimum at the half flux bias point, which becomes smaller and less distinct with increasing β_L.

Link to ToC

5.3 Experimental Apparatus

This device was first characterised at a temperature of 8 mK in December of 2022 and then again at 4 K in March of 2023. The attenuation of the fridge input lines was organised to minimise the number of thermal photons that may reach the device. Although, the total attenuation and distribution of attenuators was changed between the first and second cooldown, as summarized in Table 5.3.

Attenuation				
Temp.	December 2022		March 2023	
	Signal	Pump	Signal	Pump
50 K	1 dB	1 dB	3 dB	3 dB
4 K	-	20 dB	3 dB	3 dB
700 mK	26 dB	20 dB	6 dB	6 dB
~ 300 mK	11 dB	9 dB	20 dB	20 dB
~ 10 mK	-	-	20 dB	20 dB

Table 5.3 Summary of the attenuation used at each temperautre stage in the December and March cooldowns on both the signal and pump input lines. The temperatures stated are just the standard names of the plates at which the attenuators were mounted, in fact for the March cooldown there was no plate cooler than 4 K.

Following the example of Krinner *et al.*, the attenuation on the coldest plates was increased as the thermal load is not a significant constraint for a single input line [141]. The total cryogenic attenuation was kept relatively low at ~ 50 dB to allow for a large power range to be used in the experiments. An additional 4 - 8 dB drop in signal power may also result from the SMA input cables due to reflections and attenuation, furthermore measurements using the signal line experience an additional 20 dB reduction in power due to the directional coupler[1].

The rest of the experimental set-up remained the same between the two runs, using bias tees[2] on either side of the device to add direct current through the transmission line. A triple junction isolator [3] on the output lines is included to dampen any noise and reflected waves from the HEMT amplifiers [4] that provide a total of ~76 dB amplification. A diagram of the cryostat for the March 2023 experiment is shown in Figure 5.3 where the order of these components can be clearly seen.

Transmission measurements have been the focus of these experiments with particular interest on the effects of dc bias on S21 and harmonic generation, although a few two tone spectroscopy measurements were also run to seek amplification. Transmission datasets have been collected on an N9030A Spectrum Analyser and an E5071C Vector Network Analyser which may also be used as an rf source in addition to an E8257D Signal Generator, all of which were produced by Agilent. A dc bias was provided through an Agilent 33521B voltage source, which was paired with a Keithley 2000 ammeter in some measurements to record the current drawn.

[1] Pasternack - PE2CP000-20
[2] Marki Microwave BT0018
[3] Low Noise Factory - LNF-ISISISC4_12A
[4] Low Noise Factory - LNF-LNC1_12A s/n 764B & LNF-LNC1_12A s/n 761B

Link to ToC

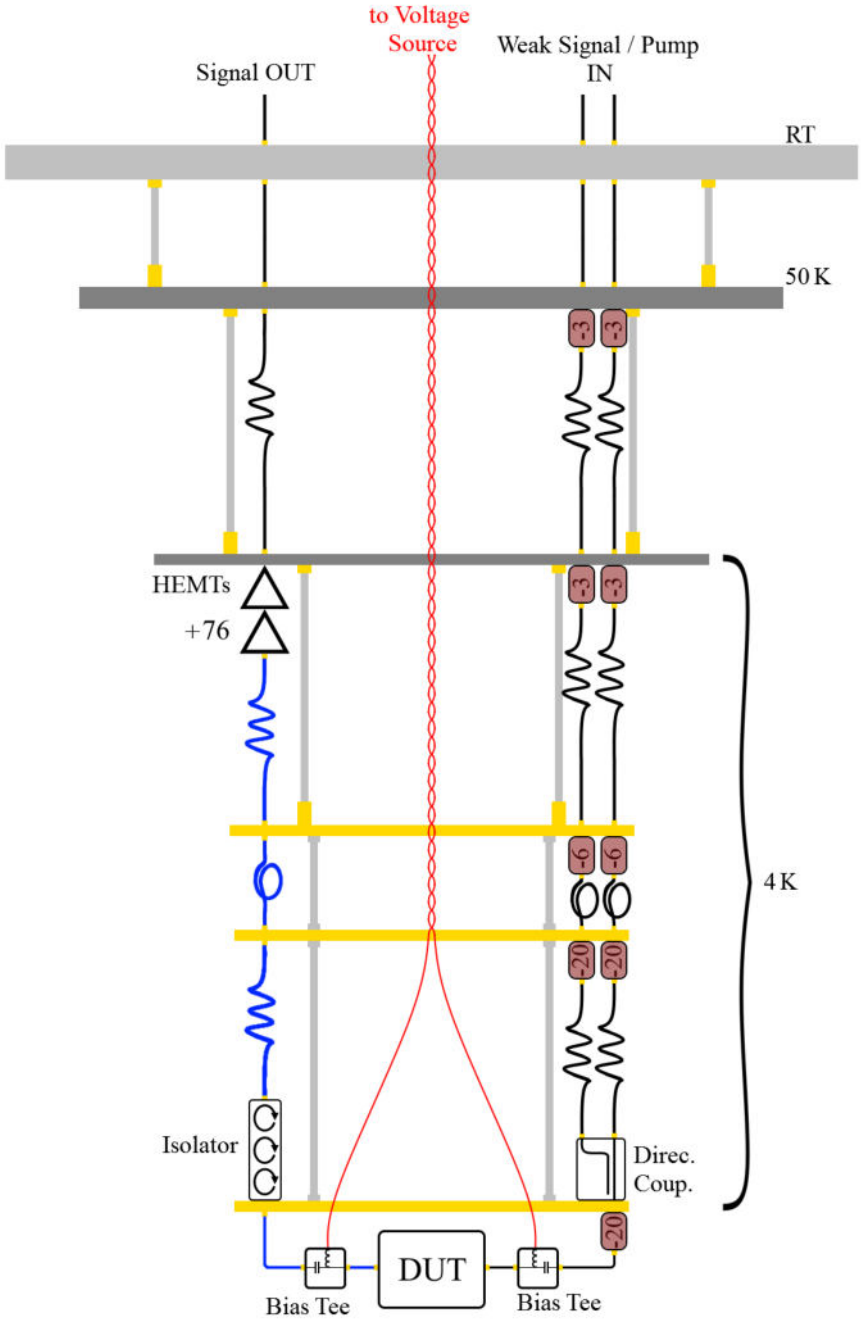

Fig. 5.3 Cryostat diagram for the March 2023 cooldown in which all lower plates are held at 4 K while a total of 52 dB cryogenic attenuation is added to both lines, alongside a directional coupler on the signal line which reduces its input power by a further 20 dB. A dc bias can be applied to the device via a pair of bias tees located on opposing ends of the JTWPA, which are followed by an isolator to prevent any backward travelling waves from higher temperatures on the ouput line. A pair of HEMT amplifiers that should provide about 76 dB amplification in our measurement range of 4 - 12 GHz are the final cryogenic devices before the signal leaves the cryostat to room temperature measurement instruments. Coaxial cables coloured blue indicate segments where supercoducting cabling was used to minimise losses.

Link to ToC

5.4

December 2022 Measurement

The overall measurement goal for this device was to observe spontaneous parametric down conversion (SPDC) and to characterise harmonic generation. SPDC may refer to either the amplification of a weak signal by a strong pump or by the splitting of a pump photon into two photons of half the pump frequency. Either effect would be useful in metrology, obviously as an amplifier or as coherent photon source [7, 149, 150].

To begin, these preliminary measurements were performed at the base temperature of the dilution refrigerator of approximately 8 mK. These measurements served to confirm transmission of a signal through the device and the modulation of the transmission by the application of a voltage bias. While some weak degenerate 3WM amplification has been seen in these measurements, the main takeaway is the introduction of the measurement and analysis techniques used to characterise the device in the next cool down.

5.4.1 Wideband Transmission

A wideband transmission measurement on a vector network analyser remains the first and most useful measurement on these JTWPA devices. As well as a useful check that the device is properly connected in the first place, it also gives an idea of losses by the gradient of S21 magnitude in frequency and a check for any resonances which may then be used for measurement, as described in [125].

Presented in Figure 5.4 is the collected transmission data through the signal line with additional room temperature attenuation of 40 dB. A clear negative gradient is present, signifying losses in the TWPA device which are assumably due to a shunt resistance across the junction, as with the previous device. With a gradient found to be -2.2 dB/GHz, we can approximate that the shunt resistance lies in the range 20-60 Ω. Of course this assumes that the resistance itself does not change with flux bias, but this is tested in simulation later.

It appears that the trend is not perfectly linear in this case as higher frequencies are not as well fit. This may be a sign that there is at least some portion of losses originating from a frequency dependent resistance such as shunt resistance over the capacitive structures or a ‘parametric resistance’. A parametric resistance which accounts for the power lost in a single tone spectroscopy measurement due to the generation of harmonics in the device may play a significant role in the case of a strong nonlinearity.

Multiple features that resemble resonances are apparent in this spectrum but determining what may be a resonance within the device and what is due to the cabling is not necessarily straightforward. It was observed that none of the sharper troughs changed frequency significantly with an applied dc bias meaning that the most distinct features are likely artefacts of the experimental setup. This type of feature may be useful if present within a JTWPA device as it could be employed for dispersion engineering and reproducing some previous results on similar devices [146]. However, it seems that if any such internal

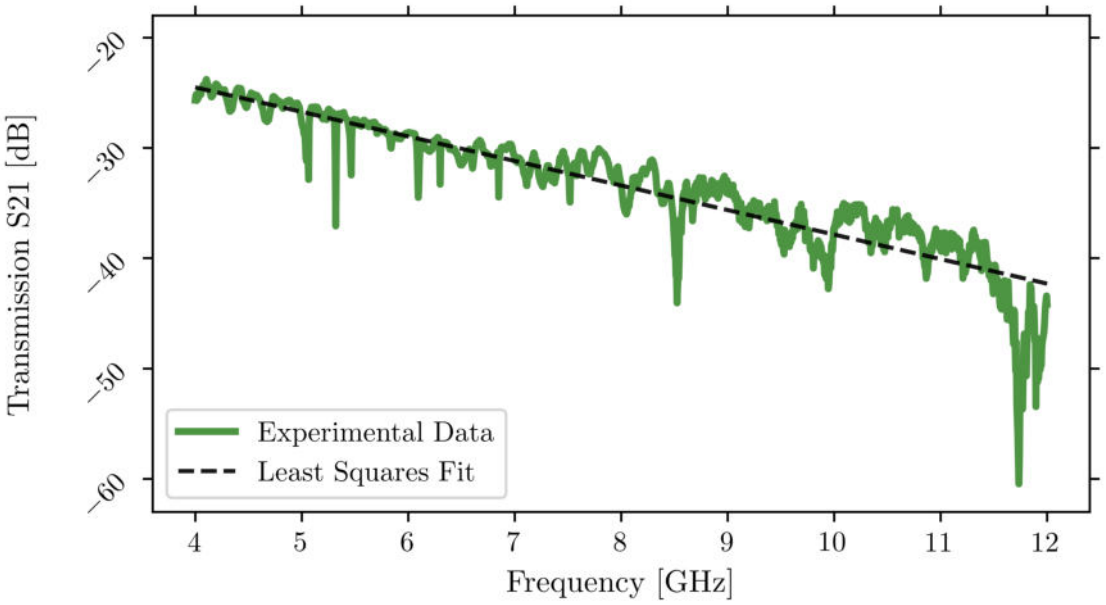

Fig. 5.4 Transmission magnitude through the JTWPA device at 8 mK over a frequency range of 4 GHz to 12 GHz. The clear negative gradient implies losses occur within the device, a least squares fit provides a gradient value of -2.22 dB/GHz with an intercept of -15.6 dB due to a mismatch between total attenuation and total amplification in the measurement setup.

resonance exists within the artificial transmission line then its width must be quite large, limiting its usefulness and making it difficult to identify.

5.4.2 Flux Modulation

This measurement was taken by performing a frequency sweep on a VNA at a given bias voltage. Presented in Figure 5.5 (a) and (b) are the S21 magnitudes versus applied voltage for a 7 GHz tone extracted from this data at two different dc bias ranges. The clear periodic behaviour confirms the presence of the Josephson nonlinearity with the shaded red regions covering a single voltage period. This can be related to the single flux quantum via the ratio of the resistance of the biasing circuit to the geometric inductance of a single rf-SQUID.

Although both datasets are taken from the same measurement there is a clear difference between their shapes, a situation which is repeated at other frequencies. This may be due to trapped flux or a gradiometric dependence of geometric inductance. This would lead to the flux periods of different SQUID's overlapping in certain ranges of applied voltages producing a larger effect on the S21 magnitude. As the behaviour at biases close to −1 V have greater distinction, we use this range for further analysis.

From measurements in the previous chapter we know that periodicity in phase can be more easily understood than that for magnitude. The periodicity in both magnitude and phase for a 7 GHz tone can be compared for this device using Figure 5.6 (a) and (b). The periodicity in phase is much more difficult to fit to the expected inverse cosine shape this time, mainly as the expected single peaks in phase at the optimal 3WM bias points seem

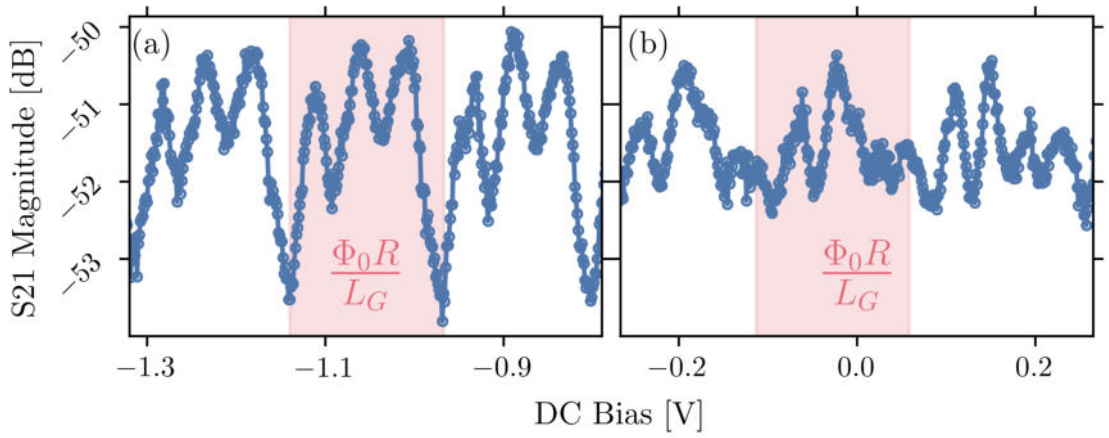

Fig. 5.5 S21 magnitude for a probe signal at 7 GHz at two different dc bias ranges between −1.3 to −0.8 V in (a) and −0.25 to 0.25 V in (b). This shows the changing shape of transmission period depending on bias range. The shaded red region shows a single flux period, equivalent to approximately 0.17 V.

to have split into three peaks. This may be another product of gradiometric dependencies as discussed in Chapter 4 or inductive coupling between SQUID's as described in Chapter 3 and will be revisited later in this chapter.

The assumed optimal 3WM bias point can be identified by the minimum in magnitude and maximum in phase curves as has been argued in Chapter 4, and these are seen to coincide relatively well for this device. The change in gradient of transmission magnitude over a flux period may also indicate the effect of the wave mixing and be used to determine the 3WM bias point which would be expected to coincide with the largest losses. However, the minima in gradient do not coincide with the previously described markers which have already been shown to be a useful determinant of the optimal 3WM bias point. It seems likely that this is an effect caused by the circuit design in this case. So despite its superior fabrication process compared to the previous device, this more complex circuit has actually provided additional complications that make the analysis more difficult.

5.4.3 Weak Amplification

Comparing a single tone transmission spectrum to another that had a pump tone simultaneously applied at 10 GHz, we can identify any amplification that may take place in the device. For a signal input at ~ −112 dBm and a pump input at approximately −72 dBm, an optimal bias for apparent gain of around −1.1 V, marked by the purple band in Figures 5.6 (a), (b) and (c), was found. The difference in transmission between Pump ON and Pump OFF for these conditions is plotted in Figure 5.7, there is an apparent gain hovering just below 1 dB except at higher frequencies where the measurement is not as stable, or at 5 GHz which is commensurate with the pump. At this degenerate amplification point the size of the 5 GHz signal increased by almost 2 dB, not significant in terms of amplification but unlikely that it is due to impedance mismatches. Therefore it is

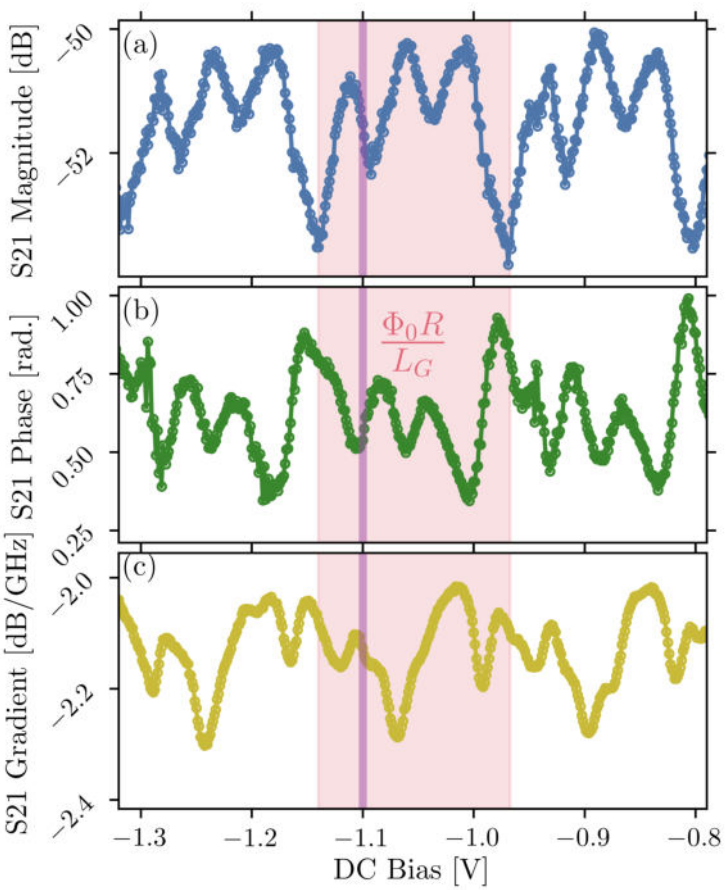

Fig. 5.6 Transmission measurements for a wave at 7 GHz over the bias range of −1.3 to −0.8 V. S21 magntiude is plotted in (a) while S21 phase is plotted in (b), both of which show a periodic shape with a single period highlighted by the shaded red region. (c) Shows the gradient of the full spectrum magnitude measurements against flux, which also shows a clearly periodic behaviour with loss changing in the device depending on dc bias. A purple band is added to all plots to mark the point at which maximum 3WM amplification was found to be present.

a sure sign of parametric effects and three wave mixing producing amplification, motivation enough to improve the performance of future devices with improved design.

The optimal bias that leads to this amplification does not coincide with either of the expected potential 3WM biases identified in phase or in gradient data. It is difficult to determine the cause of this mis-alignment, although the more complex form of the unit cells seems a likely candidate. Gradiometric effects in geometric inductance of inductive coupling between SQUID's may also explain this effect.

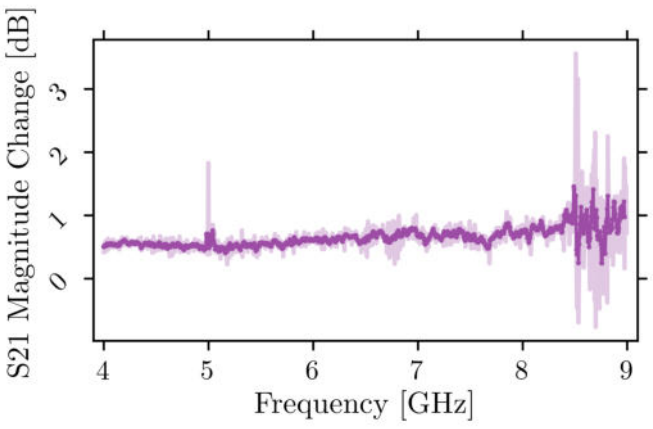

Fig. 5.7 Plot of the difference between transmission magnitudes over a frequency range from 4 to 9 GHz for a signal of applied power roughly −112 dB with and without a pump wave applied at 10 GHz.

Link to ToC

5.4.4 Flux Period Dependence on Frequency

There is a clear dependence of shape of the S21 magnitude period on probe frequency, as is shown in Figure 5.8 (a), (c) and (e) for a 4 GHz signal, 7 GHz signal and 10 GHz signal tone, respectively. This trend is not reflected in the phase data for these same signals which is shown in Figure 5.8 (b), (d) and (f). Gradient of the transmission magntiude is also extracted by linking the transmission for each frequency at a given bias point with a line of best fit, this is a useful technique to minimise measurement time.

The most fitting explanation for this effect seems to be losses within the rf-SQUID's as this will quite significantly affect the transmission magnitude but the effect on phase shift is harder to observe at these frequencies far below the transmission line cut-off. A reasonable explanation may then be the parametric resistance, or the power lost to harmonic generation in the medium. This has the required inverse proportionality to frequency due simply to the number of harmonics that may be generated in the device below the cut-off frequency of the transmission line. It is hard to draw firm conclusions from this data, after all it is expected that the rf-SQUID's would be hysteretic at this temperature which should complicate the shapes of the flux periods.

5.5 March 2023 Measurement

This experiment seeks to further investigate the hypothesis of losses in the JTWPA that have a frequency dependence caused by parametric effects, or parametric resistance. As hysteresis, potential impedance mismatches and gradiometric effects complicated the analysis and interpretation of the results of the previous experiment, these next measurements are run at a higher temperature to simplify this problem. A set of more detailed data on the flux dependence of transmission and harmonic generation at 4 K is gathered, no hysteretic effects are expected at this temperature so the extraction of useful information from the data should be more straightforward.

5.5.1 Transmission and Flux Periodicity

This transmission measurement was also carried out using a VNA, although the method has been changed. A single probe frequency is sent and transmission is measured through time with the dc bias held steady. The mean average of this sweep leads to a single transmission point, this method allows for a much higher density of dc bias points in each measurement and so the periodicity may become clearer in parts.

Three probe frequencies, applied through the pump line, have been used for this measurement, 3.4 GHz, 8 GHz and 12 GHz for which the results are shown in Figure 5.9 (a), (b) and (c), respectively. There is a remarkable difference in the shape of the S21 magnitude periods between these three frequencies, as is made clear by the dashed purple lines at the bias points A (-50.4 µA), B (0 µA), C (49.7 µA) and D (63.8 µA). As can be

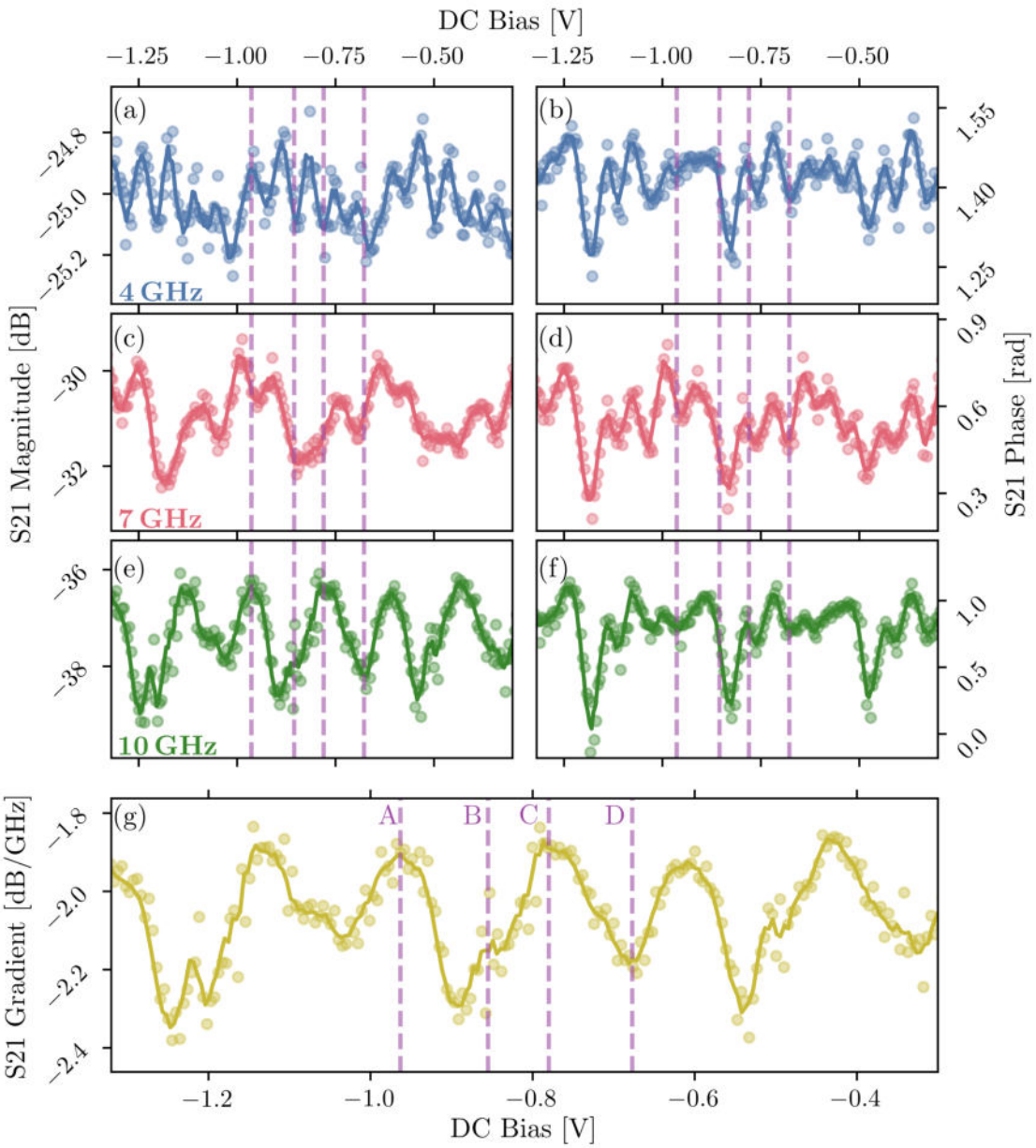

Fig. 5.8 Transmission data versus dc bias data recorded at three probe frequencies of 4, 7 and 10 GHz in both magntiude (a), (c) and (e) and phase (b), (d) and (f), respectively. (g) Shows the gradient of a line joining the transmission measurements at these three probe frequencies with a clear periodic behaviour replicating the full spectrum measurement where a periodic change in gradient (i.e. losses) was seen depending on dc bias. The vertical dashed lines, labelled A, B, C and D in plot (g) are added to all plots for easy comparison of distinguishable features.

seen what is a trough at point A in the 3.4 GHz is a peak in the 10 GHz data, and vice versa at point B. This will be shown to resemble the effects of decreasing shunt resistance in the rf-SQUID's as frequency increases in the simulations section of this chapter.

A particular improvement in this experimental run was the direct recording of current for all applied biases. This allows for a direct extraction of a value for geometric inductance from the ratio of the magnetic flux quantum to the width of the periodicity in current.

Link to ToC

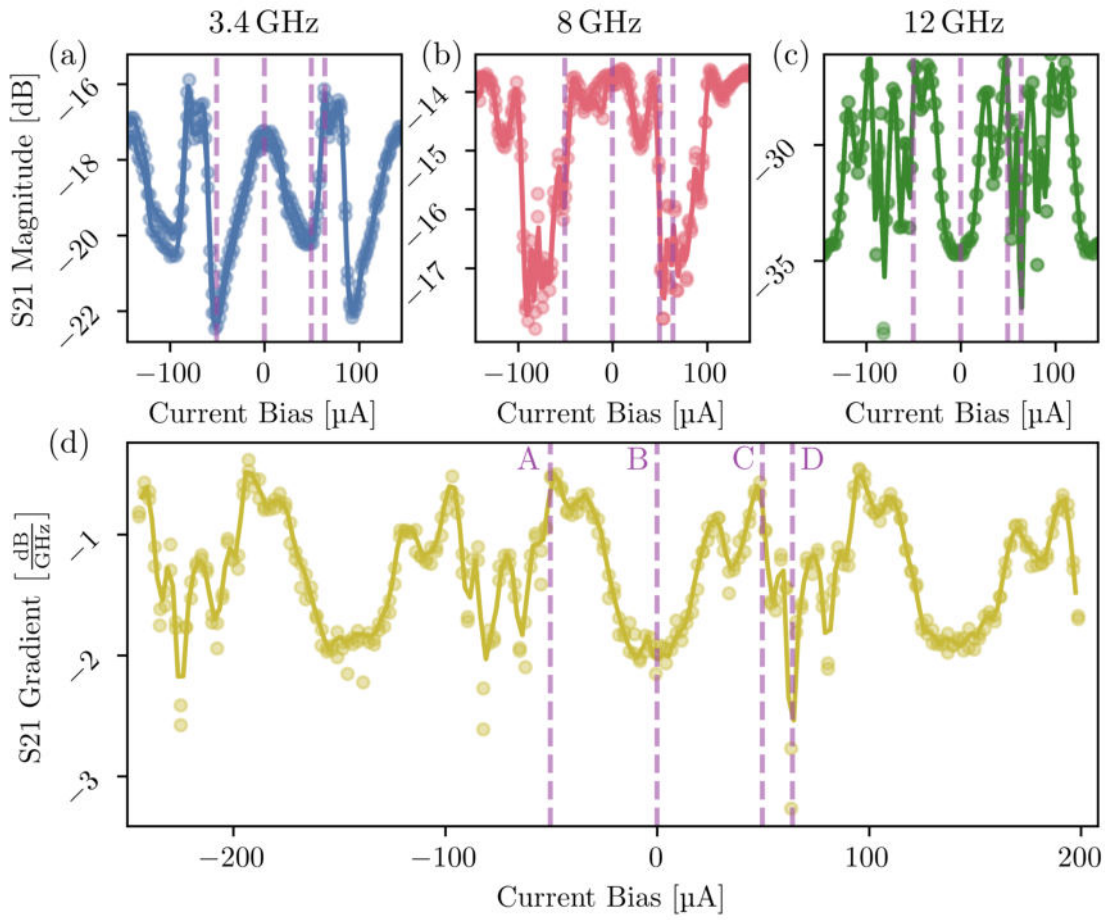

Fig. 5.9 Transmission magnitude measurements for the JTWPA device cooled to 4 K taken at three probe frequencies 3.4 GHz in (a), 8 GHz in (b) and 12 GHz in (c). (d) Shows the gradient of the line of best fit for these three transmission points against dc bias which can be directly related to loss in the device. Dashed vertical lines labelled A, B, C, and D are added to each plot for easy comparison of features and to show clearly how the shape of the transmission period changes with frequency.

By taking the mean of three current periods we arrive at a value of 144.3 µA. This translates to a geometric inductance value of approximately 14.33 pH per SQUID, just over half of the expected value. It does not appear that this is a mis-identification of half a flux period, as it matches the shape of transmission period observed in simulation later. Furthermore, the asymmetry of the response at the half flux bias point should prevent such a mis-identification in most cases. Of course, this departure from the desired values of geometric inductance is not ideal but demonstrates the difficulty of producing these devices even with state-of-the-art fabrication processes.

A linear fit can be used between these three transmission measurements to find the gradient, i.e. the loss per gighertz in the device. This is calculated and shown in Figure 5.9 (d) with dashed purple lines added at distinguishable features that can be compared to the transmission at individual frequencies. It will be shown later in this chapter that the shapes of the 12 GHz transmission periods and the shape of the period in the gradients at low input powers most closely resemble the expected behaviour for a device with low

losses. The cause of these losses will be part dissipative and part dispersive, in so far as quasiparticle generation may cause real loss and while energy transfer to harmonics may be returned to the pump to some degree.

5.5.2 Power Dependence of Transmission

It is known from research into nonlinear devices that 'parametric attenuation' (or the power lost to generation of harmonics) can be seen to be proportional to applied power [149, 151]. So the power dependence of loss in these devices should be easily observable if parametric attenuation (or parametric resistance as I have previously referred to it) is the cause. By plotting the transmission at certain dc biases against the input power we would expect to see a negative gradient that can then be fitted to an effective parametric resistance. The gradient of such a transmission versus input power measurement should be related to the wave mixing regime via the efficiency of the harmonic generation.

The results of such an experiment are shown in Figure 5.10 where (a) and (b) show the transmission periodicity in flux at input powers of −92 dB and −62 dB, respectively. The clear change in shape seen between these transmission curves should be addressed, an additional narrow peak appears at higher input powers most likely located around the half flux bias point. This appears to be a power dependent feature related to losses, similar to the frequency dependence observed previously. We can say that the transmission data at 8 GHz for low input powers corresponds to an intermediate response between the 3.4 GHz data and the 12 GHz data, where losses per cell are high and low, respectively. Despite losses per cell being lower for the higher frequencies there is no discrepancy with the observed lower transmission at higher frequencies, as simply more wavelengths will fit in the device. Therefore, as input power increases losses change such that 8 GHz transmission begins to resemble the 3.4 GHz case at higher powers.

This additional narrow peak, for which a targeted plot is available in Figure 5.10 (c) shows signs of splitting into three. Other features also may show this effect but have too many overlapping features to distinguish the splitting so clearly. As we might expect this particular region to be a single peak, per the impedance relation of Figure 5.2, the relative distance between the spilt peaks can be used to estimate the differences in geometric inductance that causes this. Taking into account an approximately - 4 µA offset in the bias, the ratio of the peak currents to half of the average value are 0.887, 0.994, and 1.191 for the peaks at 60 µA, 67.7 µA and 81.9 µA, respectively. These are significantly larger percentage changes than can be explained by inter-SQUID inductive coupling, which is estimated to be at most 3.3×10^{-2} per SQUID from Equation 3.2. A more reasonable explanation may be gradiometric dependence of the geometric inductance as described in the simulations of Chapter 4.

Figure 5.10 (d) shows the transmission through the device at three dc biases over an input power range from −100 dBm to −40 dBm. Note that the critical current of 10 µA should correspond to roughly −53 dBm, so we might already expect a significant decrease in transmission above this value due to quasiparticle generation. In fact, a very clear

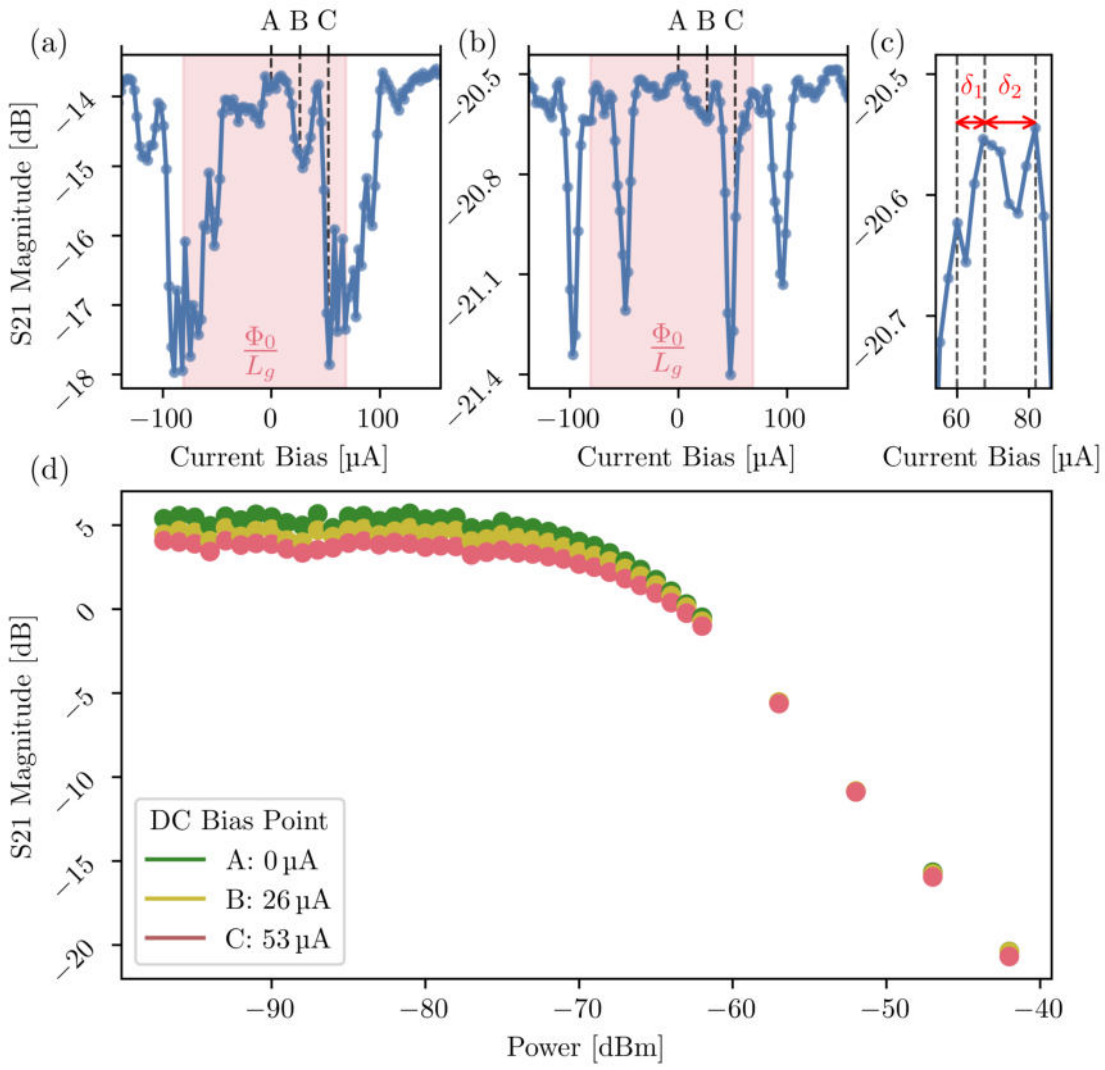

Fig. 5.10 (a) Transmission magnitude for an 8 GHz probe frequency at -92 dBm over approximately two flux periods - a single flux period highlighted in red with a width of around 144 µA. (b) Shows the flux period achieved for the same frequency at an applied power of -62 dBm while (c) shows a focussed region of (b) to highlight the splitting of the additional peak that is observed. (d) The S21 magnitude for a series of 8 GHz measurements at three dc biases. The magnitude has subtracted the additional room temperature attenuation to produce a transmission larger than zero for the lowest power measurements. The dc biases used for the three scatter plots are marked as A, B and C in plots (a) and (b).

decrease in transmission becomes evident around −70 dBm, well below the expected critical current value but this will be revisited shortly.

The low power region, up to roughly −75 dBm, is apparently slightly noisier than measurements at higher powers, although the effect of bias is clear with the points for the three dc biases having a clear separation. However, this separation does not increase with power which we might expect if parametric attenuation was significant, given that the changing efficiency of wave mixing should change the parametric attenuation's dependence on power [149, 151]. Instead, the only notable feature is the point at which the gradient

changes. This behaviour, and the early onset of increased losses, may be explained by the generation of shockwaves in the device.

As a reminder of what was described in Chapter 2, a shockwave is formed when an applied wave generates harmonics on a transmission line with small dispersion. The peak of the shockwave can then easily be at a current much larger than the amplitude of the applied wave. The generation of shockwaves due to harmonic generation neatly explains the apparent dc bias, frequency and power dependencies that are observed in this device.

5.5.3 Extracted Effective Resistance

For both this device and the previous, losses have been apparent in transmission measurements. Given the lumped element nature of these devices, the behaviours observed in the previous experiments were explained well by the the inclusion of the normal state junction resistance in our models. This same analysis method is now applied to this device where the losses and equivalent resistance are extracted from the gradient data of Figure 5.9 (d).

The gradient of the transmission, A, can be related to the attenuation constant, α, that may be found from a circuit model of N unit cells via:

$$A = \frac{-20\log\left(e^{-\alpha(f_2)N}\right) + 20\log\left(e^{-\alpha(f_1)N}\right)}{f_2 - f_1} \tag{5.3}$$

where $f_{1,2}$ are the chosen probe frequencies, or equivalently[5],

$$\frac{\partial\alpha}{\partial f} = \frac{A}{20N}\ln(10)\ . \tag{5.4}$$

The attenuation constant can then be matched to the equivalent shunt resistance via a recursive algorithm. This analysis is shown in Figure 5.11 (a), (b) and (c) where the gradient of the S21 magnitude, the y-axis intercept and the equivalent shunt resistance are plotted, respectively. Notably, the gradient and intercept appear to follow shapes similar to the expected $\chi^{(2)}$ and $\chi^{(3)}$ parameters (more clearly for the latter than the former) and the equivalent resistance also closely follows the expected relation for a Josephson inductance. While this may prove to be a useful method of extracting the parameters it is not pursued here as there are several layers of analysis that may skew the results. A more direct method for extracting the nonlinearities is pursued later in this chapter.

Another method for extracting an equivalent resistance is to use transmission at a single frequency, with a 0 Hz intercept determined from the mean of the previous fit, and to determine the required attenuation constant to match the transmission. Assuming that losses occur only across the small junction and that the large junction can be ignored then

[5]We have made the assumption that we can calculate:

$$\lim_{f_2\to f_1}\frac{\alpha(f_2)-\alpha(f_1)}{f_2-f_1}$$

as per the fundamental theoreom of calculus.

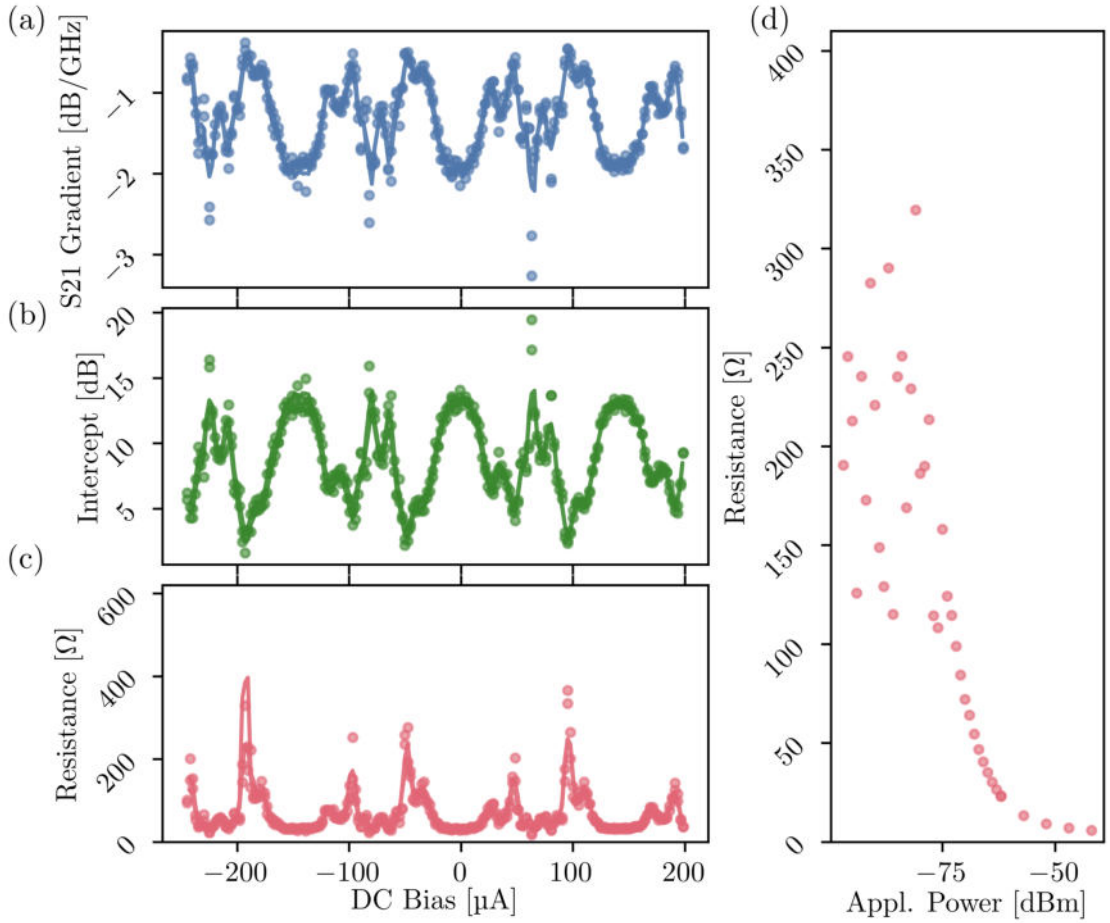

Fig. 5.11 Transmission data at 3.4, 8 and 12 GHz fitted by a line of best fit with the gradient plotted in (a), the y-axis intercept in (b) and the effective shunt resistance extracted from the gradient plotted in (c). (d) Effective shunt resistance against input wave power extracted from transmission data of a 8 GHz input wave via an iterative fitting algorithm.

S21, which is a ratio of voltage out to voltage in:

$$S21 = \frac{V_o}{V_i} \ , \tag{5.5}$$

can be described as a function of α via:

$$V_o = V_i e^{i\alpha N} \ . \tag{5.6}$$

With a given value for α then, as before, the equivalent shunt resistance is found via a recursive fitting algorithm. This analysis has been applied to the power swept data of Figure 5.10 and is plotted in Figure 5.11 (d). It can be seen at low input powers, where losses are low the equivalent resistance is accordingly high and drops in the expected manner above approximately −75 dBm. Of most interest is that the resistance appears to plateau towards a final value around ~ 10 Ω at high powers. While this value is far from the expected normal state resistance of the small junction in this device, it is much

closer to the expected normal state resistance of the larger junction. It may be the case that quasiparticles are generated due to pair breaking in the smaller junction which are then available to tunnel through the larger junction, leading to this small value of effective resistance. Such large losses are unlikely to be caused solely by harmonic generation and are more likely to arise from quasiparticle generation via the formation of shockwaves from these harmonics, explaining the apparent frequency dependence.

5.5.4 Degenerate Three Wave Mixing

No experiment on a device with amplifier in the name can be considered complete without at least looking for amplification. As opposed to the previous measurement for this device using a VNA, we now only consider 3WM degenerate amplification with a pump tone applied at 12 GHz and a signal tone applied at 6 GHz, of course. The outputs are captured on a spectrum analyser for a range of dc biases and pump powers. At this signal frequency and signal input powers >20 dBm lower than the pump any possible amplification should be maximised due to the lack of most idler products.

Shown in Figure 5.12 (a) are the spectra for the signal output at three pump powers, if there was amplification we would expect to see an increasing peak height for increasing pump power, but the trend here is reversed. While the plotted data were taken at a dc bias of −45.2 µA this trend was the same for most biases. At some specific bias the three curves did appear to overlap, but no significant amplification was seen on this occasion. The relation of the peak areas of the pump and signal tones to dc bias can be seen in Figure 5.12 (b) where a similar periodic shape is present to those observed on the VNA are clear. Importantly, the shape of the signal period is slightly different to that of the pump near what we might expect to be the half flux bias position, and as a consequence also close to the expected maximum in 3WM. Assuming that 3WM is indeed occurring there are several causes of decreasing signal power including the losses due to quasiparticle generation, as

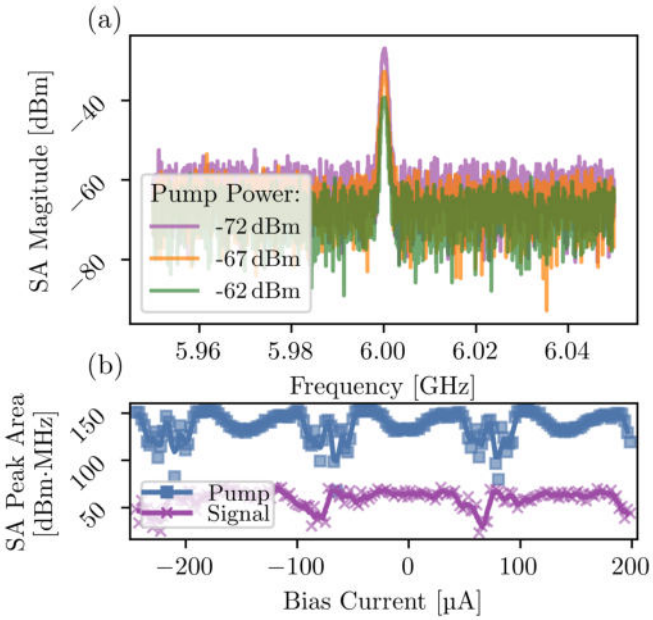

Fig. 5.12 (a) Spectrum analyser traces centered at a frequency of 6 GHz showing the peak of a weak signal applied to the device. The three traces in purple, orange and green show the signal peak decreases with increasing pump power, likely in this case due to increased harmonic generation and quasiparticle losses. (b) The peak area of the signal and pump captured on the spectrum analyser against dc bias.

Link to ToC

well as losses due to harmonic generation. The reason that this result differs to that of the December cooldown may be related to the choice of pump frequency, 12 GHz apparently being less optimal for phase matching than 10 GHz, possibly due to some weak internal resonance within the device. Nonetheless, at even lower signal powers some amplification may be possible, but this was not investigated further with focus moving to the root cause of the apparent losses in the device, harmonic generation.

5.5.5 Harmonic Generation

So far transmission measurements have been used to highlight apparent losses in the JTWPA device that are hypothesised to result from parametric effects, i.e. shockwave formation and quasiparticle generation. The measurements presented below provide a route for describing the power lost to harmonic generation depending on the dominant wave mixing regime. This is achieved by applying a single 3.4 GHz wave to the device and recording its output and the output spectra of its harmonics on a spectrum analyser. The key parameters that can then be changed are the dc bias and input power of the applied wave, which should act to increase or decrease the losses.

As has already been discussed earlier, recording the peak area is less vulnerable to noise than the peak prominence. The data presented here uses a peak area extracted from a curve fitting algorithm that finds the peak width, the background noise level and from these the area under the peak. As a consequence, the third harmonic for which the prominence is normally lower than the second harmonic has a reversed peak area relationship. The cause of this could be a lower noise floor at that particular frequency or simply that the third harmonic has a larger width, either way it does not significantly affect the conclusions of this section.

This method of measurement is validated by the close agreement in the shapes of the periods of the transmission of a 3.4 GHz wave captured on a VNA and the calculated peak areas as found via a spectrum analyser, as shown in Figure 5.13 (a).

Power Dependence

The dependence of harmonic generation on applied power should show distinct differences in the gradients of the growth of peak area for each of the harmonics. The gradient is known to increase with harmonic number and should also have a clear dependence on the applied dc bias, with the gradient of even numbered harmonics falling greatly when the $\chi^{(2)}$ nonlinearity approaches zero.

A set of dc bias working points are chosen for analysis which confines our focus to regions of interest in the data collected for the transmission of the applied wave. These working points, shown as A-F in Figure 5.13 (a), are expected to either sit in local minima of the nonlinearity relations or unstable points where the change due to applied power or bias should be most evident.

The peak area of the applied wave and its second, third and fourth harmonic are plotted against applied power in Figures 5.13 (b), (c), (d) and (e), respectively. From the simulation results of Chapter 3 we expect the gradient of this dependence to increase

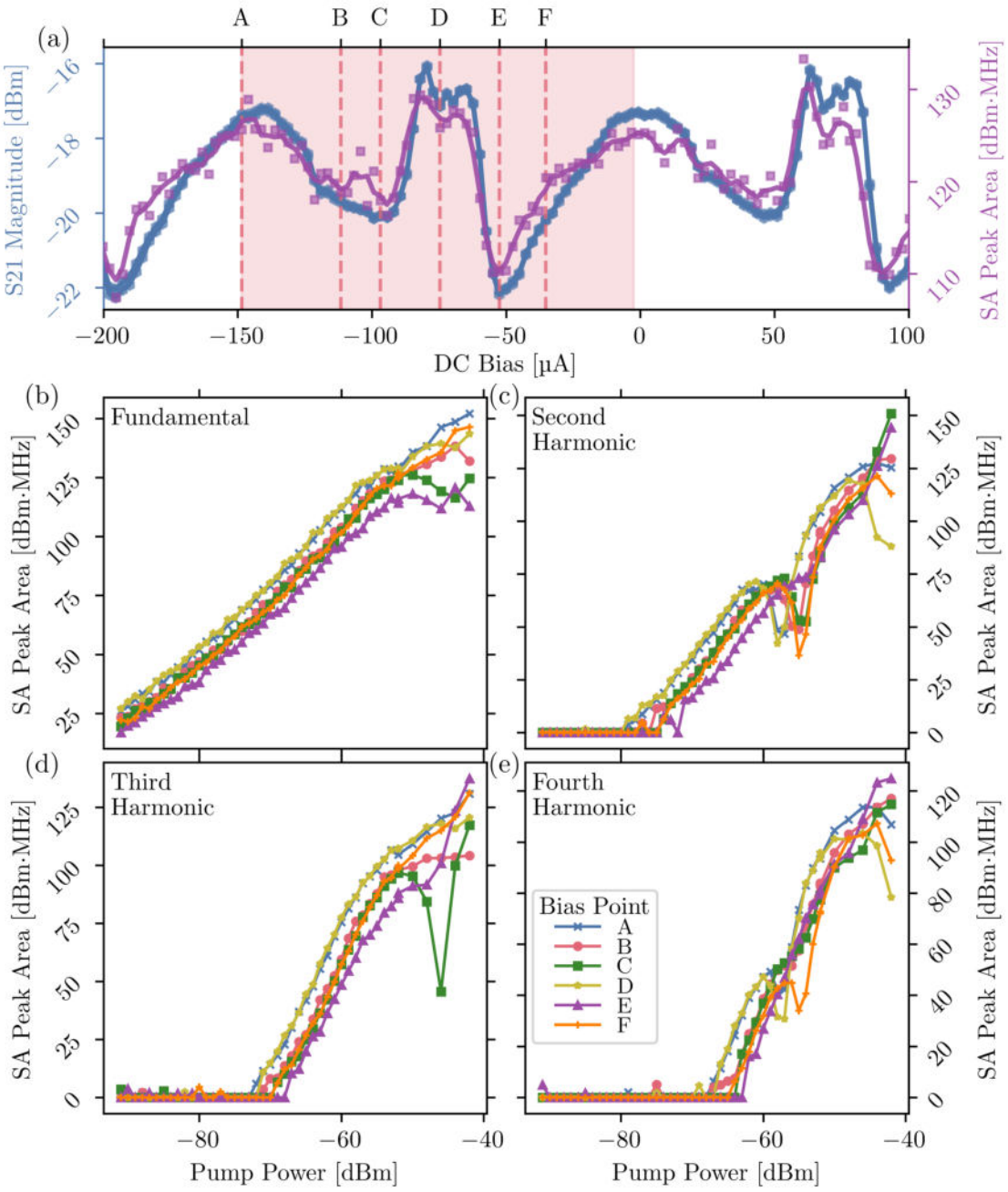

Fig. 5.13 (a) A comparison of the transmission period of a tone applied at 3.4 GHz as recorded on a VNA (blue) and with its peak area as recorded from a spectrum analyser (purple). The shaded red area covers approximately one flux period while the vertical dashed lines A-F mark the dc bias working points that are used for the power dependence plots. (b) The peak area of the applied wave versus power at a series of dc bias points, (c), (d) and (e) show the same for the second, third, and fourth harmonics, respectively.

with harmonic number, with each harmonic eventually saturating at the same power due to pump depletion. These trends are observed in this data with the second harmonic appearing above the noise floor first, followed by the third and fourth harmonics as the power increases further. While it was expected that dc bias might have a more significant effect on the gradient of the even harmonics this has not been reflected in these results.

Link to ToC

Instead, a strong dependence on the dc bias is seen in the input power required to produce a significant harmonic peak above the noise floor (which we shall dub emergence power), this is a potential sign of changing generation efficiency. The power at which the local minimum in the even numbered harmonics and the power at which saturation appears to set in (identified by plateauing or reversing of the gradient) also seems to have dependence on the dc bias. This saturation effect is likely to arise from losses due to quasiparticle generation in the device and not from pump depletion as would be the case in the simulations of Chapter 3.

Another interesting aspect of these results is a local minimum in the power dependence of the second and fourth harmonics around −55 dBm, rather close to the expected critical current value of −53 dBm. Although a similar dip seems to be present for the third harmonic, it should be noted that this is at a much higher power of -44 dBm. Given that the even numbered harmonics' feature aligns well with the expected critical current value, it seems likely that it is related in some way, although the particulars of the relationship are not so clear. If it was due to a significant increase in the quasiparticle number at this input power then similar dips should be seen in the odd numbered harmonics, which are not present. This question will be addressed more in simulations which will consider nearly all wave-mixing effects, narrowing the possible causes.

Flux Dependence

We have so far identified four features in the power dependence of harmonic generation that are worth investigating over a flux period: peak area, gradient of peak area growth, emergence power and the local minima in the even numbered harmonics. The intention with this analysis is to extract more information about the device, namely the average critical current value of small junctions in the array which should determine the wave mixing mechanism and efficiency.

First, in Figure 5.14, the peak areas of the input wave and its harmonics are plotted over approximately two flux periods. Of particular note is that the third harmonic appears to have a larger area than the second or fourth except at very specific points which may be expected to be the optimal 3WM bias points. Also, the shape of the third harmonic periodicity is very similar to that of the input tone, as such it is hard to distinguish the difference between impedance matching and parametric effects.

In an effort to separate these effects to some degree, the peak versus applied power plots are re-analysed with the gradients for each harmonic extracted at each bias point. The regions that were used to fit the gradients are shown in black in Figure 5.15 (a) where the most linear portions of the plots have been selected. The gradients of the fundamental peak area, as well as the second and third harmonics, have been plotted in Figure 5.15 (b), (c) and (d), respectively. A more distinct difference in shape between the second and third harmonic is now present, although the fundamental and the third harmonic remain similar. We can perhaps comfortably say that the region around −100 µA which demonstrates a minimum in the plots of the fundamental and the third harmonic, but not in the second harmonic, corresponds to the optimal 3WM bias position. The removal of impedance

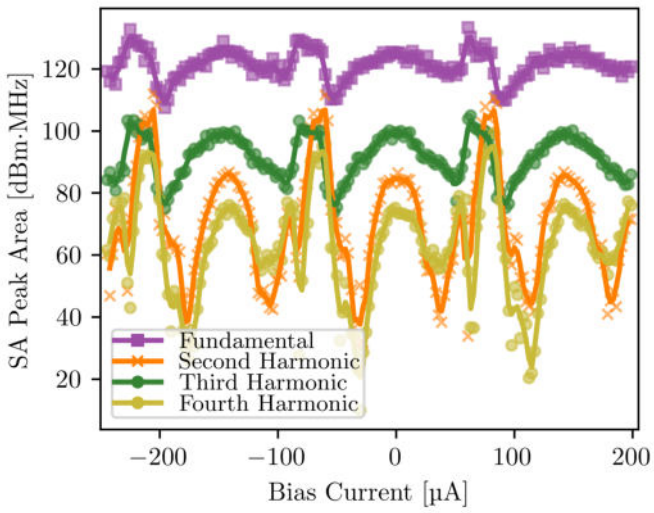

Fig. 5.14 Peak area versus dc bias for the applied wave at 3.4 GHz and the generated harmonics at 6.8 GHz, 10.2 GHz and 13.6 GHz. The effects of impedance mismatch make all trends appear similar but there are some differences between the even and odd numbered harmonics.

mismatch effects in this data has proven difficult, although another promising approach exists that has unfortunately not worked in this case, possibly due to undersampling. By taking the difference between the fractional changes of the fundamental, the second harmonic and the third harmonic the effects of impedance should be removed leaving only the changing wave mixing efficiencies. Although given the conflicting optimal 3WM points extracted from magnitude, phase and amplification data seen in Figures 5.6 and 5.7 this may be difficult in this design with multiple rf-SQUID's per cell.

There are two remaining features in this data that may still allow for the extraction of information about the device. We will tackle them simultaneously now using the second harmonic generation data. The peak area versus applied power versus dc bias heatmap plots for the region of the data around the emergence power and the local minimum near the expected critical current value are shown in Figures 5.16 (a) and (b), respectively.

Both of these features, given that they are both shown from data of the second harmonic, are expected to be related to the 3WM, $\chi^{(2)}$ nonlinearity and show little dependence on the weaker 4WM, $\chi^{(3)}$ nonlinearity. The dependence of both of these nonlinearities on dc bias are shown in Figure 5.16 (c). However, while a similar periodic behaviour in dc bias is clear in both features, it seems the $\chi^{(3)}$ more closely fits the observed peak area dependence on dc bias than the $\chi^{(2)}$. A period formed of a sharp peak followed by a more rounded curve is repeated for both the emergence power and local minimum data. This comparison can be best seen in Figure 5.16 (d) where a slice of the local minimum heatmap taken at -50 dBm is plotted alongside the 4WM nonlinearity. This is the reverse of the expectation, so the explanation requires that either some 4WM effects such as cross- or self-phase modulation become more pronounced in even numbered harmonics at this power. Otherwise some effects separate to 4WM, but that follow a similar flux relationship, is to blame. Impedance, which follows the same trend of the $\chi^{(3)}$ nonlinearity mirrored in the x-axis, as can be seen in Figure 5.2, is the most probable cause given the effects reflections may have on wave mixing [122, 134].

While the cause remains a bit amorphous, the effect is still of great interest to us. Despite the particular cause, change in impedance and the 4WM nonlinearity follows similar

Link to ToC

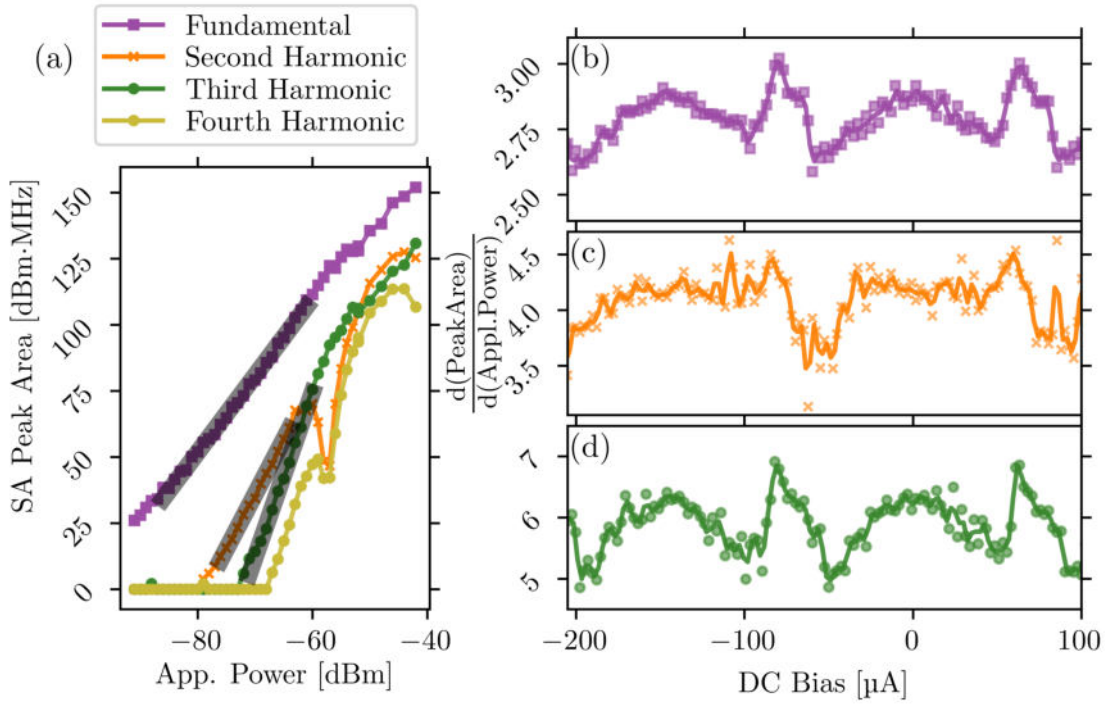

Fig. 5.15 (a) The power dependence of peak area of the applied wave and its generated harmonics on the applied power, plotted on the same axis for comparison, with the portions of each curve used for fitting the gradient marked in black. (b), (c) and (d) The gradients calculated for these regions across roughly two flux periods for the fundamental, second harmonic and third harmonic, respectively.

trends with the width of the sharper peak dependent on the critical current parameter of the rf-SQUID. Therefore, just as with extracting geometric inductance values from the current periods, the critical current can be extracted by fitting the curve of $\chi^{(3)}$ to the kink. With a thorough understanding of the cause this can be fit more exactly, although for now by eye will suffice as the difference in widths for a 1 µA change is rather large. The peak widths were then found to agree best for a critical current value of approximately 14 µA. This is quite far from the expected value of 10 µA although due to the lower geometric inductance value extracted earlier, the rf-SQUID's are still not hysteretic at 4.2 K with a hysteresis parameter equal to 0.61.

5.6 Simulation and Analysis

We can now try to better understand some aspects of these experimental results by reproducing the circuit characteristics in simulation. Our analysis will focus on the effects of loss on transmission, harmonic generation, shockwave formation and the generation of quasiparticles that we expect to cause the losses. The first approach is to linearise the circuit and find the transmission over a frequency range using AC analysis in WRspice. For this, the Josephson inductance is replaced by an equivalent linear inductance at each flux bias point and an additional shunt resistance is placed across the junction. This shunt resistance then either takes a static value (10 Ω, 15 Ω, 50 Ω, 200 Ω) to mimic constant losses

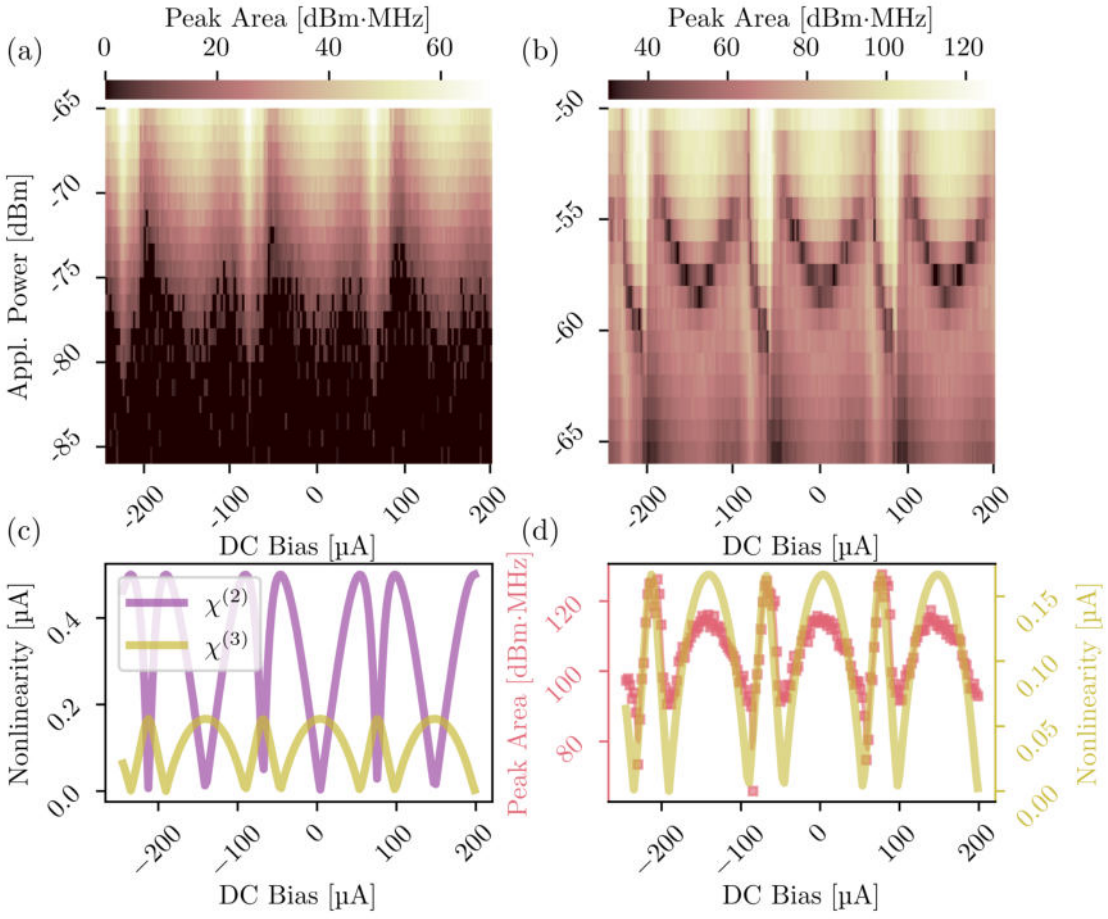

Fig. 5.16 (a) Heatmap of the second harmonic peak area in the region of applied power where the second harmonic peak emerges above the noise floor, and (b) a similar heatmap focussed on the region of applied powers that correspond to the local minimum in the second harmonic versus applied power curve. (c) The $\chi^{(2)}$ and $\chi^{(3)}$ nonlinearity strengths versus current for this device and (d) a comparison of the $\chi^{(3)}$ nonlinearity (yellow) and a slice of the local minimum in peak area of the second harmonic at a fixed applied power of −50 dBm (red points).

or a dynamic resistance that changes with flux bias. The dynamic values are extracted from the gradient fits shown in Figure 5.11 (c).

The physical argument for dynamic losses would be that the generation of quasi-particles will be frequency, power and flux dependent due to the efficiency of the wave mixing for harmonic generation. However, determining the value of a dynamical resistance may be difficult as the flux dependence will be similar to, and difficult to distinguish from, the Josephson inductance behaviour. Meanwhile, the case can be made that the effects of the wave mixing regime are only a small correction and a static value of resistance may fit better. This approach assumes that the quasiparticle population is high in certain power ranges regardless of the wave mixing regime.

From our experimental results we might expect the simulations that use a dynamic resistance to most closely mirror the transmission flux period shape of the higher frequency tones, given the shape of the gradient dependence on flux. On the other hand, the static resistance should produce transmission versus flux shapes that look like the low frequency transmission results at low resistance values and appear more similar to the high frequency transmission results at higher resistance values. The results of these simulations are shown in Figure 5.17 where these expected trends are reflected. The fact that the adaptive resistances simulations appear similar to the static resistance simulations with lower loss ($R_s \geq 50\,\Omega$) may imply that the 12 GHz data skewed the line of best fit results used to determine gradients in Figure 5.9. Notably, the simulation with $R_s = 15\,\Omega$ shows a transmission shape in flux quite reminiscent of the behaviour seen for a 3.4 GHz tone, whereas the narrow peak near the half flux bias point disappears for even higher loss at $R_s = 10\,\Omega$. The disappearance of the narrow peak must therefore be a purely loss dependent effect that may tell us something about the operating condition of the device, such as the quasiparticle generation.

This simulation set has confirmed that the losses decrease per unit cell for increasing frequency, adding weight to the hypothesis that losses are linked to frequency via the parametric resistance. The origin of the quasiparticle generation must now be determined, given that it has a known frequency dependence the obvious assumption is shockwave generation. To investigate the harmonic generation and shockwave formation in the device the nonlinearity must be included in simulations, so we must return to the already well-described WRspice transient and CME numerical methods. First, by recording the output power of the harmonics for a single input wave with a given input power, the simulation methods can be compared. The results of this study are shown in Figure 5.18 where an input wave of frequency 3.4 GHz generates harmonics up to its tenth in this device, although only the second and third are shown here as they are the most significant. As always, the CME results (displayed as lines) are a fraction higher than the WRspice results (points), although the trends are clearly the same. Notably, the plateauing that signifies pump depletion occurs at a significantly higher power in simulation than in experiment, -50 dBm compared to approximately -60 dBm. The dips in generation of the even numbered harmonics around the critical current value are also absent, implying that they are not a trivial wavemixing effect and may also be related to impedance mismatches in the experimental setup.

Link to ToC

The current profile along the arrays can be recreated from this data of the CME results by computing the overlapping sinusoidal current distributions along the SQUID array, as shown in Figure 5.19 (a), (c), (e), and (g). It is even more simple to do this for the WRspice results as the current values at a point in time can be extracted for all nodes in the array directly, this data is shown in Figure 5.19 (b), (d), (f) and (h). It can be seen clearly that the two current distributions both show shockwave formation but otherwise do not appear similar. This may be due to the different propagation speeds of each harmonic in the array and the effects of reflected waves which are included in WRspice but not the simpler CME models. Importantly, both show that the total current at some points in

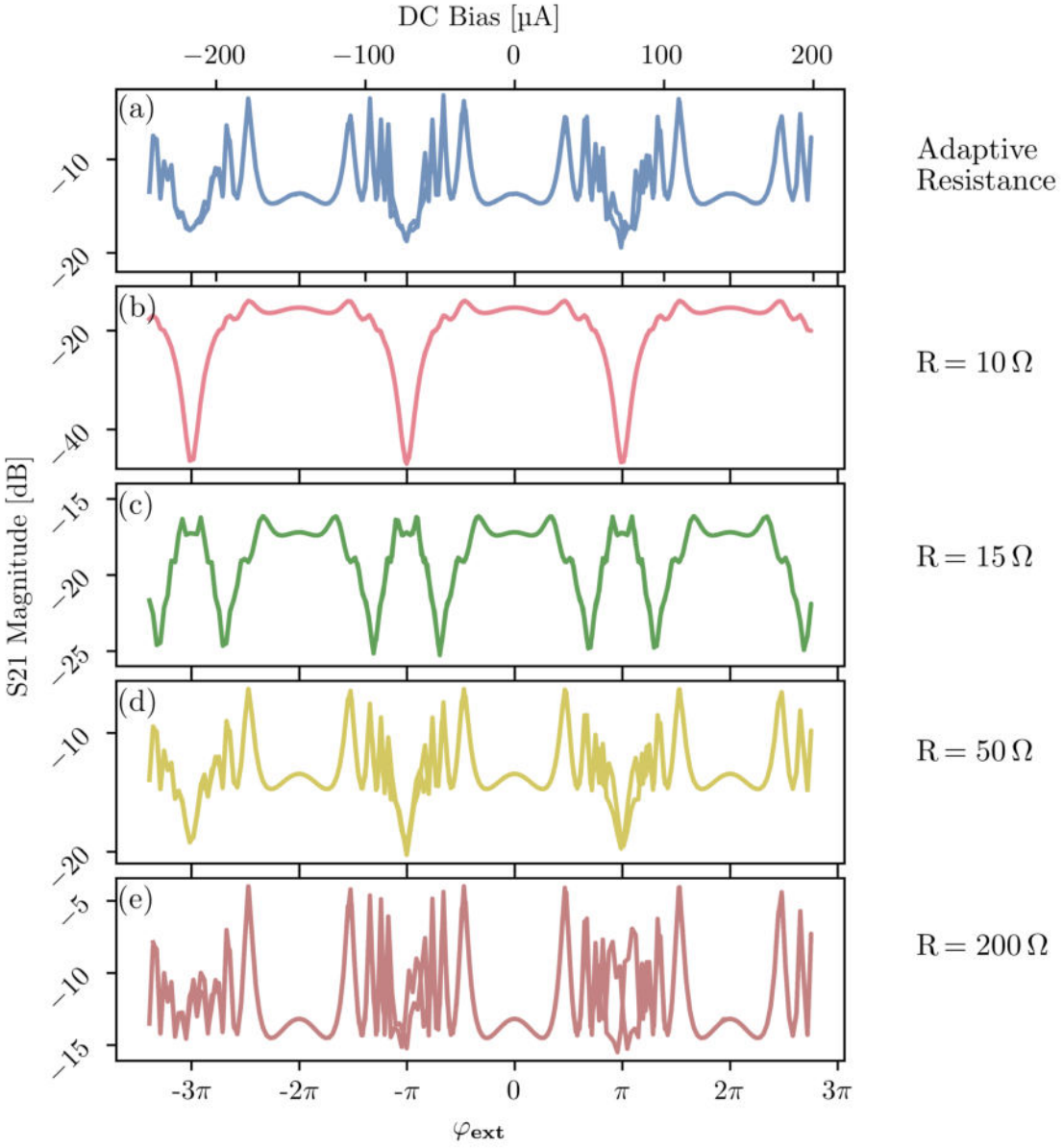

Fig. 5.17 WRspice AC analysis simulations of a linearised JTWPA device with circuit parameters equal to those extracted from experimental data. S21 magnitude versus applied flux (or dc bias) is shown for the dynamic resistance which change with the flux bias as extracted from gradient data in (a). Static resistance simualtions for resistance values of 10, 15, 50 and 200 Ω are shown in (b), (c), (d) and (e), respectively.

Link to ToC

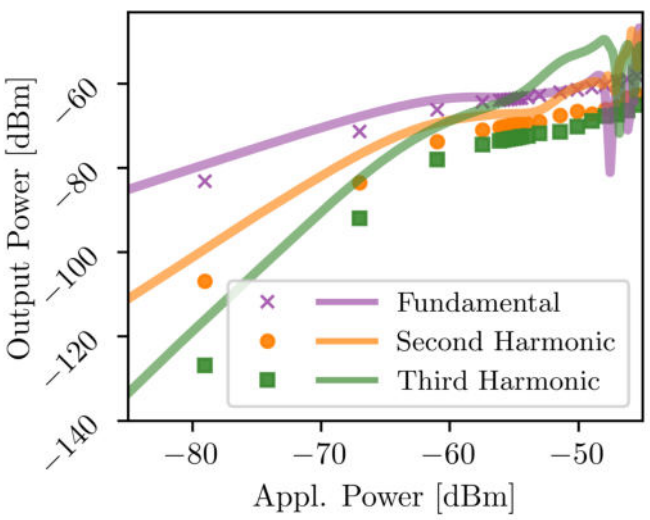

Fig. 5.18 The simulation results from the CME (solid lines) and WRspice (points) methods tracking the output power of the fundamental, second and third harmonics of a 3.4 GHz input wave as it leaves the device. Simulations are repeated for many input wave powers to demonstrate the dependence of harmonic generation on power.

the array exceeds the input amplitude (marked by dashed black lines) and for larger input powers also exceeds the extracted critical current value of the junctions (marked by dashed red lines at 14 µA).

Should a current larger than the critical current pass through a Josephson junction then some Cooper pairs are broken into individual quasiparticles which then proceed to tunnel through the barrier, producing a voltage across the junction. Given that simulations show currents exceeding the critical current, even at significantly lower input currents, losses would occur in the device at powers much below what might otherwise be expected.

In order to estimate the total number of quasiparticles generated per cycle in the device, the current over a 1 ns period is extracted from the halfway point (i.e. the 100th unit cell) of the JTWPA device simulated in WRspice. The area of the current trace that exceeds the critical current value is then found, which by:

$$N_{qp} = \frac{1}{e} \int I \cdot dt \ , \tag{5.7}$$

where N_{qp} is the number of charges, i.e. quasiparticles generated, I is the magnitude of the total current at that time with the critical current subtracted from it, and t is time. Notably the quasiparticles have some material dependent lifetime before they recombine into Cooper pairs. That means that the total quasiparticle population at any given instant may be orders of magnitude higher than the amount generated per cycle. For niobium films, we can expect this lifetime to be on the order of milli-seconds, therefore the quasiparticles generated per input wave cycle must be scaled by a factor of approximately $1{\times}10^6$ [152, 153]. This is then plotted in blue in Figure 5.19 (i), alongside the effective resistance of the junction which decreases with increasing quasiparticle number. Of course, the quasiparticle population of the metal decreases from the Fermi-level population, N_0, to zero by the relation:

$$N_{qp} = N_0 e^{-\Delta/k_b T} \ , \tag{5.8}$$

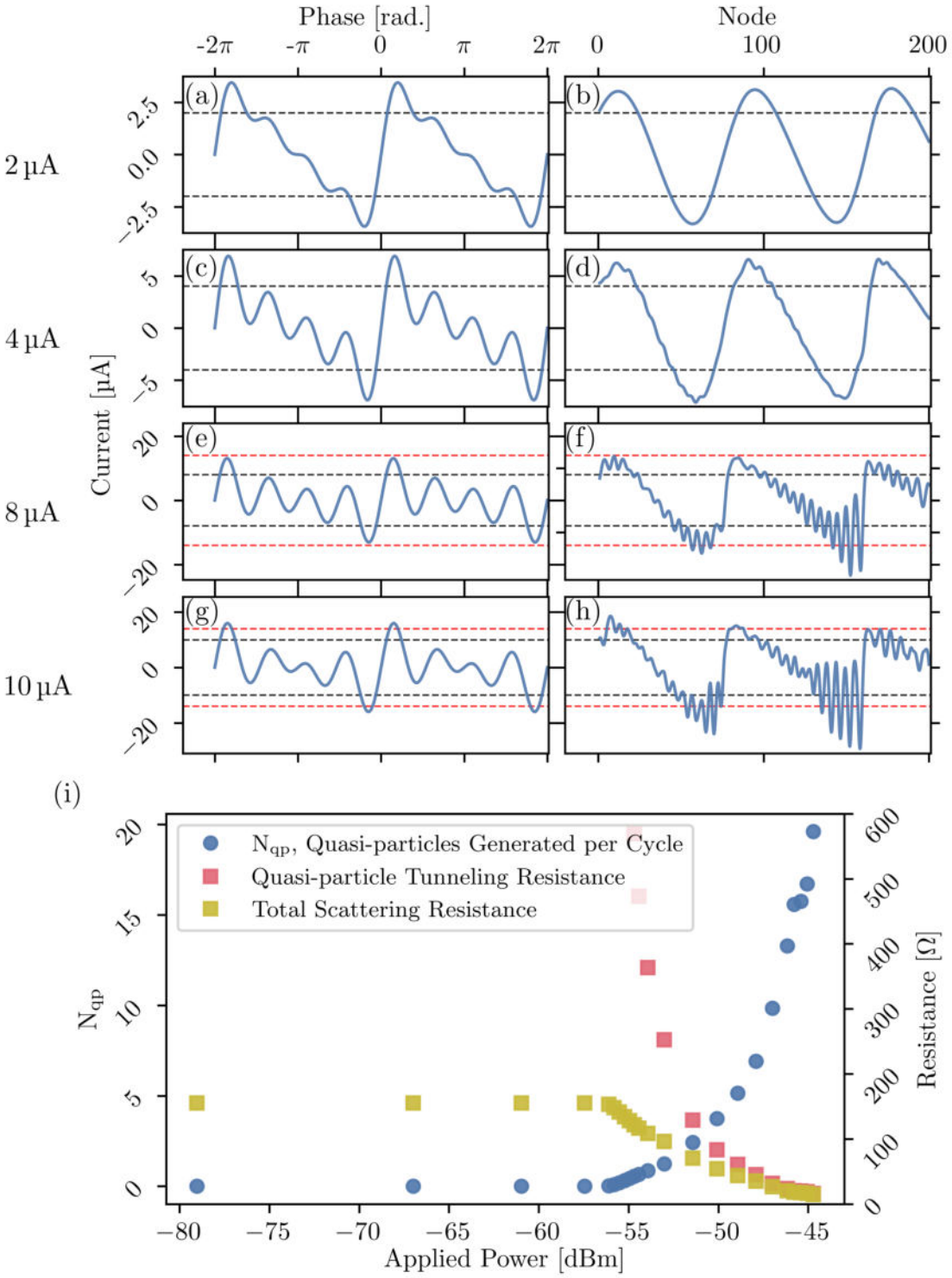

Fig. 5.19 Shockwaves in the device calculated using the CME (a), (c), (e), (f) and WRspice (b), (d), (f), (g) methods where the CME data is shown against phase angle of the input wave while WRspice data is shown equivalently in space. The simulations cover a range of currents showing the shockwave peaks exceeding the critical currents of junctions in the device despite the input currents being significantly lower. (i) The total number of quasiparticles generated per cycle at a single cell of the device alongside the quasiparticle tunneling resistance in the ideal case and in the case where it has an upper bound at low temperatures due to defects in tunnel barriers.

Link to ToC

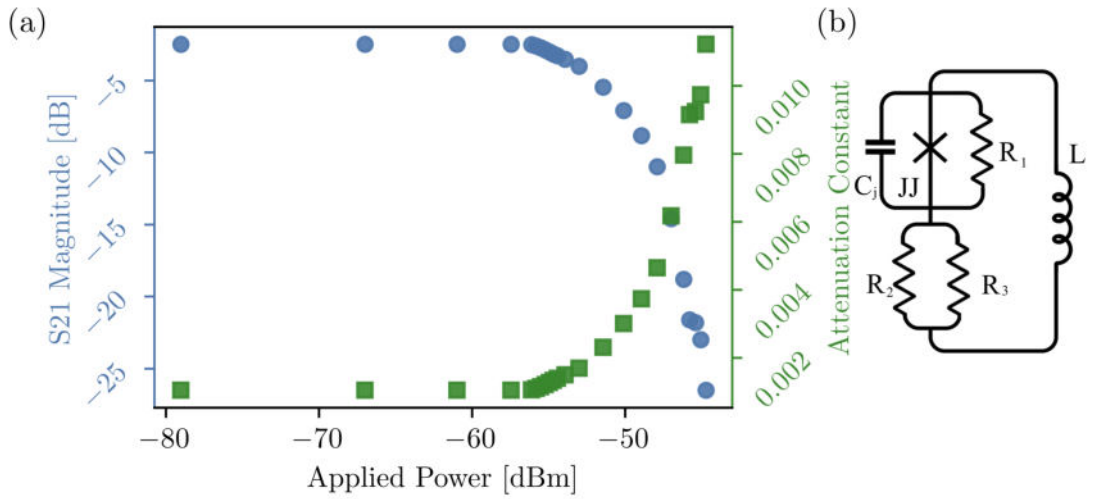

Fig. 5.20 (a) Simulated attenuation constant and transmission versus input wave power for an 8 GHz wave using the quasiparticle generation data of the previous WRspice simulations. (b) An alternative circuit that may better explain the losses observed in the experimental device where the smaller junction is responsible for the nonlinearity and the pair breaking events while the large junction, represented by a pair of resistors only, dominates losses but has little nonlinearity.

and the quasiparticle tunneling resistance scales as:

$$R = R_n \frac{N_0}{N_{qp}} \ . \tag{5.9}$$

At zero temperature this resistance should then be infinite, but it is known that the quasiparticle number never actually hits zero. Defects and scattering sites in the junction lead to an upper bound of resistance $R_{sg} \gtrsim 10R_n$ the normal state value for high-quality niobium junctions [131].

We now define R_{sg} as the quasiparticle resistance of the junction at $T = 0$ and with no additional pair breaking due to shockwaves. While $R_{qp} = R(P, T)$ is the quasiparticle resistance for a given input power, or a given rate of Cooper pair breaking in the device. This is used here as a function of power but can also be considered as a function of temperature, with the device operating at a higher effective temperature than its physical temperature if pair breaking occurs. The quasiparticle resistance, with and without a $T = 0$ limit, are plotted in Figure 5.19 (i). Obviously, this trend of resistance versus input power resembles the plot of transmission versus input power shown in Figure 5.10 (d), which indicates that these quasiparticle losses are likely the cause of this effect observed in experiment.

To compare this effective resistance with our experiments we can use Equations 5.5 and 5.6 to estimate the transmission magnitude against power using the resistance values already found. The plot of this analysis is shown in Figure 5.20 (a) where transmission drops in a manner very reminiscent of the experimental data. However, the simulated data shows an increase in quasiparticle losses at powers above -60 dBm as opposed to the approximately -75 dBm seen in experiment. Furthermore, the simulation does not

appear to reach a saturated value of resistance, which would show as a levelling out of the transmission curve at higher powers. Both these points imply that the quasiparticle generation and population are significantly different from estimations made.

Quasi-particle generation at lower powers in experiment means that the current is above the critical current more often than expected. An explanation for this may be the biasing of the rf-SQUID for operation in the 3WM regime, as a dc current equal to the critical current of the junction is flowing in the rf-SQUID at all times. A theoretical approximation has often been made that a very small pump power is used, which should mean that the critical current is never exceeded. But under these conditions a much smaller shockwave than the one generated in these simulations would be sufficient to break Cooper pairs. While this may be simulated in WRspice without issue, it is difficult to simulate accurately for the following reasons.

The Josephson inductance at the 3WM bias position is theoretically infinite, which would mean that these devices would not be affected by shockwaves in this way. Practically, however, the junction inductance is not infinite and not well defined in this case (although we can assume its maximum value will be some function of sub-gap resistance and superconducting energy gap: $\max(L_j) = f(R_{sg}, \Delta)$). Any current in excess of the critical current should theoretically reverse the direction of the screening current and allow an additional flux quantum to penetrate the loop. However, this is an inertial effect and so assuming that our microwave tones are oscillating much faster than this process can take place, Cooper-pairs may be broken without changing the sign of the inductance.

The fact that resistance values plateaued at higher powers in Figure 5.11 (d) means that the quasiparticle population was on the order of the Fermi-level population when the metal is in its normal state. While the effects of critical current distributions and reflected waves may account for some portion of this discrepancy, the largest part seems to stem from a large quasiparticle population even at the lowest temperatures. In order to ensure proper operation of these devices and the largest dynamic range possible in a future amplifier significant consideration should be given to the thermalisation of the transmission line structures.

Given the small powers that are known to cause apparent quasiparticle losses in the device, it is known that the quasiparticles must be generated in the smaller of the two junctions in the rf-SQUID. However, the large losses stem from the tunneling of these quasiparticles through the larger junction, the particular losses and effective resistance then being linked to an equivalent temperature to match the quasiparticle population. The circuit model of Figure 5.20 (b) shows an alternative circuit model that may better describe the rf-SQUID elements in this experimental device. As the large junction has a small nonlinearity and a very large capacitance, only the dissipative elements are included. Of the two resistors, one must be linked to the quasiparticle population of the system with both a power and temperature dependence: $R_1 = f(P,\ T)$. The other resistance represents the limiting resistance of the junction at $T = 0$, $R_2 \geq 10R_n$, and a resistance R_3 that depends on the quasiparticle population, directly proportional to R_1.

5.7 Conclusion

This set of experiments has attempted to extract important information about the JTWPA device under study from the transmission through and the harmonic generation that occurs within the device. The results of this chapter not only feedback into future designs of these devices but may also help to understand the difficulties observed in producing other superconducting parametric amplifiers. The generation of quasiparticles observed in this device is most likely an issue faced by most parametric amplifiers of any design, resonant or travelling wave, and may explain the difficulties in achieving high readout efficiency in some otherwise good devices [137].

The device was designed to have a characteristic impedance of 50 Ω impedance achieved by forming cells of 6 rf-SQUIDs separated by ground capacitances. Each rf-SQUID had two junctions, a small junction intended to be the primary source of the non-linearity in the circuit and a much larger junction that is a consequence of the fabrication process. The critical currents of these niobium tri-layer tunnel junctions are heavily temperature dependent with critical current values expected to be 10 µA at 4 K and over 12 µA at 8 mK, leading to hysteresis parameters of 0.82 and 1.17, respectively. The inductive coupling of each rf-SQUID to its neighbours was found to be around 3 % in this design, so considering our previous studies this parasitic reactance will not significantly hamper performance.

We began this chapter by discussing an initial set of measurements performed in December 2022 at millikelvin temperatures. While the operating conditions were not ideal as the rf-SQUID's were expected to be hysteretic at these temperatures, the transmission of microwaves through the device was confirmed as well as the modulation of impedance by a flux bias. The losses observed in the transmission measurements of -2.2 dB/GHz correspond to shunt resistances across the rf-SQUIDs in the range 20-60 Ω. Importantly, some weak degenerate 3WM parametric amplification was observed for a signal at 5 GHz, although this was not seen at other frequencies. This implies that there are certain phase matching conditions in the device that depart from the idealised theory, most likely due to fabrication choices or limitations. While the apparent gain of approximately 2 dB is not very significant for application, it is confirmation of the principle of operation of the device and certainly enough motivation to pursue improved designs.

A later measurement in March 2023 carried out at 4 K sought to further characterise the wave mixing dynamics in the device with a more thorough dataset on transmission and harmonic generation. By concurrently measuring the current drawn through the device as well as the rf outputs, a value for the geometric inductance of 14.33 pH has been extracted from the measured current period value of 144.3 µA. This is approximately half of the designed value leading to an unavoidable impedance mismatch between the device and the measurement environment. Fortunately, the analysis of loss in the device could be carried out despite this by investigating the gradients of the line of best fit through transmission measurements at probe frequencies of 3.4, 8, and 12 GHz. It was found that losses matched the behaviour of a shunt resistance that was of similar magnitude to the expected value for

the normal state resistance of the large junctions included in the rf-SQUID's of around 10 Ω. Furthermore, the shapes of S21 magnitude periods for the three probe frequencies could be phenomologically reproduced by varying the shunt resistance used in the rf-SQUID, implying some frequency dependence that is likely linked to wave mixing effects. Initially these junctions were thought to not affect the performance of the device greatly, although these results imply that it may significantly hamper the operation of these devices.

Through the analysis of harmonic generation data from the device a value for the critical current of the small junctions in the device has been found. This was done by analysing specifically the second harmonic generation of an applied 3.4 GHz wave at a range of powers, in which the behaviour of a local minimum was analysed across a flux period. The minimum occurs between applied powers of -50 dBm and -55 dBm, close to the power that corresponds to the expected value of the critical current of the small junctions of the device, just as was the case for the previous device. This may indicate an underlying effect that has not been reproduced in simulations of these devices as of yet, possibly related to the modulation of characteristic impedance of the devices. As such, the critical current can be roughly fitted to the shape of the flux periodicity for which a value of approximately 14 µA was found. Through this analysis a bias that corresponds to a maximum in the 3WM nonlinearity around -100 µA was identified by a simultaneous maximum in second harmonic output power and minima in fundamental and third harmonic output powers.

The losses in the device have been noted to be quite considerable in these measurements, significantly diminishing the prospects of a design without alterations as an amplifier. It was hypothesised that these losses arise from quasiparticle generation caused by the formation of shockwaves in the array at input powers above -75 dBm, for which a set of simulations were performed to investigate. By first linearising the circuit, a set of relatively quick simulations could confirm the dependence of loss on frequency in the device, with each variable being indirectly proportional to the other. Then by simulating the harmonic generation in the device, the pair breaking behaviour of currents exceeding the critical currents could be examined and the quasiparticle population estimated. Using this information, an effective shunt resistance could be placed across a tunnel junction and the transmission at 8 GHz estimated through analytical relations. It was found that the simulated behaviour may well explain the trends seen in experiment. However, simulations imply that the quasiparticle generation effects should occur at much larger input powers, above -50 dBm, than was observed experimentally. This remaining discrepancy may be explained by the effects of reflected waves on the current amplitudes in the device. This effect has the potential to be rather damaging to the prospects of these devices as 3WM amplifiers due to the considerable limits this may put on dynamic range. However, with proper design and operation constraints it seems likely that this problem can be overcome and a successful device produced.

Link to ToC

Chapter 6

Proposed Travelling Wave Parametric Amplifier Designs

6.1 Introduction

So far in this thesis several problems have been identified in proposed and measured TWPA devices that we now seek to overcome in the design of future devices. In order of appearance, we have noted that harmonic generation of the pump wave and phase mismatch between the pump, signal and idler waves greatly hampers amplification. Furthermore, unavoidable parameter variations and impedance mismatches in fabricated devices have been shown to lead to undesirable effects that limit the operation and bandwidth of any device. Finally, in the measured devices not only have these previous problems been demonstrated but the additional effects of poor thermalisation, shockwave formation and quasi-particle generation that leads to losses have been shown. Without addressing these drawbacks it seems unlikely that a successful 3WM TWPA device can be produced.

Fortunately, these problems are not insurmountable and may be overcome in the design phase, so we now group them into two camps based on the approaches used to solve them. For thermalisation, parameter variation and impedance mismatches, we focus on the design of the fabrication processes used. Design of the lumped element circuit is then used to resolve the problems with harmonic generation and phase mismatch via dispersion engineering techniques, which will be discussed shortly. Due to these improvements, along with careful choice of operating parameters, the rate of quasi-particle generation and quasi-particle lifetime in the device should be minimised, leading to decreased losses per cell. Any remaining losses are overcome by simply ensuring that the amplification of the signal in every cell of the array is greater than its attenuation. Of course, the pump also experiences attenuation per cell, therefore to maintain the strong pump approximation a pump amplitude $> 20\,\mathrm{dB}$ larger than the signal must be maintained by the end of the array, despite amplification and losses.

Link to ToC

To maximise amplification in these travelling wave structures we plan to implement dispersion engineering techniques, which several research groups have successfully implemented in both JTWPA [15, 21, 102, 103, 154] and KITWPA [101, 106, 155, 156] devices. Dispersion engineering is a topic that has been studied for a long time, beginning with the study of the propagation of sound waves in crystal lattices [62]. The intentional engineering of dispersion relations for transmission lines was studied more extensively with the development of travelling wave antennas [84]. A solid theoretical description came with the works of Brillouin, Oliner and others which formalized the study of periodic loading of impedance or resonant structures on the propagation characteristics of transmission lines [88, 157]. This work has continued until today with research on metamaterials and double negative transmission lines a common topic [113].

As we have already shown in Section 2.3, the main issues to performance in TWPA devices have been phase mismatch between the pump, signal and idler and the loss of power to up-conversion of the pump. To maximise amplification we therefore want to position the pump tone so that it will have maximal phase mismatch with its second harmonic, and minimal phase mismatch with the other 3WM tones. This means that we would aim to minimise the relation:

$$\frac{k_p - k_s - k_i}{k_{2p} - k_p} \ , \tag{6.1}$$

where k is the wave vector of the pump (k_p), signal (k_s), idler (k_i), and pump's second harmonic (k_{2p}). This approach to dispersion engineering is generally achieved by the alteration of the wave impedance along the length of the medium to open photonic bandgaps (PBG). Waves with frequencies that lie within the PBG regions cannot propagate in the device without significant attenuation, the dispersion relations near these regions is also significantly distorted. Mixing with these 'forbidden frequencies' becomes very inefficient and so aligning the pump harmonics with the photonic band gaps allows for almost ideal three wave mixing between the pump, signal and idler.

An alternative method that focuses on the alteration of the polarity of the nonlinearity that leads to wave mixing has also been widely used in nonlinear optics [99]. This method, termed quasi-phase matching (QPM), has been applied to great effect in the production of up-converters with very high efficiency [99, 158]. It operates on the principle of the coherent build up of the signal wave, which would otherwise oscillate in amplitude due to the phase mismatch. By changing the sign of the nonlinearity responsible for wave mixing at the point where the signal would start to de-amplify in the transmission line the continuous increase of signal amplitude can be achieved.

We apply these methods of dispersion engineering to the scheme that seems most reasonable. For kinetic inductance based TWPA design, we focus on impedance based dispersion engineering as the implementation of this is much simpler in design of the device. The case is reversed for JTWPA design in which the implementation of QPM is achieved by simply reversing the orientation of the rf-SQUID. However, for both devices we must focus on the design of the lumped element circuit to ensure impedance matching and the physical geometry of the device to minimise parasitic effects and maximise thermalisation. As both

our KITWPA and JTWPA designs are lumped element circuits they are constrained by some similar factors, most notably an inherent cut-off frequency. We must set this to be large enough that all waves of interest have wavelengths equivalent to 10 unit cells or more, otherwise it may not act as a continuous structure [84].

6.2 Kinetic Inductance TWPA

Applications of superconducting films near the Superconducting-Insulating-Transition (SIT) have become much more widespread as the reliability of fabrication technologies has improved in the last two decades [159]. The basic science and theoretical description of the superconducting effects that occur in these ultra-thin and disordered films is itself an active area of study, although not our focus here. A common route for application of the anomalously high kinetic inductance prevalent in these films is their integration into superconducting devices to produce parametric amplifiers or single photon detectors [101, 160]. This section focuses on the analysis and design process of kinetic inductance travelling wave parametric amplifiers (KITWPA's) based on a simple microwave transmission line formed of ultra-thin superconducting films nears the SIT.

Despite some early interest in the use of the kinetic inductance of superconducting films as circuit elements in the 1960's there was no significant progress in this direction for several decades [71]. Proposals to produce high frequency photon detectors from arrays of superconducting resonators for astronomical surveys reinvigorated the field around the turn of the century [12]. The development of parametric amplification technologies using kinetic inductance grew alongside this as a method to efficiently amplify the weak signals from the detectors using devices with similar fabrication processes.

The early versions of these KITWPA devices are notable for their design simplicity, consisting solely of co-planar superconducting transmission lines [101, 106]. While it might be expected that the simple design would lead to high fabrication yield, this was prevented by the large length of the device required for amplification. These works were followed by attempts to decrease the length and improve the impedance matching of the devices to the environment. Some success was seen in this by changing the transmission line geometry and adding capacitive structures, essentially forming lumped element transmission lines [155, 161].

Greater interest arose in the devices with the demonstration of 3WM via the application of a dc bias [105, 106]. Recent demonstrations of wideband 3WM parametric amplification (potentially reaching the quantum limit of added noise [104]) makes these devices the state of the art for travelling wave parametric amplification [156]. Unfortunately, the difficulty and intricacy of this task has created a high barrier to entry and success in this research has been mostly limited to only a few groups.

We now discuss the background and design of these kinetic inductance travelling wave parametric amplifiers, beginning with the selection of the superconducting metal and the limits of predictive theory in this process. The optimal choice of transmission line geometry

and calculation of the impedance are then discussed, along with the inherent constraints that the structures must be designed under.

6.2.1 Survey of Superconducting Thin Films

As described in Section 1.2.4, the surface reactance of a thin superconducting film can be shown to take the form of a nonlinear inductance. The sheet inductance (sheet resistance) or inductance (resistance) per square is often used for its convenience in characterising thin films. The number of squares is defined as the ratio of the trace length to its width: $N_{sq} = l/w$, so a doubling of N_{sq} leads to a doubling of total inductance (resistance). Kinetic inductance per square is proportional to the normal state resistivity of the film, ρ_n and inversely proportional to its thickness, t and the superconducting energy gap $\Delta \simeq 1.78 k_B T_c$ where T_c is critical temperature of the superconducting film.

$$L_k = \frac{\hbar \rho_n}{\pi t \Delta} \ . \tag{6.2}$$

As superconductivity is a consequence of coherent electron states, a change on the length scale on which this can occur will of course have an effect on the superconducting state. Therefore, granular, ultra-thin or otherwise disordered films where the electron mean free path is reduced and the resistivity is high can reasonably be expected to exhibit the highest kinetic inductance.

We can use information on resistivity, critical temperature and thickness to estimate the kinetic inductance of a metal and so design an amplifier around this parameter. These measurements can be made for any film in a relatively simple way using the Van der Pauw 4-point probe configuration, shown in the Figure 6.1. This method removes the need for patterning of the films as the evenly spaced current and voltage probes can be used for a measurement of resistivity via a simple scaling if the inter-probe distance is much less than the distance to the film edge, $R_{\text{sheet}} = \pi R_{\text{meas}} / \ln(2)$.

Sheet resistance data collected using this method for titanium-nitride films deposited with different nitrogen content and thicknesses is shown in Figure 6.2. These films were shared with us by Prof Chen ChiiDong of Academica Sinica, Taiwan as part of a

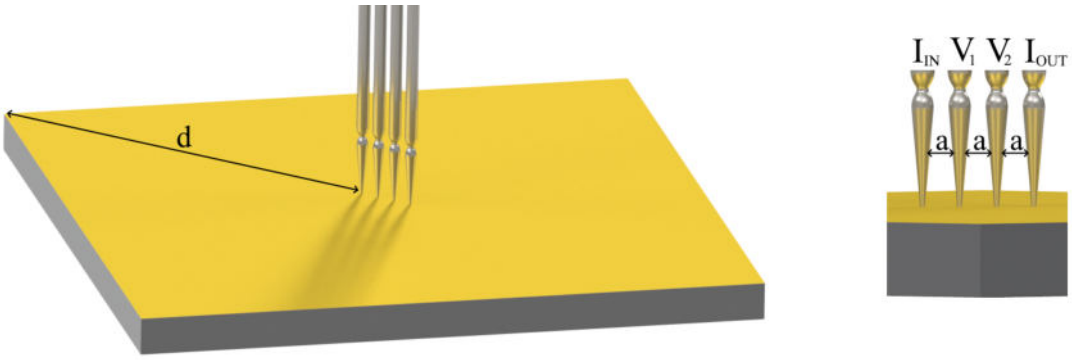

Fig. 6.1 Diagram of the Van der Pauw configuration of probes that be used to characterise films without additional fabrication steps.

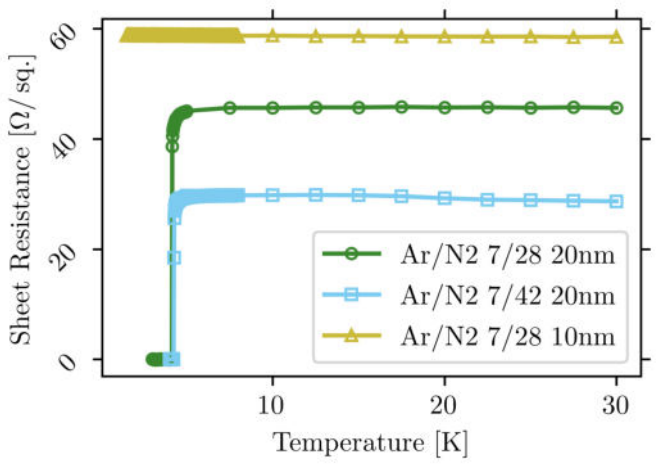

Fig. 6.2 Resistance per square versus temperature plots for three titanium nitride films deposited with different argon to nitrogen gas flow ratios and thicknesses. Different levels of disorder due to thickness or stoichiometry lead to different sheet resistances and by extension kinetic inductances.

collaboration to produce a KITWPA device. The kinetic inductance per square can then be estimated for these films as 9.9 pH, 15.5 pH, and >54.3 pH for the blue, green and yellow curves, respectively. These particular films are expected to have too high of a nitrogen content to be useful for KITWPA device fabrication, and further work on tuning the gas flows during deposition will be required before application.

Using similar methods, data for many superconducting films has been collected over the last few decades with some interesting anomalies found. For instance, the resistivity of ultra-thin films does not follow a linear relationship with the film thickness, with the superconducting properties being either enhanced [162] or diminished [159, 163] as the thickness decreases. A theoretical model is still required for this and the variety of other effects present in ultra-thin films, although a scaling law proposed by Ivry *et al.* has shown some predictive power and use in guiding fabrication [159]. The scaling law links film thickness, t to its sheet resistance, $R_\square$ and the superconducting transition temperature, T_c via two fitting parameters α and β.

$$t \cdot T_c = \alpha R_\square^{-\beta} \tag{6.3}$$

Shown in Figures 6.3 (a-c) are log-log plots of data for titanium nitride, niobium nitride and niobium titanium nitride films, extracted from publications using DataThief [164]. For these compound superconductors the relative proportions of the different elements can have a large effect on the superconducting properties. While the proportions are usually consistent within a given fabrication process it is not necessarily comparable between facilities. With this considered, the data presented in Figure 6.3 collected using DataThief can be considered a good guide but the associated error bars should be quite large, much larger than the error associated with lifting the data from the publications.

The ideal film would have high sheet resistance for relatively thick films (≥ 20 nm) and a critical temperature $T_c \geq 1$ K to ensure negligible real component of resistivity at milli-kelvin operating temperatures. Niobium titanium nitride [101, 106, 156] and niobium nitride [161] fit this criteria and have already been demonstrated several times for KITWPA devices. Titanium nitride is another excellent candidate with existing widespread

Link to ToC

fabrication capabilities, however the most promising material for investigation is arguably WSi [160] despite its rarity in application. The fitting parameters for these materials are found in Table 6.1.

Despite the usefulness of this scaling law for film selection, it provides little aid in estimation of kinetic inductance of these films as BCS theory does not well describe superconductivity near the SIT. For instance, the niobium nitride of [163, 166–168, 176] demonstrated a disagreement with BCS predictions of the kinetic inductance by almost a factor of two. This introduces a rather large uncertainty into the design of devices without thorough characterisation of the films.

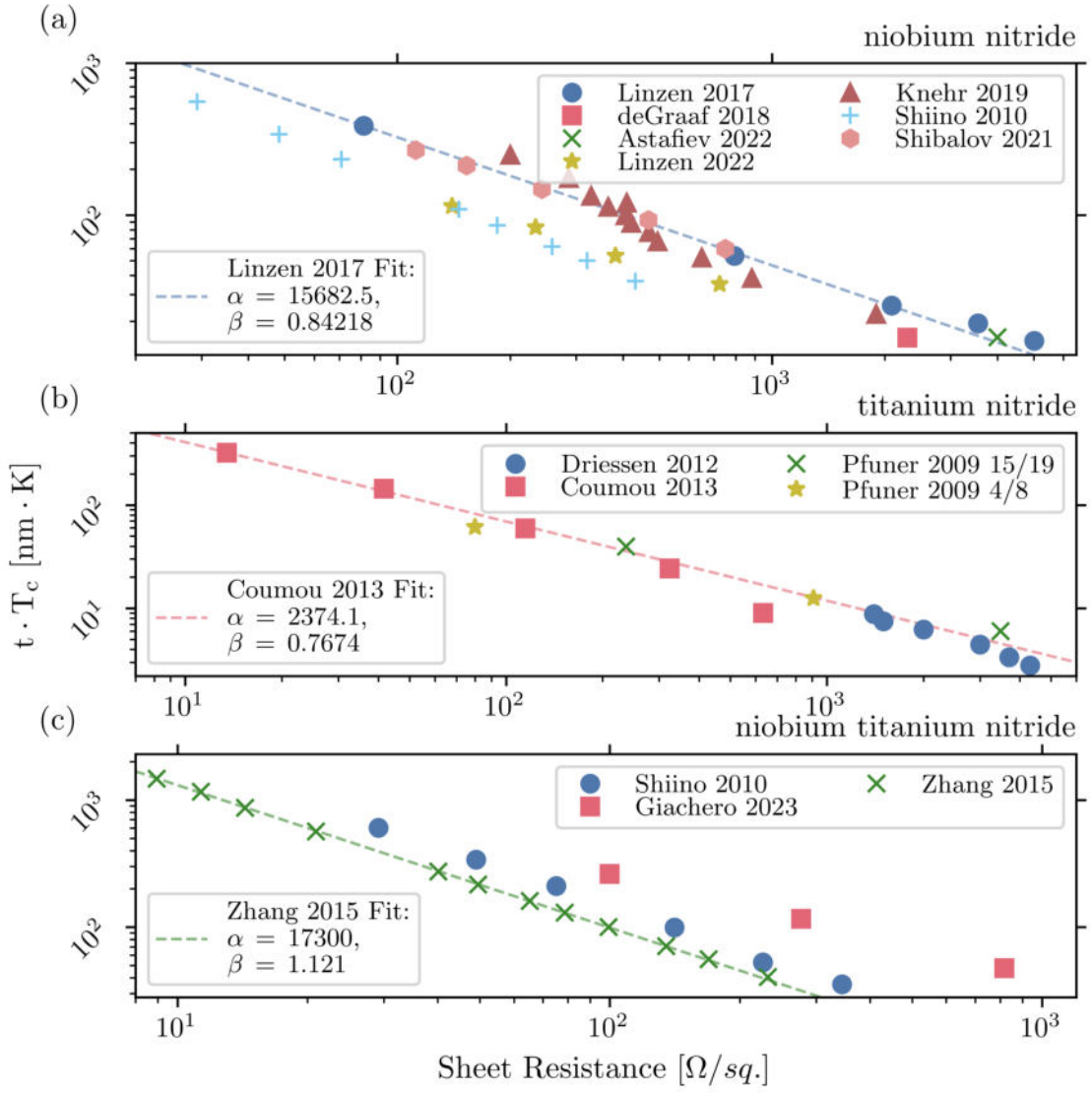

Fig. 6.3 (a-c) Plots of data collected from publications using DataThief to demonstrate the relation between sheet resistance, $R_{\square}$, and the product of film thickness, t, and its transition temperature, T_c. Data for niobium nitride collected from [163, 165–170], titanium nitride collected from [171–173] and niobium titanium nitride collected from [169, 174, 175].

Material	α	β	Publication
TiN	2374.1	0.767	[172]
NbN	15682.5	0.842	[163]
NbTiN	17299.4	1.121	[175]
WSi	44514.2	1.166	[160]

Table 6.1 Fitting parameters for a selection of compound superconducting films that predict the critical temperature and sheet resistance for a given film thickness using Ivry's scaling law [159]. Data was collected from published works using the DataThief program.

6.2.2 Wave Mixing with the Kinetic Inductance Nonlinearity

Four wave mixing can be achieved simply by modulating the parametric kinetic inductance element by alternating currents. To operate a KITWPA device in the three wave mixing regime a dc bias is required, which alters the kinetic inductance of Equation 1.50 to:

$$L_k = L_0 \left[1 + \frac{2I_{dc}}{I_{dc}^2 + I_*^2} I_{rf} + \frac{1}{I_{dc}^2 + I_*^2} I_{rf}^2 \right] , \tag{6.4}$$

where L_0 is the kinetic inductance with no applied current, I_{dc} is the applied dc, I_{rf} is the amplitude of the applied rf wave and I_* is estimated pair-breaking current for the line. The strength of the 3WM nonlinearity in this case is then:

$$\chi^{(2)} = \frac{2I_{dc}}{I_{dc}^2 + I_*^2} , \tag{6.5}$$

which will dominate in the wave mixing process on the condition that $I_{rf} \lesssim 2I_{dc}$.

An additional constraint for the operation of these devices is that the combined dc and rf currents in the transmission line should be lower than the critical current. This imposes lower power operation compared to the 4WM regime, although still much higher than the power at which most JTWPA's operate.

In order to simulate the device using the coupled mode equation method we can follow the same process as demonstrated for the Josephson nonlinearity. Of course, the kinetic inductance nonlinearity is considerably weaker so we would expect to see lower amplification per unit length. This also affects the normalization used to convert the currents used to dimensionless amplitudes, although it can take a similar form to a JTWPA's where:

$$I = \frac{\theta I_* A}{\pi} , \tag{6.6}$$

where I is the current amplitude of the wave, θ is the phase shift per unit cell for that wave, and A is the dimensionless amplitude of the wave. Although, instead of simulating these devices it may be most helpful to compare the designed device to other published works, which are summarised in Table 6.2.

Link to ToC

Physical Length [mm]	Electrical Length @ 5 GHz	Approximate Gain	Publication
200	423	15	[155]
100	60	6	[161]
330	589	16.5	[177]
50	85	15	[156]
86	184	20	[104]

Table 6.2 Example KITWPA results for NbTiN devices from published literature, including the total gain and electrical lengths over which it was achieved.

6.3 KITWPA Design

6.3.1 Superconducting Transmission Lines

While some of the early KITWPA devices were purely continuous transmission lines with no inherent cut-off frequency, at least not close to the range of operating frequencies, we will show that this is not fitting for our purposes. We choose to pursue a quasi-lumped element structure formed of a single, patterned superconducting film which should be free from much of the cell-to-cell parameter variation discussed earlier in this thesis. While the structure of this device is more simple, the design remains deceivingly complex due to the additional constraints of material selection and dispersion engineering. Much of the difficulty in the design of these transmission lines comes down to the large uncertainties in material parameters and the uncertainty in the calculation of wave impedance. Although the variation along the line is no longer as much of a concern, this uncertainty in design due to unknown material parameters may prove problematic on the first iteration of these devices.

The equations used to approximate the wave impedance and other properties of a given transmission line are experimental fits based upon the works of Wheeler [178–180]. The equations are fairly obtuse, although the associated uncertainties are lower than the uncertainties of material parameters in common industrial processes. However, these equations may be liable to over-fitting to normal metal devices or larger structures than we use [181].

The nanoscale structures used in the KITWPA devices are unlikely to be well described by any of the published transmission line impedance equations as they do not properly account for the effects of superconductivity or fringe field effects that occur at the edges of the structures. An alternative approach using an EM simulator may aid in this situation, but in practice such simulations may not resemble the realised device either. As such, the following section can be used as a guide in the design of these devices, but optimal impedance matching remains very unlikely without an iterative fabrication process.

6.3.2 Transmission Line Geometry

Shown in Figures 6.4 (a-c) are the co-planar, microstripline and inverted microstripline geometries, each of which have some advantage and disadvantage to their use for KITWPA's. Quasi-TEM (travelling electromagnetic) waves are supported in all and a small dispersion due to the asymmetries in the geometry and fringing of the fields at the trace edges is present in each.

The important quantities for these transmission lines are the characteristic impedance, Z, and the phase velocity, v_p, each of which will have some frequency dependence, although this should be negligible in the desired frequency range. Equivalent reactances per unit length can be found to describe the behaviour of the transmission line with the inductance and capacitance per unit length taking the form:

$$l = \frac{Z\sqrt{\varepsilon_r}}{v_c} \,, \tag{6.7}$$

$$c = \frac{\sqrt{\varepsilon_r}}{v_c Z} \,, \tag{6.8}$$

respectively, where ϵ_r is the relative permittivity of the dielectric material around the signal trace. The total impedance of a superconducting transmission line can then be found by including an additional kinetic inductance term in Equation 6.7.

The high kinetic inductance transmission line that we are interested in is unlikely to have sufficient capacitance per unit length to achieve $50\,\Omega$ impedance. To remedy this, microstructures can be added to the transmission line to increase the effective capacitance per unit length. This makes a quasi-lumped element transmission line where there is a mostly inductive central trace and mostly capacitive structures spaced evenly along the line.

Depending on the structure, the additional capacitance is achieved in different ways as shown in Figures 6.4 (d-f) for the co-planar, microstrip and inverted microstriplines, respectively. The increased complexity of the trace will consequentially lead to lower yield due to defects, especially for the co-planar due to the very large perimeter of the capacitive fingers [161]. Alternatively, the microstripline and inverted microstripline designs use capacitive pads with large area that are less prone to defects and involve simpler shapes, an important detail when considering the datasize of the design file. The inverted microstripline geometry is especially promising given the improved thermalisation, and protection of the transmission line from damage that may be achieved by fully enclosing it in dielectric.

However, this geometry cannot always be used as deposition of a top dielectric layer can sometimes 'kill superconductivity' in ultrathin films. We have pursued for our designs a microstripline design for ultrathin traces and where possible an inverted microstripline design that can be used for thicker trace layers.

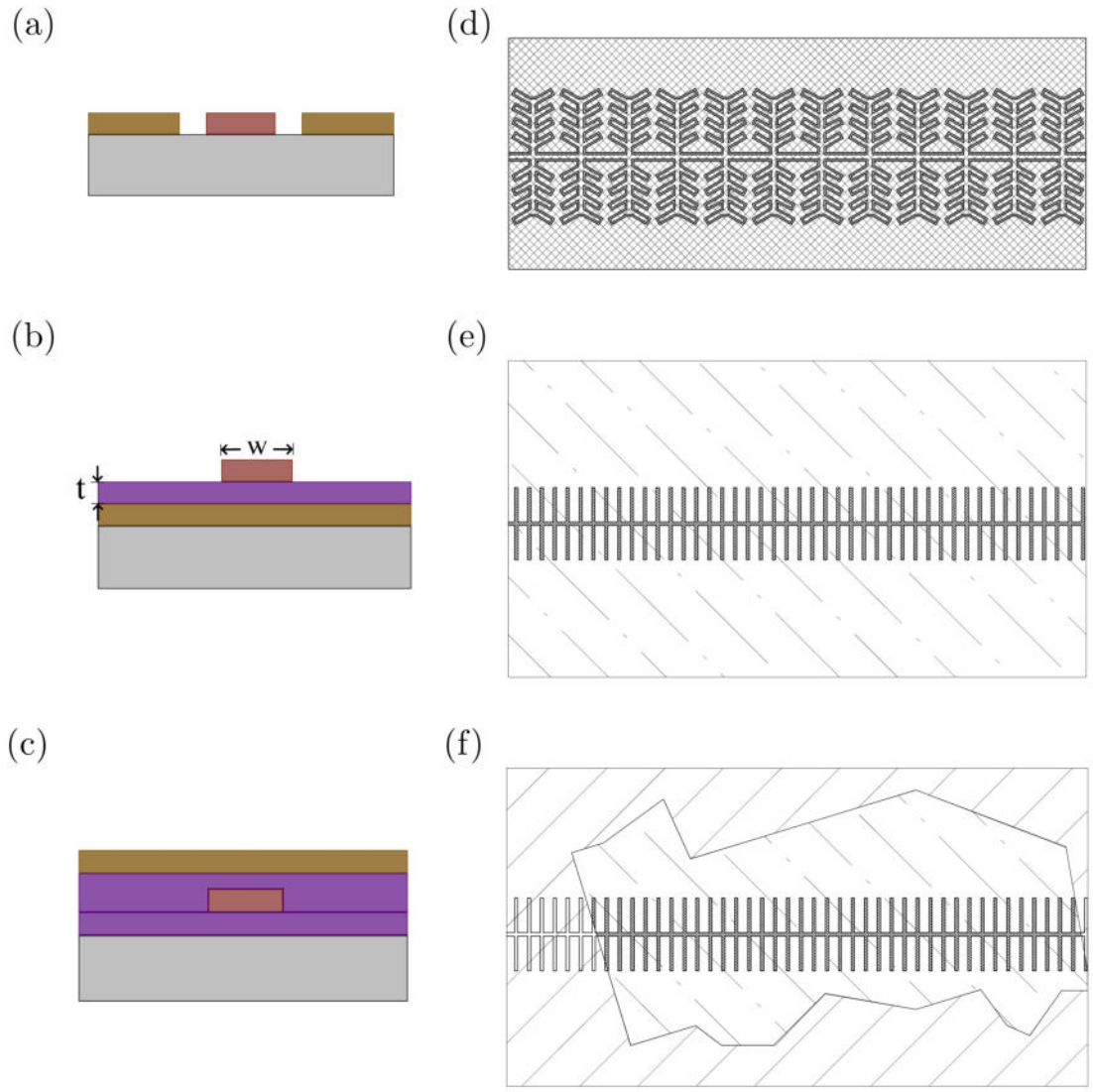

Fig. 6.4 (a-c) Cross-sections of co-planar, microstripline, and inverted microstripline transmission line geometries where the substrate is coloured grey, ground plane bronze, dielectric purple and trace is red. (d-f) The structures that would be required to impedance match these geometries in the case of a high kinetic inductance trace where co-planar geometry has large perimeter fingers while microstripline and inverted microstripline structures have large area fingers added at intervals such that capacitance per meter is high enough to achieve 50 Ω impedance.

6.3.3 Microstripline Impedance Approximation

Presented here is the industry standard impedance approximation for the chosen microstripline and inverted microstripline structures. This approximation is based on the work of Hammerstad and Jensen, with various improvements added from several sources [180–186]. The formulas presented below may be used to narrow the range of potential geometries after which the final geometry can be determined using an EM Simulator like TNT or COMSOL.

Starting with the microstripline geometry we first find the effective dielectric constant of the medium, ϵ_{eff}, which accounts for the portions of the fields present in the air or the substrate. This depends on the ratio of the width of the trace, w, to its height above the ground plane, h. If $w < h$:

$$\epsilon_{eff} = \frac{\epsilon_r + 1}{2} + \left(\frac{\epsilon_r - 1}{2}\right) \cdot \left[\sqrt{\frac{w}{w + 12h}} + 0.04\left(1 - \frac{w}{h}\right)^2\right] , \tag{6.9}$$

or if $w \geq h$:

$$\epsilon_{eff} = \frac{\epsilon_r + 1}{2} + \left(\frac{\epsilon_r - 1}{2}\right) \cdot \sqrt{\frac{w}{w + 12h}} . \tag{6.10}$$

The effective width of the trace, w_{eff}, is used as a correction for the fringing that is present at the edges of the trace.

$$w_{eff} = w + \frac{t}{\pi} \ln\left(\frac{4e^1}{\sqrt{\left(\frac{t}{h}\right)^2 + \left(\frac{t}{w\pi + 1.1t\pi}\right)^2}}\right) \cdot \left(\frac{\epsilon_{eff} + 1}{2\epsilon_{eff}}\right) \tag{6.11}$$

The impedance of the microstripline takes the form:

$$Z = \left(\frac{\eta_0}{2\sqrt{2\pi}\sqrt{\epsilon_{eff} + 1}}\right) \cdot \ln\left(1 + \frac{4h}{w_{eff}}\left[A + \sqrt{B}\right]\right) , \tag{6.12}$$

where η_0 is the impedance of free space, and:

$$A = \left(\frac{4h}{w_{eff}}\right) \cdot \left(\frac{14\epsilon_{eff} + 8}{11\epsilon_{eff}}\right) , \tag{6.13}$$

$$B = \left(\frac{4h}{w_{eff}}\right)^2 \cdot \left(\frac{14\epsilon_{eff} + 8}{11\epsilon_{eff}}\right)^2 + \frac{\epsilon_{eff} + 1}{2\epsilon_{eff}}\pi^2 . \tag{6.14}$$

For an inverted microstripline the derived impedance is altered to include the effects of an adjusted filling factor for the now symmetric dielectric layers around the trace:

$$Z_{inv} = Z \cdot \left[e^{-2b/h_1} + \frac{\epsilon_r}{\epsilon_{eff}}\left(1 - e^{-2b/h_1}\right)\right]^{-1/2} , \tag{6.15}$$

Link to ToC

where b is the difference between the total height of the dielectric, h_2, and the height of the trace above the ground plane, h_1.

$$b = h_2 - h_1 \tag{6.16}$$

The total impedance of a superconducting trace in such a geometry can then be found by finding the capacitance and inductance of the line per unit length from Equations 6.7, 6.8 as well as the expected kinetic inductance per unit length for the trace,

$$Z = \sqrt{\frac{l + l_k}{c}} \ . \tag{6.17}$$

As fields become more concentrated on the ground plane at higher frequencies the kinetic inductance of the ground plane should also be considered, but this should be a small effect in most microwave designs.

6.3.4 Capacitive Fingers

There are certain design parameters that must be set for whatever transmission line geometry is chosen, discussed here are the parameters related to the capacitive fingers. The stack-up for an example device is described in Figure 6.5 where a thin, high-kinetic inductance trace is sandwiched between two layers of dielectric and a ground plane with capacitive finger pads added along its length. Other than layer thicknesses the key parameters to be set are trace width, w_t, finger length, l_f, finger width, w_f, and spacing between fingers, D_f. Trace width and finger width are equal for simplicity and are set depending on the desired current density and operating power of the device. Finger length is chosen to achieve $50\,\Omega$ impedance, determined by finding the capacitance per unit length of the trace with the methods previously described. The main constraints in finger length are merely that fingers should not contact neighbouring traces or other fingers, additionally the finger spacing must be carefully chosen to ensure good performance in the device.

The capacitive fingers that are shown in Figure 6.5 (a) cause an abrupt change in the current density through the trace. The current paths must curve at these mismatches which creates a fringe field at the corners of each finger. Should the fingers be close enough together that the fringe fields at neighbouring corners overlap then each finger essentially loads the other and a capacitive series reactance is formed [181]. This same effect may cause hotspot formation in superconducting traces as the current paths are concentrated into smaller cross-sections and the applied current rises above the critical current density for the trace [174].

In order to avoid such an effect, fingers must be spaced further apart, leading to higher total inductance and total capacitance per cell and a lower cut-off frequency for the transmission line. Some groups have used a rule-of-thumb from microwave circuit design that these fingers should be spaced three times the width of the trace apart, however most

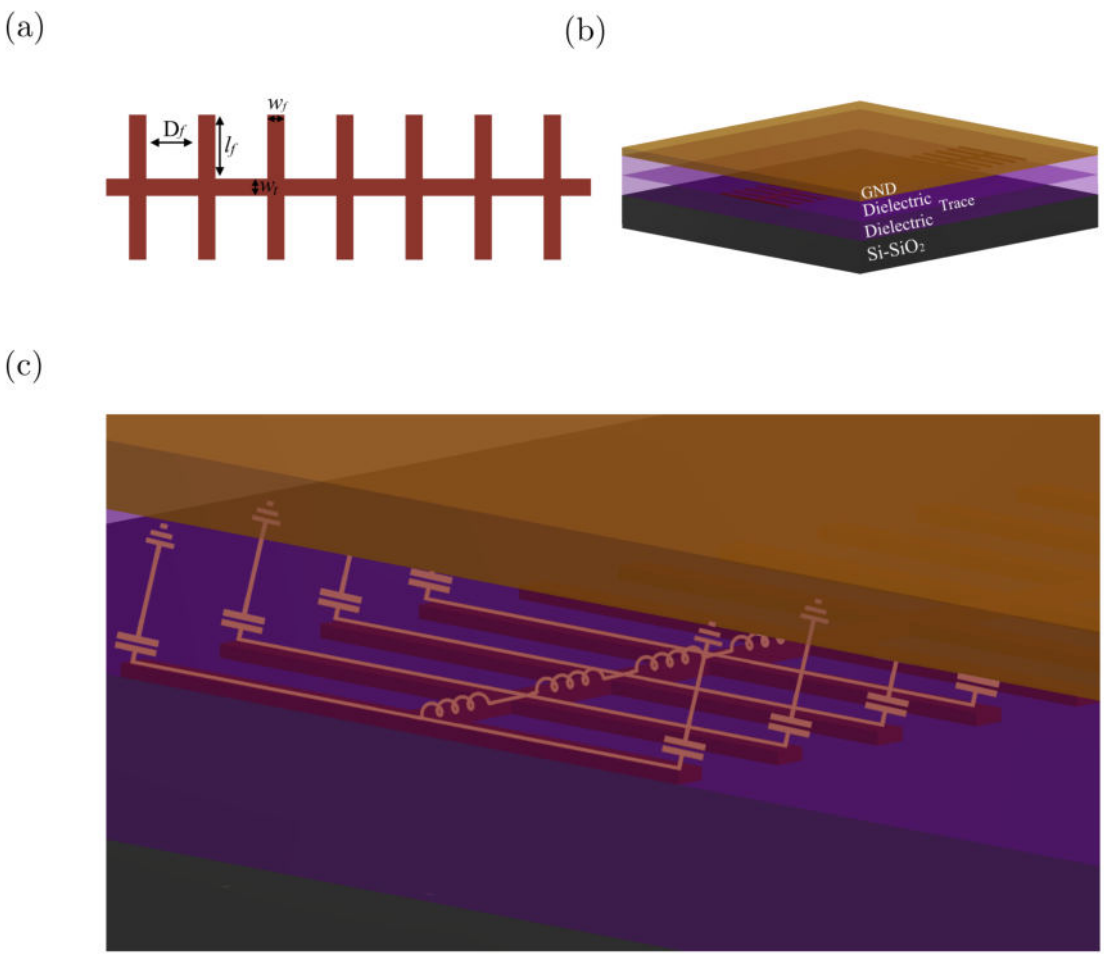

Fig. 6.5 An inverted microstripline requires added capacitive shunts to the central trace in order to increase capacitance per unit length for impedance matching. (a) Geometry of the trace with fingers where finger spacing, D_f is set by the trace width, w_t and the dielectric properties, while finger width, w_f and length, l_f can be tuned as necessary. (b) Layer stack-up of the inverted microstripline structure where the trace with fingers is sandwiched by two dielectrics (ideally of the same material) and topped with a ground plane and (c) the circuit diagram overlaid on the structure in which the trace acts predominantly as an inductance while the fingers act predominantly as capacitances.

successful devices opt for a larger separation, roughly equal to 8 times the trace width [104, 156, 181, 187].

Smaller finger spacing is desired to decrease finger length and increase cut-off frequency, so some guide on the minimum required spacing for good performance would be useful during design. It is known from microstrip patch antenna design that fringe fields decrease with decreasing dielectric thickness between the trace and ground. This effect, which should have some frequency dependence, is not very well described in literature, even more so when regarding superconducting traces [188, 189].

In order to produce some sort of guiding principle for the design of KITWPA devices, a series of microstrip pairs have been simulated in TNT to find the mutual- and self-capacitance per unit length of the strip. This method underestimates the mutual capacitance between microstrip fingers as it does not simulate the fringe fields at the points where the

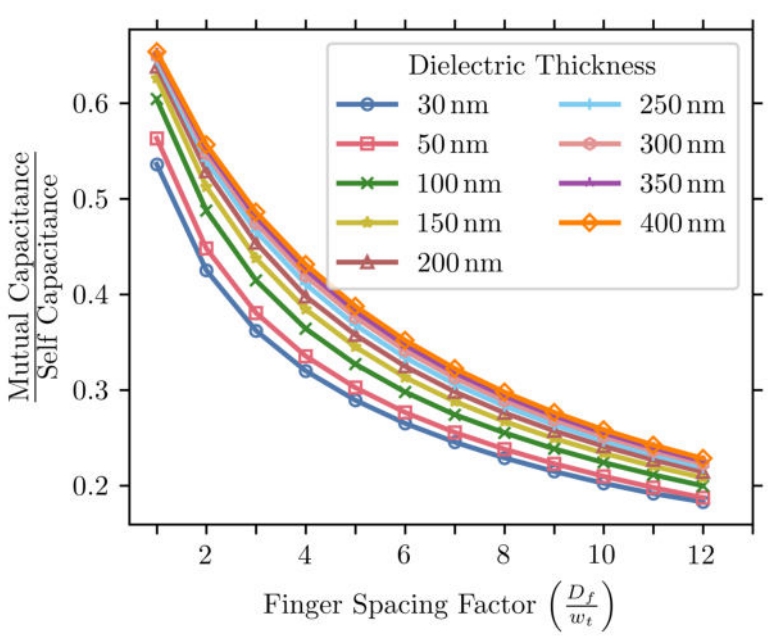

Fig. 6.6 Plot of the mutual capacitance between two edge coupled microstrips normalized to the self-capacitance of a single microstrip against spacing between capacitive fingers, D_f, normalized to the trace width, w_t. The simulation is repeated for a series of dielectric thicknesses from 30 nm to 400 nm but other parameters remain constant with trace width set at 250 nm and dielectric constant at 8.8.

fingers meet the trace. However, the effects of dielectric thickness and finger spacing can be studied and compared to similar published devices that have performed well.

Figure 6.6 shows the simulation results of this with the mutual capacitance per unit length plotted as a fraction of the self capacitance per unit length for a series of dielectric thicknesses and trace spacings. Using this result, we can expect that decreasing the dielectric layer thickness of ~ 200 nm and finger spacing of $8w_t$ seen in published devices in [104] and [156] to our desired ~ 30 nm and $6w_t$, respectively, should not lead to a detriment in performance.

6.3.5 Trace Layout

Many superconducting devices that require lengths of transmission line for resonators or otherwise tend to organise the structures in a meandered pattern. This layout has two benefits in that it minimises the space required for the device and neighbouring portions of the transmission line have waves travelling in opposite directions, preventing coupling between the two lines. However, it does not suit most KITWPA devices to use this pattern as the very long length of transmission line required for amplification necessitates that the corners of the meander become quite sharp, leading to an impedance mismatch at each bend.

An alternative layout makes use of a double spiral structure where corners are absent and curvature can be engineered to be minimised at all points in the line. The transmission line layout, shown in portions I and IV of Figure 6.7, is an Archimedes spiral in which the radius at a point, r, is a function of the angle off the horizontal at that point.

$$r = a + b\theta \tag{6.18}$$

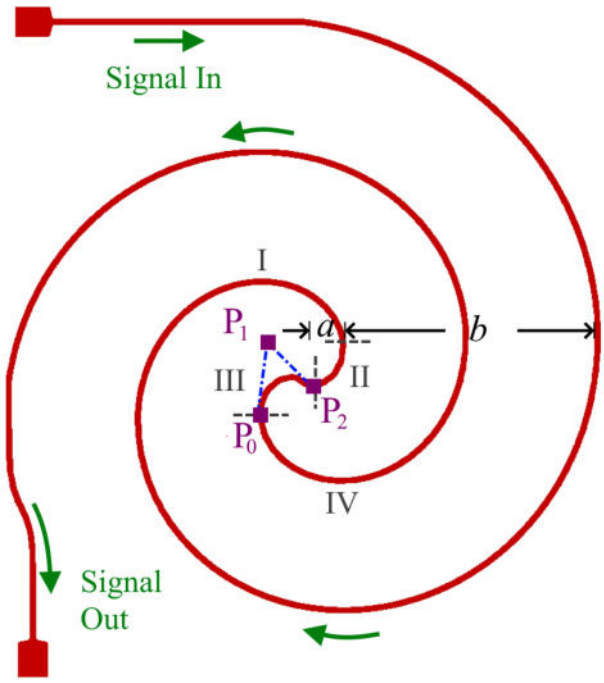

Fig. 6.7 Figure showing the layout of the superconducting transmission line that can be used for KITWPA devices to minimise parasitic reactances and maximise length. Portions I and IV of the transmission line are Archimedes spirals in opposing directions, separated by a distance a from each other at the origin and neighbouring lengths separated by a distance $b/2$. The centres are then joined by two Bézier curves that minimise curvature near the origin and prevent neighbouring capacitive fingers from contacting. The points that define the Bézier curve in segment III are marked as P_0, P_1 and P_2.

The constants a and b set the offset of the inner point of the spiral from the origin and the separation between turns, respectively. In the case of the double spiral, neighbouring portions of the transmission line will be separated by a distance $b/2$ and the two endpoints of the double spiral will be separated by a distance a at the centre.

It is possible to set the parameter $a = 0$ and so that double spiral is continuous, although the large curvature near the origin leads to the capacitive fingers contacting in some designs. To avoid this and minimise the curvature near the origin, centre separation is set to be a couple hundred micrometers, $a \sim 200\,\mu\text{m}$, and a Bézier curve is used to join the two halves of the spiral. As a function of the fraction of the total curve distance traversed, $0 \leq t \leq 1$, each point on the Bézier curve, B, can be found from a set of three points that define the curve. The start point, P_0, and the end point, P_2, of the curve and the point where the tangents to the curve at each of the other points meet, P_1.

$$B(t) = (1-t)^2 P_0 + 2(1-t)\,tP_1 + t^2 P_2 \tag{6.19}$$

The gradient of the Bézier at P_2 should be unity to minimise curvature and prevent fingers contacting each other. This curve, shown in portion II of Figure 6.7, can then be mirrored in the x- and y-axis to produce portion III of the trace and optimally join the two halves of the spiral.

In order to add the capacitive fingers along the spiral, the normal to the curve in the x- and y- coordinates must be found.

$$n_x = -\frac{dy}{d\theta}\left(\frac{1}{\sqrt{\left(\frac{dx}{d\theta}\right)^2 + \left(\frac{dy}{d\theta}\right)^2}}\right) \tag{6.20}$$

Link to ToC

$$n_y = \frac{dx}{d\theta}\left(\frac{1}{\sqrt{\left(\frac{dx}{d\theta}\right)^2 + \left(\frac{dy}{d\theta}\right)^2}}\right) \tag{6.21}$$

Then the points for the track and fingers are found by multiplying these normals by the desired offset.

As this design is fairly compact, additional structures can be added to the device such as a $\lambda/2$-resonator which would allow for the study of some material parameters not easily extracted otherwise. Furthermore, a very short version of the transmission line can be added in which no significant wave-mixing should take place. This can be used to calibrate the system to a similar structure as the KITWPA and remove some uncertainties around impedance mismatches at the bonding points [134].

6.3.6 Impedance Based Dispersion Engineering

The chromatic dispersion of both plain microstrips and lumped element transmission lines are present in the quasi-lumped element KITWPA device so far described. As discussed in Section 1.2.1, this dispersion prevents optimal parametric amplification due to a phase mismatch between the waves involved in the three wave mixing process. The other aspect of the parametric amplifiers that prevents optimal amplification is the up-conversion of the pump frequency into its harmonics, a wave mixing process for which the efficiency is related to the phase mismatch between the pump and its harmonics. In order to design an optimal KITWPA device, we should aim to minimise the phase mismatch between the pump, signal and idler waves and maximise the mismatch between the pump and its harmonics. This can be achieved via dispersion engineering.

Inserting resonant structures periodically along a transmission line can distort the dispersion relation at the resonant frequency and prevent up-conversion if the pump frequency is $\sim f_{res}/2$ [102]. Correct alignment of resonator positioning and centre frequency can be challenging if material parameters are uncertain, so alternative designs without such complications are more sought after.

Periodic modulation or loading of the transmission line impedance is much more easily achieved and leads to similar effects, although the distortion of the dispersion relation around the resonant frequency is generally weaker. The periodic change in impedance causes forward and backward propagating waves in the transmission line to interfere, leading to the opening of a photonic band gap (PBG) [157]. Waves with frequencies that fall within the PBG, where the width of the PBG is set by the impedance change and the centre frequency set by double the period of modulation (or quadruple the interval of loading) cannot propagate in the transmission line. Examples of this PBG around 18 GHz are shown in Figure 6.8 for both the impedance modulation technique (a and c) and the impedance mismatch technique (b and d), where the phase shift per cell is found by unwrapping the phase shift derived from the ABCD transfer matrix method. Unwrapping refers to taking the sum of the magnitudes of the difference of points in the dispersion

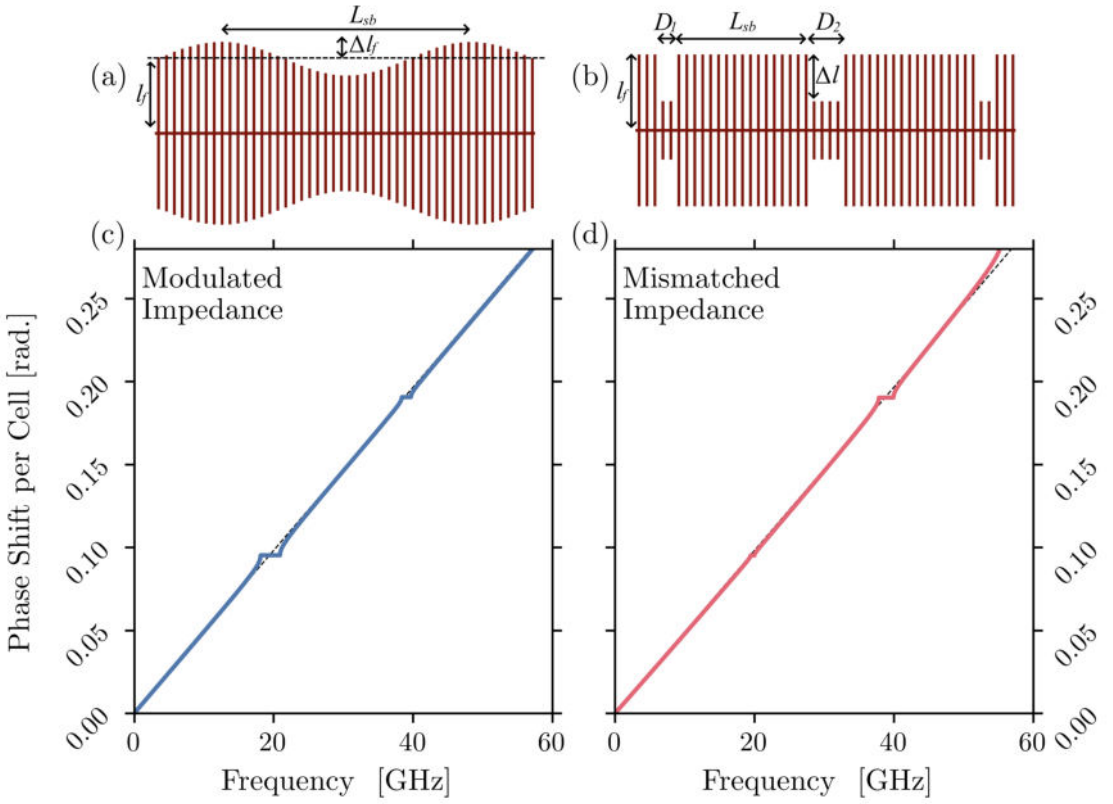

Fig. 6.8 (a) Modulation of the length of the capacitive fingers over a period of $L_{sb} = 1750\,\text{nm}$, l_f by a factor Δ (0.3) leads to the opening of a photonic band gap in the dispersion relation shown in (c) at a frequency that corresponds to a wavelength $2L_{sb}$ on the transmission line. (b) A similar effect can be achieved by discrete periods of shortened (or lengthened) fingers in which a stopband is opened at a frequency with a wavelength corresponding to $4L_{sb}$ as shown in (d).

relation obtained from the ABCD-matrix method. It should follow:

$$f\left(k\right) = \sum_{n=0}^{N} \left| k_{(n+1)} - k_n \right| \ . \tag{6.22}$$

.

Each dispersion engineering technique creates a PBG at the designed frequency and its harmonics, however they have opposite trends in that the widths of the PBGs created by impedance modulation decrease with order and vice versa for the impedance mismatch technique. For the impedance mismatch technique the second PBG can be widened further if every second impedance mismatch is slightly wider than the previous, as demonstrated in Figure 6.8 where $D_1 \neq D_2$.

While the modulation and mismatch factors used for these figures (30 %) are exaggerated for clarity, there are some key differences that should be noted. Mainly, the impedance modulation technique has wider peaks at the PBG's which makes the 3WM phase matching at all frequencies much worse compared to the mismatch technique, as can be seen by comparing Figures 6.9 (a) and (b). Shown in Figures 6.9 (c and d) is the difference in the phase shift per cell for a transmission line with and one without any dispersion engineering.

Link to ToC

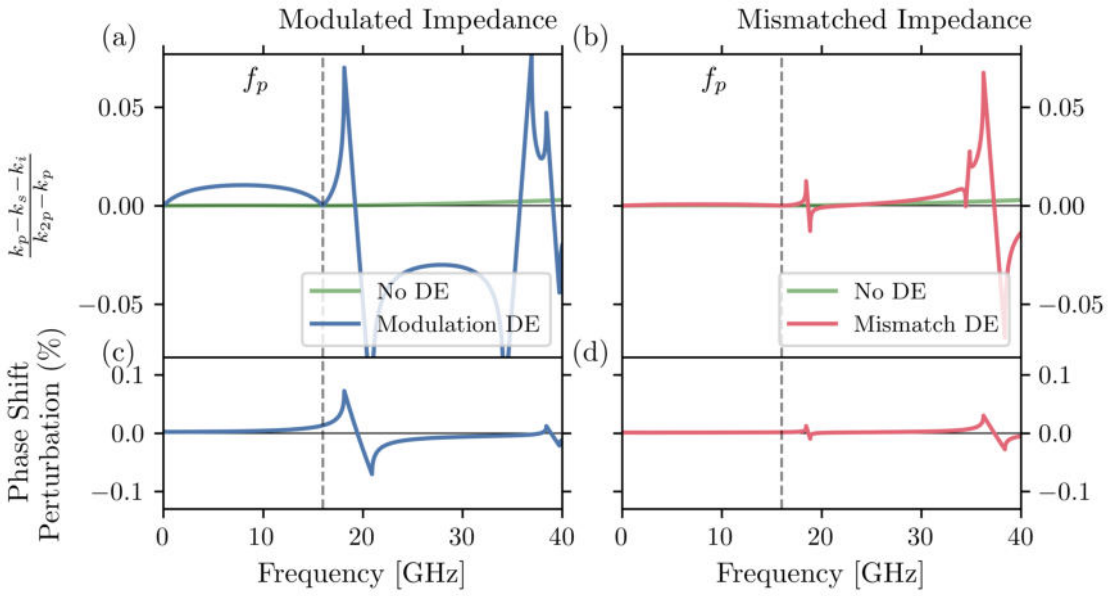

Fig. 6.9 Plots of the ratio of the phase difference in the 3WM amplification process to the phase difference between the pump and its second harmonic for the KITWPA that uses modulated impedance dispersion engineering in (a) and mismatched impedances in (b). The modulation and impedance mismatch factor corresponds to a 30 % change in the lengths of the capacitive fingers, this is an exaggerated value chosen for clarity. (c and d) The percentage difference of the phase shift per cell against frequency for the dispersion engineered lines with respect to the transmission lines without dispersion engineering.

The mismatch technique therefore is the optimal candidate for dispersion engineering in TWPA devices, contrary to the current trends in the technology [103, 104, 156].

The optimal dispersion engineering scheme for any chosen pump frequency can be found through an iterative process of minimising the quantity given by Equation 6.1 against the impedance modulation or mismatch factor. Alternatively, to maximise amplification in operation, the pump frequency can be tuned within a range around the first PBG so that a minimum in Equation 6.1 is maintained for all signal frequencies [110].

6.3.7 Design Process

Many approaches can be taken in the design of the KITWPA devices so far described, one of which is presented in the flow chart of Figure 6.10. A large parameter space exists for the device design, so it is most useful to constrain ourselves to setting just three parameters from which the rest arise as a consequence. Beginning with a known impedance (50 Ω), a cut-off frequency (~ 100GHz) with mostly linear dispersion in the C and X bands, and a finger spacing factor of 6 as previously justified, we can determine the trace thickness from the required kinetic inductance per square:

$$f_c = \frac{1}{2\pi} \frac{w_t}{D_f} \frac{Z}{L_{k\square}} \ . \tag{6.23}$$

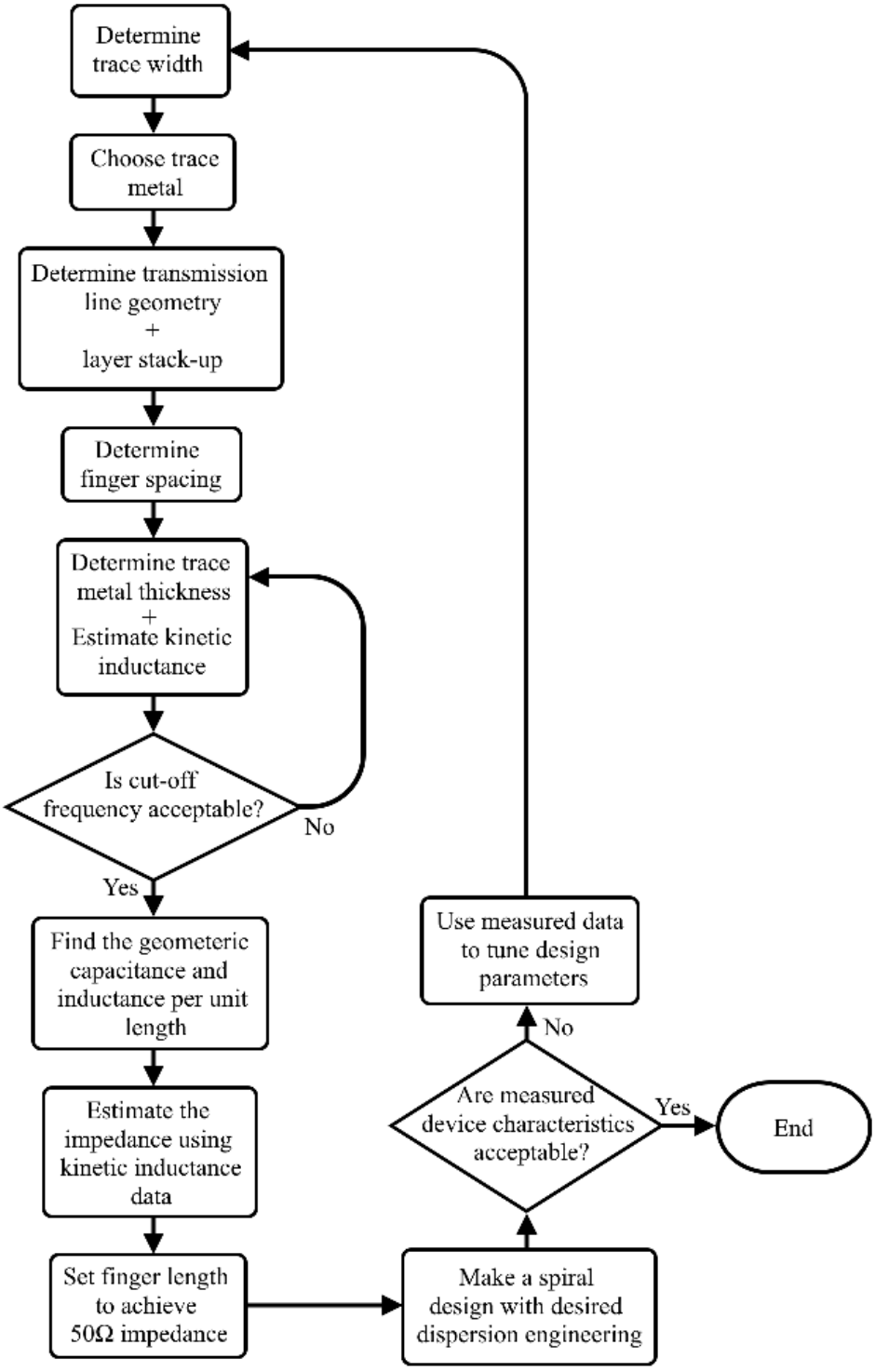

Fig. 6.10 Flowchart of the design process for a KITWPA device that begins with decisions on the materials and design parameters before becoming an iterative process to determine optimal trace metal thickness to set kinetic inductance. Once a device is fabricated and measured it is likely that the estimates for material characteristics can be improved which can be included in device designs for further fabrication runs.

Link to ToC

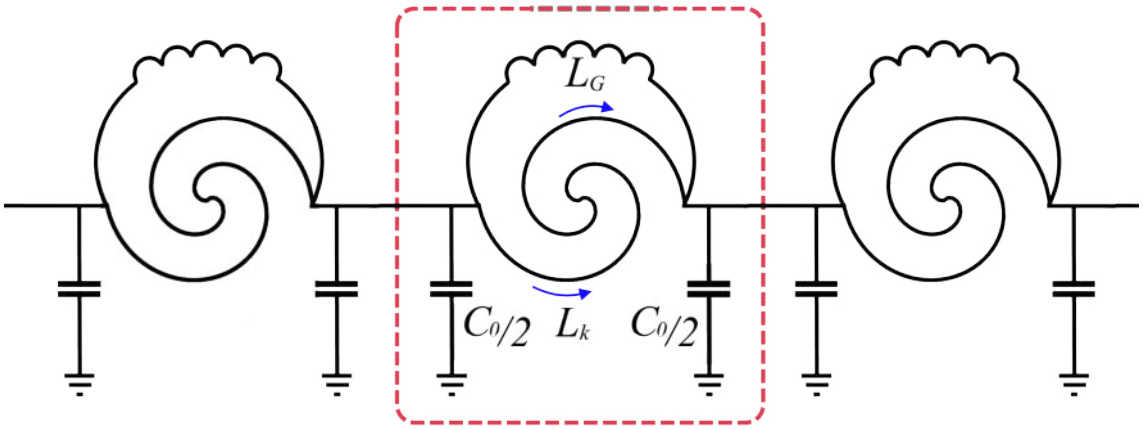

Fig. 6.11 An alternative approach to KITWPA design using a lumped element structure formed of a capacitance to ground, C_0, and a series arm consisting of a geometric inductance, L_G, in parallel with a large kinetic inductance element, L_k, which provides the desired nonlinearity for wavemixing. So long as $L_k \gg L_G$ the kinetic inductance should not affect the impedance of the transmission line, removing the largest uncertainty in the design.

This arises as a consequence as, regardless of the trace width w_t, the capacitance per cell of the quasi-lumped element transmission line must increase or decrease to match the kinetic inductance and maintain a $50\,\Omega$ impedance. The actual width of the trace, w_t is irrelevant, and can be set alongside trace thickness so that the total current density is lower than the pair breaking current density at the desired operating power. This process is necessarily iterative to find an acceptable trace thickness, although a large uncertainty in kinetic inductance values in ultra-thin films may prove a limiting factor in the success of these designs.

The condition of Equation 6.23 essentially disqualifies the highest kinetic inductance films from consideration. Furthermore, many of the most interesting films have large uncertainties in the kinetic inductance per square that may be achieved, even between runs on the same fabrication equipment. To overcome these drawbacks and persist with the use of the most novel materials in these devices an alternative, truly lumped element design may be pursued.

By shunting a high kinetic inductance element with a linear geometric inductance the uncertainty in the material parameters may be reduced and impedance matching ensured through good design. This is shown schematically in Figure 6.11, where a lumped element transmission line similar to the JTWPA studied in previous sections is formed of a kinetic inductance element replacing the Josephson elements of rf-SQUID's. The ratio of the geometric to kinetic inductances may be chosen to maximise the nonlinearity in the design or to err on the side of caution by ensuring impedance matching, providing an additional degree of freedom to the designer. However, the nonlinearity of the line is therefore inversely proportional to the ratio of geometric to kinetic inductances. As we wish for a highly nonlinear inductance in the transmission line this marks a distinct downside of this design. However, the added confidence with which a device may be produced makes such a design useful for applications where iteration or additional fabrication steps are undesirable, for instance single photon detectors.

Link to ToC

6.3.8 Discussion

This section has covered the understanding and design of a proposed kinetic inductance travelling wave parametric amplifier (KITWPA) that can operate in the three-wave mixing regime. The identification and selection of the superconducting films for use as the high-kinetic inductance elements in the device has been discussed. To this end, a scaling law that relates transition temperature and film thickness to the sheet resistance of ultra-thin films aided in the prediction of superconducting properties and expected values of kinetic inductance in the chosen films. Uncertainty in the superconducting properties of the thin films of greatest interest (niobium nitride, niobium titanium nitride etc.) alone makes the accurate prediction of device performance very unlikely.

A significant obstacle to success in making these devices is the impedance matching of the high-inductance transmission line to the measurement circuitry, which has been achieved via the addition of capacitive fingers to the transmission line structure. The parasitic effects that can arise from the spacing of these fingers and the layout of the transmission line have been discussed and the process of their minimisation described. Periodic changes in impedance, also referred to as dispersion engineering techniques, have been described and a justification for their inclusion in the device design made. The most popular dispersion engineering techniques of impedance modulation and impedance mismatches have been compared, with periodic impedance mismatches proving to be the optimal choice for this type of amplifier. The iterative process to optimize the design of these devices has also been given that initially makes use of material parameter estimations and replaces these with measured values after characterisation of a device.

There are several open questions in terms of the physics of the ultra-thin films and granular films that demonstrate anomalously high kinetic inductance, making prediction of their properties in these devices quite difficult without repeated characterisations. Further to this, it has been shown that due to the $50\,\Omega$ impedance matching constraint it is not worthwhile to use these most interesting films as the chromatic dispersion in such a continuous device would be very large. An alternative KITWPA design has been proposed which is more similar to the lumped element rf-SQUID based travelling wave parametric amplifier described elsewhere in this thesis. In this case, an ultra high-kinetic inductance spiral element would shunt a much smaller geometric inductance, with each individual cell being separated by a capacitance to ground. In this design the kinetic inductance element would not affect the impedance matching so long as it is much greater than the geometric inductance, furthermore its large uncertainty would no longer prove to be so detrimental.

The tools developed for design, analysis and simulation of KITWPA devices developed in this thesis are available for use from [190]. By making these tools available I hope to reduce the time taken to understand and design successful devices in the work of other graduate students. I do this as I have found that most work on this topic, while difficult, confusing and frustrating, is certainly not novel. Much of the theoretical work was already completed on the kinetic inductance of thin films and the wave propagation in metamaterials decades ago. Therefore, with this head start perhaps the hidden novelties in these topics can be pursued more straightforwardly by future investigators.

Link to ToC

6.4 rf-SQUID TWPA Design

The dominant topic of this thesis has been the study 3WM in rf-SQUID based travelling wave parametric amplifiers, and specifically why proposed and produced devices have not functioned as desired. I now aim to finish this thesis with a proposal for a 3WM device that should actually work, overcoming all the problems laid out so far in our studies. The previous KITWPA device is likely to be more robust to non-idealities and fabrication limitations than the rf-SQUID devices. However, the added complexity of fabrication comes with an increase in the nonlinear inductance that may be achieved as the kinetic inductance of thin films is theoretically limited to at most a 17% change due to applied currents. There is no such constraint in rf-SQUID's, where if the hysteresis parameter is selected correclty a degree of modulation of the total inductance may be close to 100%. Therefore, the use of rf-SQUID's remains very desirable due to the possible reduction in transmission line length and miniaturisation of the amplifier device. Although it is perhaps better put that longer devices have distinct disadvantages, including larger chance of defects, parameter variation and a longer distance for losses to deplete the pump wave.

As has been repeatedly stated throughout this thesis, all published JTWPA devices with purported gain have operated in the 4WM regime. The previous chapters have made the case that this is not just a consequence of phase mismatches or harmonic generation but instead on the fundamental mode of operation of 3WM in JTWPA's. The quasi-particle losses that are shown to be present in the TWPA devices lead to more loss of the signal wave per cell than possible gain. We cover in this section a scheme that should reverse this trend, showing that significant amplification may be achieved in a device, even with non-negligible losses.

To achieve this result we have focused on a dispersion engineering technique that does not distort the dispersion relation of the medium, as the impedance based techniques would do. Instead, using the phase mismatch between the pump, signal and idler to set a period of modulation of the wave mixing sign we can achieve coherent build up of a signal wave across the length of a device. This QPM technique has previously been proposed for application to rf-SQUID based TWPA's [125, 191], although no one has so far implemented it or studied it in the way that we do here.

This section starts with a brief description of the dispersion engineering technique that is implemented, followed by a discussion of the choice of lumped element parameters. A fabrication process for the proposed device is also discussed, with the importance of specific processes and material selections stressed for the proper operation of the device. Finally, the simulation methods developed throughout this thesis have been applied to the analysis of this device leading to a high degree of confidence that such a design, when fabricated, will produce the long sought 3WM amplification of weak microwave signals.

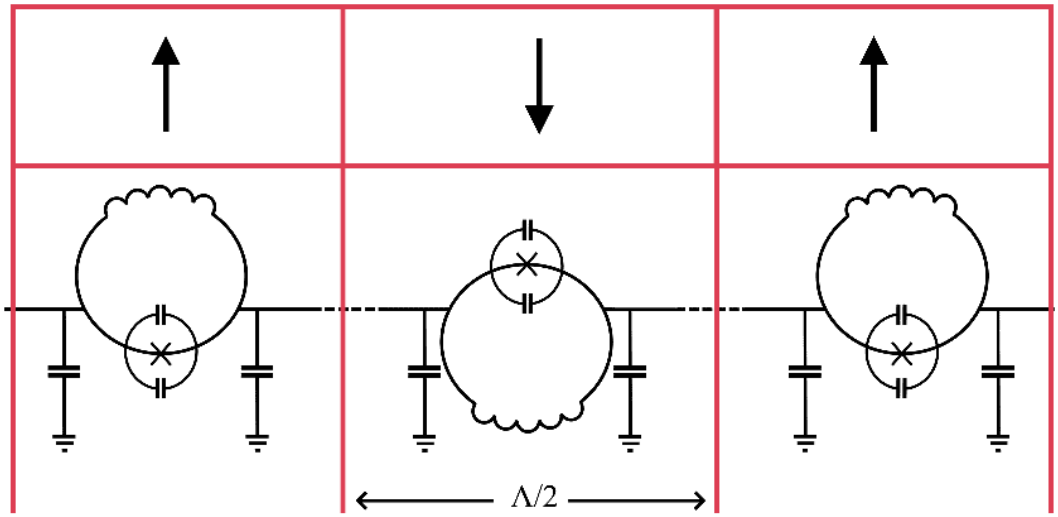

Fig. 6.12 Dispersion engineered rf-SQUID based JTWPA similar to previous designs except that the orientation of the SQUID is purposely flipped after a certain number of unit cells, $\Lambda/2$. This changes the polarity of the nonlinearity responsible for wave mixing and leads to the coherent build up of signal and idler waves along the entire length of transmission line.

6.4.1 Quasi-Phase Matching

As seen in the simulations of Chapter 4, the amplitude of a signal wave may periodically increase or decrease due to the phase mismatch between the pump, signal and idler tones. The period of modulation is set by, $\Lambda = \pi/\kappa_3$, where κ_3 is the phase mismatch of the 3WM tones. The length of transmission line for which the signal amplitude increases is therefore half this value, which we term L_{coh}, or the coherent build up length.

By reversing the polarity of the wave mixing nonlinearity at the point in the transmission line where the signal would begin to de-amplify we extend the coherent build up length of the signal wave. Quasi-phase matching uses this effect to ensure continuous growth of the signal amplitude along the entire length of the device. This effect is achieved in the JTWPA structures by flipping the orientation of the rf-SQUID, similar to what was done in Chapter 4, although at a much greater interval than every second unit cell. A scheme of such a device is shown in Figure 6.12, where a dc bias through two SQUID's with opposing orientations reverses the induced magnetic field penetrating the loops. In the mathematics, this is equivalent to making the $\chi^{(2)}$ parameter a function of distance with a negative or positive value depending on the orientation of the rf-SQUID,

$$\chi^{(2)} = \mathrm{sgn}\left[\sin\left(\frac{2\pi x}{L_{coh}}\right)\right]\frac{\beta_L \sin\left(\varphi_{dc}\right)}{4} \ . \tag{6.24}$$

This new form of the nonlinearity may then be included directly in CME simulations, while the altered circuit is easy to implement in WRspice. The remarkable similarity to what already exists, and lack of constrictions placed on pump operating frequency, is what makes this dispersion engineering technique particularly interesting.

Link to ToC

6.4.2 Lumped Element Design

Similar to the case with the KITWPA, the selection of lumped element parameters is constrained by the conditions previously set. For instance, in order to achieve a $\beta_L \sim 0.9$ in an operating range around - 70 dBm, the geometric inductance becomes set at ~ 120 pH. Then to achieve 50 Ω impedance, the capacitance to ground must be set at 48 fF. Therefore, without engaging with the more complex designs with multiple rf-SQUID's per cell we are restricted to a limited parameter set. For our purposes here, and in the interest of maximising electrical length for a given physical length, we pursue a device with the same parameter set as that presented in Chapter 4. These parameters are summarised in Table 6.3, with the expected L_{coh} derived from the phase mismatch between pump, signal and idler also noted.

To make losses negligible in this device we must ensure two things, the normal state resistance of the junction is high and the signal wave loss per cell is much smaller than the gain per cell. The first condition is a firmly material dependent parameter as can be seen by the direct proportionality of the normal state resistance to the superconducting energy gap in the Ambegaokar-Baratoff relation of Equation 5.1. Therefore to maximise this we must maximise the superconducting energy gap of the material used to form junctions. For our purposes the niobium junction technology appears to work well with a normal state resistance of approximately 1072 Ω for a 2 µA critical current. This is much larger than the value obtained for an aluminium junction used in the previous device of only 160 Ω.

If we calculate the losses that a signal wave at 7.2 GHz may face with such a shunt resistance due to niobium tunnel junctions we find a value of approximately -9E-4 dB/cell. Compare this to the approximately +5E-3 dB/cell gain taken from the simulations of Figure 4.9. We can see that over 3000 cells in a quasi-phase matched device a gain of at least 12 dB should be achieved. It should be noted that as QPM also hampers the generation of pump harmonics the gain is likely to be significantly higher than this estimation, as will be demonstrated in simulations later. Finally, we must ensure that with this amount of losses the pump remains at least 20 dB larger than the signal at the end of the array to enforce the strong pump approximation. This is achieved easily as we would expect only 8 dB reduction in pump power in this design due to quasi-particle losses. Of course, by operating at lower powers we can likely avoid even this level of loss but by considering it now we allow ourselves confidence of higher power operation.

I_c [µA]	L_G [pH]	C_j [fF]	C_0 [fF]	L_{coh}
2	132.6	212	53	235

Table 6.3 The parameter set of the transmission line unit cells where critical current, I_c, geometric inductance, L_G, junction capacitance, C_j, and return capacitance, C_0, are the same as those used in Chapter 4. The coherent build up length of a signal wave at 7.2 GHz for a pump wave at 12 GHz is also included as L_{coh}.

6.4.3 Fabrication Process

As stated we must use the niobium junction technology to ensure that the quasi-particle tunneling resistance is large enough to not be too detrimental to performance. For this we could use the tri-layer process already described in Chapter 5. However, I will now make some proposed alterations that will improve thermalization, minimise parasitic couplings in the device and remove the unnecessary large junction from the rf-SQUID devices. The changes made should not significantly worsen the reliability of this process, meaning that parameter variation should still be minimised.

We must first note that niobium tri-layer junctions are known to have a much smaller sub-gap resistance than their aluminium counterparts [131, 145]. A low sub-gap resistance in niobium junctions compared to aluminium tunnel junctions arises due to defects and scattering at the tunnel barrier. This can apparently be overcome by making the sandwich deposition symmetric in terms of metal. In other words the junction should be formed of a lower niobium layer, a lower aluminium layer, an aluminium oxide grown during oxidation, an upper aluminium layer and finally an upper niobium layer. The thickness of the aluminium layers are $< 10\,\text{nm}$ while the niobium layer thicknesses can be around 100 nm as is fairly common in tri-layer processes. This method has shown promise in producing niobium based qubits, where the sub-gap resistance would usually prevent such an application [131, 192].

We begin then by depositing a sputtered sandwich of silver, SiO_2, niobium, aluminium - (Al_2O_3) - aluminium, niobium, SiO_2. The stack is then patterned and an aluminium liftoff process completed to produce an aluminium etch mask over the junction area. This step is shown in Figure 6.13 (1a) for the stack-up and (1b) for the top down view.

A flourine based dry etch (SF6) can then be used to etch through SiO_2 and niobium down to the aluminium layers, defining the junction area, as shown in Figure 6.13 (2a) and (2b). Another optical lithography step is used to define an etch mask for the lower electrode of the rf-SQUID, which can then be dry etched with SF6 + Ar. To avoid the inclusion of a large junction as proved to be a problem in the device of Chapter 5, we must now do another lithography step to define a via to the opposite side of the lower electrode to the junction ((3a) and (3b)). After ion milling to remove the aluminium layers, niobium can be deposited and lift-off performed. Another SiO_2 is then added to cover both electrodes, and chemical mechanical polishing performed to level the surface at the tops of the niobium electrodes, as is shown in Figure 6.13 (4a) and (4b). The top rf-SQUID electrode can then be patterned and deposited using lift-off or etching, so long as an ion milling step is included before deposition, (5a) and (5b). A final SiO_2 layer is then deposited (6a) and (6b), followed by a dry etch to define the vias to the lower silver ground plane (7), silver may then be sputtered to form the vias and add the top ground plane (8). A final etch down to the top niobium electrode at the edges of the device must be added to allow for bonding to the transmission line structure, (9).

The reason for using a normal metal for the ground planes is to improve thermalisation of the device, which is also aided by the stripline structure used. Some added benefits of this are the reduced inductive coupling between cells of the array due to the close proximity

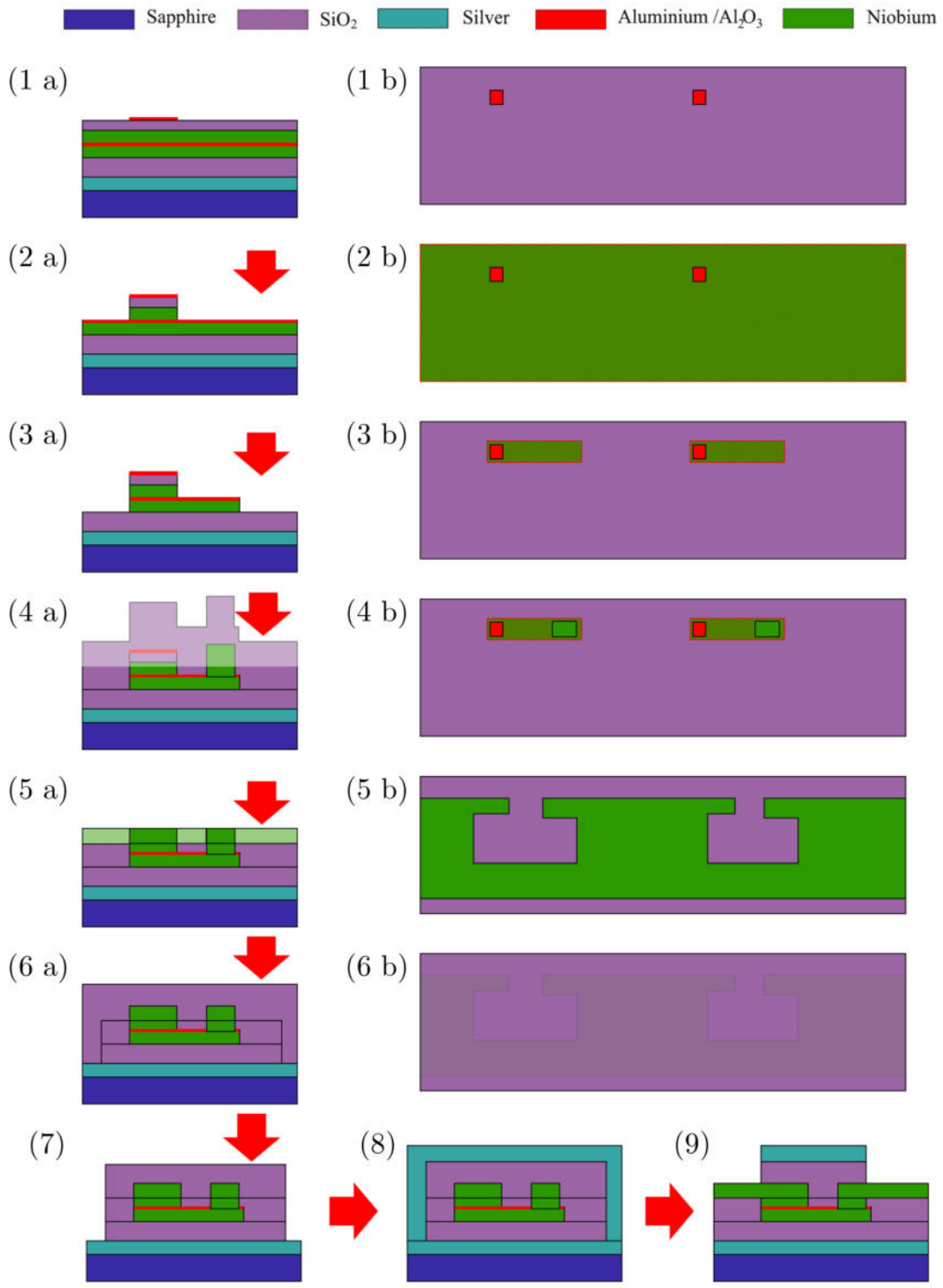

Fig. 6.13 Proposed fabrication process for the production of well thermalised quasi-phase matched JTWPA devices absent of spurious junctions or parasitic reactances, described in text.

of the top and bottom ground layers, and the absence of trapped flux in the ground planes. Although with such a large structure pin-hole defects in the dielectric layers may become more likely, with a good fabrication process and thick enough dielectric layers these should not be a worry.

6.4.4 Device Performance Simulation

Only now at the end of this thesis can we use the simulation tools applied so far to describe why devices will not work to describe why this proposed device *will* work. We can state this with some certainty only because such careful analysis of the previous devices has been carried out. To convince the reader of this design's viability, we investigate amplification, losses, harmonic generation and shockwave formation in the proposed device using WRspice and CME simulations. We limit our scope to some degree by neglecting parameter variation and parasitic reactances in these simulations, but we have already considered and minimised these in our device design.

We begin by investigating the amplitude of a signal wave at 7.2 GHz along the length of a 1200-cell long array while it mixes with a 12 GHz pump tone. This simulation, which can be carried out in both WRspice and with CME's, will demonstrate the effects of QPM on amplification in the device as well as the effects of losses that might be expected from an aluminium junction or a niobium junction. As we have shown, the quasi-particle tunneling resistance depends on the pump power via the quasi-particle generation rate. For this study we consider the largest reasonable losses by including the normal state shunt resistances calculated via the Ambegaokar-Baratoff formula, although in normal operation the losses may be considerably smaller.

The results of these simulations are shown in Figure 6.14 (a) and (b) for the signal and idler power profiles along the transmission line, respectively. This simulation uses a pump wave input at -75 dBm (800 nA) and a signal wave at -127 dBm (2 nA), while the orientation of the rf-SQUID's was reversed after 260 unit cells. This coherent build up length does not match exactly the calculated 235 cell L_{coh}, but it was found that this scheme provided larger amplification. The light coloured lines show CME results while the solid coloured lines show WRspice results, the general agreement between the two allows for an accelerated simulation method across the device bandwidth. The simulation without QPM or losses (blue) shows minimal amplification while the results with QPM added (green) show about 30 dB gain by the end of the 1200-cell long array. The inclusion of losses due to the use of niobium junctions (purple) diminishes the gain to only 12 dB, and the use of aluminium junctions shows only loss (red) due to the lower normal state tunneling resistance.

This result clearly demonstrates the importance of using niobium junction technologies as opposed to aluminium tunnel junctions, justifying the more complex fabrication process. Importantly, we have achieved 12 dB gain despite including the expected losses in a device length less than half the length of the 3000-cell long array used in our previous approximations. This demonstrates that 3WM amplification is actually more efficient in QPM devices due to decreased harmonic generation resulting from the incoherent build up

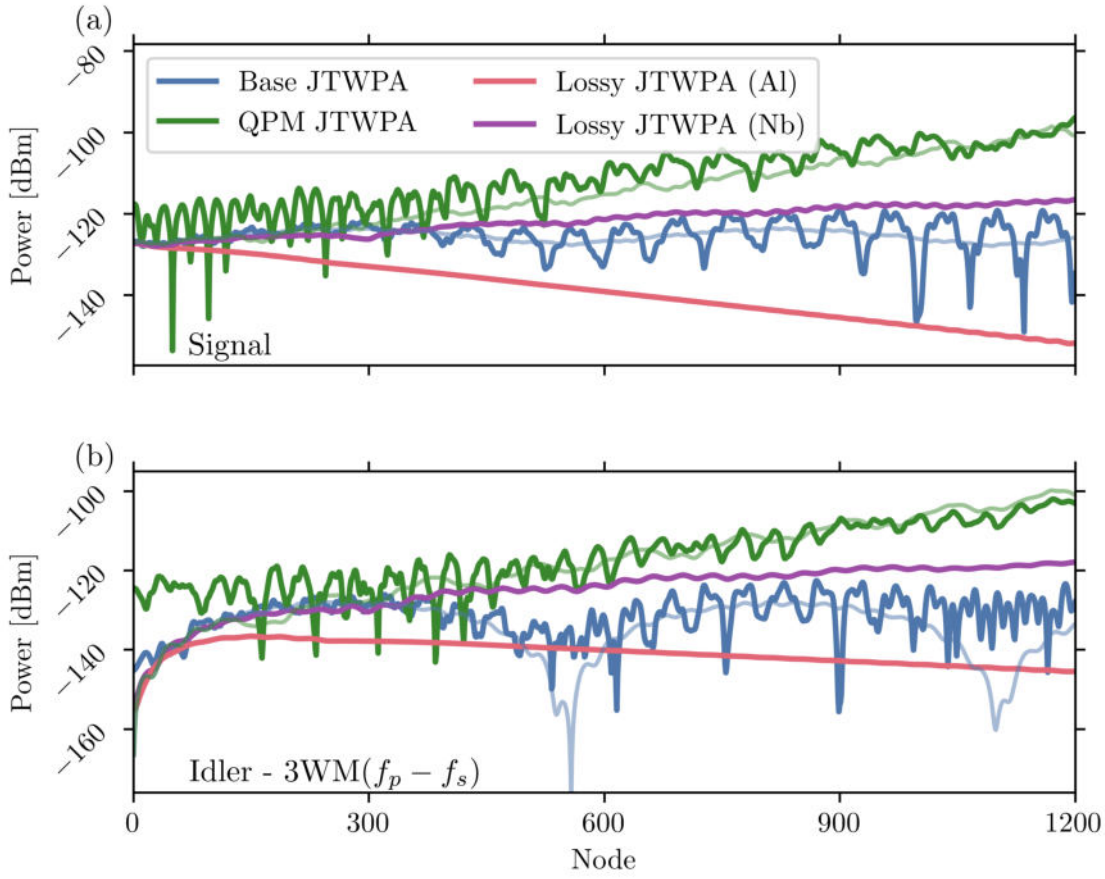

Fig. 6.14 Simulation results for a signal wave at 7.2 GHz in (a) and an idler wave at 4.8 GHz in (b) due to a pump wave applied at 12 GHz, -75 dBm. WRspice results are shown with solid lines while CME results are shown in the faded lines. JTWPA device with no dispersion engineering or losses is shown in blue, with QPM added for the green curve, while losses due to a niobium junction or aluminium junction are shown in purple and red, respectively.

of the second harmonic due to nonlinearity reversals. This result can then be improved if the quasi-particle population is kept low, which would require that the currents through the junctions do not exceed the critical current. Even though in 3WM operation this is unavoidable, the decreased harmonic generation should prevent shockwave formation and so decrease the total quasi-particle number generated per pump cycle.

To ensure the absence of shockwave formation in the device we can look at the current profile in the transmission line which is shown in Figure 6.15 for an input pump wave of amplitude 0.8 µA. Although some distortion of the sine wave is present, this is likely due to the signal wave and is not significant enough to cause the problems of quasi-particle generation witnessed previously. Therefore, the losses are likely to be considerably less than simulated in the niobium device and so under the right operating conditions 20 dB amplification should certainly be possible.

To determine the minimum pump power that may be used that will still lead to significant amplification, we must perform a set of simulations in WRspice where the input pump current is swept. As can be seen in Figure 6.16 the amplification of a weak signal is

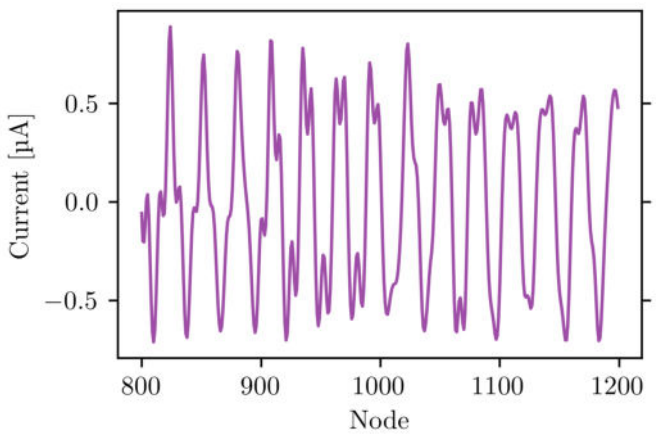

Fig. 6.15 WRspice simulation result showing the current at each node in the JTWPA in the QPM device, without losses. While a distorted shape is present, no shock front is notable which indicates that harmonic generation is prevented within the device.

greater than 20 dB for input powers above -78 dBm. Given that this input power is roughly 11 dB smaller than the critical current of around -67 dB, the actual losses to be expected are considerably lower than simulation, as per the previous chapter's results. Therefore, there is no significant advantage to be seen in operating at higher powers where quasi-particle generation may become a larger problem, which may in fact diminish amplification.

The greatest advantage of QPM compared to other dispersion engineering techniques is that there is no significant distortion of the dispersion relation of the transmission line. It should therefore be possible to use the device over a rather wide bandwidth by tuning the pump to maintain a constant phase mismatch between the pump, signal and idler. The phase relation shown in Figure 6.17 (a) is the case for the simulated device with and without losses included, shown by the blue and red lines, respectively. Then for any given signal frequency a pump frequency can be found for which the value:

$$\left[\frac{L_{coh}}{2} - \frac{\pi}{\kappa_3}\right]^{-1} \tag{6.25}$$

is maximised. The optimal pump frequency for a signal in the range up to 12 GHz is shown by the bright line in the heat map of Figure 6.17 (b). This optimal line is then extracted and plotted separately in Figure 6.17 (c) where coloured bands match the CME simulations completed in (d)-(h) for signals at 4, 6, 8, 10, and 12 GHz, respectively.

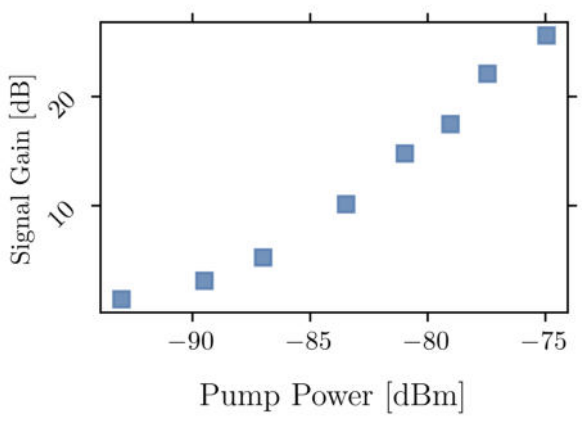

Fig. 6.16 WRspice simulation results showing the final gain for a signal wave at 7.2 GHz achieved in a lossless, 1200 unit cell long JTWPA device. Pump input powers above -78 dBm produce 20 dB gain, although lower power performance is sufficient in longer devices.

Link to ToC

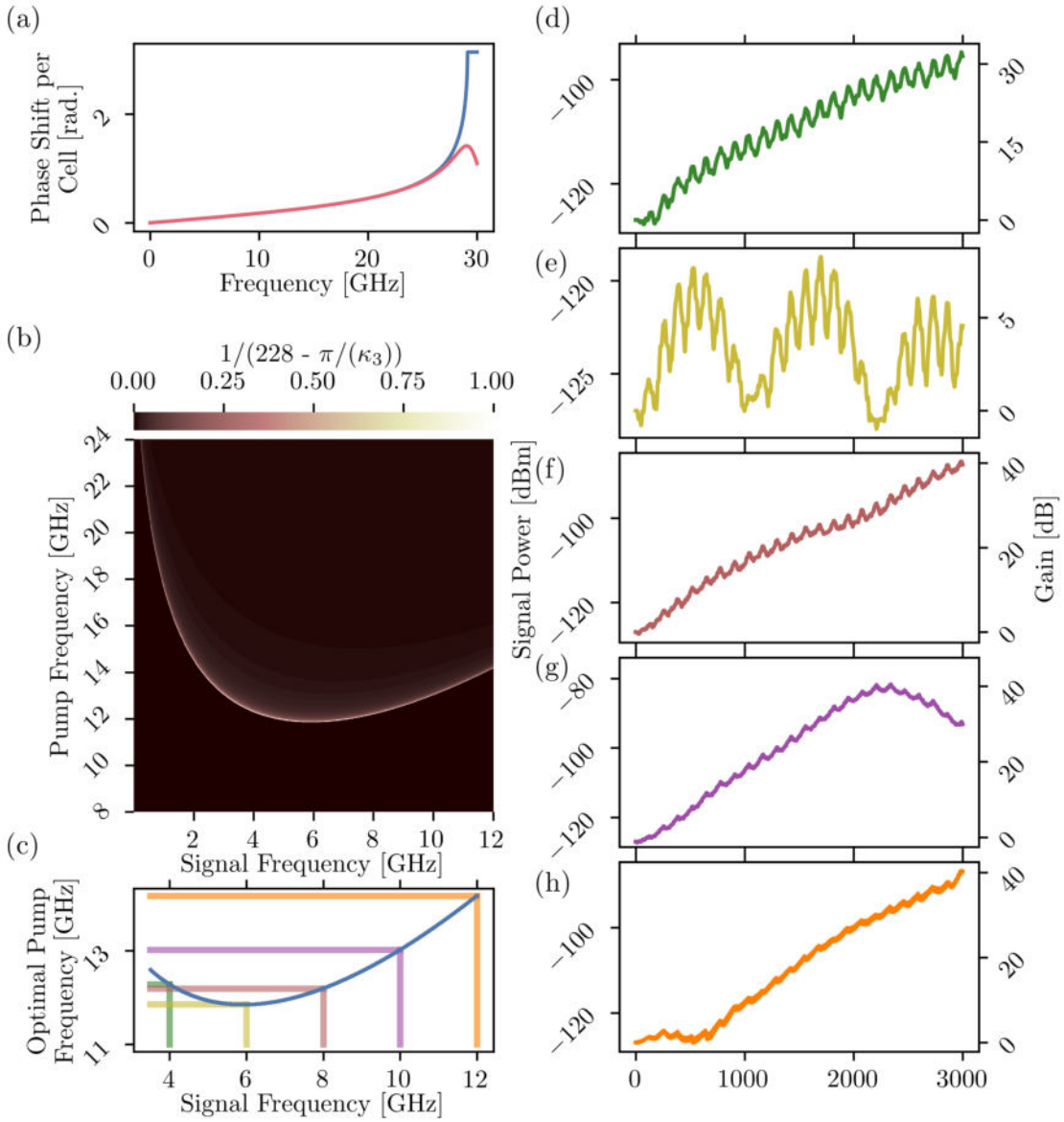

Fig. 6.17 (a) Dispersion relation for the device under study with and without losses in red and blue, respectively. (b) Reciprocal of the difference between the coherent build up length and the three wave mixing phase mismatch with the bright areas indicating optimal pump frequency for a given signal frequency. (c) Optimal pump frequency curve extracted and the pump frequency - signal frequency pairs marked with coloured bands that correspond to the CME simulations in (d-h).

Each of these simulations show amplification occurring in the 3000-unit cell long device, in which losses were neglected for convenience. However, while 8 and 12 GHz signals experience over 40 dB gain the 4 and 10 GHz signals only see 30 dB , and the 6 GHz signal has a paltry 5 dB. This clearly implies some variation from predictions is required of the optimal QPM period for maximal gain. This effect is going to be due not only to the phase mismatch between the mixing tones but also increased harmonic generation due to improved phase matching at some pump frequencies.

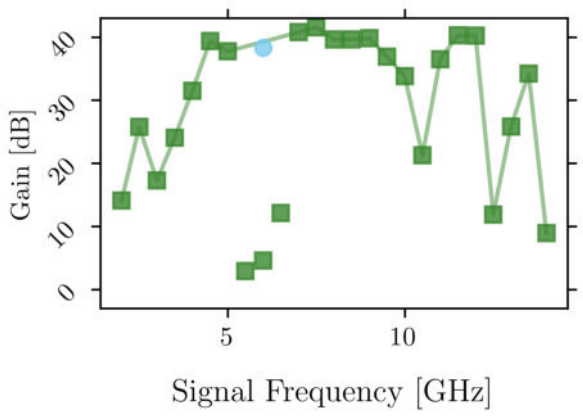

Fig. 6.18 Final gain for a signal wave with its frequency swept from 2 to 14 GHz in steps of 0.5 GHz. Regions with lower gain around 6 GHz are repeated with a de-tuned pump but approximately 40 dB gain is recovered.

To investigate further, these simulations are expanded across the full range of signal frequencies of interest, using a step of 0.5 GHz the final gains are plotted in Figure 6.18. If not for the outliers at 6 and 10 GHz, almost 40 dB gain may be achieved in an octave bandwidth around 8 GHz. To improve this situation, the pump may be de-tuned from the predicted optimal value. For instance, for a 6 GHz signal and a pump at 12.3 GHz (where the predicted optimal value was 11.85 GHz) 40 dB gain was recovered, as shown by the blue circle in Figure 6.18. Ironically, this is a process that will be easier done experimentally than in simulation, but nonetheless should be applicable to all outliers extending the bandwidth of the proposed device.

6.4.5 Discussion

This section has presented a quasi-phase matched JTWPA device based on the nonlinearity of rf-SQUID like elements. It has been shown that significant amplification of a signal in an octave bandwidth around 8 GHz is possible with the right choice of pump parameters. Implementation of QPM in simulations has succeeded in two aims in this device: extending the coherent build up length of the signal wave amplitude to the full device length, and decreasing second harmonic generation of the pump. This has been achieved by flipping the orientation, and by extension the polarity of the nonlinearity, of the rf-SQUID's after a period of 260 unit cells in the artificial transmission line. The proposed device has been tested in both WRspice and CME simulations under a variety of conditions, producing signal gain in realistic scenarios.

Previous chapters have demonstrated that losses due to quasi-particle generation in 3WM JTWPA's prevent significant amplification of a signal wave. Our intention here has been to maximise gain via dispersion engineering and minimise losses via good fabrication choices and operating conditions selection. Simply put, we must ensure that losses per cell are much lower than gain per cell for a signal wave. This has been shown to only be possible in a niobium tri-layer process for which the normal state tunnelling resistance is relatively high. A fabrication process has then been suggested to remove spurious junctions and improve thermalisation of the device in operation, which will further reduce the effects of quasi-particle losses. In fact, with low pump power operation it has been shown that a lossless device will still achieve 20 dB gain. This should actually be similar to a realised

Link to ToC

device as losses will be negligible at input pump powers >10 dB lower than the critical current.

This performance in simulation has been extended over a wide bandwidth via a method for identifying the optimal pump frequency for a given signal frequency. The bandwidth that may be achieved in such a QPM device may be considerably larger than that from other dispersion engineering techniques due to the limited distortion of the dispersion relation with this method. It should be noted that a caveat in this result has been the need to de-tune the pump from the calculated optimal value in order to achieve maximal gain at some signal frequencies. This has most likely been due to an increased efficiency of second harmonic generation in some circumstances.

6.5 Comparison of TWPA Technologies

The most appropriate of TWPA technology depends, of course, on the intended application and the fabrication capabilities of the reader. With key differences in power handling, nonlinearity, wave mixing regime and fabrication difficulty there are a diverse set of factors that must be compared between the two approaches to travelling wave amplification. Some of the key parameters of this comparison are summarised in Table 6.4, although we will expand on them below.

The KITWPA can be used at much higher powers than the JTWPA devices without incurring losses, comparing the pair-breaking current of thin films with the critical current of a Josephson junction. This allows for the use of very high pump powers in KITWPA's, extending the saturation power of a input signal to around -60 dBm while it is generally around -100 dBm for JTWPA's [21, 156]. However, this increased power handling does come at the cost of a much weaker nonlinearity per unit length of KITWPA devices. The inductance of a unit cell in a KITWPA device can be modulated by a maximum of 17 % compared to a maximum of 50 % in an rf-SQUID based JTWPA. As a result, the wave mixing effects in KITWPA devices are weaker than JTWPA counterparts and so the required length of transmission line, both in terms of physical length and number of unit

		KITWPA	JTWPA
nonlinearity modulation		$\sim 17\%$	$\leq 100\%$
saturation power	[dBm]	~ -60	~ -100
wave mixing regime		multi-WM	3WM
length	[cells]	>10,000	> 700
length	[cm]	~ 20	~ 2
smallest dimension	[nm]	250	500

Table 6.4 A comparison of some key parameters from the KITWPA and JTWPA technologies in terms of nonlineraity strength, power handling capabilities and device length.

cells, must be much larger in order to achieve similar amplification. The wave mixing regime also differs between the two technologies with JTWPA's operating in both the 4WM and 3WM regimes but the KITWPA may only operate in the 4WM regime. With the addition of a dc bias a KITWPA may operate in a multiwave mixing regime that behaves similarly to 3WM in most applications.

The structure of the devices are quite different with the JTWPA devices being unavoidably lumped element while the KITWPA devices may be continuous or quasi-lumped element. Although the KITWPA unit cell structure is considerably simpler the nature of the rf-SQUID based unit cell in JTWPA's gives the designer a far greater space to engineer the particular dispersion characteristics required from the device.

As has been discussed at length in this thesis the choice between these technologies comes down to fabrication capabilities. Although both devices have minimum feature sizes of similar values a KITWPA device requires only a single lithography step while JTWPA devices generally require at least two lithography steps. If it is possible to produce many near identical rf-SQUID unit cells then a JTWPA device may appear optimal, although if this is not possible then the KITWPA device formed of a single metallic film may be better. However, yield for these devices can prove equally troubling with the complex nature of JTWPA devices and sheer length of the KITWPA devices allowing many opportunities for film breaks, pin hole defects or multitude other defects that prevent device use. The advantage of KITWPA's primarily lies in the subtractive fabrication process used to produce them, which is favoured by industry and is in principle more easily mass produced.

It seems likely that a laboratory capable of producing a JTWPA device may also produce a KITWPA device with some limited changes to metal deposition steps, although the reverse is not true. Although these technologies may be regarded as competing with each other, the truth is that they are best used in conjunction with a JTWPA as a first stage amplifier and a KITWPA as a second stage. This would provide a totally quantum noise limited amplification chain up to room temperature measurement equipment, removing the heat load and added noise of HEMT amplifiers completely.

6.6 Conclusion

This chapter has presented proposals for two travelling wave parametric amplifiers based upon the kinetic inductance and rf-SQUID nonlinearities. We have attempted in these designs to overcome the problems identified in previous iterations of these devices. Namely, poor thermalisation, phase mismatch between mixing waves, harmonic generation and quasi-particle losses. These goals have been achieved by a series of improvements, including the implementation of dispersion engineering techniques in the circuit designs. Dispersion engineering based on either impedance modulation or polarity reversal of the wave mixing nonlinearity in the devices have been applied to the kinetic inductance TWPA (KITWPA) and rf-SQUID JTWPA, respectively. It should be noted that either method may be applied to either device in principle. Given our well developed models and understanding of the

problems with previous devices, we can now say with confidence that the proposed devices *will* work.

The design of the lumped element circuits used to form the travelling wave structures in both proposals has been discussed. The constraints placed upon the designer due to experimental realities such as the 50 Ω impedance environment, avoidance of hysteresis in SQUID elements or a cut-off frequency on the order of 100 GHz have been shown to severely limit the parameter space available. Fortunately, this also means that only a single parameter must be chosen for either device, film thickness for the KITWPA and junction critical current for the JTWPA. Even this may be a constrained parameter if operation in a particular power range is specifically desired. Of course, more complex circuit designs may be pursued but it seems likely that the added complications would not be worth the improved circuit characteristics in most imaginable cases.

The circuit design, when set, has been shown to already be sufficient to set the optimal operating parameters for the device in terms of both power and frequency. A large part of the motivation for setting these operating ranges is to avoid the increased losses due to quasi-particle generation in the devices. Another method to minimise these losses has been through the proper material selection and fabrication design of the circuits. Metals with large superconducting energy gaps have been selected to minimise quasi-particle generation, for which niobium junctions have been deemed critical to the production of a successful JTWPA device. It was shown that the proposed device would only attenuate signals if the fabricated device had a large quasi-particle population and aluminium tunnel junctions, while high gain may still be achieved for niobium tunnel junctions due to the higher resistance. On the other hand, material selection for the KITWPA has been shown to be more forgiving with many alloy superconductors suitable for use. A series of titanium nitride films were characterised for the eventual production of a KITPWA device, with kinetic inductances per square determined to be 9.9 pH/□, 15.5 pH/□ and >54.3 pH/□. However, the most interesting and novel superconducting materials, such as tungsten silicide, have been shown to require an alternative circuit design more similar to that used for JTWPA devices, although with significant disadvantages. For the quasi-continuous KITWPA structure that we propose it was shown that the spacing of the capacitive fingers required for impedance matching must be separated by at least 6 trace widths to minimise the capacitive loading between the fingers themselves. It was hypothesised that this loading may lead to detrimental quenching effects in KITWPA devices if not properly regarded. Finally, circuit geometries with improved thermalisation, such as striplines, have been selected to minimise quasi-particle lifetime.

By developing these design rules for KITWPA development we have examined the criteria for success in producing a functional kinetic inductance based travelling wave parametric amplifier. It has been shown via comparison with published examples that a device that demonstrates gain in the region of 15 - 20 dB across an octave bandwidth in the microwave regime is achievable using a transmission line of length on the order of 10 cm. This does not require the most novel superconducting materials and with good design can be achieved with the relatively common titanium nitride films.

A proposal for a JTWPA device employing a quasi-phase matching technique over the 3000-cell long transmission line that can achieve amplifications of $> 40\,\mathrm{dB}$ over an octave bandwidth has also been presented. This device would be formed of the well-described rf-SQUID based unit cell with circuit elements in each cell L_G : 132.6 pH, C_0: 53 fF, C_j: 212 fF, and I_c: 2 µA. These are the same parameters as were used in the aluminium tunnel junction based device of Chapter 4, but there are key differences in design including the use of a more complex niobium tri-layer process to form the junctions. Simulations of the basic scheme showed that signal gain was limited by the large phase mismatch between the pump, signal and idler waves. Quasi-phase matching resolves this problem by reversing the orientation of the rf-SQUID after every 260 unit cells, a period equal to the inverse of the phase mismatch of the mixing waves. This device has been shown to produce $> 20\,\mathrm{dB}$ gain even in the limit of high loss due to quasi-particle tunnelling across the niobium junctions, and $> 40\,\mathrm{dB}$ amplification in the lossless case.

The tools developed for the design and simulation of these devices have been made publicly available in the hope that a successful 3WM JTWPA device may be produced shortly. During the course of my studies I have developed several interesting JTWPA proposals, but for this thesis it was decided to focus on this particular QPM device. This is simply because it is not incredibly novel, the engineering challenges that must be overcome to produce this device are absolutely surmountable and may be implemented almost immediately. It is my hope that such a device is made which may act as a proof of concept of a 3WM JTWPA so that the many interesting applications and novelties that lie beyond may be investigated fruitfully.

Chapter 7

Conclusion

In this thesis the theory and operation of travelling wave parametric amplifiers operating in the three wave mixing regime has been studied. A significant amount of effort has been made to give the reader a good understanding of the history and mechanism of parametric amplification, as well as of the topic of parametric effects more generally. Chapter 1 has introduced the concepts key to the work presented in this thesis, including kinetic and Josephson inductance in superconducting circuits and microwave transmission line design for both continuous and lumped element structures.

The simulation methods used to analyse the circuits and structures under study in this thesis have been thoroughly described with examples in Chapter 2. The WRspice superconducting circuit simulator has been introduced, alongside a numerical method for solving coupled mode equations that describe wave mixing in distributed structures. The results of these simulation methods where shown to agree for Zorin's proposed JTWPA device [107] to within 2 dB, however the total gain was shown to also be an underwhelming 12 dB, considerably less than the theorised 20 dB. This is shown to be primarily due to parasitic wave mixing effects like pump wave up-conversion which can also form shockwaves in the device. The shockwaves were shown to produce current spikes exceeding two times the amplitude of the input wave, which was hypothesised to cause quasi-particle generation when these spikes exceed the critical currents of the Josephson junctions. The associated pros and cons of each simulation approach have been given, with WRspice proving to be the optimal method whenever reasonable, as it can be applied to general circuits without much alteration. However, the simulation is only as good as the simulator, and the required knowledge of circuit analysis has proven to be a significant barrier to entry for many groups that wish to work on this topic. To aid this, a robust description and a comprehensive bibliography have been put together to answer any questions that may arise about the methods, applicability or validity of the simulation methods used.

These simulation methods have been applied to the study of two important questions: what effect do parameter variations and parasitic reactances have on the performance of a JTWPA device? For this study, the theoretical device proposed by Zorin [107] was again simulated in WRspice. To investigate parameter variations a stochastic modelling approach was used, where each reactance in each unit cell of the lumped element transmission line

was varied with a Gaussian distribution of standard deviation 0%, 1 %, 3 %, 5 %, 7 %, and 10 %. This work showed that reflections within the device become very significant for parameter variations that might be expected in a fabricated device, leading to completely unpredictable performance. The uncertainties in gain that arise from standard deviations of 0.5 %, 2 %, 2 %, and 4 % in geometric inductance, junction capacitance, critical current and capacitance to ground, respectively, is larger than 10 dB. Fortunately, the effects of this variation are highly frequency dependent resulting in spikes of high or low gain across a bandwidth without significantly affecting the amplifier performance across the frequency range in general. Simulations of this device also demonstrated pump depletion due to harmonic generation occurring at -75 dBm input power. This is a similar value to the power that corresponds to the critical currents of the junctions in the device. Possibly, the features that are associated with this depletion effect may lead to a method of experimentally identifying a critical current value in the device. Pump harmonics behaviour in flux can be used as an indicator of optimal 3WM bias position by identifying the flux bias corresponding to maximum amplitude. The difference between 3WM and 4WM output amplitudes for all pump harmonics is at least 10 dB. The effects of parasitic reactances and losses where studied, with results showing a similar detrimental effect on amplification. Inductive coupling of $\kappa \geq 0.3$ between neighbouring rf-SQUID loops of opposite orientations completely nullifies amplification. Dielectric losses in these JTWPA devices that employ lumped capacitive elements are shown to be unlikely to cause large problems, with expected equivalent resistances in the circuit of $R_{cap} \geq 3\,M\Omega$ causing no significant loss of signal power.

Following these purely theoretical studies, a series of experiments were run on two JTWPA devices, shared with us by our collaborators of Bauman Moscow State Technical University and PTB, Germany. The devices, made using an aluminium double angle and a niobium tri-layer process, respectively, were investigated with transmission measurements. The dependencies of transmission on input power, frequency and dc bias were discussed. Phase mismatch and harmonic generation are known problems in this generation of devices and the negative effects of these on amplification were investigated. Degenerate 3WM amplification was seen in the niobium device at 5 GHz, although with only 2 dB gain. This amplification is very difficult to distinguish over the effects of impedance modulation by flux bias which is shown to modulate transmission by more than 15 dB. The observed amplification matches the value that might be expected from the device under the conditions of no pump depletion. However, losses in the devices proved to be so significant that it was deemed unlikely that amplification of a signal could occur even if no other detrimental effect was present. The cause of these losses was found to most likely be the tunneling of quasi-particles through the Josephson junction structures. After some comparison to simulations, the dependence of loss on input wave power was found to be quite similar to expected behaviour of shockwave formation and Cooper pair breaking in the tunnel junctions. This conclusion is reinforced by the fact that fitting of transmission data showed losses may be explained by a shunt resistance across the rf-SQUIDs with a value approximately equal to the expected normal state resistance of junctions in the devices. With 160 Ω for the aluminium junctions, and 10 Ω for the large niobium junctions in use.

Link to ToC

This is also shown to have a power dependence with pump powers required to be 30 dB lower than the equivalent critical current power in order to avoid increased losses. This sets a new bound on the operation of Josephson junction based parametric amplifiers that is not known to have been considered to date in preceding works.

The task of designing amplifiers that overcame the identified problems of previous devices and proposals was undertaken in the final chapter of this thesis. To this end, two amplifiers, one based on the Josephson effect in an rf-SQUID and one based on the kinetic inductance of superconducting films, have been investigated and proposed. Key in both proposals are the material selection, circuit design and fabrication process used. Materials with high kinetic inductance per square have been identified for use in the production of KITWPA devices, with two titanium nitride films that have 9.9 pH/□ and 15.5 pH/□ sheet kinetic inductances characterised. A thorough comparison of the proposal to published devices suggests that a gain of 15-20 dB should be achievable over an octave bandwidth for this design.

Materials with a large superconducting energy gap, like niobium, have been deemed vital for the production of JTWPA devices in order to minimise quasi-particle losses. This is because the normal state resistance of these junction will be much higher for a given critical current than in a junction using a metal with a lower critical temperature (like aluminium). If a junction with a low normal state resistance is used in the device, then it has been shown that even with the added amplification efficiency due to dispersion engineering in circuit designs, no amplification will be seen. On the other hand the $\sim 1\,\mathrm{k}\Omega$ resistance expected from a niobium tunnel junction with equal critical current would still maintain 20 dB amplification in the case of saturated losses and 40 dB gain in the loss-less operation. This high gain is achievable over an octave bandwidth with potential to be wider with finetuning of the pump frequency used so that the phase mismatch of pump, signal and idler wave is kept constant. This is a criteria of the quasi-phase matching dispersion engineering that is key to the high gain performance. This dispersion engineering technique is selected due to the ease of implementation, where the orientation of the rf-SQUID elements is simply reversed after a period equal to the inverse of the phase mismatch between the pump signal and idler waves, i.e. every 260 unit cells of the transmission line. This technique is also shown to produce more efficient amplification due to the suppression of spurious wave mixing products such as pump harmonics. For the production of a JTWPA device that will operate successfully in the three wave mixing regime, a niobium tri-layer process has been proposed for the fabrication of a quasi-phase matched rf-SQUID based lumped element transmission line. Given the extreme care and thought that has gone into the analysis of these devices, it can be stated with confidence that the proposed device will work as intended, making it the first JTWPA device to demonstrate broad band and high dynamic range three wave mixing amplification.

Future work in this topic should focus on improvements to the dispersion engineering schemes implemented in the travelling wave structures. Generally, dispersion engineering prevents the generation of noise squeezed states, either completely or over a large bandwidth due to the frequency dependent nature of the phase matching. The already ubiquitous resonant based Josephson parametric amplifiers can produde squeezed states over a gigahertz

Link to ToC

bandwidth, so to compete with these a method of dispersion engineering that does not distort the dispersion relation around the pump frequency must be found. Although not presented in this thesis, such schemes can be implemented with only minor added complication to the design of the QPM device already presented. However, a more complex task is to improve the directionality of these TWPA devices such that reflections from the output end of the transmission line may not travel back to the device under test. While these TWPA devices are commonly referred to as directional this only means that the signal is only amplified if it co-propagates with the pump wave. With true directionality and filtering implemented, a two stage amplification scheme that uses a JTWPA first stage and KITWPA second stage amplifier would provide the best possible read out method for weak signal measurements in the microwave range.

Bibliography

[1] F. Meylahn, B. Willke, and H. Vahlbruch, "Squeezed States of Light for Future Gravitational Wave Detectors at a Wavelength of 1550 nm," *Phys. Rev. Lett.*, vol. 129, no. 12, p. 121 103, Sep. 2022. DOI: 10.1103/PhysRevLett.129.121103.

[2] X. Pan *et al.*, *Protecting the quantum interference of cat states by phase-space compression*, Dec. 2022. arXiv: 2212.01271 [quant-ph].

[3] Antonio Barone and Gianfranco Paterno, *Physics and Applications of the Josephson Effect*. John Wiley & Sons, Ltd, 1982, ISBN: 978-3-527-60278-0. DOI: 10.1002/352760278X.fmatter.

[4] J. Aumentado, "Superconducting Parametric Amplifiers: The State of the Art in Josephson Parametric Amplifiers," *IEEE Microwave Magazine*, vol. 21, no. 8, pp. 45–59, Aug. 2020, ISSN: 1557-9581. DOI: 10.1109/MMM.2020.2993476.

[5] J. M. Kreikebaum, K. P. O'Brien, A. Morvan, and I. Siddiqi, "Improving wafer-scale Josephson junction resistance variation in superconducting quantum coherent circuits," *Supercond. Sci. Technol.*, vol. 33, no. 6, 06LT02, Apr. 2020, ISSN: 0953-2048. DOI: 10.1088/1361-6668/ab8617.

[6] D. Cattiaux *et al.*, "A macroscopic object passively cooled into its quantum ground state of motion beyond single-mode cooling," *Nat Commun*, vol. 12, no. 1, p. 6182, Oct. 2021, ISSN: 2041-1723. DOI: 10.1038/s41467-021-26457-8.

[7] P. Livreri *et al.*, "Microwave Quantum Radar using a Josephson Traveling Wave Parametric Amplifier," in *2022 IEEE Radar Conference (RadarConf22)*, Mar. 2022, pp. 1–5. DOI: 10.1109/RadarConf2248738.2022.9764353.

[8] A. J. Leggett, "Macroscopic Quantum Systems and the Quantum Theory of Measurement," *Progress of Theoretical Physics Supplement*, vol. 69, pp. 80–100, Mar. 1980, ISSN: 0375-9687. DOI: 10.1143/PTP.69.80.

[9] Y. Nakamura, Y. A. Pashkin, and J. S. Tsai, "Coherent control of macroscopic quantum states in a single-Cooper-pair box," *Nature*, vol. 398, no. 6730, pp. 786–788, Apr. 1999, ISSN: 1476-4687. DOI: 10.1038/19718.

[10] F. Arute *et al.*, "Quantum supremacy using a programmable superconducting processor," *Nature*, vol. 574, no. 7779, pp. 505–510, Oct. 2019, ISSN: 1476-4687. DOI: 10.1038/s41586-019-1666-5.

[11] Y. Kim *et al.*, "Evidence for the utility of quantum computing before fault tolerance," *Nature*, vol. 618, no. 7965, pp. 500–505, Jun. 2023, ISSN: 1476-4687. DOI: 10.1038/s41586-023-06096-3.

[12] S. McHugh *et al.*, "A readout for large arrays of microwave kinetic inductance detectors," *Review of Scientific Instruments*, vol. 83, no. 4, p. 044 702, Apr. 2012, ISSN: 0034-6748, 1089-7623. DOI: 10.1063/1.3700812.

[13] S. Khan *et al.*, "Superconducting optoelectronic single-photon synapses," *Nat Electron*, vol. 5, no. 10, pp. 650–659, Oct. 2022, ISSN: 2520-1131. DOI: 10.1038/s41928-022-00840-9.

[14] Rosenberg, "MOT002.pdf," in *Searching for the Axion*, 2004.

Link to ToC

[15] M. Esposito *et al.*, "Observation of Two-Mode Squeezing in a Traveling Wave Parametric Amplifier," *Phys. Rev. Lett.*, vol. 128, no. 15, p. 153 603, Apr. 2022. DOI: 10.1103/PhysRevLett.128.153603.

[16] M. Sweeny and R. Mahler, "A travelling-wave parametric amplifier utilizing Josephson junctions," *IEEE Transactions on Magnetics*, vol. 21, no. 2, pp. 654–655, Mar. 1985, ISSN: 1941-0069. DOI: 10.1109/TMAG.1985.1063777.

[17] J. M. Manley and H. E. Rowe, "Some General Properties of Nonlinear Elements-Part I. General Energy Relations," *Proceedings of the IRE*, vol. 44, no. 7, pp. 904–913, Jul. 1956, ISSN: 2162-6634. DOI: 10.1109/JRPROC.1956.275145.

[18] M. J. Feldman, P. T. Parrish, and R. Y. Chiao, "Parametric amplification by unbiased Josephson junctions," *Journal of Applied Physics*, vol. 46, no. 9, pp. 4031–4042, Sep. 1975, ISSN: 0021-8979, 1089-7550. DOI: 10.1063/1.322157.

[19] M. T. Levinsen, R. Y. Chiao, M. J. Feldman, and B. A. Tucker, "An inverse ac Josephson effect voltage standard," *Applied Physics Letters*, vol. 31, no. 11, pp. 776–778, Aug. 2008, ISSN: 0003-6951. DOI: 10.1063/1.89520.

[20] J. Niemeyer, J. H. Hinken, and R. L. Kautz, "Near-Zero Bias Arrays of Josephson Tunnel Junctions Providing Standard Voltages up to 1 V," *IEEE Transactions on Instrumentation and Measurement*, vol. IM-34, no. 2, pp. 185–187, Jun. 1985, ISSN: 1557-9662. DOI: 10.1109/TIM.1985.4315297.

[21] C. Macklin *et al.*, "A near-quantum-limited Josephson traveling-wave parametric amplifier," *Science*, vol. 350, no. 6258, pp. 307–310, Oct. 2015, ISSN: 1095-9203. DOI: 10.1126/science.aaa8525.

[22] M. Esposito, A. Ranadive, L. Planat, and N. Roch, "Perspective on traveling wave microwave parametric amplifiers," *Appl. Phys. Lett.*, vol. 119, no. 12, p. 120 501, Sep. 2021, ISSN: 0003-6951, 1077-3118. DOI: 10.1063/5.0064892.

[23] K. O. H, "The superconductivity of mercury," *Comm. Phys. Lab. Univ. Leiden*, vol. 122, pp. 122–124, 1911.

[24] W. Meissner and R. Ochsenfeld, "Ein neuer Effekt bei Eintritt der Supraleitfähigkeit," *Naturwissenschaften*, vol. 21, no. 44, pp. 787–788, Nov. 1933, ISSN: 1432-1904. DOI: 10.1007/BF01504252.

[25] F. London, H. London, and F. A. Lindemann, "The electromagnetic equations of the supraconductor," *Proceedings of the Royal Society of London. Series A - Mathematical and Physical Sciences*, vol. 149, no. 866, pp. 71–88, Jan. 1997. DOI: 10.1098/rspa.1935.0048.

[26] F. London, "On the Problem of the Molecular Theory of Superconductivity," *Phys. Rev.*, vol. 74, no. 5, pp. 562–573, Sep. 1948, ISSN: 0031-899X. DOI: 10.1103/PhysRev.74.562.

[27] L. D. Landau and V. L. Ginzburg, "On the theory of superconductivity," *Zh. Eksp. Teor. Fiz.*, vol. 20, p. 1064, 1950.

[28] L. P. Gor'Kov, "Microscopic Derivation of the Ginzburg-Landau Equations in the Theory of Superconductivity,"

[29] M. Cyrot, "Ginzburg-Landau theory for superconductors," *Rep. Prog. Phys.*, vol. 36, no. 2, p. 103, Feb. 1973, ISSN: 0034-4885. DOI: 10.1088/0034-4885/36/2/001.

[30] A. B. Pippard and W. L. Bragg, "An experimental and theoretical study of the relation between magnetic field and current in a superconductor," *Proceedings of the Royal Society of London. Series A. Mathematical and Physical Sciences*, vol. 216, no. 1127, pp. 547–568, Jan. 1997. DOI: 10.1098/rspa.1953.0040.

[31] J. Bardeen, L. N. Cooper, and J. R. Schrieffer, "Microscopic Theory of Superconductivity," *Phys. Rev.*, vol. 106, no. 1, pp. 162–164, Apr. 1957, ISSN: 0031-899X. DOI: 10.1103/PhysRev.106.162.

[32] J. Bardeen, L. N. Cooper, and J. R. Schrieffer, "Theory of Superconductivity," *Phys. Rev.*, vol. 108, no. 5, pp. 1175–1204, Dec. 1957. DOI: 10.1103/PhysRev.108.1175.

[33] L. N. Cooper, "Bound Electron Pairs in a Degenerate Fermi Gas," *Phys. Rev.*, vol. 104, no. 4, pp. 1189–1190, Nov. 1956, ISSN: 0031-899X. DOI: 10.1103/PhysRev.104.1189.

[34] M. Tinkham, *Introduction to Superconductivity*, 2nd ed. Mineola, N.Y: Dover Publications, 2004, ISBN: 978-1-62198-598-3.

[35] I. Giaever, "Electron Tunneling Between Two Superconductors," *Phys. Rev. Lett.*, vol. 5, no. 10, pp. 464–466, Nov. 1960. DOI: 10.1103/PhysRevLett.5.464.

[36] I. Giaever, "Energy Gap in Superconductors Measured by Electron Tunneling," *Phys. Rev. Lett.*, vol. 5, no. 4, pp. 147–148, Aug. 1960. DOI: 10.1103/PhysRevLett.5.147.

[37] J. Nicol, S. Shapiro, and P. H. Smith, "Direct Measurement of the Superconducting Energy Gap," *Phys. Rev. Lett.*, vol. 5, no. 10, pp. 461–464, Nov. 1960. DOI: 10.1103/PhysRevLett.5.461.

[38] B. D. Josephson, "Possible new effects in superconductive tunnelling," *Physics Letters*, vol. 1, no. 7, pp. 251–253, Jul. 1962, ISSN: 0031-9163. DOI: 10.1016/0031-9163(62)91369-0.

[39] P. W. Anderson and J. M. Rowell, "Probable Observation of the Josephson Superconducting Tunneling Effect," *Phys. Rev. Lett.*, vol. 10, no. 6, pp. 230–232, Mar. 1963. DOI: 10.1103/PhysRevLett.10.230.

[40] K. K. Likharev, *Dynamics of Josephson Junctions and Circuits*. London: Routledge, Feb. 2022, ISBN: 978-1-315-14157-2.

[41] T. A. Fulton, "Equivalent Circuits and Analogs of the Josephson Effect," in *Superconductor Applications: SQUIDs and Machines*, ser. NATO Advanced Study Institutes Series, B. B. Schwartz and S. Foner, Eds., Boston, MA: Springer US, 1977, pp. 125–187, ISBN: 978-1-4684-2805-6. DOI: 10.1007/978-1-4684-2805-6_4.

[42] D. E. McCumber, "Tunneling and Weak-Link Superconductor Phenomena Having Potential Device Applications," *Journal of Applied Physics*, vol. 39, no. 6, pp. 2503–2508, May 1968, ISSN: 0021-8979, 1089-7550. DOI: 10.1063/1.1656597.

[43] D. E. McCumber, "Effect of ac Impedance on dc Voltage-Current Characteristics of Superconductor Weak-Link Junctions," *Journal of Applied Physics*, vol. 39, no. 7, pp. 3113–3118, Nov. 2003, ISSN: 0021-8979. DOI: 10.1063/1.1656743.

[44] W. C. Stewart, "Current-Voltage Characteristics of Josephson Junctions," *Applied Physics Letters*, vol. 12, no. 8, pp. 277–280, Oct. 2003, ISSN: 0003-6951. DOI: 10.1063/1.1651991.

[45] R. C. Jaklevic, J. Lambe, A. H. Silver, and J. E. Mercereau, "Quantum Interference Effects in Josephson Tunneling," *Phys. Rev. Lett.*, vol. 12, no. 7, pp. 159–160, Feb. 1964. DOI: 10.1103/PhysRevLett.12.159.

[46] O. V. Lounasmaa, *Experimental Principles and Methods Below 1 K*. Academic Press, 1974, ISBN: 978-0-12-455950-9.

[47] F. Lombardi and T. Bauch, "9 - d-Wave YBCO dc superconductive quantum interference devices (dc SQUIDs)," in *High-Temperature Superconductors*, ser. Woodhead Publishing Series in Electronic and Optical Materials, X. G. Qiu, Ed., Woodhead Publishing, Jan. 2011, pp. 370–389, ISBN: 978-1-84569-578-1. DOI: 10.1533/9780857091031.3.370.

[48] W. Anacker, "Josephson Computer Technology: An IBM Research Project," *IBM Journal of Research and Development*, vol. 24, no. 2, pp. 107–112, Mar. 1980, ISSN: 0018-8646. DOI: 10.1147/rd.242.0107.

[49] R. E. Jewett, "Josephson Junctions in SPICE 2G5," Dec. 1982.

Link to ToC

[50] S. Whiteley, "Josephson junctions in SPICE3," *IEEE Transactions on Magnetics*, vol. 27, no. 2, pp. 2902–2905, Mar. 1991, ISSN: 1941-0069. DOI: 10.1109/20.133816.

[51] S. R. Whitely, *Wrsmanual.pdf*, http://wrcad.com/manual/wrsmanual.pdf.

[52] *QUCS Manual*.

[53] C. M. Caves, "Quantum limits on noise in linear amplifiers," *Phys. Rev. D*, vol. 26, no. 8, pp. 1817–1839, Oct. 1982. DOI: 10.1103/PhysRevD.26.1817.

[54] J. B. Johnson, "Thermal Agitation of Electricity in Conductors," *Phys. Rev.*, vol. 32, no. 1, pp. 97–109, Jul. 1928. DOI: 10.1103/PhysRev.32.97.

[55] H. Nyquist, "Thermal Agitation of Electric Charge in Conductors," *Phys. Rev.*, vol. 32, no. 1, pp. 110–113, Jul. 1928. DOI: 10.1103/PhysRev.32.110.

[56] H. Friis, "Noise Figures of Radio Receivers," *Proceedings of the IRE*, vol. 32, no. 7, pp. 419–422, Jul. 1944, ISSN: 2162-6634. DOI: 10.1109/JRPROC.1944.232049.

[57] W. W. Mumford, "Some Notes on the History of Parametric Transducers," *Proceedings of the IRE*, vol. 48, no. 5, pp. 848–853, May 1960, ISSN: 2162-6634. DOI: 10.1109/JRPROC.1960.287620.

[58] L. N. Factory, "LNF- 4-8 GHz cryogenic low noise amplifier," Tech. Rep., Feb. 2024.

[59] M. Faraday, "On a peculiar class of acoustical figures; and on certain forms assumed by groups of particles upon vibrating elastic surfaces," *Proc. R. Soc. Lond.*, vol. 3, pp. 49–51, Dec. 1837, ISSN: 0365-5695, 2053-9142. DOI: 10.1098/rspl.1830.0024.

[60] Melde, "Über Erregung stehender Wellen eines fadenförmigen Körpers [On the excitation of standing waves on a string]," *Annalen der Physik und Chemie*, Ser. 2, vol. vol. 109, pages 193–215. 1859.

[61] J. W. S. Rayleigh, *The Theory of Sound*. London: Macmillan and co., 1877.

[62] J. Rayleigh, "VII. On the crispations of fluid resting upon a vibrating support," *Philosophical Magazine Series 1*, vol. 16, no. 97, pp. 50–58, Jul. 1883, ISSN: 1941-5796. DOI: 10.1080/14786448308627392.

[63] J. Rayleigh, "XVII. *On the maintenance of vibrations by forces of double frequency, and on the propagation of waves through a medium endowed with a periodic structure*," *The London, Edinburgh, and Dublin Philosophical Magazine and Journal of Science*, vol. 24, no. 147, pp. 145–159, Aug. 1887, ISSN: 1941-5982, 1941-5990. DOI: 10.1080/14786448708628074.

[64] A. Van Der Ziel, "On the Mixing Properties of Non-Linear Condensers," *Journal of Applied Physics*, vol. 19, no. 11, pp. 999–1006, Apr. 2004, ISSN: 0021-8979. DOI: 10.1063/1.1698106.

[65] J. Manley, "Some General Properties of Magnetic Amplifiers," *Proceedings of the IRE*, vol. 39, no. 3, pp. 242–251, Mar. 1951, ISSN: 2162-6634. DOI: 10.1109/JRPROC.1951.231835.

[66] E. Alexanderson and S. Nixdorff, "A Magnetic Amplifier for Radio Telephony," *Proceedings of the Institute of Radio Engineers*, vol. 4, no. 2, pp. 101–120, Apr. 1916, ISSN: 2162-6626. DOI: 10.1109/JRPROC.1916.217224.

[67] Engelbrecht, "A low -noise nonlinear reactance traveling-wave amplifier," vol. 46, p. 1655, 1958.

[68] M. Currie and R. Gould, "Coupled-Cavity Traveling-Wave Parametric Amplifiers: Part I-Analysis," *Proc. IRE*, vol. 48, no. 12, pp. 1960–1973, Dec. 1960, ISSN: 0096-8390. DOI: 10.1109/JRPROC.1960.287564.

[69] R. H. Parmenter, "Nonlinear Electrodynamics of Superconductors with a Very Small Coherence Distance," *RCA (Radio Corporation of America) Review (U.S.)*, vol. Vol: 23, Sep. 1962.

[70] ̇*Gittleman*, B. Rosenblum, T. Seidel, and ̇*Wicklund*, "The Dependence of the Microwave Impedance of a Superconductor on Direct Currentf," in *Proceedings of the International Conference on Low Temperature Physics and Chemistry*, vol. 8, 1963, p. 336.

[71] A. Clorfeine, "Microwave amplification with superconductors," *Proceedings of the IEEE*, vol. 52, no. 7, pp. 844–845, Jul. 1964, ISSN: 1558-2256. DOI: 10.1109/PROC.1964.3130.

[72] J. R. Schrieffer and D. M. Ginsberg, "Calculation of the Quasiparticle Recombination Time in a Superconductor," *Phys. Rev. Lett.*, vol. 8, no. 5, pp. 207–208, Mar. 1962, ISSN: 0031-9007. DOI: 10.1103/PhysRevLett.8.207.

[73] A. S. Clorfeine, "Nonlinear reactance and frequency conversion in superconducting films at millimeter wavelengths," *Appl. Phys. Lett.*, vol. 4, no. 7, pp. 131–132, Apr. 1964, ISSN: 0003-6951. DOI: 10.1063/1.1753996.

[74] P. Bura, "Parametric amplification with superconducting films," *Proceedings of the IEEE*, vol. 54, no. 4, pp. 687–688, Apr. 1966, ISSN: 1558-2256. DOI: 10.1109/PROC.1966.4805.

[75] H. Zimmer, "Parametric amplification of microwaves in superconducting josephson tunnel junctions," *Appl. Phys. Lett.*, vol. 10, no. 7, pp. 193–195, Apr. 1967, ISSN: 0003-6951. DOI: 10.1063/1.1754906.

[76] S. Wahlsten, S. Rudner, and T. Claeson, "Parametric amplification in arrays of Josephson tunnel junctions," *Applied Physics Letters*, vol. 30, no. 6, pp. 298–300, Aug. 2008, ISSN: 0003-6951. DOI: 10.1063/1.89381.

[77] J. Mygind, N. F. Pedersen, and O. H. Soerensen, "X-band singly degenerate parametric amplification in a Josephson tunnel junction," *Applied Physics Letters*, vol. 32, no. 1, pp. 70–72, Aug. 2008, ISSN: 0003-6951. DOI: 10.1063/1.89844.

[78] H. Kanter and A. H. Silver, "Self-Pumped Josephson Parametric Amplification," *Applied Physics Letters*, vol. 19, no. 12, pp. 515–517, Oct. 2003, ISSN: 0003-6951. DOI: 10.1063/1.1653795.

[79] M. Pospieszalski, S. Weinreb, R. Norrod, and R. Harris, "FETs and HEMTs at cryogenic temperatures-their properties and use in low-noise amplifiers," *IEEE Transactions on Microwave Theory and Techniques*, vol. 36, no. 3, pp. 552–560, Mar. 1988, ISSN: 1557-9670. DOI: 10.1109/22.3548.

[80] B. Yurke *et al.*, "Observation of parametric amplification and deamplification in a Josephson parametric amplifier," *Phys. Rev. A*, vol. 39, no. 5, pp. 2519–2533, Mar. 1989. DOI: 10.1103/PhysRevA.39.2519.

[81] B. Yurke *et al.*, "Vacuum-noise squeezing at microwave frequencies using Josephson-parametric amplifier," *Physica B: Condensed Matter*, vol. 169, no. 1, pp. 432–435, Feb. 1991, ISSN: 0921-4526. DOI: 10.1016/0921-4526(91)90263-E.

[82] M. A. Castellanos-Beltran and K. W. Lehnert, "Widely tunable parametric amplifier based on a superconducting quantum interference device array resonator," *Applied Physics Letters*, vol. 91, no. 8, p. 083 509, Aug. 2007, ISSN: 0003-6951. DOI: 10.1063/1.2773988.

[83] M. A. Castellanos-Beltran, K. D. Irwin, G. C. Hilton, L. R. Vale, and K. W. Lehnert, "Amplification and squeezing of quantum noise with a tunable Josephson metamaterial," *Nature Phys*, vol. 4, no. 12, pp. 929–931, Dec. 2008, ISSN: 1745-2481. DOI: 10.1038/nphys1090.

[84] G. Matthaei, E. Jones, and L. Young, *Microwave Filters, Impedance Matching Networks, And Coupling Structures*. 1980.

[85] N. Engheta and R. W. Ziolkowski, "Physics and Engineering Explorations,"

[86] J. C. Bose and R. J. Strutt, "On the rotation of plane of polarisation of electric wave by a twisted structure," *Proceedings of the Royal Society of London*, vol. 63, no. 389-400, pp. 146–152, Jan. 1997. DOI: 10.1098/rspl.1898.0019.

Link to ToC

[87] F. Bloch, "Über die Quantenmechanik der Elektronen in Kristallgittern," *Z. Physik*, vol. 52, no. 7, pp. 555–600, Jul. 1929, ISSN: 0044-3328. DOI: 10.1007/BF01339455.

[88] Leon Brillouin, *Wave Propagation In Periodic Structures Electric Filters And Crystal Lattices First Edition*. 1946.

[89] V. G. Veselago, "The Electrodynamics of Substances with Simultaneously Negative Values of ε and μ," *Sov. Phys. Usp.*, vol. 10, no. 4, p. 509, Apr. 1968, ISSN: 0038-5670. DOI: 10.1070/PU1968v010n04ABEH003699.

[90] S. Tetenbaum, F. Olson, and A. Savarin, "A traveling-wave variable reactance type parametric amplifier," in *1960 International Electron Devices Meeting*, Oct. 1960, pp. 82–82. DOI: 10.1109/IEDM.1960.187200.

[91] W. R. Corliss, "A history of the deep space network," Tech. Rep. NASA-CR-151915, Nov. 1976.

[92] P. K. Tien, "Parametric Amplification and Frequency Mixing in Propagating Circuits," *Journal of Applied Physics*, vol. 29, no. 9, pp. 1347–1357, Sep. 1958, ISSN: 0021-8979, 1089-7550. DOI: 10.1063/1.1723440.

[93] R. W. DeGrasse, E. O. Schulz-DuBois, and H. E. D. Scovil, "The Three-Level Solid State Traveling-Wave Maser*," *Bell System Technical Journal*, vol. 38, no. 2, pp. 305–334, Mar. 1959, ISSN: 00058580. DOI: 10.1002/j.1538-7305.1959.tb03890.x.

[94] A. L. Cullen, "A Travelling-Wave Parametric Amplifier," *Nature*, vol. 181, no. 4605, pp. 332–332, Feb. 1958, ISSN: 1476-4687. DOI: 10.1038/181332a0.

[95] A. Cullen, "Theory of the travelling-wave parametric amplifier," *Proc. IEE, B Electron. Commun. Eng. UK*, vol. 107, no. 32, p. 101, 1960, ISSN: 03698890. DOI: 10.1049/pi-b-2.1960.0085.

[96] R. Landauer, "Shock Waves in Nonlinear Transmission Lines and Their Effect on Parametric Amplification," *IBM Journal of Research and Development*, vol. 4, no. 4, pp. 391–401, Oct. 1960, ISSN: 0018-8646. DOI: 10.1147/rd.44.0391.

[97] R. Landauer, "Parametric Amplification along Nonlinear Transmission Lines," *Journal of Applied Physics*, vol. 31, no. 3, pp. 479–484, Jun. 2004, ISSN: 0021-8979. DOI: 10.1063/1.1735612.

[98] B. Yurke, M. L. Roukes, R. Movshovich, and A. N. Pargellis, "A low-noise series-array Josephson junction parametric amplifier," *Appl. Phys. Lett.*, vol. 69, no. 20, pp. 3078–3080, Nov. 1996, ISSN: 0003-6951, 1077-3118. DOI: 10.1063/1.116845.

[99] R. W. Boyd, *Nonlinear Optics, Third Edition*, 3rd. USA: Academic Press, Inc., 2008, ISBN: 978-0-12-369470-6.

[100] P. Eugene, "Magnetic amplifier," US1884845A, Oct. 1932.

[101] B. Ho Eom, P. K. Day, H. G. LeDuc, and J. Zmuidzinas, "A wideband, low-noise superconducting amplifier with high dynamic range," *Nature Phys*, vol. 8, no. 8, pp. 623–627, Aug. 2012, ISSN: 1745-2481. DOI: 10.1038/nphys2356.

[102] T. C. White *et al.*, "Traveling wave parametric amplifier with Josephson junctions using minimal resonator phase matching," *Applied Physics Letters*, vol. 106, no. 24, p. 242 601, Jun. 2015, ISSN: 0003-6951. DOI: 10.1063/1.4922348.

[103] L. Planat *et al.*, "Photonic-Crystal Josephson Traveling-Wave Parametric Amplifier," *Phys. Rev. X*, vol. 10, no. 2, p. 021 021, Apr. 2020, ISSN: 2160-3308. DOI: 10.1103/PhysRevX.10.021021.

[104] N. Klimovich, P. Day, S. Shu, B. H. Eom, H. Leduc, and A. Beyer, *Demonstration of a Quantum Noise Limited Traveling-Wave Parametric Amplifier*, Jun. 2023. arXiv: 2306.11028 [astro-ph, physics:quant-ph].

[105] R. P. Erickson and D. P. Pappas, "Theory of multiwave mixing within the superconducting kinetic-inductance traveling-wave amplifier," *Phys. Rev. B*, vol. 95, no. 10, p. 104 506, Mar. 2017. DOI: 10.1103/PhysRevB.95.104506.

Link to ToC

[106] M. R. Vissers *et al.*, "Low-noise kinetic inductance traveling-wave amplifier using three-wave mixing," *Appl. Phys. Lett.*, vol. 108, no. 1, p. 012 601, Jan. 2016, ISSN: 0003-6951. DOI: 10.1063/1.4937922.

[107] A. B. Zorin, "Josephson Traveling-Wave Parametric Amplifier with Three-Wave Mixing," *Phys. Rev. Appl.*, vol. 6, no. 3, p. 034 006, Sep. 2016. DOI: 10.1103/PhysRevApplied.6.034006.

[108] A. Zorin, "Flux-Driven Josephson Traveling-Wave Parametric Amplifier," *Phys. Rev. Appl.*, vol. 12, no. 4, p. 044 051, Oct. 2019. DOI: 10.1103/PhysRevApplied.12.044051.

[109] T. Dixon, J. Dunstan, G. Long, J. Williams, P. Meeson, and C. Shelly, "Capturing Complex Behavior in Josephson Traveling-Wave Parametric Amplifiers," *Phys. Rev. Appl.*, vol. 14, no. 3, p. 034 058, Sep. 2020. DOI: 10.1103/PhysRevApplied.14.034058.

[110] V. Gaydamachenko, C. Kissling, R. Dolata, and A. B. Zorin, "Numerical analysis of a three-wave-mixing Josephson traveling-wave parametric amplifier with engineered dispersion loadings," *Journal of Applied Physics*, vol. 132, no. 15, p. 154 401, Oct. 2022, ISSN: 0021-8979. DOI: 10.1063/5.0111111.

[111] J. R. Sanmartfn, "O Botafumeiro: Parametric pumping in the Middle Ages," 1984.

[112] A. K. Walton, *Network Analysis and Practice*. Cambridge: Cambridge University Press, 1987, ISBN: 978-0-521-26459-4. DOI: 10.1017/CBO9781139171816.

[113] "Artificial Transmission Lines based on Periodic Structures," in *Artificial Transmission Lines for RF and Microwave Applications*, John Wiley & Sons, Ltd, 2015, ch. 2, pp. 47–118, ISBN: 978-1-119-05840-3. DOI: 10.1002/9781119058403.ch2.

[114] K. Armstrong, "PCB design techniques for lowest-cost EMC compliance. 2," *Electronics & Communication Engineering Journal*, vol. 11, pp. 218–226, Nov. 1999. DOI: 10.1049/ecej:19990503.

[115] Pozar, *Microwave Engineering, 4th Edition | Wiley*. 2011.

[116] G. J. Dolan, "Offset masks for lift-off photoprocessing," *Applied Physics Letters*, vol. 31, no. 5, pp. 337–339, Jun. 1977, ISSN: 0003-6951. DOI: 10.1063/1.89690.

[117] C. Kittel, *Introduction to Solid State Physics*, 8th ed. Hoboken, NJ: Wiley, 2005, ISBN: 978-0-471-41526-8.

[118] A. S. Kher, "Superconducting Nonlinear Kinetic Inductance Devices,"

[119] J. Zmuidzinas, "Superconducting Microresonators: Physics and Applications," *Annu. Rev. Condens. Matter Phys.*, vol. 3, no. 1, pp. 169–214, Mar. 2012, ISSN: 1947-5454, 1947-5462. DOI: 10.1146/annurev-conmatphys-020911-125022.

[120] D. C. Mattis and J. Bardeen, "Theory of the Anomalous Skin Effect in Normal and Superconducting Metals," *Phys. Rev.*, vol. 111, no. 2, pp. 412–417, Jul. 1958. DOI: 10.1103/PhysRev.111.412.

[121] A. Anthore, H. Pothier, and D. Esteve, "Density of States in a Superconductor Carrying a Supercurrent," *Phys. Rev. Lett.*, vol. 90, no. 12, p. 127 001, Mar. 2003. DOI: 10.1103/PhysRevLett.90.127001.

[122] S. Ó Peatáin, T. Dixon, P. J. Meeson, J. M. Williams, S. Kafanov, and Y. A. Pashkin, "Simulating the effects of fabrication tolerance on the performance of Josephson travelling wave parametric amplifiers," *Supercond. Sci. Technol.*, vol. 36, no. 4, p. 045 017, Apr. 2023, ISSN: 0953-2048, 1361-6668. DOI: 10.1088/1361-6668/acba4e.

[123] S. G. O Peatáin, T. Dixon, P. J. Meeson, J. M. Williams, S. Kafanov, and Y. A. Pashkin, "Modelling Losses in Superconducting Travelling Wave Parametric Amplifiers," in *Proceedings of the 29th International Conference on Low Temperature Physics (LT29)*, ser. JPS Conference Proceedings, vol. 38, Journal of the Physical Society of Japan, May 2023. DOI: 10.7566/JPSCP.38.011188.

Link to ToC

[124] O. Yaakobi, L. Friedland, C. Macklin, and I. Siddiqi, "Parametric amplification in Josephson junction embedded transmission lines," *Phys. Rev. B*, vol. 87, no. 14, p. 144 301, Apr. 2013, ISSN: 1098-0121, 1550-235X. DOI: 10.1103/PhysRevB.87.144301.

[125] T. Dixon, "Resolving Many Mode Processes in Josephson Travelling Wave Parametric Amplifiers,"

[126] A. H. Silver and J. E. Zimmerman, "Quantum States and Transitions in Weakly Connected Superconducting Rings," *Phys. Rev.*, vol. 157, no. 2, pp. 317–341, May 1967, ISSN: 0031-899X. DOI: 10.1103/PhysRev.157.317.

[127] L. Planat, "Amplification paramétrique en résonance et à ondes progressives proche de la limite quantique," These de Doctorat, Université Grenoble Alpes, Jun. 2020.

[128] Nagel, Laurence W. and Pederson, D.O., *SPICE (Simulation Program with Integrated Circuit Emphasis)*, Apr. 1973.

[129] F. Kuo, Whiteley, S.R., and Faris, S.M., "A fast Josephson SFQ shift register," *IEEE Transactions on Magnetics*, vol. 25, no. 10, pp. 841–844, 1989. DOI: 10.1109/20.92417.

[130] T. A. Davis and E. Palamadai Natarajan, "Algorithm 907: KLU, A Direct Sparse Solver for Circuit Simulation Problems," *ACM Trans. Math. Softw.*, vol. 37, no. 3, 36:1–36:17, Sep. 2010, ISSN: 0098-3500. DOI: 10.1145/1824801.1824814.

[131] C. Kaiser, "High Quality Nb/Al-AlOx/Nb Josephson Junctions: Technological Development and Macroscopic Quantum Experiments," Ph.D. dissertation.

[132] C. D. Shelly, P. See, I. Rungger, and J. M. Williams, "Existence of Shapiro Steps in the Dissipative Regime in Superconducting Weak Links," *Phys. Rev. Applied*, vol. 13, no. 2, p. 024 070, Feb. 2020, ISSN: 2331-7019. DOI: 10.1103/PhysRevApplied.13.024070.

[133] B. A. Kochetov and A. Fedorov, "Higher-order nonlinear effects in a Josephson parametric amplifier," *Phys. Rev. B*, vol. 92, no. 22, p. 224 304, Dec. 2015. DOI: 10.1103/PhysRevB.92.224304.

[134] S. Kern *et al.*, "Reflection-enhanced gain in traveling-wave parametric amplifiers," *Phys. Rev. B*, vol. 107, no. 17, p. 174 520, May 2023. DOI: 10.1103/PhysRevB.107.174520.

[135] N. Lazarides and G. P. Tsironis, "Rf superconducting quantum interference device metamaterials," *Applied Physics Letters*, vol. 90, no. 16, p. 163 501, Apr. 2007, ISSN: 0003-6951. DOI: 10.1063/1.2722682.

[136] M. Green *et al.*, "Doped, conductive SiO2 nanoparticles for large microwave absorption," *Light Sci Appl*, vol. 7, no. 1, p. 87, Nov. 2018, ISSN: 2047-7538. DOI: 10.1038/s41377-018-0088-8.

[137] C. S. Macklin, "Quantum Feedback and Traveling-wave Parametric Amplification in Superconducting Circuits,"

[138] A. Greco, "Theoretical development and characterisation of a Josephson Traveling Wave Parametric Amplifier for very low power microwave signals,"

[139] J. Baker-Jarvis *et al.*, "Measuring the permittivity and permeability of lossy materials : Solids, liquids, metals, building materials, and negative-index materials,"

[140] ASTM International, *Test Methods for AC Loss Characteristics and Permittivity (Dielectric Constant) of Solid Electrical Insulation*. DOI: 10.1520/D0150-11.

[141] S. Krinner *et al.*, "Engineering cryogenic setups for 100-qubit scale superconducting circuit systems," *EPJ Quantum Technol.*, vol. 6, no. 1, pp. 1–29, Dec. 2019, ISSN: 2196-0763. DOI: 10.1140/epjqt/s40507-019-0072-0.

[142] Keithley, *Keithley Low Level Measurements Handbook - 7th Edition*, 7th ed. Tektronix.

[143] F. W. Grover, "Methods for the derivation and expansion of formulas for the mutual inductance of coaxial circles and for the inductance of single-layer solenoids," *BUR. STAN. J. RES.*, vol. 1, no. 4, p. 487, Oct. 1928, ISSN: 0091-1801. DOI: 10.6028/jres.001.016.

[144] E. J. Patiño and N. G. Kelkar, "Experimental determination of tunneling characteristics and dwell times from temperature dependence of Al/Al2O3/Al junctions," *Applied Physics Letters*, vol. 107, no. 25, p. 253 502, Dec. 2015, ISSN: 0003-6951. DOI: 10.1063/1.4938209.

[145] R. Dolata, H. Scherer, A. B. Zorin, and J. Niemeyer, "Single-charge devices with ultrasmall Nb/AlOx/Nb trilayer Josephson junctions," *J. Appl. Phys.*, vol. 97, no. 5, p. 054 501, 2005. DOI: 10.1063/1.1855399.

[146] A. Zorin, M. Khabipov, J. Dietel, and R. Dolata, "Traveling-wave parametric amplifier based on three-wave mixing in a josephson metamaterial," Jun. 2017, pp. 1–3. DOI: 10.1109/ISEC.2017.8314196.

[147] V. Ambegaokar and A. Baratoff, "Tunneling Between Superconductors," *Phys. Rev. Lett.*, vol. 10, no. 11, pp. 486–489, Jun. 1963, ISSN: 0031-9007. DOI: 10.1103/PhysRevLett.10.486.

[148] C. Enss and S. Hunklinger, *Low-Temperature Physics*. Springer Science & Business Media, Dec. 2005, ISBN: 978-3-540-26619-8.

[149] C. Couteau, "Spontaneous parametric down-conversion," *Contemporary Physics*, vol. 59, no. 3, pp. 291–304, Jul. 2018, ISSN: 0010-7514, 1366-5812. DOI: 10.1080/00107514.2018.1488463. arXiv: 1809.00127 [physics, physics:quant-ph].

[150] G. Kulkarni, J. Rioux, B. Braverman, M. V. Chekhova, and R. W. Boyd, "Classical model of spontaneous parametric down-conversion," *Phys. Rev. Research*, vol. 4, no. 3, p. 033 098, Aug. 2022, ISSN: 2643-1564. DOI: 10.1103/PhysRevResearch.4.033098.

[151] X. Guo, C.-l. Zou, C. Schuck, H. Jung, R. Cheng, and H. X. Tang, "Parametric down-conversion photon-pair source on a nanophotonic chip," *Light Sci Appl*, vol. 6, no. 5, e16249–e16249, May 2017, ISSN: 2047-7538. DOI: 10.1038/lsa.2016.249.

[152] S. B. Kaplan, C. C. Chi, D. N. Langenberg, J. J. Chang, S. Jafarey, and D. J. Scalapino, "Quasiparticle and phonon lifetimes in superconductors," *Phys. Rev. B*, vol. 14, no. 11, pp. 4854–4873, Dec. 1976. DOI: 10.1103/PhysRevB.14.4854.

[153] S. A. H. de Rooij, J. J. A. Baselmans, V. Murugesan, D. J. Thoen, and P. J. de Visser, "Strong reduction of quasiparticle fluctuations in a superconductor due to decoupling of the quasiparticle number and lifetime," *Phys. Rev. B*, vol. 104, no. 18, p. L180506, Nov. 2021. DOI: 10.1103/PhysRevB.104.L180506.

[154] J. Y. Qiu *et al.*, "Broadband squeezed microwaves and amplification with a Josephson travelling-wave parametric amplifier," *Nat. Phys.*, pp. 1–8, Feb. 2023, ISSN: 1745-2481. DOI: 10.1038/s41567-022-01929-w.

[155] S. Chaudhuri *et al.*, "Broadband parametric amplifiers based on nonlinear kinetic inductance artificial transmission lines," *Applied Physics Letters*, vol. 110, no. 15, p. 152 601, Apr. 2017, ISSN: 0003-6951. DOI: 10.1063/1.4980102.

[156] S. Shu *et al.*, "Nonlinearity and wide-band parametric amplification in a (Nb,Ti)N microstrip transmission line," *Phys. Rev. Res.*, vol. 3, no. 2, p. 023 184, Jun. 2021. DOI: 10.1103/PhysRevResearch.3.023184.

[157] E. Cassedy and A. Oliner, "Dispersion relations in time-space periodic media: Part I—Stable interactions," *Proceedings of the IEEE*, vol. 51, no. 10, pp. 1342–1359, Oct. 1963, ISSN: 1558-2256. DOI: 10.1109/PROC.1963.2566.

[158] J. A. Armstrong, N. Bloembergen, J. Ducuing, and P. S. Pershan, "Interactions between Light Waves in a Nonlinear Dielectric," *Phys. Rev.*, vol. 127, no. 6, pp. 1918–1939, Sep. 1962, ISSN: 0031-899X. DOI: 10.1103/PhysRev.127.1918.

Link to ToC

[159] Y. Ivry *et al.*, "Universal scaling of the critical temperature for thin films near the superconducting-to-insulating transition," *Phys. Rev. B*, vol. 90, no. 21, p. 214 515, Dec. 2014. DOI: 10.1103/PhysRevB.90.214515.

[160] A. E. Lita, V. B. Verma, R. D. Horansky, J. M. Shainline, R. P. Mirin, and S. Nam, "Materials Development for High Efficiency Superconducting Nanowire Single-Photon Detectors," *MRS Online Proceedings Library (OPL)*, vol. 1807, pp. 1–6, 2015/ed, ISSN: 0272-9172, 1946-4274. DOI: 10.1557/opl.2015.544.

[161] A. A. Adamyan, S. E. de Graaf, S. E. Kubatkin, and A. V. Danilov, "Superconducting microwave parametric amplifier based on a quasi-fractal slow propagation line," *Journal of Applied Physics*, vol. 119, no. 8, p. 083 901, Feb. 2016, ISSN: 0021-8979. DOI: 10.1063/1.4942362.

[162] R. W. Cohen and B. Abeles, "Superconductivity in Granular Aluminum Films," *Phys. Rev.*, vol. 168, no. 2, pp. 444–450, Apr. 1968, ISSN: 0031-899X. DOI: 10.1103/PhysRev.168.444.

[163] S. Linzen *et al.*, "Structural and electrical properties of ultrathin niobium nitride films grown by atomic layer deposition," *Supercond. Sci. Technol.*, vol. 30, no. 3, p. 035 010, Jan. 2017, ISSN: 0953-2048. DOI: 10.1088/1361-6668/aa572a.

[164] B. Tummers, *DataThief version 1.6*, 2006.

[165] E. Knehr *et al.*, "Nanowire single-photon detectors made of atomic layer-deposited niobium nitride," *Supercond. Sci. Technol.*, vol. 32, no. 12, p. 125 007, Dec. 2019, ISSN: 0953-2048, 1361-6668. DOI: 10.1088/1361-6668/ab48d7.

[166] S. E. de Graaf *et al.*, "Charge quantum interference device," *Nature Phys*, vol. 14, no. 6, pp. 590–594, Jun. 2018, ISSN: 1745-2481. DOI: 10.1038/s41567-018-0097-9.

[167] R. S. Shaikhaidarov *et al.*, "Quantized current steps due to the a.c. coherent quantum phase-slip effect," *Nature*, vol. 608, no. 7921, pp. 45–49, Aug. 2022, ISSN: 1476-4687. DOI: 10.1038/s41586-022-04947-z.

[168] S. V. Vegesna, S. V. Lanka, D. Bürger, Z. Li, S. Linzen, and H. Schmidt, "Analysis of Low-Temperature Magnetotransport Properties of NbN Thin Films Grown by Atomic Layer Deposition," *Magnetochemistry*, vol. 8, no. 3, p. 33, Mar. 2022, ISSN: 2312-7481. DOI: 10.3390/magnetochemistry8030033.

[169] T. Shiino *et al.*, "Improvement of the critical temperature of superconducting NbTiN and NbN thin films using the AlN buffer layer," *Supercond. Sci. Technol.*, vol. 23, no. 4, p. 045 004, Apr. 2010, ISSN: 0953-2048, 1361-6668. DOI: 10.1088/0953-2048/23/4/045004.

[170] M. V. Shibalov *et al.*, "A Study of Ultrathin Superconducting Films of Niobium Nitride Obtained by Atomic Layer Deposition," *Tech. Phys.*, vol. 66, no. 5, pp. 658–663, May 2021, ISSN: 1090-6525. DOI: 10.1134/S1063784221040174.

[171] P. C. J. J. Coumou, E. F. C. Driessen, J. Bueno, C. Chapelier, and T. M. Klapwijk, "Electrodynamic response and local tunneling spectroscopy of strongly disordered superconducting TiN films," *Phys. Rev. B*, vol. 88, no. 18, p. 180 505, Nov. 2013. DOI: 10.1103/PhysRevB.88.180505.

[172] P. C. J. J. Coumou, M. R. Zuiddam, E. F. C. Driessen, P. J. de Visser, J. J. A. Baselmans, and T. M. Klapwijk, "Microwave Properties of Superconducting Atomic-Layer Deposited TiN Films," *IEEE Transactions on Applied Superconductivity*, vol. 23, no. 3, pp. 7 500 404–7 500 404, Jun. 2013, ISSN: 1558-2515. DOI: 10.1109/TASC.2012.2236603.

[173] F. Pfuner, L. Degiorgi, T. I. Baturina, V. M. Vinokur, and M. R. Baklanov, "Optical properties of TiN thin films close to the superconductor–insulator transition," *New J. Phys.*, vol. 11, no. 11, p. 113 017, Nov. 2009, ISSN: 1367-2630. DOI: 10.1088/1367-2630/11/11/113017.

Link to ToC

[174] A. Giachero *et al.*, "Characterization of NbTiN Films With Thicknesses Below 20 nm for Low Power Kinetic Inductance Amplifiers," *IEEE Transactions on Applied Superconductivity*, vol. 33, no. 5, pp. 1–5, Aug. 2023, ISSN: 1558-2515. DOI: 10.1109/TASC.2023.3253069.

[175] L. Zhang, W. Peng, L. X. You, and Z. Wang, "Superconducting properties and chemical composition of NbTiN thin films with different thickness," *Appl. Phys. Lett.*, vol. 107, no. 12, p. 122 603, Sep. 2015, ISSN: 0003-6951, 1077-3118. DOI: 10.1063/1.4931943.

[176] E. Knehr *et al.*, "Wafer-level uniformity of atomic-layer-deposited niobium nitride thin films for quantum devices," *Journal of Vacuum Science & Technology A*, vol. 39, no. 5, p. 052 401, Sep. 2021, ISSN: 0734-2101. DOI: 10.1116/6.0001126.

[177] M. Malnou *et al.*, "Three-Wave Mixing Kinetic Inductance Traveling-Wave Amplifier with Near-Quantum-Limited Noise Performance," *PRX Quantum*, vol. 2, no. 1, p. 010 302, Jan. 2021, ISSN: 2691-3399. DOI: 10.1103/PRXQuantum.2.010302.

[178] H. Wheeler, "The transmission-line properties of a round wire between parallel planes," *IRE Transactions on Antennas and Propagation*, vol. 3, no. 4, pp. 203–207, Oct. 1955, ISSN: 1558-3643. DOI: 10.1109/TAP.1955.1144325.

[179] H. Wheeler, "Transmission-Line Properties of a Strip on a Dielectric Sheet on a Plane," *IEEE Transactions on Microwave Theory and Techniques*, vol. 25, no. 8, pp. 631–647, Aug. 1977, ISSN: 1557-9670. DOI: 10.1109/TMTT.1977.1129179.

[180] E. Hammerstad and O. Jensen, "Accurate Models for Microstrip Computer-Aided Design," in *1980 IEEE MTT-S International Microwave Symposium Digest*, May 1980, pp. 407–409. DOI: 10.1109/MWSYM.1980.1124303.

[181] Brian C. Waddell, *Transmission Line Design Handbook*. Artech House, 1991, ISBN: 978-0-89006-436-8.

[182] E. Bogatin, "Design rules for microstrip capacitance," *IEEE Transactions on Components, Hybrids, and Manufacturing Technology*, vol. 11, no. 3, pp. 253–259, Sep. 1988, ISSN: 1558-3082. DOI: 10.1109/33.16649.

[183] R. P. Owens and M. H. N. Potok, "Analytical methods for calculating the characteristic impedance of finite-thickness microstrip lines," *International Journal of Electronics*, vol. 41, no. 4, pp. 399–403, Oct. 1976, ISSN: 0020-7217, 1362-3060. DOI: 10.1080/00207217608920650.

[184] H. Atwater, "Tests of microstrip dispersion formulas," *IEEE Transactions on Microwave Theory and Techniques*, vol. 36, no. 3, pp. 619–621, Mar. 1988, ISSN: 1557-9670. DOI: 10.1109/22.3561.

[185] M. V. Schneider, "Microstrip lines for microwave integrated circuits," *The Bell System Technical Journal*, vol. 48, no. 5, pp. 1421–1444, May 1969, ISSN: 0005-8580. DOI: 10.1002/j.1538-7305.1969.tb04274.x.

[186] M. Schneider, "Microstrip dispersion," *Proceedings of the IEEE*, vol. 60, no. 1, pp. 144–146, Jan. 1972, ISSN: 1558-2256. DOI: 10.1109/PROC.1972.8581.

[187] N. S. Klimovich, "Traveling Wave Parametric Amplifiers and Other Nonlinear Kinetic Inductance Devices," Ph.D. dissertation, California Institute of Technology, 2022. DOI: 10.7907/w980-rs97.

[188] N. M. Martin, "The computer-aided design of rectangular microstrip antennas / by Noel Maxwell Martin," Thesis, 1984.

[189] C. A. Balanis, *Antenna Theory: Analysis and Design*, 3. ed. Hoboken, N.J: Wiley-Interscience, 2005, ISBN: 978-0-471-66782-7.

[190] S. G. Ó Peatáin, *Github.com/searbhan/JTWPA_Analytical_Sim*.

[191] A. B. Zorin, "Quasi-phasematching in a poled Josephson traveling-wave parametric amplifier with three-wave mixing," *Appl. Phys. Lett.*, vol. 118, no. 22, p. 222 601, 2021. DOI: 10.1063/5.0050787. eprint: https://doi.org/10.1063/5.0050787.

Link to ToC

[192] A. Anferov, K.-H. Lee, F. Zhao, J. Simon, and D. I. Schuster, "Improved coherence in optically defined niobium trilayer-junction qubits," *Phys. Rev. Appl.*, vol. 21, no. 2, p. 024 047, Feb. 2024. DOI: 10.1103/PhysRevApplied.21.024047.

Appendix A

Impedance and Transfer Function Derivation from the Π-Cell Model

The following derivation is reproduced with some extra steps from *"Network Analysis and Practice" - A. K. Walton, 1987* [112]. This derivation should give some clarity on the characteristics of wave propagation in lumped element transmission lines.

The characteristic impedance of an infinite chain of impedances, Z_s and Z_p for the series and parallel (or return) impedances, respectively, can be calculated using a Π-cell model. The impedance to ground, Z_p, is split equally between neighbouring cells as shown in Figure 1.7. The following derivation can be repeated for other cases as shown in [112]. A Π-cell added to the end of the infinite chain has its impedance, Z_Π, calculated from the impedance network as:

$$Z_\Pi^{-1} = \left[\left(\frac{2Z_{\Pi L}Z_p}{Z_{\Pi L}+2Z_p}\right)+Z_s\right]^{-1}+[2Z_p]^{-1} \ , \tag{A.1}$$

where, the characteristic impedance is a function of the elements of the added cell as well as the characteristic impedance of the transmission line preceding it, $Z_{\Pi L}$. Expanded, this takes the form:

$$Z_\Pi = \frac{2Z_p\left[Z_sZ_{\Pi L}+2Z_sZ_p+2Z_pZ_{\Pi L}\right]}{2Z_p\left[2Z_{\Pi L}+Z_s+2Z_p\right]+Z_sZ_{\Pi L}} \ . \tag{A.2}$$

Assuming that each cell is equally loaded, i.e. that $Z_\Pi \equiv Z_{\Pi L}$, this equation is reduced to:

$$Z_\Pi = \sqrt{\frac{Z_sZ_p}{1+Z_s/4Z_p}} \ . \tag{A.3}$$

Z_Π is imaginary when the denominator of the above equation is negative, meaning waves cannot propagate. Therefore, at $Z_s/4Z_p = -1$ a critical frequency for wave propagation, ω_c, can be determined.

Link to ToC

Writing impedances Z_s and Z_p in terms of the reactances used in the JTWPA circuit of Figure 2.3, we come to:

$$\frac{Z_s}{4Z_p} \equiv \frac{\omega_c C_0 L_G / C_J}{4\omega_c L_G - 4/\omega_c C_J} = -1 \ , \tag{A.4}$$

and:

$$\omega_c = \frac{2}{\sqrt{L_G\left(C_0 + 4C_J\right)}} \ . \tag{A.5}$$

Therefore, rewriting Z_Π in terms of ω_c:

$$Z_\Pi = \sqrt{\frac{L_G}{C_0\left(1 - \omega^2/\omega_c^2\right)}} \ . \tag{A.6}$$

To better understand the wave propagation and dispersion in the device the transfer function between cells must be found. Looking at the current flows in the $(n+1)^{th}$ cell of the chain shown in Fig. 1.7, we find:

$$\left[Z_p + Z_s + \frac{2Z_p Z_\Pi}{2Z_p + Z_\Pi}\right] I_{n+1} = Z_p I_n \ . \tag{A.7}$$

This leads to a transfer function, $\mathscr{T}$, in terms of I_n and I_{n+1} such that:

$$\mathscr{T}^{-1} = \frac{I_n}{I_{n+1}} \equiv \frac{Z_p + Z_s + \frac{2Z_p Z_\Pi}{2Z_p + Z_\Pi}}{Z_p} \ , \tag{A.8}$$

or expanded,

$$\mathscr{T}^{-1} = \frac{Z_p\left(2Z_s + 2Z_p + 3Z_\Pi\right) + Z_s Z_\Pi}{2Z_p^2 + Z_p Z_\Pi} \ . \tag{A.9}$$

Using A.3 and substituting $Z_s/4Z_p$ as u, we can rewrite the above as:

$$\mathscr{T}^{-1} = 1 + \frac{Z_s}{Z_p} + \frac{2\sqrt{Z_s Z_p}}{2Z_p\sqrt{1+u} + \sqrt{Z_s Z_p}} \ , \tag{A.10}$$

$$= \frac{2\sqrt{Z_s Z_p}\left(2Z_p\sqrt{1+u} - \sqrt{Z_s Z_p}\right)}{4Z_p^2\left(1+u\right) - Z_s Z_p} \ , \tag{A.11}$$

$$= \frac{2\sqrt{Z_s Z_p}\sqrt{1+u} - Z_s}{2Z_p} \ , \tag{A.12}$$

$$= 1 + \frac{Z_s}{2Z_p} + \sqrt{\frac{Z_s}{Z_p}\left(1+u\right)} \ , \tag{A.13}$$

$$= \left[1 + 2u + \sqrt{4u\left(1+u\right)}\right]^{-1} \ . \tag{A.14}$$

The relation between the transfer function and propagation constant, $\mathscr{T} = \exp(-\gamma)$, can be used to find analytical solutions for the attenuation and phase shift constants.

$$\cosh\gamma = \frac{1}{2}\left(\mathscr{T} + \mathscr{T}^{-1}\right) \ . \tag{A.15}$$

We can expand this relation to:

$$\cosh\gamma = \frac{1}{2}\left[\frac{\left(1+2u+\sqrt{4u\,(1+u)}\right)^2+1}{1+2u+\sqrt{4u\,(1+u)}}\right]\left[\frac{1+2u-\sqrt{4u\,(1+u)}}{1+2u-\sqrt{4u\,(1+u)}}\right] \ , \tag{A.16}$$

$$= 1+2u \ . \tag{A.17}$$

Expanding the propagation constant into its constituent parts of attenuation, α, and phase shift, β, constants:

$$\cosh\gamma = \cosh\left(\alpha+i\beta\right) = 1+2u \ , \tag{A.18}$$

$$= \cosh\alpha\cos\beta + i\sinh\alpha\sin\beta \ . \tag{A.19}$$

Using the assumption of lossless transmission, i.e. $\alpha = 0$, and the relation for the wavevector, $k = i\gamma$, we can find a simple relation for the dispersion relation of waves propagating along the chain:

$$k = \arccos\left(1+\frac{Z_s}{2Z_p}\right) \ , \tag{A.20}$$

or using the small angle approximation:

$$k = 1+\frac{\omega C_0 L_G/C_J}{2\omega L_G - 2/\omega C_J} \ . \tag{A.21}$$

While the specific reactances may change this method is broadly applicable to similar schemes making it useful in characterizing travelling wave parametric amplifier schemes.

The above relation can be simplified with the substitutions $\omega_c = 1/\sqrt{L_T C_0}$ and $\omega_j = 1/\sqrt{L_T C_J}$ and the approximation that $\arccos\left(1-u\right) \simeq \sqrt{2u} \sim k$.

Appendix B

Wave Equation Derivation

B.1

Current through an rf-SQUID

Beginning with the transcendental equation (Equation 2.1) which described the effect of a flux bias on the current-phase relation of an rf-SQUID, we take a Taylor expansion around $\varphi_{ac} = 0$:

$$I_J = I_c\left(2\pi\frac{\Phi_{ac}}{\Phi_0}\right)\cos\left(2\pi\frac{\Phi_{dc}}{\Phi_0}\right) - I_c\left(2\pi\frac{\Phi_{ac}}{\Phi_0}\right)^2\frac{\sin\left(2\pi\frac{\Phi_{dc}}{\Phi_0}\right)}{2} \tag{B.1}$$

$$-I_c\left(2\pi\frac{\Phi_{ac}}{\Phi_0}\right)^3\frac{\cos\left(2\pi\frac{\Phi_{dc}}{\Phi_0}\right)}{6} + I_c\left(2\pi\frac{\Phi_{ac}}{\Phi_0}\right)^4\frac{\sin\left(2\pi\frac{\Phi_{dc}}{\Phi_0}\right)}{24}$$

$$+I_c\left(2\pi\frac{\Phi_{ac}}{\Phi_0}\right)^5\frac{\cos\left(2\pi\frac{\Phi_{dc}}{\Phi_0}\right)}{120} + \mathcal{O}... \tag{B.2}$$

We can replace the prefactors of the φ_{ac} terms with $\tilde{\chi}^{(n)}$ terms for simpler comparison with similar optics descriptions of wave mixing in media with nonlinear responses.

$$\tilde{\chi}^{(1)} = I_c\cos\left(2\pi\frac{\Phi_{dc}}{\Phi_0}\right) \tag{B.3}$$

$$\tilde{\chi}^{(2)} = -\frac{I_c}{2}\sin\left(2\pi\frac{\Phi_{dc}}{\Phi_0}\right) \tag{B.4}$$

$$\tilde{\chi}^{(3)} = -\frac{I_c}{6}\cos\left(2\pi\frac{\Phi_{dc}}{\Phi_0}\right) \tag{B.5}$$

$$\tilde{\chi}^{(4)} = \frac{I_c}{24}\sin\left(2\pi\frac{\Phi_{dc}}{\Phi_0}\right) \tag{B.6}$$

$$\tilde{\chi}^{(5)} = \frac{I_c}{120}\cos\left(2\pi\frac{\Phi_{dc}}{\Phi_0}\right) \tag{B.7}$$

The $\tilde{\chi}^{(2)}$ and $\tilde{\chi}^{(3)}$ correspond to three wave mixing (3WM) and four wave mixing (4WM, Kerr-like) nonlinearities, respectively.

Link to ToC

B.2 Flux Nodes

The concept of flux nodes is key to the building of a circuit model for superconducting devices. By describing the potential difference across the nth cell in the array as the derivative of the flux through SQUID loop:

$$-\frac{d\Phi_n}{dt} = V_{n+1} - V_n \ , \tag{B.8}$$

we are able to relate the previously defined current relation to magnetic flux through the loop and hence the superconducting phase gradient across the junction. As the SQUID loops are galvanically connected to each other we must introduce the idea of a flux node to describe the potential at the points where the loops meet and there is a return capacitance. We state that at these points:

$$V_n = -\frac{d\tilde{\Phi}_n}{dt} \tag{B.9}$$

which then leads to:

$$-\frac{d\Phi_n}{dt} = \frac{d\tilde{\Phi}_{n+1}}{dt} - \frac{d\tilde{\Phi}_n}{dt} \ , \tag{B.10}$$

$$\Phi_n = \Phi_n - \Phi_{n+1} \ . \tag{B.11}$$

B.3 Continuum Approximation

Following from Equation 2.17, neglecting losses and grouping similar terms, we can come to:

$$\begin{aligned} 0 = \quad & \left[\frac{1}{\beta_L} + \chi^{(1)} + C_j\frac{d^2}{dt^2}\right]\left(\tilde{\Phi}_{n+1} + \tilde{\Phi}_{n-1} - 2\tilde{\Phi}_n\right) \\ & +\chi^{(2)}\left(\frac{2\pi}{\Phi_0}\right)^2\left(\tilde{\Phi}_{n+1} + \tilde{\Phi}_{n-1} - 2\tilde{\Phi}_n\right)^2 \\ & +\chi^{(3)}\left(\frac{2\pi}{\Phi_0}\right)^3\left(\tilde{\Phi}_{n+1} + \tilde{\Phi}_{n-1} - 2\tilde{\Phi}_n\right)^3 \end{aligned} \tag{B.12}$$

We can make a continuity approximation for the medium, with the estimates that:

$$\Phi_{n+1} - \Phi_n \approx a\frac{\partial\Phi}{\partial x} + \frac{a^2}{2}\frac{\partial^2\Phi}{\partial x^2} \tag{B.13}$$

$$\Phi_n - \Phi_{n-1} \approx a\frac{\partial\Phi}{\partial x} - \frac{a^2}{2}\frac{\partial^2\Phi}{\partial x^2} \tag{B.14}$$

$$\Phi_{n+1} + \Phi_{n-1} - 2\Phi_n = a^2\frac{\partial^2\Phi}{\partial x^2} \tag{B.15}$$

Link to ToC

Substituting these into B.12 we arrive at a wave equation for the medium.

$$\frac{a^2}{2L_G}\frac{\partial^2\tilde{\Phi}}{\partial x^2}+\chi^{(1)}\left[\frac{a^2}{2}\frac{\partial^2\tilde{\Phi}}{\partial x^2}\right]+\chi^{(2)}\left[2a^3\frac{\partial\tilde{\Phi}}{\partial x}\left(\frac{\partial^2\tilde{\Phi}}{\partial x^2}\right)\right]+\chi^{(3)}\left[a^4\left(\frac{\partial\tilde{\Phi}}{\partial x}\right)^2\frac{\partial^2\tilde{\Phi}}{\partial x^2}\right]$$
$$+C_j\frac{a^2}{2}\frac{\partial^4\tilde{\Phi}}{\partial t^2\partial x^2}+C_0\frac{a^2}{2}\frac{\partial^2\tilde{\Phi}}{\partial t^2}=0 \tag{B.16}$$

B.4 Reduced Wave Equation

If the substitution of superconducting phase gradient for flux is made via 1.36, this wave equation can be rewritten as:

$$-\frac{\Phi_0}{2\pi}\left[\frac{1}{L_T}+C_j\frac{\partial^2}{\partial t^2}+R_j\frac{\partial}{\partial t}\right]\frac{\partial^2\tilde{\varphi}}{\partial x^2}+2\tilde{\chi}^{(2)}\frac{\partial}{\partial x}\left(\frac{\partial\tilde{\varphi}}{\partial x}\right)^2+3\tilde{\chi}^{(3)}\frac{\partial}{\partial x}\left(\frac{\partial\tilde{\varphi}}{\partial x}\right)^3$$
$$+\frac{\Phi_0 C_0}{2\pi}\frac{\partial^2\tilde{\varphi}}{\partial t^2}=0\ . \tag{B.17}$$

Then making some substitutions $\omega_c=1/\sqrt{L_TC_0}$ and $\omega_j=1/\sqrt{L_TC_J}$ and redefining the nonlinearities $\chi^{(2)}=2\pi\tilde{\chi}^{(2)}L_G/\Phi_0$

$$-\frac{\partial^2\tilde{\varphi}}{\partial x^2}+\frac{1}{\omega_J^2}\frac{\partial^4\tilde{\varphi}}{\partial x^2\partial t^2}+2\chi^{(2)}\frac{\partial}{\partial x}\left(\frac{\partial\tilde{\varphi}}{\partial x}\right)^2+3\chi^{(3)}\frac{\partial}{\partial x}\left(\frac{\partial\tilde{\varphi}}{\partial x}\right)^3+\frac{1}{\omega_c^2}\frac{\partial^2\tilde{\varphi}}{\partial t^2}=0 \tag{B.18}$$

A reduced form of the wave equation can be found using a trial solution:

$$\tilde{\phi}=\frac{1}{2}\left\{Ae^{i(kx-\omega t)}+A^*e^{-i(kx-\omega t)}\right\}, \tag{B.19}$$

were the appropriate derivatives are:

$$\frac{\partial\tilde{\phi}}{\partial x}=ik\tilde{\phi}+\frac{1}{2}\left(\frac{\partial A}{\partial x}e^{i(kx-\omega t)}+c.c.\right) \tag{B.20}$$
$$\frac{\partial^2\tilde{\phi}}{\partial x^2}=-k^2\tilde{\phi}+ik\left(\frac{\partial A}{\partial x}e^{i(kx-\omega t)}+c.c.\right)+\frac{1}{2}\left(\frac{\partial^2 A}{\partial x^2}e^{i(kx-\omega t)}+c.c.\right) \tag{B.21}$$
$$\frac{\partial\tilde{\phi}}{\partial t}=-i\omega\tilde{\phi} \tag{B.22}$$
$$\frac{\partial^2\tilde{\phi}}{\partial t^2}=-\omega^2\tilde{\phi} \tag{B.23}$$

and using the slow-wave approximation (Equation 2.21) we can write:

$$\frac{\partial^4\tilde{\phi}}{\partial x^2\partial t^2}=\omega^2k^2\tilde{\phi}-i\omega^2k\left(\frac{\partial A}{\partial x}e^{i(kx-\omega t)}+c.c.\right)\ . \tag{B.24}$$

Link to ToC

An approximation of the wave numbers in terms of the cut-off (ω_c)and plasma frequencies (ω_j) of the line, assuming the operating frequency is well below both ($\omega \ll \omega_j, \omega_c$), allows us to further simplify this.

$$k \simeq \arccos\left(1 + \frac{Z_1}{2Z_2}\right) \simeq \sqrt{\frac{Z_1}{2Z2}} \tag{B.25}$$

For a linear transmission line (without the $\chi^{(2)}$ and $\chi^{(3)}$ non-linear terms) we then have:

$$k = \frac{\omega}{\omega_c} \frac{1}{\sqrt{1 - \omega^2/\omega_j^2}} \ . \tag{B.26}$$

This allows the wave equation rewritten for the Ansatz of Equation B.19 as:

$$\overbrace{\left[\frac{\omega^2}{\omega_c^2} + \frac{\omega^2 k^2}{\omega_j^2} - k^2\right]}^{=0} \tilde{\phi} \ - \ \left[\frac{1+\omega^2}{\omega_j^2}\right] \left(ik\frac{\partial A}{\partial x} e^{i(kx-\omega t)} + c.c.\right) + \tag{B.27}$$

$$+ \ 2\chi^{(2)} \frac{\partial}{\partial x}\left(\frac{\partial \tilde{\varphi}}{\partial x}\right)^2 + 3\chi^{(3)} \frac{\partial}{\partial x}\left(\frac{\partial \tilde{\varphi}}{\partial x}\right)^3 = 0 \ . \tag{B.28}$$

This leaves us with:

$$\left[ik\frac{dA}{dx} e^{i(kx-\omega t)} + \text{c.c.}\right] = \chi^{(2)} \frac{\partial}{\partial x}\left(\frac{\partial \phi}{\partial x}\right)^2 + \chi^{(3)} \frac{\partial}{\partial x}\left(\frac{\partial \phi}{\partial x}\right)^3 \ , \tag{B.29}$$

from which coupled mode equations can easily be derived as described in Section 2.3.

Appendix C

Coupled Mode Equation Derivation

C.1

Coupled Mode Equation Simulations

A derivative to describe how amplification occurs in a travelling wave structure will take the form of change in amplitude, A_n for wave n as it moves through the medium in the x-direction. This is shown by Manley-Rowe in their seminal papers on the work [17, 65]. To derive the coupled mode equations which model how waves mix in the medium we begin with equation 2.20 and make the approximations that the amplitude changes only in distance and not in time, and that the derivatives of the amplitude in space are much smaller than the amplitude itself.

Coupled Mode Equations

We can formulate coupled mode equations to describe the mixing of the minimal amount of waves viable for wave mixing, a pump, signal and a generated idler wave at the difference frequency.

$$\phi = \begin{cases} 1/2\left(A_p e^{i(\omega_p t - k_p x)} + A_p^* e^{-i(\omega_p t - k_p x)}\right) \\ + \\ 1/2\left(A_s e^{i(\omega_s t - k_s x)} + A_s^* e^{-i(\omega_s t - k_s x)}\right) \\ + \\ 1/2\left(A_i e^{i(\omega_i t - k_i x)} + A_i^* e^{-i(\omega_i t - k_i x)}\right) \end{cases} \tag{C.1}$$

Link to ToC

These waves mix as they travel through the medium, mediated by either the $\chi^{(2)}$ or $\chi^{(3)}$ nonlinearity. The formulation of these coupled mode equations is fairly trivial, especially for the ideal case of only the bare minimum three mixing terms of pump, signal and idler propagating in the device.

$$\begin{aligned}\frac{\partial\phi}{\partial x} &= 1/2\Big\{ik_pA_pe^{i(\omega_pt+k_px)} + \frac{\partial A_p}{\partial x}e^{i(\omega_pt+k_px)} \\ &+ik_sA_se^{i(\omega_st+k_sx)} + \frac{\partial A_s}{\partial x}e^{i(\omega_st+k_sx)} \\ &+ik_iA_ie^{i(\omega_it+k_ix)} + \frac{\partial A_i}{\partial x}e^{i(\omega_it+k_ix)} + c.c.\Big\}\end{aligned} \tag{C.2}$$

$$\begin{aligned}\frac{\partial\phi}{\partial x} &= 1/2\Big\{ik_pA_pe^{i(k_px-\omega_pt)} - ik_pA_p^*e^{-i(k_px-\omega_pt)} \\ &+ik_sA_se^{i(k_sx-\omega_st)} - ik_sA_s^*e^{-i(k_sx-\omega_st)} \\ &+ik_iA_ie^{i(k_ix-\omega_it)} - ik_iA_i^*e^{-i(+k_ix-\omega_it)}\Big\}\end{aligned} \tag{C.3}$$

C.1.1 3WM Expansion

Then, using 2.21 again we can neglect the differential terms. Then the square of this gives us the 3WM terms from which we can formulate CME's.

$$\begin{aligned}\left(\frac{\partial\phi}{\partial x}\right)^2 &= 1/4\Big(-k_p^2A_p^2e^{i(\kappa_{2p}x-\Omega_{2p}t)} + k_p^2A_pA_p^*e^{i(\kappa_0x-\Omega_0t)} \\ &-k_pk_sA_pA_se^{i(\kappa_{p+s}x-\Omega_{p+s}t)} + k_pk_sA_pA_s^*e^{i(\kappa_{p-s}x)-\Omega_{p-s}t} \\ &-k_pk_iA_pA_ie^{i(\kappa_{p+i}x-\Omega_{p+i}t)} + k_pk_iA_pA_i^*e^{i(\kappa_{p-i}x-\Omega_{p-i}t)} \\ &+k_p^2A_pA_p^*e^{i(\kappa_0x-\Omega_0t)} - k_p^2A_p^{*2}e^{-i(\kappa_{2p}x-\Omega_{2p}t)} \\ &+k_pk_sA_p^*A_se^{-i(\kappa_{p-s}x-\Omega_{p-s}t)} - k_pk_sA_p^*A_s^*e^{-i(\kappa_{p+s}x-\Omega_{p+s}t)} \\ &+k_pk_iA_p^*A_ie^{-i(\kappa_{p-i}x-\Omega_{p-i}t)} - k_pk_iA_p^*A_i^*e^{-i(\kappa_{p+i}x-\Omega_{p+i}t)} \\ &-k_pk_sA_pA_se^{i(\kappa_{p+s}x-\Omega_{p+s}t)} + k_pk_sA_p^*A_se^{-i(\kappa_{p-s}x-\Omega_{p-s}t)} \\ &-k_s^2A_s^2e^{i(\kappa_{2s}x-\Omega_{2s}t} + k_s^2A_sA_s^*e^{i(\kappa_0x-\Omega_0t)} \\ &-k_sk_iA_sA_ie^{i(\kappa_{s+i}x-\Omega_{s+i}t)} + k_sk_iA_sA_i^*e^{i(\kappa_{s-i}x-\Omega_{s-i}t)} \\ &+k_sk_pA_s^*A_pe^{i(\kappa_{p-s}x-\Omega_{p-s}t)} - k_pk_sA_p^*A_s^*e^{-i(\kappa_{p+s}x-\Omega_{p+s}t)} \\ &+k_s^2A_sA_s^*e^{i(\kappa_0x-\Omega_0t)} - k_s^2A_s^{*2}e^{-i(\kappa_{2s}x-\Omega_{2s}t)} \\ &+k_sk_iA_s^*A_ie^{-i(\kappa_{s-i}x-\Omega_{s-i}t)} - k_sk_iA_s^*A_i^*e^{-i(\kappa_{s+i}x-\Omega_{s+i}t)} \\ &-k_pk_iA_pA_ie^{i(\kappa_{p+i}x-\Omega_{p+i}t)} + k_pk_iA_p^*A_ie^{-i(\kappa_{p-i}x-\Omega_{p-i}t)} \\ &-k_sk_iA_sA_ie^{i(\kappa_{s+i}x-\Omega_{s+i}t)} + k_sk_iA_s^*A_ie^{-i(\kappa_{s-i}x-\Omega_{s-i}t)} \\ &-k_i^2A_i^2e^{i(\kappa_{2i}x-\Omega_{2i}t)} + k_i^2A_iA_i^*e^{i(\kappa_0x-\Omega_0t)}\end{aligned}$$

$$
\begin{aligned}
&+k_p k_i A_i^* A_p e^{i(\kappa_{p-i}x-\Omega_{p-i}t)} - k_p k_i A_p^* A_i^* e^{-i(\kappa_{p+i}x-\Omega_{p+i}t)} \\
&+k_s k_i A_s A_i^* e^{i(\kappa_{s-i}x-\Omega_{s-i}t)} - k_s k_i A_s^* A_i^* e^{-i(\kappa_{s+i}x-\Omega_{s+i}t)} \\
&+k_i^2 A_i^* A_i e^{i(\kappa_0 x-\Omega_0 t)} - k_i^2 A_i^{*2} e^{-i(\kappa_{2i}x-\Omega_{2i}t)}\Big) \qquad \text{(C.4)}
\end{aligned}
$$

Sorted by common frequency, in the 3WM regime where $\omega_s = \Omega_{p-i}$, and removing the complex conjugate terms of the mixing products and optical rectification terms, we arrive at:

$$
\begin{aligned}
\left(\frac{\partial\phi}{\partial x}\right)^2 \;=\; & {}^1\!/_4\,\{-\overbrace{2k_s k_i A_s A_i e^{i(k_p x-\omega_p t)}}^{P} + \overbrace{2k_p k_i A_p A_i^* e^{i(k_s x-\omega_s t)}}^{S} \qquad \text{(C.5)} \\
&+\overbrace{2k_p k_s A_p^* A_s e^{i(k_i x-\omega_i t)}}^{\delta} - \overbrace{2k_p k_s A_p A_s e^{i(\kappa_\sigma x-\Omega_\sigma t)}}^{\sigma} \\
&-\overbrace{k_p^2 A_p^2 e^{i(\kappa_{2p}x-\Omega_{2p}t)}}^{2P} - \overbrace{k_s^2 A_s^2 e^{i(k_{2S}x-\omega_{2S}t}}^{2S} - \overbrace{k_i^2 A_i^2 e^{i(k_{2i}x-\omega_{2i}t)}}^{2I} \\
&-\overbrace{2k_p k_i A_p A_i e^{i(\kappa_{P+I}x-\Omega_{P+I}t)}}^{P+I} + \overbrace{2k_s k_i A_s A_i^* e^{i(\kappa_{S-I}x-\Omega_{S-I}t)}}^{S-I} \\
&+\mathbf{c.c.} + \mathbf{O.R.}\}\ . \qquad \text{(C.6)}
\end{aligned}
$$

C.1.2 4WM Expansion

The OR terms of Equation C.6 now mix with the propagating waves to alter the dispersion relation, in opposite action to the chromatic dispersion described in the previous section. Again, we consider only the three basic frequencies for wave mixing to occur, pump, signal and idler. We arrive at a differential equation for 4WM:

$$
\begin{aligned}
\left(\frac{\partial\phi}{\partial x}\right)^3 \;=\; & {}^1\!/_8\,\Big\{-ik_p^3 A_p^3 e^{i(\kappa_{3p}x-\Omega_{3p}t)} + ik_p^3 A_p^2 A_p^* e^{i(\kappa_p x-\Omega_p t)} \\
&-ik_p^2 k_s A_p^2 A_s e^{i(\kappa_{2p+s}x-\Omega_{2p+s}t)} + ik_p^2 k_s A_p^2 A_s^* e^{i(\kappa_{2p-s}x-\Omega_{2p-s}t)} \\
&-ik_p^2 k_i A_p^2 A_i e^{i(\kappa_{2p+i}x-\Omega_{2p+i}t)} + ik_p^2 k_i A_p^2 A_i^* e^{i(\kappa_{2p-i}x-\Omega_{2p-i}t)} \\
&+ik_p^3 A_p^2 A_p^* e^{i(\kappa_p x-\Omega_p t)} - ik_p^3 A_p A_p^{*2} e^{-i(\kappa_p x-\Omega_p t)} \\
&+ik_p^2 k_s A_p A_p^* A_s e^{i(\kappa_s x-\Omega_s t)} - ik_p^2 k_s A_p A_p^* A_s^* e^{-i(\kappa_s x-\Omega_s t)} \\
&+ik_p^2 k_i A_p A_p^* A_i e^{i(\kappa_i x-\Omega_i t)} - ik_p^2 k_i A_p A_p^* A_i^* e^{-i(\kappa_i x-\Omega_i t)} \\
&-ik_p^2 k_s A_p^2 A_s e^{i(\kappa_{2p+s}x-\Omega_{2p+s}t)} + ik_p^2 k_s A_p A_p^* A_s e^{i(\kappa_s x-\Omega_s t)} \\
&-ik_p k_s^2 A_p A_s^2 e^{i(\kappa_{p+2s}x-\Omega_{p+2s}t)} + ik_p k_s^2 A_p A_s A_s^* e^{i(\kappa_p x-\Omega_p t)} \\
&-ik_p k_s k_i A_p A_s A_i e^{i(\kappa_{p+s+i}x-\Omega_{p+s+i}t)} + ik_p k_s k_i A_p A_s A_i^* e^{i(\kappa_{p+s-i}x-\Omega_{p+s-i}t)} \\
&+ik_p^2 k_s A_s^* A_p^2 e^{i(\kappa_{2p-s}x-\Omega_{2p-s}t)} - ik_p^2 k_s A_p A_p^* A_s^* e^{-i(\kappa_s x-\Omega_s t)} \\
&+ik_p k_s^2 A_p A_s A_s^* e^{i(\kappa_p x-\Omega_p t)} - ik_p k_s^2 A_p A_s^{*2} e^{i(\kappa_{p-2s}x-\Omega_{p-2s}t)} \\
&+ik_p k_s k_i A_p A_s^* A_i e^{i(\kappa_{p-s+i}x-\Omega_{p-s+i}t)} - ik_p k_s k_i A_p A_s^* A_i^* e^{i(\kappa_{p-s-i}x-\Omega_{p-s-i}t)} \\
&-ik_p^2 k_i A_p^2 A_i e^{i(\kappa_{2p+i}x-\Omega_{2p+i}t)} + ik_p^2 k_i A_p A_p^* A_i e^{i(\kappa_i x-\Omega_i t)} \\
&-ik_p k_s k_i A_p A_s A_i e^{i(\kappa_{p+s+i}x-\Omega_{p+s+i}t)} + ik_p k_s k_i A_p A_s^* A_i e^{i(\kappa_{p-s+i}x-\Omega_{p-s+i}t)}
\end{aligned}
$$

$$
\begin{aligned}
&-ik_p k_i^2 A_p A_i^2 e^{i(\kappa_{p+2i}x-\Omega_{p+2i}t)} + ik_p k_i^2 A_p A_i A_i^* e^{i(\kappa_p x-\Omega_p t)} \\
&+ik_p^2 k_i A_i^* A_p^2 e^{i(\kappa_{2p-i}x-\Omega_{2p-i}t)} - ik_p^2 k_i A_p A_p^* A_i^* e^{-i(\kappa_i x-\Omega_i t)} \\
&+ik_p k_s k_i A_p A_s A_i^* e^{i(\kappa_{p+s-i}x-\Omega_{p+s-i}t)} - ik_p k_s k_i A_p A_s^* A_i^* e^{i(\kappa_{p-s-i}x-\Omega_{p-s-i}t)} \\
&+ik_p k_i^2 A_p A_i^* A_i e^{i(\kappa_p x-\Omega_p t)} - ik_p k_i^2 A_p A_i^{*2} e^{i(\kappa_{p-2i}x-\Omega_{p-2i}t)}
\end{aligned}
$$

+

$$
\begin{aligned}
&+ik_p^3 A_p^* A_p^2 e^{i(\kappa_p x-\Omega_p t)} - ik_p^3 A_p A_p^{*2} e^{-i(\kappa_p x-\Omega_p t)} \\
&+ik_p^2 k_s A_p A_p^* A_s e^{i(\kappa_s x-\Omega_s t)} - ik_p^2 k_s A_p^* A_p A_s^* e^{-i(\kappa_s x-\Omega_s t)} \\
&+ik_p^2 k_i A_p^* A_p A_i e^{i(\kappa_i x-\Omega_i t)} - ik_p^2 k_i A_p^* A_p A_i^* e^{-i(\kappa_i x-\Omega_i t)} \\
&-ik_p^3 A_p A_p^{*2} e^{-i(\kappa_p x-\Omega_p t)} + ik_p^3 A_p^{*3} e^{-i(\kappa_{3p} x-\Omega_{3p} t)} \\
&-ik_p^2 k_s A_p^{*2} A_s e^{-i(\kappa_{2p-s}x-\Omega_{2p-s}t)} + ik_p^2 k_s A_p^{*2} A_s^* e^{-i(\kappa_{2p+s}x-\Omega_{2p+s}t)} \\
&-ik_p^2 k_i A_p^{*2} A_i e^{-i(\kappa_{2p-i}x-\Omega_{2p-i}t)} + ik_p^2 k_i A_p^{*2} A_i^* e^{-i(\kappa_{2p+i}x-\Omega_{2p+i}t)} \\
&+ik_p^2 k_s A_p^* A_p A_s e^{i(\kappa_s x-\Omega_s t)} - ik_p^2 k_s A_p^{*2} A_s e^{-i(\kappa_{2p-s}x-\Omega_{2p-s}t)} \\
&+ik_p k_s^2 A_p^* A_s^2 e^{-i(\kappa_{p-2s}x-\Omega_{p-2s}t)} - ik_p k_s^2 A_p^* A_s A_s^* e^{-i(\kappa_p x-\Omega_p t)} \\
&+ik_p k_s k_i A_p^* A_s A_i e^{-i(\kappa_{p-s-i}x-\Omega_{p-s-i}t)} - ik_p k_s k_i A_p^* A_s A_i^* e^{-i(\kappa_{p-s+i}x-\Omega_{p-s+i}t)} \\
&-ik_p^2 k_s A_p^* A_s^* A_p e^{-i(\kappa_s x-\Omega_s t)} + ik_p^2 k_s A_p^{*2} A_s^* e^{-i(\kappa_{2p+s}x-\Omega_{2p+s}t)} \\
&-ik_p k_s^2 A_p^* A_s A_s^* e^{-i(\kappa_p x-\Omega_p t)} + ik_p k_s^2 A_p^* A_s^{*2} e^{-i(\kappa_{p+2s}x-\Omega_{p+2s}t)} \\
&-ik_p k_s k_i A_p^* A_s^* A_i e^{-i(\kappa_{p+s-i}x-\Omega_{p+s-i}t)} + ik_p k_s k_i A_p^* A_s^* A_i^* e^{-i(\kappa_{p+s+i}x-\Omega_{p+s+i}t)} \\
&+ik_p^2 k_i A_p^* A_p A_i e^{i(\kappa_i x-\Omega_i t)} - ik_p^2 k_i A_p^{*2} A_i e^{-i(\kappa_{2p-i}x-\Omega_{2p-i}t)} \\
&+ik_p k_s k_i A_p^* A_s A_i e^{-i(\kappa_{p-s-i}x-\Omega_{p-s-i}t)} - ik_p k_s k_i A_p^* A_s^* A_i e^{-i(\kappa_{p+s-i}x-\Omega_{p+s-i}t)} \\
&+ik_p k_i^2 A_p^* A_i^2 e^{-i(\kappa_{p-2i}x-\Omega_{p-2i}t)} - ik_p k_i^2 A_p^* A_i A_i^* e^{-i(\kappa_p x-\Omega_p t)} \\
&-ik_p^2 k_i A_p^* A_i^* A_p e^{-i(\kappa_i x-\Omega_i t)} + ik_p k_i A_p^{*2} A_i^* e^{-i(\kappa_{2p+i}x-\Omega_{2p+i}t)} \\
&-ik_p k_s k_i A_p^* A_s A_i^* e^{-i(\kappa_{p-s+i}x-\Omega_{p-s+i}t)} + ik_p k_s k_i A_p^* A_s^* A_i^* e^{-i(\kappa_{p+s+i}x-\Omega_{p+s+i}t)} \\
&-ik_p k_i^2 A_p^* A_i^* A_i e^{-i(\kappa_p x-\Omega_p t)} + ik_p k_i^2 A_p^* A_i^{*2} e^{-i(\kappa_{p+2i}x-\Omega_{p+2i}t)}
\end{aligned}
$$

+

$$
\begin{aligned}
&-ik_s k_p^2 A_s A_p^2 e^{i(\kappa_{2p+s}x-\Omega_{2p+s}t)} + ik_s k_p^2 A_s A_p A_p^* e^{i(\kappa_s x-\Omega_s t)} \\
&-ik_s^2 k_p A_p A_s^2 e^{i(\kappa_{p+2s}x-\Omega_{p+2s}t)} + ik_s^2 k_p A_p A_s A_s^* e^{i(\kappa_p x-\Omega_p t)} \\
&-ik_s k_p k_i A_s A_p A_i e^{i(\kappa_{p+s+i}x-\Omega_{p+s+i}t)} + ik_s k_p k_i A_s A_p A_i^* e^{i(\kappa_{p+s-i}x-\Omega_{p+s-i}t)} \\
&+ik_s k_p^2 A_s A_p A_p^* e^{i(\kappa_s x-\Omega_s t)} - ik_s k_p^2 A_s A_p^{*2} e^{-i(\kappa_{2p-s}x-\Omega_{2p-s}t)} \\
&+ik_s^2 k_p A_p^* A_s^2 e^{-i(\kappa_{p-2s}x-\Omega_{p-2s}t)} - ik_s^2 k_p A_p A_s^2 e^{-i(\kappa_{p+2s}x-\Omega_{p+2s}t)} \\
&+ik_s k_p k_i A_s A_p^* A_i e^{-i(\kappa_{p-s-i}x-\Omega_{p-s-i}t)} - ik_s k_p k_i A_s A_p^* A_i^* e^{-i(\kappa_{p-s+i}x-\Omega_{p-s+i}t)} \\
&-ik_s^2 k_p A_p A_s^2 e^{i(\kappa_{p+2s}x-\Omega_{p+2s}t)} + ik_p k_s^2 A_p^* A_s^2 e^{-i(\kappa_{p-2s}x-\Omega_{p-2s}t)} \\
&-ik_s^3 A_s^3 e^{i(\kappa_{3s}x-\Omega_{3s}t)} + ik_s^3 A_s^2 A_s^* e^{i(\kappa_s x-\Omega_s t)} \\
&-ik_s^2 k_i A_s^2 A_i e^{i(\kappa_{2s+i}x-\Omega_{2s+i}t)} + ik_s^2 k_i A_s^2 A_i^* e^{i(\kappa_{2s-i}x-\Omega_{2s-i}t)} \\
&+ik_s^2 k_p A_s A_s^* A_p e^{i(\kappa_p x-\Omega_p t)} - ik_p k_s^2 A_p^* A_s A_s^* e^{-i(\kappa_p x-\Omega_p t)} \\
&+ik_s^3 A_s^2 A_s^* e^{i(\kappa_s x-\Omega_s t)} - ik_s^3 A_s A_s^{*2} e^{-i(\kappa_s x-\Omega_s t)} \\
&+ik_s^2 k_i A_s A_s^* A_i e^{i(\kappa_i x-\Omega_i t)} - ik_s^2 k_i A_s A_s^* A_i^* e^{-i(\kappa_i x-\Omega_i t)}
\end{aligned}
$$

$$
\begin{aligned}
&-ik_sk_pk_iA_sA_pA_ie^{i(\kappa_{p+s+i}x-\Omega_{p+s+i}t)} + ik_sk_pk_iA_sA_p^*A_ie^{-i(\kappa_{p-s-i}x-\Omega_{p-s-i}t)}\\
&-ik_s^2k_iA_s^2A_ie^{i(\kappa_{2s+i}x-\Omega_{2s+i}t)} + ik_s^2k_iA_sA_s^*A_ie^{i(\kappa_ix-\Omega_it)}\\
&-ik_sk_i^2A_sA_i^2e^{i(\kappa_{s+2i}x-\Omega_{s+2i}t)} + ik_sk_i^2A_sA_iA_i^*e^{i(\kappa_sx-\Omega_st)}\\
&+ik_sk_pk_iA_sA_i^*A_pe^{i(\kappa_{p+s-i}x-\Omega_{p+s-i}t)} - ik_sk_pk_iA_p^*A_sA_i^*e^{-i(\kappa_{p-s+i}x-\Omega_{p-s+i}t)}\\
&+ik_s^2k_iA_s^2A_i^*e^{i(\kappa_{2s-i}x-\Omega_{2s-i}t)} - ik_s^2k_iA_sA_s^*A_i^*e^{-i(\kappa_ix-\Omega_it)}\\
&+ik_sk_i^2A_sA_i^*A_ie^{i(\kappa_sx-\Omega_st)} - ik_sk_i^2A_sA_i^{*2}e^{i(\kappa_{s-2i}x-\Omega_{s-2i}t)}\\
+&\\
&+ik_sk_p^2A_s^*A_p^2e^{i(\kappa_{2p-s}x-\Omega_{2p-s}t)} - ik_sk_p^2A_s^*A_pA_p^*e^{-i(\kappa_sx-\Omega_st)}\\
&-ik_pk_s^2A_pA_s^*A_se^{i(\kappa_px-\Omega_pt)} - ik_pk_s^2A_pA_s^{*2}e^{i(\kappa_{p-2s}x-\Omega_{p-2s}t)}\\
&+ik_sk_pk_iA_s^*A_pA_ie^{i(\kappa_{p-s+i}x-\Omega_{p-s+i}t)} - ik_sk_pk_iA_s^*A_pA_i^*e^{i(\kappa_{p-s-i}x-\Omega_{p-s-i}t)}\\
&-ik_sk_p^2A_s^*A_pA_p^*e^{-i(\kappa_sx-\Omega_st)} + ik_sk_p^2A_s^*A_p^{*2}e^{-i(\kappa_{2p+s}x-\Omega_{2p+s}t)}\\
&-ik_pk_s^2A_p^*A_s^*A_se^{-i(\kappa_px-\Omega_pt)} + ik_pk_s^2A_p^*A_s^{*2}e^{-i(\kappa_{p+s}x-\Omega_{p+s}t)}\\
&-ik_sk_pk_iA_s^*A_p^*A_ie^{-i(\kappa_{p+s-i}x-\Omega_{p+s-i}t)} + ik_sk_pk_iA_s^*A_p^*A_i^*e^{-i(\kappa_{p+s+i}x-\Omega_{p+s+i}t)}\\
&+ik_pk_s^2A_pA_s^*A_se^{i(\kappa_px-\Omega_pt)} - ik_pk_s^2A_p^*A_s^*A_se^{-i(\kappa_px-\Omega_pt)}\\
&+ik_s^3A_s^2A_s^*e^{i(\kappa_sx-\Omega_st)} - ik_s^3A_sA_s^{*2}e^{-i(\kappa_sx-\Omega_st)}\\
&+ik_s^2k_iA_s^*A_sA_ie^{i(\kappa_ix-\Omega_it)} - ik_s^2k_iA_s^*A_sA_i^*e^{-i(\kappa_ix-\Omega_it)}\\
&-ik_s^2k_pA_s^{*2}A_pe^{i(\kappa_{p-2s}x-\Omega_{p-2s}t)} + ik_pk_s^2A_p^*A_s^{*2}e^{-i(\kappa_{p+2s}x-\Omega_{p+2s}t)}\\
&-ik_s^3A_sA_s^{*2}e^{-i(\kappa_sx-\Omega_st)} + ik_s^3A_s^{*3}e^{-i(\kappa_{3s}x-\Omega_{3s}t)}\\
&-ik_s^2k_iA_s^{*2}A_ie^{-i(\kappa_{2s-i}x-\Omega_{2s-i}t)} + ik_s^2k_iA_s^{*2}A_i^*e^{-i(\kappa_{2s+i}x-\Omega_{2s+i}t)}\\
&+ik_sk_pk_iA_s^*A_pA_ie^{i(\kappa_{p-s+i}x-\Omega_{p-s+i}t)} + ik_sk_pk_iA_p^*A_s^*A_ie^{-i(\kappa_{p+s-i}x-\Omega_{p+s-i}t)}\\
&+ik_s^sk_iA_s^*A_sA_ie^{i(\kappa_ix-\Omega_it)} + ik_s^2k_iA_s^{*2}A_ie^{-i(\kappa_{2s-i}x-\Omega_{2s-i}t)}\\
&+ik_sk_i^2A_s^*A_i^2e^{-i(\kappa_{s-2i}x-\Omega_{s-2i}t)} + ik_sk_i^2A_s^*A_iA_i^*e^{-i(\kappa_sx-\Omega_st)}\\
&-ik_sk_pk_iA_s^*A_i^*A_pe^{i(\kappa_{p-s-i}x-\Omega_{p-s-i}t)} + ik_sk_pk_iA_s^*A_p^*A_i^*e^{-i(\kappa_{p+s+i}x-\Omega_{p+s+i}t)}\\
&-ik_s^2k_iA_sA_s^*A_i^*e^{-i(\kappa_ix-\Omega_it)} + ik_s^2k_iA_s^{*2}A_i^*e^{-i(\kappa_{2s+i}x-\Omega_{2s+i}t)}\\
&-ik_sk_i^2A_s^*A_i^*A_ie^{-i(\kappa_sx-\Omega_st)} - ik_sk_i^2A_s^*A_i^{*2}e^{-i(\kappa_{s+2i}x-\Omega_{s+2i}t)}\\
+&\\
&-ik_ik_p^2A_iA_p^2e^{i(\kappa_{2p+i}x-\Omega_{2p+i}t)} + ik_ik_p^2A_iA_pA_p^*e^{i(\kappa_ix-\Omega_it)}\\
&-ik_ik_pk_sA_iA_pA_se^{i(\kappa_{p+s+i}x-\Omega_{p+s+i}t)} + ik_ik_pk_sA_iA_pA_s^*e^{i(\kappa_{p-s+i}x-\Omega_{p-s+i}t)}\\
&-ik_pk_i^2A_pA_i^2e^{i(\kappa_{p+2i}x-\Omega_{p+2i}t)} + ik_pk_i^2A_pA_i^*A_ie^{i(\kappa_px-\Omega_pt)}\\
&+ik_ik_p^2A_iA_pA_p^*e^{i(\kappa_ix-\Omega_it)} - ik_ik_p^2A_iA_p^{*2}e^{-i(\kappa_{2p-i}x-\Omega_{2p-i}t)}\\
&+ik_ik_pk_sA_iA_p^*A_se^{-i(\kappa_{p-s-i}x-\Omega_{p-s-i}t)} - ik_ik_pk_sA_iA_p^*A_s^*e^{-i(\kappa_{p+s-i}x-\Omega_{p+s-i}t)}\\
&+ik_i^2k_pA_p^*A_i^2e^{-i(\kappa_{p-2i}x-\Omega_{p-2i}t)} - ik_pk_i^2A_p^*A_iA_i^*e^{-i(\kappa_px-\Omega_pt)}\\
&-ik_ik_pk_sA_iA_pA_se^{i(\kappa_{p+s+i}x-\Omega_{p+s+i}t)} + ik_ik_pk_sA_iA_p^*A_se^{-i(\kappa_{p-s-i}x-\Omega_{p-s-i}t)}\\
&-ik_ik_s^2A_iA_s^2e^{i(\kappa_{2s+i}x-\Omega_{2s+i}t)} + ik_ik_s^2A_iA_sA_s^*e^{i(\kappa_ix-\Omega_it)}\\
&-ik_sk_i^2A_sA_i^2e^{i(\kappa_{s+2i}x-\Omega_{s+2i}t)} + ik_sk_i^2A_sA_iA_i^*e^{i(\kappa_sx-\Omega_st)}\\
&+ik_ik_sk_pA_iA_s^*A_pe^{i(\kappa_{p-s+i}x-\Omega_{p-s+i}t)} - ik_ik_pk_sA_iA_p^*A_s^*e^{-i(\kappa_{p+s-i}x-\Omega_{p+s-i}t)}
\end{aligned}
$$

$$
\begin{aligned}
&+ik_ik_s^2A_iA_sA_s^*e^{i(\kappa_ix-\Omega_it)} - ik_ik_s^2A_iA_s^{*2}e^{-i(\kappa_{2s-i}x-\Omega_{2s-i}t)}\\
&+ik_sk_i^2A_s^*A_i^2e^{-i(\kappa_{s-i2}x-\Omega_{s-2i}t)} - ik_sk_i^2A_s^*A_iA_i^*e^{-i(\kappa_sx-\Omega_st)}\\
&-ik_pk_i^2A_pA_i^2e^{i(\kappa_{p+2i}x-\Omega_{p+2i}t)} + ik_pk_i^2A_p^*A_i^2e^{-i(\kappa_{p-2i}x-\Omega_{p-2i}t)}\\
&-ik_sk_i^2A_sA_i^2e^{i(\kappa_{s+2i}x-\Omega_{s+2i}t)} + ik_sk_i^2A_s^*A_i^2e^{-i(\kappa_{s-2i}x-\Omega_{s-2i}t)}\\
&-ik_i^3A_i^3e^{i(\kappa_{3i}x-\Omega_{3i}t)} + ik_i^3A_i^2A_i^*e^{i(\kappa_ix-\Omega_it)}\\
&+ik_pk_i^2A_i^*A_iA_pe^{i(\kappa_px-\Omega_pt)} - ik_pk_i^2A_p^*A_i^*A_ie^{-i(\kappa_px-\Omega_pt)}\\
&+ik_sk_i^2A_sA_iA_i^*e^{i(\kappa_sx-\Omega_st)} - ik_sk_i^2A_s^*A_i^*A_ie^{-i(\kappa_sx-\Omega_st)}\\
&+ik_i^3A_i^*A_i^2e^{i(\kappa_ix-\Omega_it)} - ik_i^3A_i^{*2}A_ie^{-i(\kappa_ix-\Omega_it)}
\end{aligned}
$$

$+$

$$
\begin{aligned}
&+ik_ik_p^2A_i^*A_p^2e^{i(\kappa_{2p-i}x-\Omega_{2p-i}t)} - ik_ik_p^2A_i^*A_pA_p^*e^{-i(\kappa_ix-\Omega_it)}\\
&+ik_ik_pk_sA_i^*A_pA_se^{i(\kappa_{p+s-i}x-\Omega_{p+s-i}t)} - ik_ik_pk_sA_pA_s^*A_i^*e^{i(\kappa_{p-s-i}x-\Omega_{p-s-i}t)}\\
&+ik_ik_pA_pA_iA_i^*e^{i(\kappa_px-\Omega_pt)} - ik_i^2k_pA_pA_i^{*2}e^{i(\kappa_{p-2i}x-\Omega_{p-2i}t)}\\
&-ik_ik_p^2A_i^*A_pA_p^*e^{-i(\kappa_ix-\Omega_it)} + ik_ik_p^2A_i^*A_p^{*2}e^{-i(\kappa_{2p+i}x-\Omega_{2p+i}t)}\\
&-ik_ik_pk_sA_i^*A_p^*A_se^{-i(\kappa_{p-s+i}x-\Omega_{p-s+i}t)} + ik_ik_pk_sA_i^*A_p^*A_s^*e^{-i(\kappa_{p+s+i}x-\Omega_{p+s+i}t)}\\
&-ik_i^2k_pA_p^*A_iA_i^*e^{-i(\kappa_px-\Omega_pt)} + ik_i^2k_pA_p^*A_i^{*2}e^{-i(\kappa_{p+2i}x-\Omega_{p+2i}t)}\\
&+ik_ik_pk_sA_i^*A_pA_se^{i(\kappa_{p+s-i}x-\Omega_{p+s-i}t)} - ik_ik_pk_sA_i^*A_p^*A_se^{-i(\kappa_{p-s+i}x-\Omega_{p-s+i}t)}\\
&+ik_ik_s^2A_i^*A_s^2e^{i(\kappa_{2s-i}x-\Omega_{2s-i}t)} - ik_ik_s^2A_i^*A_sA_s^*e^{-i(\kappa_ix-\Omega_it)}\\
&+ik_i^2k_sA_sA_iA_i^*e^{i(\kappa_sx-\Omega_st)} - ik_i^2k_sA_sA_i^{*2}e^{i(\kappa_{s-2i}x-\Omega_{s-2i}t)}\\
&-ik_ik_sk_pA_i^*A_s^*A_pe^{i(\kappa_{p-s-i}x-\Omega_{p-s-i}t)} + ik_ik_pk_sA_i^*A_p^*A_s^*e^{-i(\kappa_{p+s+i}x-\Omega_{p+s+i}t)}\\
&-ik_ik_s^2A_i^*A_sA_s^*e^{-i(\kappa_ix-\Omega_it)} + ik_ik_s^2A_i^*A_s^{*2}e^{-i(\kappa_{2s+i}x-\Omega_{2s+i}t)}\\
&-ik_i^2k_sA_i^*A_s^*A_ie^{-i(\kappa_sx-\Omega_st)} + ik_i^2k_sA_s^*A_i^{*2}e^{-i(\kappa_{s+2i}x-\Omega_{s+2i}t)}\\
&+ik_i^2k_pA_i^*A_pA_ie^{i(\kappa_px-\Omega_pt)} - ik_i^2k_pA_p^*A_i^*A_ie^{-i(\kappa_px-\Omega_pt)}\\
&+ik_i^2k_sA_sA_iA_i^*e^{i(\kappa_sx-\Omega_st)} - ik_i^2k_sA_s^*A_iA_i^*e^{-i(\kappa_sx-\Omega_st)}\\
&+ik_i^3A_i^2A_i^*e^{i(\kappa_ix-\Omega_it)} - ik_i^3A_iA_i^{*2}e^{-i(\kappa_ix-\Omega_it)}\\
&-ik_i^2k_pA_i^{*2}A_pe^{i(\kappa_{p-2i}x-\Omega_{p-2i}t)} + ik_i^2k_pA_p^*A_i^{*2}e^{-i(\kappa_{p+2i}x-\Omega_{p+2i}t)}\\
&-ik_i^2k_sA_sA_i^{*2}e^{i(\kappa_{s-2i}x-\Omega_{s-2i}t)} + ik_i^2k_sA_s^*A_i^{*2}e^{-i(\kappa_{s+2i}x-\Omega_{s+2i}t)}\\
&-ik_i^3A_i^{*2}A_ie^{-i(\kappa_ix-\Omega_it)} + ik_i^3A_i^{*3}e^{-i(\kappa_{3i}x-\Omega_{3i}t)}\Big\}\ . \qquad \text{(C.7)}
\end{aligned}
$$

We can then group by the mixing product, say the signal, and formulate an ordinary differential equation that describes the change of its amplitude along the x-axis of the metamaterial. The grouped terms for the 3WM and 4WM cases for only the basic three waves are:

$$
\begin{aligned}
\frac{\partial A_p}{\partial x} \;=\;& \frac{\chi^{(2)}}{2}e^{-i(k_px-\omega_pt)}\frac{\partial}{\partial x}\left[k_sk_\delta A_sA_\delta e^{i(\kappa_{s+\delta}x-\Omega_{s+\delta}t)}\right]\\
&\frac{\chi^{(3)}}{6}e^{-i(k_px-\omega_pt)}\frac{\partial}{\partial x}\left[6ik_pA_pe^{i(k_px-\omega_pt)}\left(\frac{1}{2}k_p^2A_pA_p^* + k_s^2A_sA_s^* + k_i^2A_iA_i^*\right)\right.\\
&\left.+ik_pk_sk_iA_p^*A_sA_ie^{i(\kappa_{s+i-p}x-\Omega_{s+i-p}t)}\right] \qquad \text{(C.8)}
\end{aligned}
$$

Link to ToC

(C.9)

$$\begin{aligned}
\frac{dA_s}{dx} &= \frac{\chi^{(2)}}{2}e^{-ik_s x}\left[k_p k_\delta A_p A_\delta e^{i((k_p-k_\delta)x-(\omega_p-\omega_\delta)t)}\right] \\
&+\frac{\chi^{(3)}}{6}e^{-ik_s x}\left[-6k_p^2k_s^2A_pA_p^*A_se^{i(k_sx-\omega_st)}\right. \\
&-6k_\Delta^2k_s^2A_\Delta A_\Delta^*A_se^{i(k_sx-\omega_st)} \\
&-3k_s^4A_s^2A_s^{*2}e^{i(k_sx-\omega_st)} \\
&\left.+k_\Delta k_p^2\left(2k_p-k_i\right)A_\Delta^*A_p^2e^{i((2k_p-k_\Delta)x-(2\omega_p-\omega_i)t)}\right] \qquad \text{(C.10)} \\
\frac{dA_\delta}{dx} &= \frac{\chi^{(2)}}{2}e^{-ik_\delta x}\left(k_p-k_s\right)\left[k_pk_sA_pA_se^{i((k_p-k_s)x-(\omega_p-\omega_s)t)}\right] \qquad \text{(C.11)} \\
\frac{dA_\Delta}{dx} &= \frac{\chi^{(3)}}{6}e^{-ik_\Delta x}\left[-6k_p^2k_\Delta^2A_pA_p^*A_\Delta e^{i(k_\Delta x-\omega_\Delta t)}\right. \\
&-6k_s^2k_\Delta^2A_sA_s^*A_\Delta e^{i(k_\Delta x-\omega_\Delta t)} \\
&-3k_\Delta^4A_\Delta^2A_\Delta^{*2}e^{i(k_\Delta x-\omega_st)} \\
&\left.+k_sk_p^2\left(2k_p-k_s\right)A_s^*A_p^2e^{i((2k_p-k_s)x-(2\omega_p-\omega_s)t)}\right] \qquad \text{(C.12)}
\end{aligned}$$

We have made a distinction between the 3WM and 4WM idlers using δ and Δ to denote them, respectively. The change in a wave's amplitude is equal to the product of the waves that mix to form it at that point in the metamaterial.

If we assume that $A_p \gg A_s, A_\delta, A_\Delta$ we can simplify the above relations to:

$$\begin{aligned}
\frac{dA_p}{dx} &= -\frac{\chi^{(3)}}{6}3k_p^4A_p^2A_p^{*2} \qquad \text{(C.13)} \\
&\Rightarrow A_p = A_{p_0}e^{-i\chi^{(3)}k_p^4A_p^3/2} \qquad \text{(C.14)} \\
\frac{dA_s}{dx} &= \frac{\chi^{(2)}}{2}e^{-ik_s x}\left(k_p-k_\delta\right)\left[k_pk_\delta A_pA_\delta e^{i((k_p-k_\delta)x-(\omega_p-\omega_\delta)t)}\right] \\
&+\frac{\chi^{(3)}}{6}e^{-ik_s x}\left[-6k_p^2k_s^2A_pA_p^*A_se^{i(k_sx-\omega_st)}\right. \\
&\left.+k_\Delta k_p^2\left(2k_p-k_i\right)A_\Delta^*A_p^2e^{i((2k_p-k_\Delta)x-(2\omega_p-\omega_i)t}\right]\ , \qquad \text{(C.15)} \\
\frac{dA_\delta}{dx} &= \frac{\chi^{(2)}}{2}e^{-ik_\delta x}\left[k_pk_sA_pA_se^{i(k_p-k_s)x}\right] \qquad \text{(C.16)} \\
\frac{dA_\Delta}{dx} &= \frac{\chi^{(3)}}{6}e^{-ik_\Delta x}\left[-6k_p^2k_\Delta^2A_pA_p^*A_\Delta e^{i(k_\Delta x-\omega_\Delta t)}\right. \\
&\left.+k_sK_p^2\left(2k_p-k_s\right)A_s^*A_p^2e^{i((2k_p-k_s)x-(2\omega_p-\omega_s)t}\right] \qquad \text{(C.17)}
\end{aligned}$$

Link to ToC

Appendix D

Gain Relation Derivation

The most simple case of only the pump, signal and idler waves propagating can have an analytical solution found for it in either the three- or four-wave mixing regimes. Generally this does not match simulated or experimental performance, but it can still be a useful tool for comparison of proposals. For the 3WM case, we start with:

$$\vartheta_{SPM} = \frac{3\chi^{(3)}}{8} k_p^3 A_p A_p^* \tag{D.1}$$

$$\vartheta_{XPM} = \frac{6\chi^{(3)}}{8} k_{s,i} k_p^2 A_p A_p^* \tag{D.2}$$

$$\vartheta = \vartheta_{SPM} - \vartheta_{XPM_s} - \vartheta_{XPM_i} \tag{D.3}$$

$$\vartheta = \frac{3\chi^{(3)}}{8} k_p^3 A_p A_p^* - \frac{6\chi^{(3)}}{8} k_s k_p^2 A_p A_p^* - \frac{6\chi^{(3)}}{8} k_i k_p^2 A_p A_p^* \tag{D.4}$$

$$\vartheta = \frac{3\chi^{(3)}}{8} k_p^2 |A_p|^2 \left[k_p - 2k_s - 2k_i\right] \tag{D.5}$$

the nonlinear phase mismatch between the 3WM tones takes the form:

$$\vartheta_3 = -\vartheta_{SPM} \tag{D.6}$$

$$\vartheta_4 = -3\vartheta_{SPM} \tag{D.7}$$

Sub in strong pump approximation:

$$\frac{dA_p}{dx} = i\vartheta_3 A_p \tag{D.8}$$

$$\Rightarrow A_p = A_{p_0} e^{i\vartheta_3 x} \tag{D.9}$$

then the total phase mismatch will take the form: $\tilde{\kappa}_{3,4} = \kappa - \vartheta$.

Link to ToC

With these non-linear phase shifts due to the $\chi^{(3)}$ non-linearity we can then simplify Equations C.15 through C.17.

$$\frac{dA_s}{dx} = 2i\vartheta_3 A_s + \frac{\chi^{(2)}}{2} k_p k_\delta A_{p_0} A_\delta e^{i\tilde{\kappa}_3 x} + \frac{3\chi^{(3)}}{8} k_\Delta k_p^2 A_\Delta^* A_p^2 e^{i\tilde{\kappa}_4 x} \ , \tag{D.10}$$

$$\frac{dA_\delta}{dx} = 2i\vartheta_3 A_\delta + \frac{\chi^{(2)}}{2} k_p k_s A_{p_0} A_s^* e^{i\tilde{\kappa}_3 x} \tag{D.11}$$

$$\frac{dA_\Delta}{dx} = 2i\vartheta_3 A_\Delta + \frac{3\chi^{(3)}}{8} k_s k_p^2 A_s |A_{p_0}|^2 e^{i\tilde{\kappa}_4 x} \tag{D.12}$$

To find an analytical solution for signal gain we must rewrite the signal and idler amplitudes in the form:

$$\tilde{A}_s = A_s e^{-i2\vartheta x} \tag{D.13}$$

$$\tilde{A}_\delta = A_\delta e^{-i2\vartheta x} \tag{D.14}$$

$$\tilde{A}_\Delta = A_\Delta e^{-i2\vartheta x} \tag{D.15}$$

Incorporating these into the ODE's we get:

$$\begin{aligned} \frac{d\tilde{A}_s}{dx} =& -2i\vartheta_3 A_s e^{-i\vartheta_3 x} + \frac{dA_s}{dx} e^{-i\vartheta_3 x} \\ =& \frac{\chi^{(2)}}{4} k_p k_\delta A_{p_0} \tilde{A}_\delta^* e^{i\tilde{\kappa}_3 x} + \frac{\chi^{(3)}}{8} k_\Delta k_p^2 \tilde{A}_\Delta^* A_p^2 e^{i\tilde{\kappa}_4 x} \ , \end{aligned} \tag{D.16}$$

$$\begin{aligned} \frac{d\tilde{A}_\delta^*}{dx} =& -2i\vartheta_3 A_\delta e^{i\vartheta_3 x} + \frac{dA_\delta}{dx} e^{i\vartheta_3 x} \\ =& \frac{\chi^{(2)}}{4} k_p k_s \tilde{A}_s A_{p_0}^* e^{-i\tilde{\kappa}_3 x} \ , \end{aligned} \tag{D.17}$$

$$\begin{aligned} \frac{d\tilde{A}_\Delta^*}{dx} =& -2i\vartheta_3 A_\Delta e^{i\vartheta_3 x} + \frac{dA_\Delta}{dx} e^{i\vartheta_3 x} \\ =& \frac{\chi^{(3)}}{8} k_s k_p^2 \tilde{A}_s A_p^{*2} e^{-i\tilde{\kappa}_4 x} \ . \end{aligned} \tag{D.18}$$

Taking the second derivative of the signal amplitude, we arrive at:

$$\begin{aligned} \frac{d^2\tilde{A}_s}{dx^2} =& i\tilde{\kappa_3} \frac{\chi^{(2)}}{4} k_p k_\delta A_{p_0} \tilde{A}_\delta^* e^{i\tilde{\kappa}_3 x} + i\tilde{\kappa_4} \frac{\chi^{(3)}}{8} k_\Delta k_p^2 \tilde{A}_\Delta^* A_p^2 e^{i\tilde{\kappa}_4 x} \\ &+ \frac{\chi^{(2)}}{4} k_p k_\delta A_{p_0} \frac{d\tilde{A}_\delta^*}{dx} e^{i\tilde{\kappa}_3 x} + \frac{\chi^{(3)}}{8} k_\Delta k_p^2 A_p^2 \frac{d\tilde{A}_\Delta^*}{dx} e^{i\tilde{\kappa}_4 x} \ . \end{aligned} \tag{D.19}$$

Then, with the approximation of mostly linear dispersion, $\tilde{\kappa}_3 \approx \tilde{\kappa}_4 \equiv \tilde{\kappa}$, we form a wave equation in $\tilde{A}_s$:

$$\frac{d^2\tilde{A}_s}{dx^2} - i\tilde{\kappa}\frac{d\tilde{A}_s}{dx} - \left[\left(\frac{\chi^{(2)}}{4} k_p A_{p_0} \right)^2 k_s k_\delta + \left(\frac{\chi^{(3)}}{8} k_p^2 A_p^2 \right)^2 k_s k_\Delta \right] \tilde{A}_s = 0 \ . \tag{D.20}$$

This will have solutions of the form:

$$\tilde{A}_s = \left(\alpha_s e^{gx} - \beta_s e^{-gx}\right) e^{-i\kappa x/2} \ , \tag{D.21}$$

where $\lambda = -\frac{i\kappa}{2} \pm g$, and g, the gain factor is:

$$g = \pm \left[-\frac{\kappa^2}{4} + \left(\frac{\chi^{(2)}}{4} k_p A_{p_0} \right)^2 k_s k_\delta + \left(\frac{\chi^{(3)}}{8} k_p^2 A_p^2 \right)^2 k_s k_\Delta \right]^{1/2} \ . \tag{D.22}$$

Using the boundary condition that all waves are launched at $x = 0$, we can differentiate Equation D.20 to find:

$$\frac{d}{dx}\left[\left(\alpha_s e^{gx} - \beta_s e^{-gx}\right) e^{-i\kappa x/2}\right] = \frac{\chi^{(2)}}{4} k_p k_\delta A_{p_0} \tilde{A}_\delta^* e^{i\tilde{\kappa}_3 x} + \frac{\chi^{(3)}}{8} k_\Delta k_p^2 \tilde{A}_\Delta^* A_p^2 e^{i\tilde{\kappa}_4 x} \tag{D.23}$$

$$g\left(\alpha_s e^{gx} - \beta_s e^{-gx}\right) = \frac{i\kappa}{2}\left(\alpha_s e^{gx} + \beta_s e^{-gx}\right) + \frac{\chi^{(2)}}{4} k_p k_\delta A_{p_0} \tilde{A}_\delta^* e^{i\tilde{\kappa}_3 x} + \frac{\chi^{(3)}}{8} k_\Delta k_p^2 \tilde{A}_\Delta^* A_p^2 e^{i\tilde{\kappa}_4 x} \tag{D.24}$$

$$g\left(\alpha_s - \beta_s\right) = \frac{i\kappa}{2}\left(\alpha_s + \beta_s\right) + \frac{\chi^{(2)}}{4} k_p k_\delta A_{p_0} \tilde{A}_\delta^* + \frac{\chi^{(3)}}{8} k_\Delta k_p^2 \tilde{A}_\Delta^* A_p^2 \tag{D.25}$$

With

$$\alpha_s + \beta_s = \tilde{A}_s\left(0\right) \tag{D.26}$$

and $\beta = B - \alpha$, we can solve for α_s and β_s:

$$\alpha_s = \frac{1}{2}\left(1 + \frac{i\kappa}{2g}\right)\tilde{A}_s(0) + \overbrace{\frac{k_p A_{p_0}}{8g}\left[\chi^{(2)} k_\delta \tilde{A}_\delta^* + \frac{\chi^{(3)}}{2} k_\Delta k_p \tilde{A}_\Delta^* A_{p_0}\right]}^{K_0} \tag{D.27}$$

$$\beta_s = \frac{1}{2}\left(1 - \frac{i\kappa}{2g}\right)\tilde{A}_s(0) - \frac{k_p A_{p_0}}{8g}\left[\chi^{(2)} k_\delta \tilde{A}_\delta^* + \frac{\chi^{(3)}}{2} k_\Delta k_p \tilde{A}_\Delta^* A_{p_0}\right] \tag{D.28}$$

Now evaluated at a distance x from the start of the array:

$$\tilde{A}_s(x) = \left[\frac{1}{2}\left(1 + \frac{i\kappa}{2g}\right)\tilde{A}_s(0) + K_0\right] e^{gx} + \left[\frac{1}{2}\left(1 - \frac{i\kappa}{2g}\right)\tilde{A}_s(0) - K_0\right] e^{-gx} \tag{D.29}$$

$$\tilde{A}_s(x) = \left[\tilde{A}_s(0)\left(\cosh\left(gx\right) + \frac{i\kappa}{2g}\sinh\left(gx\right)\right) + 2K_0 \sinh\left(gx\right)\right] e^{-i\kappa x/2} \tag{D.30}$$

Then if we assume both idler waves have zero amplitude at the start of the array this can be simplified to the form stated commonly:

$$G_s = 1 + \sinh^2\left(\sqrt{1 - \delta^2} g_0 N\right) \tag{D.31}$$

or, equivalently,

$$G_s = \left| \cosh(gL) + \frac{i\Delta k}{2g} \sinh(gl) \right|^2 . \tag{D.32}$$


I CAN FEEL MY BRAIN BEGINNING TO ATROPHY ALREADY.
SHHH..